Gesellschaft für Anlagen- und Reaktorsicherheit (GRS) mbH

Software Package r^3t

Model for Transport and Retention in Porous Media

Final Report

GRS - 192

Gesellschaft für Anlagen- und Reaktorsicherheit (GRS) mbH

Software Package r^3t

Edited by
Eckhard Fein

April 2004

Acknowledgement:

The underlying work of this report was supported by the Federal Ministry of Economics and Labour (BMWA) under the identification number 02 E 9148/2 titled “Entwicklung eines Programms zur dreidimensionalen Modellierung des Schadstofftransportes”. The work was carried out under the auspices of GRS - Gesellschaft für Anlagen- und Reaktorsicherheit mbH.
Responsibility for the content of this publication lies solely with the authors.

GRS - 192
ISBN 3-931995-60-7

Acknowledgement

In this place we like to thank everyone who contributed with his work to the successful conclusion of the project “Entwicklung eines Programms zur dreidimensionalen Modellierung des Schadstofftransportes” and the accomplishment of this report.

In the first place the members of the working groups of Prof. Kinzelbach at ETH Zurich, Prof. Kröner at the University Freiburg, Prof. Rumpf at the University of Duisburg, and Prof. Wittum at the University of Heidelberg have to be mentioned. We say thank-you to them for their excellent and cooperative teamwork and their personal commitment which was far beyond the completion of their order.

As well we like to express our thanks to the members of the Final Repository Research Division of GRS for performing test case simulations and their consultation.

Last but not least we thank Prof. Brewitz, and Dr. Stock from GRS and as well Dr. Steininger from Forschungszentrum Karlsruhe who supported the realisation of the project.

Eckhard Fein

Abstract

In long-term safety analyses for final repositories for hazardous wastes in deep geological formations the impact to the biosphere due to potential release of hazardous materials is assessed for relevant scenarios. The model for migration of wastes from repositories to men is divided into three almost independent parts: the near field, the geosphere, and the biosphere.

With the development of r^3t the feasibility to model the pollutant transport through the geospere for porous or equivalent porous media in large, three-dimensional, and complex regions is established. Furthermore one has at present the ability to consider all relevant retention and interaction effects which are important for long-term safety analyses. These are equilibrium sorption, kinetically controlled sorption, diffusion into immobile pore waters, and precipitation. The processes of complexing, colloidal transport and matrix diffusion may be considered at least approximately by skilful choice of parameters. Speciation is not part of the very recently developed computer code r^3t.

With r^3t it is possible to assess the potential dilution and the barrier impact of the overburden close to reality.

The underlying work of this report was funded by The Federal Ministry of Economics and Labour under the identification number 02 E 9148 2 titled "Entwicklung eines Programms zur dreidimensionalen Modellierung des Schadstofftransportes" from October 1, 1998 until December 31, 2003. The project was carried out by a team of scientists of GRS and of four universities. The team includes members of the Institute of Hydromechanics and Water Resources Management of the Swiss Federal Institute of Technology in Zurich, Section Groundwater and Hydromechanics (Prof. Wolfgang Kinzelbach), of the Department of Mathematics of the University of Freiburg, Applied Mathematics (Prof. Dietmar Kröner), of the Department of Mathematics of the University of Duisburg-Essen, Numerical Analysis and Scientific Computing (Prof. Martin Rumpf), and of the Interdisciplinary Center of Scientific Computing of the University of Heidelberg, Technical Simulation Group (Prof. Gabriel Wittum).

This report is based on the final reports of the involved institutions [82], [89], [118] and [52]. Parts of the final reports were editorially revised and adopted into this report. Simultaneously a “User’s guide” and a “Test Case Library” are prepared besides this final report.

Table of Contents

1 Introduction

In long-term safety assessments for final repositories in deep geological formations the hazards of environmental impacts of potential releases of pollutants are evaluated for relevant scenarios. To describe the migration of pollutants from the repository to the biosphere the system is usually divided into three areas: the near-field, the geosphere, and the biosphere (cp. Fig. 1.1).

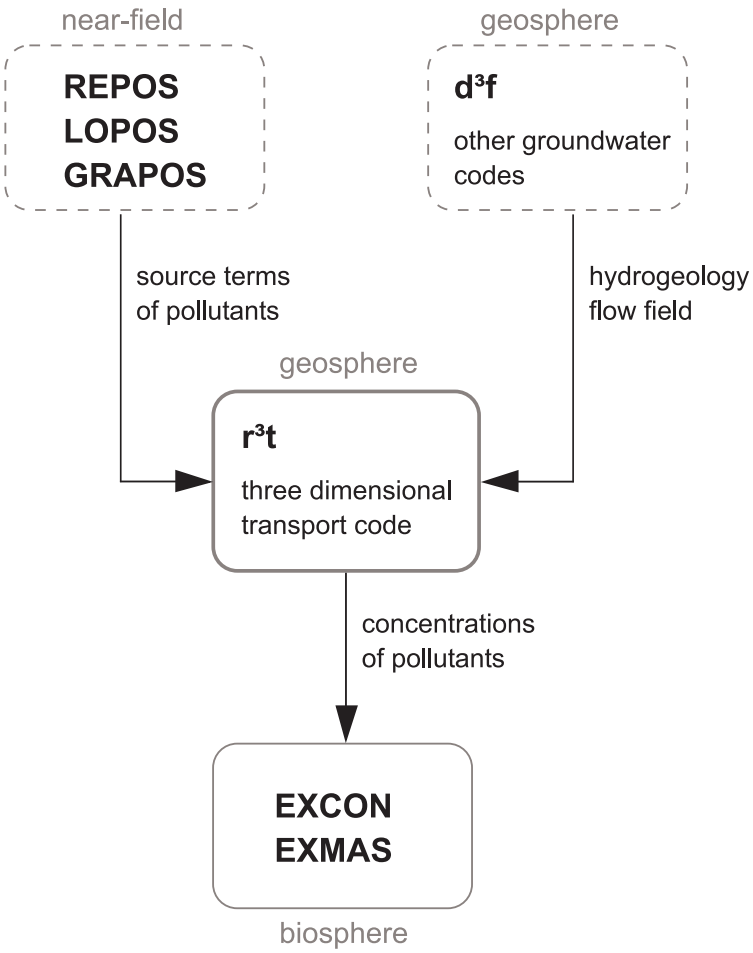

Fig. 1.1 Transport modelling through near field, geosphere, and biosphere
The code d^3f is a new development to model density-driven flow [45].

In Germany, the software package EMOS [128] is used for integral long term safety assessments for entire repository systems. This software can be used to treat repository systems both in deterministic and probabilistic ways. Within EMOS one can simulate the release of pollutants by means of the near-field modules REPOS, LOPOS, and GRAPOS,

the migration of pollutants through the geosphere by using CHET, and TRAPIC, and the exposure to pollutants by means of the biosphere modules EXCON, and EXMAS, respectively.

In previous safety assessments the migration of pollutants through the geosphere was generally simulated in a one-dimensional way. This is, among other things, caused by the fact that up to now no computer code able to consider all relevant retention processes simultaneously for large three-dimensional regions was available. For one-dimensional transport models one has to calculate the migration pathway from the velocity field of a three-dimensional flow model by using particle tracking algorithms. In previous safety assessments migration along such representative one-dimensional pathways took into account advection, diffusion, radioactive decay, longitudinal dispersion and the retention by adsorption.

To simulate the above specified one-dimensional pollutant transport through the geosphere the modules CHET (**CHE**mie und **T**ransport) [90] and TRAPIC (**TRA**nsport of **P**ollutants **I**nfluenced by **C**olloids) [95] are available. Because of the one-dimensional modelling of the migration pathways dilution due to transverse dispersion could only be considered approximately. Therefore, the concentration dependent sorption and precipitation processes are in particular reproduced only insufficiently.

During the analysis of the Projekt Sicherheitsstudien Entsorgung (PSE) [114] the 3d transport code SWIFT [3] was used to model of the pollutant transport through the overburden. To perform the transport simulations, a smaller modelling region was cut out of the original flow model. Again the same transport effects were taken into account and the retention was modelled by using the K_d-concept (Henry isotherm).

Existing three-dimensional transport codes are not applicable to model large regions and advanced retention effects for radionuclides and toxic pollutants, respectively. The SWIFT code is a finite difference code, and can be used for flow and transport simulations. However, due to the numerical algorithms which are not state of the art it is not possible to model large and heterogeneous regions three-dimensionally.

One-dimensional transport codes will in future be used in safety assessments simply to reduce CPU-times to acceptable values. However, for showing the validity of geometrically simplified models detailed deterministic simulations will be used for more thorough

analyses. The aim of these deterministic simulations is to show that the restriction to one dimension is sufficiently accurate and nearly close to reality. Therefore, performing 3d simulations for large regions considering all relevant retention effects is necessary. Furthermore it is important to deduce input parameters (like dilution, cross-section etc.) for one-dimensional simulations from three-dimensional calculations.

It was the main objective of the project to develop a computer code that is able to model transport of pollutants through porous and fractured-porous media for large and complex regions and to process all available retention data, respectively. A deeper understanding of the relevant retention processes on pollution transport is achievable with such a transport code.

2 The Task

2.1 State of Science and Technology

The software package EMOS [128] is used to perform deterministic or probabilistic long-term safety analyses. With EMOS the release of pollutants from the near field, the transport of pollutants through the geosphere, and the resultant radiation exposure in the biosphere can be assessed. To model the transport through the geosphere one-dimensionally, the modules CHET [90] and TRAPIC [95] are applied. Due to the one-dimensional modelling the dilution of the pollution concentration can be taken into account only approximately. Thus, the concentration dependent processes like sorption and precipitation are insufficiently reproduced.

For a three-dimensional modelling of pollution transport only the computer code SWIFT [3] is available in GRS. Beside the well-known effects advection, diffusion, and dispersion only radioactive decay and sorption after K_d-concept can be considered. Due to the special discretising methods used, modelling of hydrogeological features close to reality is very restricted.

The geometrical decomposition of heterogeneities can only be achieved by use of unstructured grids in context with effective solving algorithms for large systems of equations. In the range of density-driven flow modelling new ground was broken with the development of the computer code d^3f (**d**istributed **d**ensity **d**riven **f**low) [45]. For this code adaptive procedures, which locally refine or coarsen the grids according to the particular physical effects, and effective solving algorithms for linear and non-linear problems are developed for parallel computer architectures.

In long term safety analyses of other countries [102] transport through the geosphere is modelled predominantly one-dimensionally, too. Depending on the considered host rock formations computer codes for porous [64] and fractured media [102], [122], [132], [137] are applied. Every code takes into account advective and dispersive transport, linear equilibrium sorption, and radioactive decay even for decay chains. The codes used for modelling fractured media are based on double porosity models. Additionally the process of matrix diffusion is taken into consideration.

A two-dimensional modelling of pollutant transport is carried out for the safety analyses of the WIPP site [42]. Due to the much higher computing times in comparison with one-dimensional modelling the probabilistic simulations are only performed for a single nuclide instead of the whole spectrum of nuclides. Starting from the results for the single nuclide the release of the remaining nuclides were deduced.

In NAGRA a computer code to be used for long term safety analyses is developed which exceeds the one-dimensional modelling of transport. The computer code [123] can explicitly handle the transport within a network of intersecting fractures.

Within the safety analysis Kristallin I [102] the enhanced code RANCHMDNL was used to model sorption of cesium after Freundlich isotherm. Many experimental measurements show that beside cesium many other elements have a concentration dependent sorption [105].

2.2 Overall Objective

The overall objective of the project was the development of a computer code to simulate pollutant transport which has to meet the following demands:

- simulation of three-dimensional transport through porous or equivalently porous media,
- treatment of spacious and heterogeneous areas,
- consideration of advection, diffusion, and dispersion and interaction processes which are relevant to long-term safety analysis,
- applicability for radionuclide migration as well as for chemotoxical pollutants.

Due to the demands defined above it will be possible to assess close to reality the dilution potential and the barrier effects caused by the interaction, respectively. But it was not planned to couple the new developed transport code with speciation models.

The pollutant transport through the geosphere is influenced by various impacts. Beside mechanisms which lead to retention, some effects accelerate the transport. For that reason in a more general sense they are called interactions.

Often single processes are not independent but coupled. Transport of pollutants is often governed by other matters, which are migrating, too. These matters are natural (e.g. humic material) or artificial substances (e.g. EDTA). Their presence influence retention and precipitation of the pollutants. In the following they are called complexing agents. Their impact on the transport of pollutants is thus considered by a dependency of parameters like solubility limits, sorption parameters, etc. on the concentration of these complexing agents. Thereby these parameters explicitly become space and time dependent. In addition, for radionuclides the decay is considered within decay chains. Hence transport simulations of various radionuclides cannot be independently performed, since isotopes affect each other.

In Tab. 2.1 the individual interaction processes which affect the pollutants transport are given together with their consideration in r^3t. They are will be explained in more detail in the following.

Tab. 2.1 Processes and their consideration in r^3t

processes	consideration
equilibrium sorption	yes
kinetically controlled sorption	yes
diffusion into immobile porewater	yes
precipitation	yes
complexation	yes
colloidal transport	simplified
matrix diffusion	simplified
speciation	no

In the geosphere pollutants are transported by groundwater flow. Transport mechanisms are advection, diffusion, and dispersion. The underlying three-dimensional flow field can be stationary or transient and is derived from a simulation with d^3f [45].

2.2.1 Equilibrium Sorption

In general sorption is the agglomeration of pollutants at the surface of the rock matrix. This process of sorption is reversible. In a closed system equilibrium is reached after a sufficient time, then adsorption and desorption rates become equal. For equilibrium sorption one assumes that the time to reach equilibrium is negligibly small in comparison with the time scale of flow. Thus one expects instantaneous achievement of equilibrium. For equilibrium sorption both the well-known K_d-concept and isotherms after Langmuir und Freundlich [90] are realised as options in r^3t. The retention of special elements like uranium and cesium can better be described with non-linear sorption models.

2.2.2 Kinetically Controlled Sorption

If the time to reach equilibrium is not negligible in comparison with the time scale of flow, one has to incorporate the temporal development of sorption processes or equilibrium restoration. This is the case if

- sorption is irreversible or
- sorption and desorption coefficients are different or
- sorption processes are slower than time scale of flow.

Approximately this can be described by a basic modelling approach with kinetics of first order. That means change of concentration with time is assumed to be proportional to concentration difference.

2.2.3 Diffusion into Immobile Pore Water

Generally, the flow through porous or equivalent-porous media does not involve the total pore space. The part of immobile pore water is only accessible for pollutants by diffusion. Therefore the exchange of pollutants between mobile and immobile pore water has to be considered. The modelling of the pollutants exchange is arranged by use of the linear approach after Coats and Smith [25]. Formally such a modelling approach corresponds to reaction kinetics of first order.

2.2.4 Precipitation

In the pore water of an aquifer only a limited amount of pollutants can be dissolved. These amounts are limited by pollutant-specific solubility limits. If these limits are locally exceeded, pollutants will precipitate immediately. This goes on until the solubility limit is attained again. The precipitated pollutants form a solid phase and do not participate any longer in transport processes. If in contrast due to other processes (such as dilution or change of solubility limits due to a modified chemical environment) the concentrations fall below solubility limits the precipitates will be dissolved either until solubility limits are attained or are entirely dissolved. In case of radioactive pollutants the solubility limits are element specific. The concentration of an element is the sum of the concentration of all isotopes of the particular element.

2.2.5 Complexation

In aqueous solutions ions of pollutants can undergo bindings with other constituents of the solution. This process is called complexation. Complexes can exist as additional mobile species, which cause a significant enhancement of solubility or for a decrease of the sorption coefficient of the pollutant. Example for complexing agents are hydroxyl ions, EDTA, citrate, carbonate, and humic substances. Their impact will be modelled by consideration of a functional correlation between concentration of complexing agent and sorption coefficient and solubility limit, respectively.

In order to consider the impact of complexing agents transport of complexing agents is modelled, too. Since the concentration of the complexing agents are space and time dependent, sorption and solubility parameters itself become space and time dependent.

2.2.6 Colloidal Transport

Colloids are particles with diameters between10^{-7} and 10^{-9} m which are transported by groundwater flow. They consist of conglomerations of 10^{3} to 10^{9} atoms. According to that colloids sometimes behave like molecules. However, they are large enough to show features of discrete particles with a particular surface. That means with respect to their transport pollutants are sorbed onto colloids and are transported afterwards by flow.

For a simplified modelling of colloid-borne pollutant transport one starts with equilibrium condition of pollutants which are either dissolved, bound onto colloids, or sorbed onto the rock matrix. This causes a reduction of sorption in the presence of colloids. Hence the influence of colloids can be considered analogous to the impact of complexing agents, i.e. the impact of colloids can be modelled by a functional correlation between sorption coefficient and colloid concentration.

Moreover, in the special transport code TRAPIC [95] it is possible to model kinetically controlled, non-linear sorption processes as well as irreversible sorption onto colloids. Furthermore the filtration of colloids, i.e. the interaction between colloids and rock matrix, is considered. The two-dimensional model TRAPIC is applied for special analyses of colloid-borne pollutant transport. Because of the complexity such a model cannot be transferred to three-dimensional situations in a simple way. For that reason only the described simplified approach is included in r^3t.

2.2.7 Matrix Diffusion

Beside the dominant pathways in fractured systems the porous, water-saturated and relatively impermeable rock matrix exists. Pollutants are able to enter those areas by diffusion. Adsorption of pollutants onto the inner surface of the rock can lead to a considerable retardation of the migration of pollutants.

In simplified models to assess the retardation of migration due to matrix diffusion with adjacent adsorption one assumes that the rock matrix is only accessible by diffusion and only up to a certain penetration depth. With the assumption that the concentration equilibrium between mobile and immobile regions exists the effect of retardation can be considered with of effective retention parameters [74].

2.2.8 Speciation

Dissolved pollutants can exist as different species, e.g. hydrated ions or various complexes. Speciation codes model the partitioning of the particular pollutant into the individual species. This partitioning depends on various influencing factors like temperature, Eh-pH

value, ionic strength, and concentration of complexing agents. Typically for geochemical analysis speciation codes like EQ3/6 [143], [144], PHREEQE [112], and MINEQL [120] are used.

Coupled codes consisting of transport and speciation codes are applied until now for special studies like column experiments and locally limited model areas. Within the framework of long term safety analyses this coupling of transport and speciation codes does not seem presently to be helpful. The main part of computing time is used during geochemical simulations and the required data base is incomplete. For this reasons r^3t does not allow for any coupling between transport and speciation.

2.3 Scientific Objectives

With the availability of r^3t the possibility to model three-dimensional transport of pollutants through large and heterogeneous areas will be established. Thereby every interaction relevant for long-term safety assessment besides advection, diffusion, and dispersion will be considered. The computer code is not restricted to the simulation of radionuclide migration and can also be applied to transport simulations for chemotoxical pollutants, too. Therewith the following progress will be achieved:

- deeper understanding of the impacts of relevant interaction effects,
- more realistic description of the impacts of heterogeneities in large areas,
- realistic assessment of the dilution potential and the barrier properties of the overburden.

Due to the requirements defined above not only improvements in the field of long-term safety assessment but also in the range of numerics and software engineering are achieved.

3 The Organisation

The r^{3}t (**r**adionuclide, **r**eaction, **r**etardation, and **t**ransport) code was developed by a team which consists of the following members:

Department of Mathematics at the University of Freiburg,
Section of Applied Mathematics:
Prof. Dietmar Kröner,
Dr. Mario Ohlberger,
Dr. Thomas Gessner,
David Bürkle,
Robert Klöfkorn

Interdisciplinary Center for Scientific Computing at the University of Heidelberg,
Technical Simulation Group:
Prof. Gabriel Wittum,
Dr. Peter Frolkovič,
Dr. Jürgen Geiser,
Dr. Michael Lampe

Institute of Hydromechanics and Water Resources Management at the Swiss Federal Institute of Technology Zurich, Section Groundwater and Hydromechanics:
Prof. Wolfgang Kinzelbach,
Dr. Sabine Attinger,
Dr. Jiva Dimitrova Micha,
Peter Bauer

Institute of Mathematics at the University of Duisburg,
Department of Numerical Analysis and Scientific Computing:
Prof. Martin Rumpf,
Dr. Tobias Preusser,
Martin Lenz,
Oliver Nemitz

Additional work especially performing test calculations was done by members of the Department Long Term Safety Analyses of the Final Repository Safety Research Division of GRS:
Heinz Birthler,
Dr. Eckhard Fein,
Dr. Thomas Kühle,
Dr. Klaus-Peter Kröhn,
Dr. Ulrich Noseck,
Anke Schneider,
and the students:
Sabine Krüger,
Olaf Misgeld

In App. E the publications which were produced during the project and in App. F the project meetings are listed.

4 Conceptual Model and Mathematical Description

The transport of radioactive or chemical pollutants through porous or equivalent-porous media is described by time-dependent partial differential equations. In addition to transport processes these equations characterise first-order reactions, for instance radioactive decay, chemical and biological degradation and kinetically controlled sorption. By the description of these reactions the appropriate differential equations are in general non-linearly coupled. As well as kinetically controlled sorption equilibrium sorption can be applied. In both cases one can use isotherms after Henry, Langmuir, and Freundlich, respectively. Additional options are immobile pore waters after Coats-Smith and element specific solubility limits. It is assumed that the distribution in the various phases (solved, adsorbed and precipitated) will not be affected by the radioactive decay and degradation processes, respectively. That means no additional coupling between the phases exist.

Notations are described in chapter 11.

4.1 Density Driven Flow and Pollutant Transport

The transport modelling of radionuclides (pollutants) shall be valid for both potential flow and density driven flow. Density driven flow is described by the following equations, the flow equation and the equation for the transport of salt [45]:

$$\frac{\partial}{\partial t}(\phi\rho_f) + \nabla \cdot (\boldsymbol{q}\rho_f) = 0 \qquad (4.1)$$

$$\frac{\partial}{\partial t}(\phi\rho_f\chi_s) + \nabla \cdot (\boldsymbol{q}\rho_f\chi_s - \boldsymbol{D}_s\rho_f\nabla\chi_s) = 0 \qquad (4.2)$$

Similar the transport of pollutants with neglected impact on fluid density is described by:

$$\frac{\partial}{\partial t}(\phi\rho_f\chi_i) + \nabla \cdot (\boldsymbol{q}\rho_f\chi_i - \boldsymbol{D}\rho_f\nabla\chi_i) = Q_i \qquad (4.3)$$

Here Q_i [kg m^{-3} s^{-1}] are the sinks and the sources of the i^{th} pollutant, i.e. the direct in- and outflow, and in case of radioactive decay the decay and the buildup of the mother nuclides.

Accepting precipitation and sorption one ends up with

$$\begin{aligned} &\frac{\partial}{\partial t}\left(\phi \rho_f \chi_i^l + \phi \rho_f \chi_i^p + \phi \frac{1-\phi}{\phi} \rho_r \chi_i^{ad} \right) \\ &\quad + \nabla \cdot (\boldsymbol{q} \rho_f \chi_i^l - \boldsymbol{D} \rho_f \nabla \chi_i^l) \\ &\quad = Q_i \end{aligned} \quad . \qquad (4.4)$$

If the source or sink terms $\overline{Q}_i$ are given with dimension [mol m^{-3} s^{-1}] it has the form

$$\overline{Q}_i = \tilde{Q}_i^d - \lambda_i \phi C_i + \sum_{k(i)} \lambda_k \phi C_k . \qquad (4.5)$$

With the aid of the flow equation (4.1) the transport equation (4.2) can be converted.

$$\begin{aligned} &\phi \rho_f \frac{\partial \chi_i^l}{\partial t} + \frac{\partial}{\partial t}\left(\phi \rho_f \chi_i^p + \phi \frac{1-\phi}{\phi} \rho_r \chi_i^{ad} \right) \\ &\quad + \boldsymbol{q} \rho_f \nabla \chi_i^l - \nabla \boldsymbol{D} \rho_f \nabla \chi_i^l \\ &\quad = Q_i \end{aligned} \qquad (4.6)$$

In order to combine equations (4.5) and (4.6) they have to have the same units. Since it is intended to use results from the EMOS code [128], the unit mol m^{-3} is chosen. Dividing by the molecular weigth M_i and by appropriate expansion with ρ_f equation (4.6) can be converted to:

$$\phi\rho_f\frac{\partial}{\partial t}\left(\frac{1}{\rho_f}\frac{\overset{l}{\chi_i}}{M_i}\rho_f\right) + \frac{\partial}{\partial t}\left(\phi\frac{\rho_f\overset{p}{\chi_i}}{M_i} + \phi\frac{1-\phi}{\phi}\rho_r\frac{\overset{ad}{\chi_i}}{M_i}\right)$$

$$+ \boldsymbol{q}\rho_f\nabla\left(\frac{1}{\rho_f}\frac{\overset{l}{\chi_i}\rho_f}{M_i}\right) - \nabla\boldsymbol{D}\rho_f\nabla\left(\frac{1}{\rho_f}\frac{\overset{l}{\chi_i}\rho_f}{M_i}\right) \quad . \qquad (4.7)$$

$$= \frac{Q_i}{M_i}$$

With $C_i^l = \rho_f\frac{\overset{l}{\chi_i}}{M_i}$, $C_i^p = \rho_f\frac{\overset{p}{\chi_i}}{M_i}$, $C_i^{ad} = \frac{\overset{ad}{\chi_i}}{M_i}$, and $\tilde{Q}_i = \frac{Q_i}{M_i}$ one gets

$$\phi\rho_f\frac{\partial}{\partial t}\left(\frac{1}{\rho_f}C_i^l\right) + \frac{\partial}{\partial t}\left(\phi C_i^p + \phi\frac{1-\phi}{\phi}\rho_r C_i^{ad}\right)$$

$$+ \boldsymbol{q}\rho_f\nabla\left(\frac{1}{\rho_f}C_i^l\right) - \nabla\boldsymbol{D}\rho_f\nabla\left(\frac{1}{\rho_f}C_i^l\right) \quad . \qquad (4.8)$$

$$= \tilde{Q}_i$$

Finally, taking into account the immobile part of pollutants the coupled transport equations for N radionuclides (pollutants) read:

$$\phi\rho_f\frac{\partial}{\partial t}\left(\frac{1}{\rho_f}C_i^l\right) + \frac{\partial}{\partial t}\left(\phi C_i^p + g\phi\frac{1-\phi-\phi_{im}}{\phi}\rho_r C_i^{ad}\right)$$

$$+ \boldsymbol{q}\rho_f\nabla\left(\frac{1}{\rho_f}C_i^l\right) - \nabla\left(\boldsymbol{D}\rho_f\nabla\left(\frac{1}{\rho_f}C^l{}_i\right)\right)$$

$$= -\lambda_i\left(\phi C_i^l + \phi C_i^p + g\phi\frac{1-\phi-\phi_{im}}{\phi}\rho_r C_i^{ad}\right) \quad . \qquad (4.9)$$

$$+ \sum_{k(i)}\lambda_k\left(\phi C_k^l + \phi C_k^p + g\phi\frac{1-\phi-\phi_{im}}{\phi}\rho_r C_k^{ad}\right)$$

$$-\alpha^{e(i)}(C_i^l - G_i^l)$$

$$+ \tilde{Q}_i^d$$

4.2 Diffusion and Dispersion

$\boldsymbol{D}$ denotes the tensor of diffusion and dispersion. In general it is composed of the element-specific molecular diffusion coefficient and the dispersion tensor. In analogy to d^{3}f Scheidegger's approach is used.

$$\boldsymbol{D}^{e(i)} = \phi D_m^{e(i)} \boldsymbol{I} + \alpha_T |\boldsymbol{q}| \boldsymbol{I} + \frac{\alpha_L - \alpha_T}{|\boldsymbol{q}|} \boldsymbol{q}\boldsymbol{q} \qquad (4.10)$$

4.3 Equilibrium Sorption

Equilibrium sorption is expressed element-specifically with isotherms.

$$C_i^{ad} = K_d^{e(i)} C_i^l \qquad \text{Henry} \qquad (4.11)$$

$$C_i^{ad} = \frac{b\kappa}{1 + bC_{e(i)}^l} C_i^l \qquad \text{Langmuir} \qquad (4.12)$$

$$C_i^{ad} = K_{nl} (C_{e(i)}^l)^{p-1} C_i^l \qquad \text{Freundlich} \qquad (4.13)$$

Relating to the isotherm after Freundlich attention should be paid to the fact that formally the term $(C_{e(i)}^l)^{p-1}$ has to be dimensionless. It is achieved by formally dividing through the appropriate unit of concentration. But with the tacit understanding this will never be expressed in the formulae.

With a appropriate $K^{e(i)}(C_{e(i)}^l)$ all of the three isothermes can be expressed as follows:

$$C_i^{ad} = K^{e(i)}(C_{e(i)}^l) C_i^l \qquad (4.14)$$

Each of the parameters in equations (4.11) through (4.14) is element specific.

In the case of equilibrium sorption a so-called retardation factor R_f can be defined, as long as flow conservation is not taken into account explicitly.

$$R_f = 1 + \frac{1-\phi}{\phi}\rho_r K^{e(i)}(C^l_{e(i)}) \qquad (4.15)$$

4.4 Kinetically Controlled Sorption

In analogy to equilibrium sorption the following formulations for kinetically controlled sorption are used:

Henry:

$$\frac{\partial}{\partial t}C_i^{ad} = k_\alpha^{e(i)}(K_d^{e(i)}C_i^l - C_i^{ad}) - \lambda_i C_i^{ad} + \sum_{k(i)}\lambda_k C_k^{ad} \qquad (4.16)$$

Langmuir

$$\frac{\partial}{\partial t}C_i^{ad} = k_\alpha^{e(i)}\left(\frac{b\kappa}{1+bC^l_{e(i)}}C_i^l - C_i^{ad}\right) - \lambda_i C_i^{ad} + \sum_{k(i)}\lambda_k C_k^{ad} \qquad (4.17)$$

Freundlich

$$\frac{\partial}{\partial t}C_i^{ad} = k_\alpha^{e(i)}\left(K_{nl}(C^l_{e(i)})^{p-1}C_i^l - C_i^{ad}\right) - \lambda_i C_i^{ad} + \sum_{k(i)}\lambda_k C_k^{ad} \qquad (4.18)$$

It is assumed that radioactive decay does not affect the phases of the radionuclides (solved, adsorbed and precipitated).

4.5 Precipitation

If the concentration of an element $C^l_{e(i)}$ exceeds the element-specific solubility limit $L^{e(i)}$ the pollutant precipitates until the concentration of the element equals the element-specific solubility limit. Accordingly the concentration C_i^p of the precipitated pollutant rises. But when the concentration of the element $C^l_{e(i)}$ falls below the element-specific solubility limit $L^{e(i)}$, the pollutant dissolves.

$$\left.\begin{array}{l} C^l_{e(i)} \le L^{e(i)} \\ C^l_{e(i)} > L^{e(i)} \end{array}\right\} \Rightarrow \qquad C^p_i = \begin{cases} 0 \\ \dfrac{C^l_i}{C^l_{e(i)}}\,(C^l_{e(i)} - L^{e(i)}) \end{cases}$$

and

$$\left.\begin{array}{l} C^l_{e(i)} \le L^{e(i)} \\ C^l_{e(i)} > L^{e(i)} \end{array}\right\} \Rightarrow \qquad C^l_i = \begin{cases} C^l_i \\ \dfrac{C^l_i}{C^l_{e(i)}}\,L^{e(i)} \end{cases} \qquad (4.19)$$

4.6 Immobile Pore Water

If pores filled with immobile water exist, pollutants possibly can enter in it and be adsorbed. Instead of matrix diffusion which can be modelled by effective sorption parameters the approach after Coats-Smith [25] has been used. It yields much better agreement to experimental results, especially for the description of the tailing [34]. The approach after Coats-Smith is described by the local concentration difference between mobile and immobile pore space.

$$\begin{aligned} &\frac{\partial}{\partial t}(\phi_{im} G^l_i + (1-g)(1-\phi-\phi_{im})\rho_r G^{ad}_i) \;=\; \\ &\alpha^{e(i)}(C^l_i - G^l_i) - \lambda^i(\phi_{im} G^l_i + (1-g)(1-\phi-\phi_{im})\rho_r G^{ad}_i) \\ &\quad + \sum\nolimits_{k(i)} \lambda^k(\phi_{im} G^l_k + (1-g)(1-\phi-\phi_{im})\rho_r G^{ad}_k) \end{aligned} \qquad (4.20)$$

In that case the relationship between G^l_i and G^{ad}_i is analogue to equations (4.11) to (4.13). But for immobile pore water only equilibrium sorption after Henry without dependence on complexing agents is assumed (cp. chapter 4.7). Modelling of precipitation and immobile pore water is not allowed to be taken into account at the same time.

4.7 Impact of Complexing Agents

There exist substances which affect sorption features and solubility limits if they are dissolved in ground water. They are called complexing agents. Only the K_d-coefficients and solubility limits L are allowed to be modified by complexing agents.

$$K_d^{e(i)} = K_d^{e(i)}(C^1, ..., C^M) = K_d^{e(i)} f(C^1, ..., C^M) \quad (4.21)$$

$$L^{e(i)} = L^{e(i)}(C^1, ..., C^M) = L^{e(i)} g(C^1, ..., C^M) \quad (4.22)$$

where $f(0) = g(0) = 1$.

The functional dependency on the concentration of the complexing agents is limited to simple functions, like step functions, power series, rational functions, exponentials, etc. Here the concentrations C^1, C^2, ..., C^M describe the concentration of M complexing agents and not the concentrations of pollutants.

Agents can enter the modelled area on different ways:

- release from mine workings analogous to pollutants (cp. subchapter 4.11)
- release from a special source (cp. subchapter 4.11)
- as initial concentration distribution which is transported (cp. subchapter 4.9)
- as instantaneous, constant concentration distribution independent of time

4.8 Stochastic Modelling of Sorption

Beside the possibilities described above one has the possibility to model retention by sorption stochastically. This can only be done for the mobile phase. In chapter 5 “Transport in Heterogeneous Porous Media” this way of modelling is described in detail.

4.9 Initial Conditions

To solve time dependent partial differential equations initial conditions $C_l^i\big|_{t\,=\,t_0}$ have to be specified. They are required for N pollutants and, if it is taken into account, for M complexing agents (i = 1, ..., N+M). If kinetically controlled sorption or immobile pore water regions are modelled, accordingly initial conditions $C_{ad}^i\big|_{t\,=\,t_0}$ and $G_l^i\big|_{t\,=\,t_0}$ have to be given. In order to avoid the prescription of N+M separate initial conditions, first of all initial conditions are fixed which are valid for every pollutant and agent. Subsequently for individual substances exceptions can be defined. The sequence of input is C_l^i, C_{ad}^i and G_l^i. The declaration of C_{ad}^i and G_l^i is necessary only on demand. It is assumed that in the area of immobile pore water always equilibrium sorption is valid. In the case of precipitation it is assumed that the initial concentration of precipitated substances is always zero.

4.10 Boundary Conditions

Boundary conditions have to be fixed for N pollutants (nuclides) and, if they are modelled for M agents, too. In the case of kinetically controlled sorption or immobile pore water modelling the boundary conditions are identical to those of dissolved pollutants. One has to keep in mind that at every piece of boundary the type of boundary conditions has to be equal for every substance. If no boundary conditions are given explicitly it is assumed that the diffusive/dispersive flux vanishes (cp. chapter 4.10.2).

4.10.1 Dirichlet Boundary Condition

The concentration $C_i(x,\ t)\,|_{x\,\in\,\Gamma_j}$ of pollutant i is given at the surface Γ_j of the modelled area.

$$C_i^l(x,\ t)\,|_{x\,\in\,\Gamma_j} \;=\; C_i^D(x,t)\ \text{[mol m}^{-3}\text{]}, \qquad (4.23)$$

where $C_i^D(x,t)$ is constant or a function of space and/or time for pollutant i.

4.10.2 Flux Boundary Condition

The total flux of pollutant i over the boundary Γ_j is fixed by this boundary condition.

$$\vec{n}\rho_f \cdot \left[\vec{q}\frac{1}{\rho_f}C_i^l - \boldsymbol{D}\frac{1}{\rho_f}\nabla C_i^l\right]\Big|_{x \in \Gamma_k} = h_i^{flux}(x,t) \text{ [mol m}^{-2}\text{ s}^{-1}\text{]}, \qquad (4.24)$$

where $h_i^{flux}(x,t)$ is constant or a function of space and/or time for pollutant i.

4.10.3 Leaching Boundary Condition

This boundary condition fixes the total flux of pollutant i over the boundary Γ_j to be proportional to the difference of the actual concentration and some reference concentration $C_i^{l,ref}$. This is the common formulation of leaching. Thereby the reference concentration corresponds to the particular solubility limit of pollutant i. The constant α_i^d is the so-called leaching constant.

$$\vec{n}\rho_f \cdot \left[\vec{q}\frac{1}{\rho_f}C_i^l - \boldsymbol{D}\frac{1}{\rho_f}\nabla C_i^l\right]\Big|_{x \in \Gamma_j} \text{ [mol m}^{-2}\text{ s}^{-1}\text{]} \qquad (4.25)$$

$$= \alpha_i^d(C_i^l x,\ t - C_i^{l,ref})$$

4.10.4 Outflow Boundary Condition

For outflow boundary the diffusiv/dispersive flux across a boundary is fixed. In this case various alternatives exist:

4.10.4.1 Standard Outflow Boundary Condition

Standard-outflow boundary condition means the diffusiv/dispersive flux is set to zero, while the pollutants are leaving the modelled area according to the actual concentration and flow velocity.

$$\vec{n}\rho_f \cdot \boldsymbol{D}\nabla\frac{1}{\rho_f}C_i\Big|_{x \in \Gamma_k} = 0 \text{ [mol m}^{-2}\text{ s}^{-1}\text{]} \qquad (4.26)$$

This is the usual outflow boundary condition. As long as no other boundary condition is given this standard outflow condition is valid.

4.10.4.2 In- and Outflow Boundary Condition

$$\begin{aligned} C_i^l(x,t)\,|_{x \in \Gamma_k} &= C_i^{l,in} && \vec{n} \cdot \vec{q} < 0 \\ \vec{n}\rho_f \boldsymbol{D}\nabla\frac{1}{\rho_f}C_i^l(x,t)\Big|_{x \in \Gamma_k} &= 0 && \text{if} \quad \vec{n} \cdot \vec{q} > 0 \end{aligned} \qquad (4.27)$$

For this boundary condition the flow simulation itself fixes the domains where different flow situations are valid. At the inflow domain $\vec{n} \cdot \vec{q} < 0$ one assumes that the inflowing fluid carries the concentration C_i^{in} while at the outflow domain $\vec{n} \cdot \vec{q} > 0$ the diffusive/dispersive flux is set to zero. The various fluxes are known but not the exact locations of turning points.

4.10.4.3 Transmission Boundary Condition

This transmissions boundary condition requires the total flux across the boundary to be constant [69].

$$\nabla \cdot \boldsymbol{D}\rho_f \nabla\frac{1}{\rho_f}C_i(x,\,t)\,|_{x\,=\,0} = 0 \qquad (4.28)$$

Physically this boundary condition means that the internal advection-diffusion/dispersion flux continues across the boundary. The flux boundary condition (4.24) stipulates that the diffusive/dispersive flux vanishes across the boundary. Hence it is a special case of equation (4.28).

4.11 Sources and Sinks

Since water inflow and outflow normally can be neglected sources and sinks are only defined for pollutants. If these neglects are incorrect one has already to take into consideration appropriate sources and/or sinks for water. This amount of water will modify the flow field.

Sources and sinks can have various geometrical shapes. They can be:

- punctiform,
- linear,
  - parallel to axes,
  - arbitrarily oriented,
- quadrilateral (one axis $\perp$ to area),
- shaped like a parallelepiped (axes $\perp$ to lateral surface) or
- piece of boundary
  - two-dimensional: linear,
  - three-dimensional: plane.

The temporal characteristics are given by a rectangular distribution (cp. Fig. 4.1) or by the explicit declaration of strength of source or sink at discrete times.Depending on the modelled time T_{Mod} and the inflow time T either δ-shaped or constant sources can be modelled.

$T_{Mod} \gg T$ δ-shaped

$T_{Mod} = T$ constant

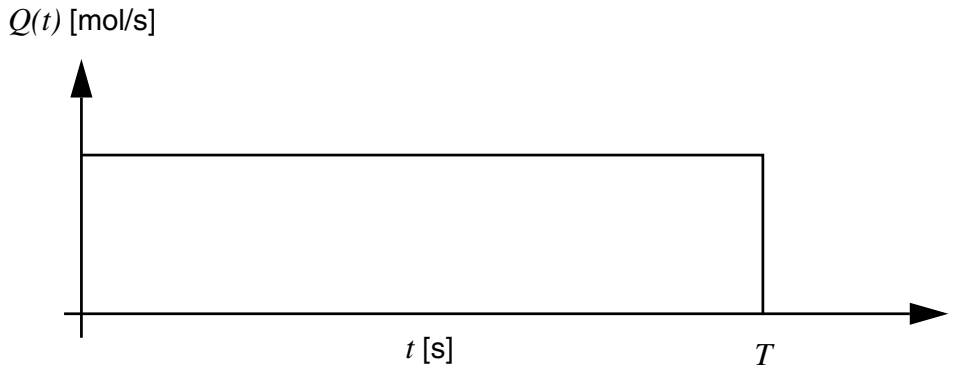

$$Q(t) = \begin{cases} \dfrac{Q_s}{T} & t \le T \\ 0 & t > T \end{cases} \quad \text{with} \int Q(t)\,dt = Q_s$$

Fig. 4.1 Possible temporal distribution of pollutant inflow

For sources the pollutants rate $Q(t)$ [mol s^{-1}] is always given as

$$Q(t) = \int_{F(\Gamma)} \left(\vec{n}\rho_f \cdot \left[\vec{q}\frac{1}{\rho_f} C_i^l - \boldsymbol{D}\nabla\frac{1}{\rho_f} C_i^l \right] \right) df \qquad [\text{ mol s}^{-1}\text{ }]. \qquad (4.29)$$

$$= \int_{F(\Gamma)} h_i^{flux}(x,\ t)\,df$$

If the source is located at the boundary it can be modelled as a boundary condition. In that case the flux is given by

$$h_i^{flux}(x,\ t) \approx \frac{Q(t)}{F} \quad [\text{ mol s}^{-1}\text{ m}^{-2}\text{ }]. \qquad (4.30)$$

Here F is the surface area which is attached to the boundary condition. Equation (4.30) is only exact for a homogeneous flow field.

For every geometrical shape of sources and sinks first of all the patches are discriminated which overlap with the sources and sinks. According to the overlaps which are expressed as percentage the pollutants are distributed to the concerned patches. This shows that the initial grid has to take into consideration the locations of sources and sinks. Otherwise the dilution of the pollutants become will be overestimated.

5 Transport in Heterogeneous Porous Media

Natural aquifers show a wide range of spatial variability in the underlying formation of materials and their physical and chemical properties. Usually, they can be modelled as heterogeneous porous media characterised by spatially fluctuating parameters. Physical heterogeneity is commonly associated with the spatial variability in the hydraulic conductivity field. Chemical heterogeneity (as produced by non uniform distribution of reactive materials) is associated with variable Freundlich constant $K_{nl} = K_{nl}(\boldsymbol{x})$ or Freundlich exponent $p = p(\boldsymbol{x})$.

The spatial variability in the physical and chemical properties can essentially affect the overall mobility of contaminants in the subsurface. Especially, the typical flow, mixing and reactive behaviour on very large length and time scales can strongly differ from the local, small-scale model description.

In this chapter two questions will be answered: Can one find an effective transport equation describing the transport behaviour on the large scale, which incorporates the impact of the small-scale variations in averaged transport parameters? What is the magnitude of the averaged transport parameters?

5.1 Stochastic Modelling

5.1.1 Equivalent Homogeneous Medium

Transport behaviour on scales larger than the typical length scale of heterogeneity can be analysed using a stochastic modelling approach: In a stochastic approach the spatially fluctuating parameter is considered to be a random field $\mathcal{Z}(\boldsymbol{x})$ representing a single realisation of a stochastic process with given statistical properties. Such statistical information is in general accessible experimentally, whereas there is no intention to resolve the exact spatial structure of a given realisation. Thus, the random field is described by the probability distribution $P(\mathcal{Z}(\boldsymbol{x}))$ where $P(\mathcal{Z})d\mathcal{Z}$ denotes the probability that the property $\mathcal{Z}$ lies between $\mathcal{Z}$ and $\mathcal{Z} + d\mathcal{Z}$. The average over the probability distribution is equivalent to an average over the ensemble of all possible realisations of the parameter $\mathcal{Z}(\boldsymbol{x})$. The average of functions $f(\mathcal{Z}(\boldsymbol{x}))$ over the probability function

$$\int P(Z)\, f(Z)\, dZ \equiv \bar{f} \qquad (5.1)$$

is denoted as ensemble averaged quantity. The corresponding correlation function is given as

$$w(\boldsymbol{x} - \boldsymbol{x}') = \int P(Z)\, f(Z(\boldsymbol{x}))\, f(Z(\boldsymbol{x}'))\, dZ \qquad (5.2)$$

Due to the assumed stationarity of the stochastic process, the two-point correlation function is a function of the distance $\boldsymbol{x} - \boldsymbol{x}'$ only.

The ensemble averaged quantities reflect the statistical properties of the ensemble. In contrast, the transport parameters in one realisation, which we are mainly interested in, depend on the given spatial distribution of the heterogeneities and consequently fluctuate around the ensemble averaged quantities. However, under ergodic conditions the stochastic process approaches its mean value. This so-called self-averaging property makes the stochastic modelling approach very useful for representing processes also in a single realisation.

For many practical applications it is significant to study the impact that the small-scale variations might have on the large-scale transport behaviour avoiding costly computer simulations of the fully heterogeneous medium. In linear transport theory it is convenient to characterise the large-scale transport by the same type of differential equation as on small scales replacing the pore-scale parameters by appropriately averaged parameters using the ergodicity of the medium. This up-scaled large-scale equation is known as the so-called “equivalent homogeneous equation”.

5.1.2 Ensemble and Effective Parameters

In this work large-scale transport parameters are defined following the concept of ensemble [27], [63] and effective [4], [32], [37], [116], [146], [147] transport parameters. These two quantities are based on two conceptually different ensemble averaging procedures and have widely been discussed for linear transport processes.

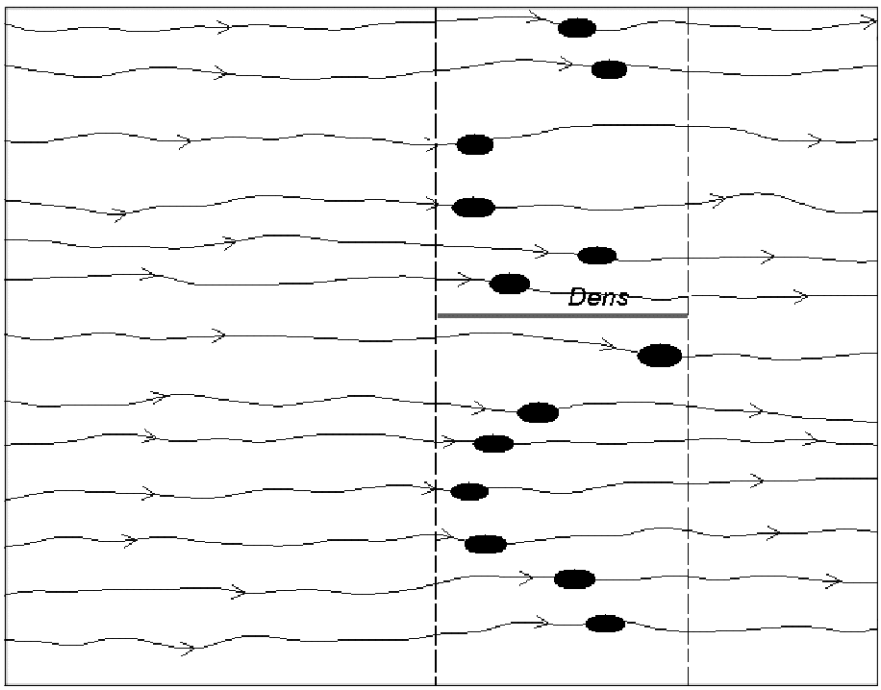

Fig. 5.1 Illustration of ensemble and effective mixing behaviour for purely advective conservative transport ($\boldsymbol{D}$=0)

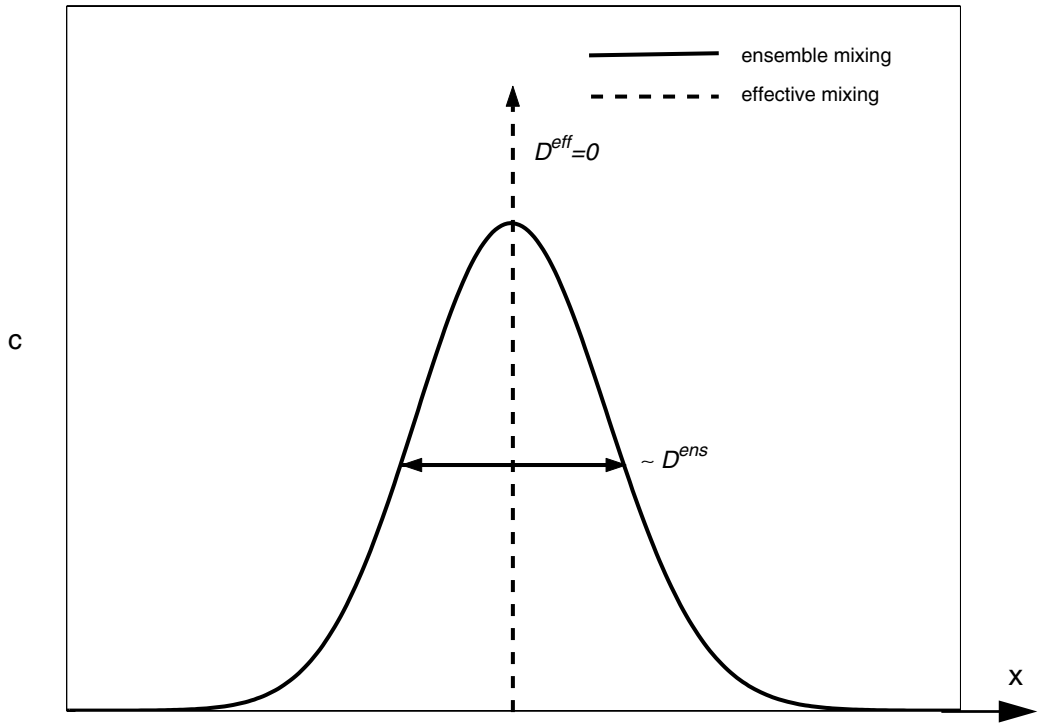

Fig. 5.2 Ensemble and effective dispersion coefficient for purely advective conservative transport

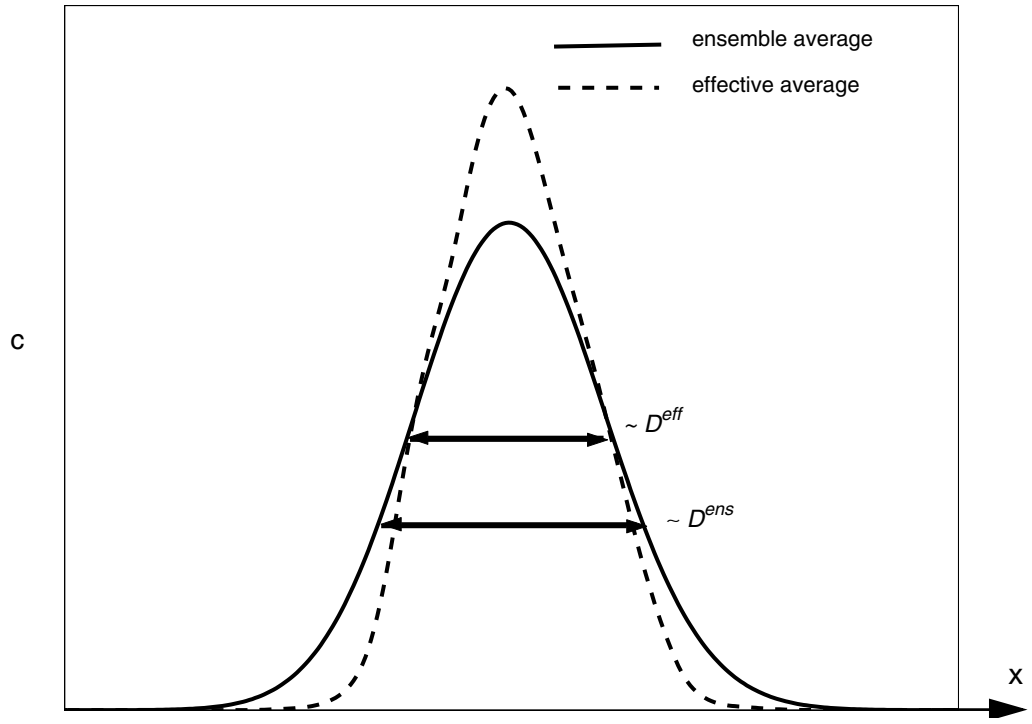

Fig. 5.3 Ensemble and effective dispersion coefficient with non-vanishing transverse component

In order to demonstrate the difference between $\boldsymbol{D}^{\mathrm{ens}}$ and $\boldsymbol{D}^{\mathrm{eff}}$ it is considered the purely advective conservative transport in a physically heterogeneous medium. Fig. 5.1 illustrates the advective transport of a point-like tracer in a heterogeneous velocity field. Every streamline represents a single realisation of the medium. If one performs the ensemble average over the ensemble of different streamlines one ends up with the ensemble averaged concentration related to the ensemble dispersion. As plotted in Fig. 5.2 it is widely spread. This is an artificial effect caused by fluctuations of the center-of-mass positions of the concentration distribution in different realisations of the heterogeneous medium. This effect is suppressed in the effective dispersion coefficient because the center-of-mass positions are superimposed before performing the average. As can be seen in Fig. 5.2, the averaged concentration distribution in this case is unspread indicating vanishing effective dispersion. Moreover, it is the physically reasonable quantity because there is no spreading mechanism in the transport system. However, if the solute is spread over many different flow paths, corresponding to transport with non-vanishing local transverse dispersion, the center-of-mass differences will be smoothed out. For very long times resp. very long travel distances, the ensemble average reflects the effective mixing process in

the transport system. Ensemble and effective transport parameters become equivalent. For transient times, however, effective and ensemble transport parameters differ from each other. This behaviour is illustrated in Fig. 5.3.

5.1.3 Research Background

The stochastic theory is based on the fundamental work of Gelhar [63] and Dagan [27]. The concepts of stochastic modelling have been applied in many theoretical and numerical studies for conservative and linearly adsorbing solutes in physically [22], [27], [29], [63], [134] as well as chemically [4], [12], [13], [37], [100] heterogeneous media.

Especially, a large amount of research has been done for transport in macroscopically uniform flow fields. The qualitative behaviour of linear transport processes is well understood: Spatial fluctuations in the hydraulic conductivity cause local variations in the groundwater flow field. Solutes injected into the groundwater are dominated by the heterogeneity of the medium. With time the solute is distributed over many different streamlines and velocity fluctuations from streamline to streamline lead to a strong increase of the dispersion in the mean flow direction known as macrodispersion. For mildly heterogeneous media macrodispersion was calculated using a perturbation theory approach [27], [63]. Complementary numerical calculations [22], [134], [134] and experimental studies [131], [58] were carried out. The macrodispersion overestimates the real dilution in aquifers. The concept of effective dispersion, correcting the definition of ensemble dispersion for transient times, was introduced [31], [32], [83]. The difference between ensemble and effective dispersion is qualitatively discussed by [23], [24], [46], [47], [115], [146]. Explicit results are presented by [4], [37], [99].

Most of the studies cited above involve a local large-scale dispersive flux according to a Fickian type law [27], [62]. Using a local dispersive flux seems to be reasonable for conservative transport processes and relative small variances [26], [36], [101], [103] because of the symmetric, smooth concentration profiles resulting in this case.

The reactive nature of subsurface systems can significantly impact the general migration behaviour within a contaminant mixture [135], [125], [126], especially, if non-linear processes are involved. Reactive transport processes are more complicated to investigate due to the larger number of parameters which can be viewed as spatially variable

and/or because the transport equation may be non-linear in the concentration distribution. Serious difficulties occur already in the analytical description of transport with non-linear adsorption in a homogeneous medium. For solutes undergoing non-linear adsorption of Freundlich type the transport behaviour can only be described by scaling analysis [35], [65], [77], [137]. A closed solution is not known. In heterogeneous media, transport with Freundlich adsorption involves a higher theoretical and computational effort. Monte Carlo simulations can be accomplished in a straightforward manner in analogy to conservative transport [1], [14], [17], [73], [125], [133]. As for conservative transport, the numerical solution of the dissolved concentrations is analysed by considering the first and second central moments. However, all these studies point out that standard moment analysis cannot be applied in order to quantitatively reveal the impact of heterogeneities on the transport behaviour at large scales. Semi-analytical results are presented in [14], [121]. They studied the impact of heterogeneous velocity fields on breakthrough curves of non-linearly adsorbing solutes neglecting the pore-scale dispersion. However, such assumptions can lead to significant errors in the local concentration [14], [16].

Another complication might occur when using a local large-scale dispersive flux in the large-scale transport equation. As demonstrated in [26], [72], [86], [103] the localisation approximation in many reactive transport situations may cause errors in the calculation of all spatial moments of the ensemble averaged concentration distribution.

Additionally, solute migration through natural aquifers is strongly impacted by the different chemical properties of the underlying materials. Especially, the sorption behaviour depends on the soil affinity for the solute and the free available sorption sites. In general, these properties appear as different sorption parameters at different soils or different locations in the domain, respectively. The soil dependence of the Freundlich exponent and the Freundlich distribution coefficient was investigated in laboratory experiments [140], [141]. Moreover, field measurements confirmed the spatial variability [119].

Transport in a randomly distributed field of adsorption coefficients was investigated numerically [1], [17], [133]. Especially, the combined effect of spatial fluctuations in both the hydraulic conductivity field and the Freundlich constant was extensively studied.

However, in the existing literature there is a lack of consistent research of the impact of chemical heterogeneity on the transport behaviour of non-linearly adsorbing solutes. For the case of transport with a variable distribution coefficient a comparison with theoretical results is missing. Moreover, the effect that a variable Freundlich exponent may have on the transport behaviour is an open question.

5.2 Transport in Physically Heterogeneous Media

In this section ensemble and effective transport parameters are derived for transport with non-linear adsorption in a physically heterogeneous medium associated with log-normally distributed conductivities in space [58], [131]. Consequently, the groundwater velocity varies locally, $\boldsymbol{u} = \boldsymbol{u}(\boldsymbol{x})$. Furthermore, the effect of variations in the porosity ϕ and the local dispersion coefficient D_{ij} is assumed to be insignificant compared to the influence of the hydraulic conductivity variations [37], [62]. Therefore, these parameters can be taken to be constant. For the spatially fluctuating velocity field it is assumed that small deviations from the mean flow field occur:

$$\boldsymbol{u}(\boldsymbol{x}) \equiv \bar{\boldsymbol{u}} + \tilde{\boldsymbol{u}}(\boldsymbol{x}) . \qquad (5.3)$$

By construction, one has $\overline{\tilde{\boldsymbol{u}}(\boldsymbol{x})} = 0$. The corresponding velocity correlation functions are denoted by

$$\overline{\tilde{u}_i(\boldsymbol{x})\tilde{u}_j(\boldsymbol{x}')} = w_{ij}(\boldsymbol{x} - \boldsymbol{x}') . \qquad (5.4)$$

5.2.1 Transport Parameters in Lowest Order Perturbation Theory

It is proposed to define large-scale transport parameters by using expressions (7.18) and (7.19) and average them over an ensemble of possible realisations of the medium. The concept of effective and ensemble averaging from subsection 5.1.2 is followed and effective transport parameters are defined as

$$u_i^{\mathrm{eff}} \equiv \overline{\left(\frac{\frac{\partial}{\partial t} \int d^d x x_i \left(c(\boldsymbol{x},t) + k_d c^p(\boldsymbol{x},t) \right)}{\int d^d x c(\boldsymbol{x},t)} \right)} \tag{5.5}$$

and

$$D_{ii}^{\mathrm{eff}} \equiv \overline{\left(\frac{\frac{\partial}{\partial t} \int d^d x x_i^2 \left(c(\boldsymbol{x},t) + k_d c^p(\boldsymbol{x},t) \right)}{2 \int d^d x c(\boldsymbol{x},t)} \right)} + \overline{\left(u_i \frac{\int d^d x x_i c(\boldsymbol{x},t)}{\int d^d x c(\boldsymbol{x},t)} \right)} . \tag{5.6}$$

They have to be distinguished from the ensemble transport parameters which follow from ensemble averaging the transport equation as e.g. presented in [27], [63]. The effective velocity and the ensemble velocity are equivalent, $\boldsymbol{u}^{\mathrm{eff}} = \boldsymbol{u}^{\mathrm{ens}}$. However, the ensemble dispersion coefficient are introduced as

$$D_{11}^{\mathrm{ens}} \equiv \overline{\left(\frac{\frac{\partial}{\partial t} \int d^d x x_i^2 \left(c(\boldsymbol{x},t) + k_d c^p(\boldsymbol{x},t) \right)}{2 \int d^d x c(\boldsymbol{x},t)} \right)} + u_i^{\mathrm{ens}} \overline{\left(\frac{\int d^d x x_i c(\boldsymbol{x},t)}{\int d^d x c(\boldsymbol{x},t)} \right)} . \tag{5.7}$$

Note that in the following the index l for the dissolved concentration is skipped. Obviously, $\boldsymbol{D}^{\mathrm{ens}}$ differs from the effective dispersion coefficient in the second term where the averaged velocity is used. In general, ensemble dispersion coefficients tend to overestimate

the impact of heterogeneities on the dispersive mixing process describing artificial ensemble averaging effects. Especially, the real mixing behaviour at the concentration front is much better described by the effective than by the ensemble dispersion coefficient which can be very essential in modelling reactive transport. This is the subject of subsection 5.2.5.

The integral expressions for the effective and ensemble transport parameters can be solved in a perturbation theory ansatz. For this reason, a perturbation theory is constructed in terms of $\tilde{\boldsymbol{u}}(\boldsymbol{x})$ and $c(\boldsymbol{x},t)$ is expanded around the homogeneous concentration $c_0(\boldsymbol{x},t)$:

$$c(\boldsymbol{x},t) \;=\; c_0(\boldsymbol{x},t) \;+\; c_1(\boldsymbol{x},t) \;+\; c_2(\boldsymbol{x},t) \;+\; \ldots . \qquad (5.8)$$

The terms c_1 and c_2 denote the lowest order corrections to the homogeneous solution. c_1 depends linearly, c_2 in second order on $\tilde{u}$. For small variations of the velocity we neglect corrections of higher order. Additionally, the non-linear term c^p is also expanded with respect to the fluctuating velocity field,

$$c^p \;=\; c_0^p \;+\; p c_0^{p-1} c_1 \;+\; p c_0^{p-1} c_2 \;+\; p(p-1) c_0^{p-2} c_1^2 \;+\; \ldots . \qquad (5.9)$$

(5.8) and (5.9) are inserted into (5.5) - (5.7) and the ensemble average is performed. After some mathematical manipulations we end up with the following expressions: As expected, the ensemble averaged transport velocity is given by the averaged velocity of the groundwater flow:

$$u_i^{\mathrm{ens}}(t) \;=\; \bar{u}_i \delta_{i,1} . \qquad (5.10)$$

One finds the same result in linear transport theory [62]. This result is also consistent with numerical simulations of the transport with non-linear adsorption performed by [1], [17].

For the dispersion coefficients one obtains the following integral expressions:

$$D_{ii}^{\mathrm{ens}}(t) = D_{ii} + \int_0^t \left(\int d^d x\, w_{ii}(\boldsymbol{x})\, g_0(\boldsymbol{x},t') \right) dt' \qquad (5.11)$$

$$D_{ii}^{\mathrm{eff}}(t) = D_{ii}^{\mathrm{ens}}(t) - \frac{\int d^d x\, d^d x'\, d^d x''\, c_0(\boldsymbol{x},t) \int_0^t dt'\, w_{ii}(\boldsymbol{x}-\boldsymbol{x}'')\, g_0(\boldsymbol{x}'-\boldsymbol{x}'',t-t')\, c_0(\boldsymbol{x}'',t')}{\left(\int d^d x\, c_0(\boldsymbol{x},t) \right)^2} \qquad (5.12)$$

Obviously, in order to evaluate D_{ii}^{ens} and D_{ii}^{eff} explicitly, we have to specify the solution of the homogeneous transport case $c_0(\boldsymbol{x},t)$ and the corresponding Green's function $g_0(\boldsymbol{x},t)$ as well as the spatial correlation function of the fluctuating velocity field. We choose a Gaussian shaped correlation function the explicit shape of which is given in appendix B.

5.2.2 Purely Advective Transport

This subsection is focused on purely advective transport of solutes (neglecting small scale dispersive spreading of the plume, $\boldsymbol{D}$=0). In this case, the explicit form of c_0 is known and the transport parameters can be evaluated explicitly. For c_0 one uses the one-dimensional analytical solution (7.36) from subsection 7.1.5.2.

It is started with the explicit evaluation of the longitudinal ensemble dispersion coefficient D_{11}^{ens}. Inserting the homogeneous solution (7.36) into (5.11), performing time integration and the spatial integration over the y coordinate one obtains

$$
\begin{aligned}
D_{11}^{\mathrm{ens}}(t) &= D_{11} + \int_0^t \left(\int dx_1 \, w_{11}(\boldsymbol{x}) \, c_0(\boldsymbol{x},t') \right) dt' \\
&= D_{11} + \frac{\sqrt{\pi}}{2} \sigma_f^2 \bar{u} \, l_x \int_0^{\eta_2} v_0^p(p\,\eta) \, F(\eta,t) \, d\eta
\end{aligned}
\quad , \qquad (5.13)
$$

where the spatial coordinate x is rewritten in terms of the dimensionless variable η, defined in (7.36). The function $F(\eta,t)$ is given in two spatial dimensions by

$$
\begin{aligned}
F(\eta,t) &= \operatorname{erf}\left(\frac{B}{l_x}\right) \\
&\quad + \frac{2}{\sqrt{\pi}} \left(\frac{l_x^3 \exp\left(-\frac{B^2}{l_x^2}\right)}{\sqrt{8}\,B^3} - \frac{l_x \exp\left(-\frac{B^2}{l_x^2}\right)}{\sqrt{2}\,B} - \frac{l_x^3}{\sqrt{8}\,B^3} + \frac{3\,l_x}{\sqrt{8}\,B} \right)
\end{aligned}
\qquad (5.14)
$$

and $B = \eta t^p \bar{u}^p \phi^{p-1} M_0^{1-p} / k_d$. The time behaviour of D_{11}^{ens} is essentially determined by the time behaviour of the function $F(\eta,t)$: For very long times, $t \to \infty$, the error function in (5.14) becomes one, all other terms vanish and $F(\eta,t)$ approaches the constant value one. Thus, the longitudinal ensemble averaged dispersion coefficient is simply given by

$$
D_{11}^{\mathrm{ens}}(\infty,p) = D_{11} + \frac{\sqrt{\pi}}{2} \sigma_f^2 \bar{u} \, l_x = D_{11}^{\mathrm{ens}}(\infty,p=1) \, . \qquad (5.15)
$$

The result is identical to the asymptotic behaviour of linearly adsorbing transport [27], [62].

For finite times one can evaluate the integrals in (5.13) as well, leading to an explicit result for the transient behaviour of $D_{11}^{\mathrm{ens}}(t)$. Its explicit form is rather complicated and is stated in appendix C only. The time behaviour of $D_{11}^{\mathrm{ens}}(t)$ is plotted in Fig. 5.4 (p=0.9, 0.8, 0.7, 0.6, 0.5). For different values of the Freundlich exponent p the asymptotic dispersion

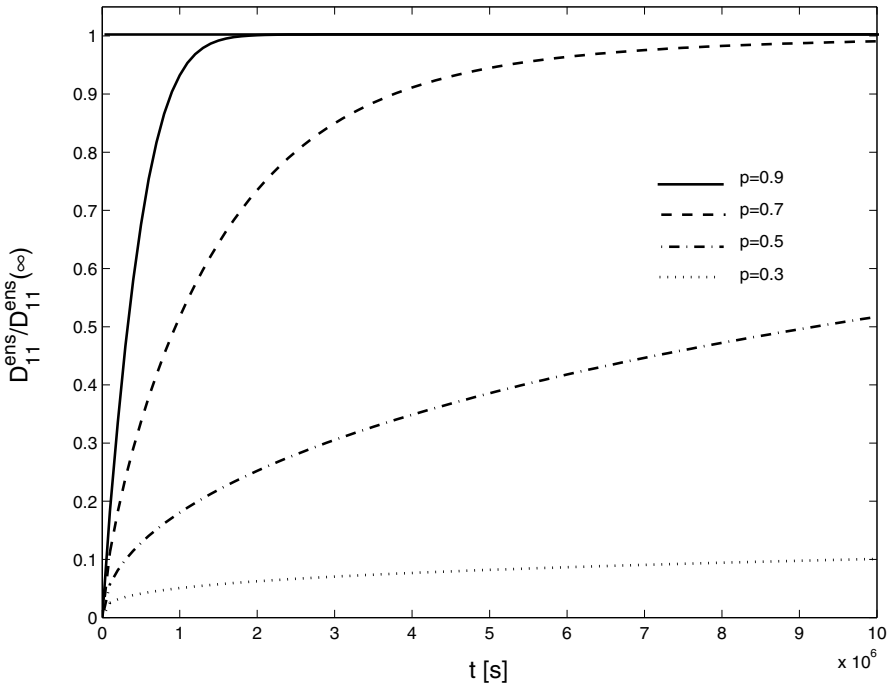

Fig. 5.4 Longitudinal ensemble dispersion coefficients against time in the case $\boldsymbol{D}$=0 for different Freundlich exponents

coefficient is independent of p but it is approached at different times: The smaller p, the stronger is the non-linear character of the transport process and the concentration movement becomes more strongly retarded. In order to approach the asymptotic behaviour, the solute concentration has to sample at least several correlation lengths of the heterogeneous medium which takes the more time the smaller the Freundlich exponent p is.

More precisely, the temporal behaviour of $D_{11}^{\mathrm{ens}}(t)$ is characterised by an advective time scale τ_{adv} which can be identified directly from the explicit expression of D_{11}^{ens} in appendix C as

$$\tau_{adv} = \frac{l_0^{\frac{1}{p}} k_d^{\frac{1}{p}}}{\left(\frac{M_0}{\phi}\right)^{\frac{1-p}{p}} \bar{u}} . \qquad (5.16)$$

It describes the time in which the center of mass moves advectively over the distance of one correlation length. For p=1, τ_{adv} reduces to the linear advective time scale, $\tau_u = l_0 R/\bar{u}$ where R is a constant retardation factor. For p<1 the advective time scale is essentially influenced by the non-linearity and the total mass of the solute. The larger the total mass, the faster the concentration distribution moves through the medium which in turn reduces the time it needs to sample one correlation length.

Finally, the behaviour of D_{11}^{eff} is briefly discussed. For infinite Peclet numbers the second term in (5.12) equals D_{11}^{ens} and the effective dispersion coefficient is zero

$$D_{11}^{\text{eff}} = 0. \qquad (5.17)$$

The reason for this behaviour is simple: After a point-like injection of solute the distribution follows a single flow streamline. Obviously, the dispersion coefficient is zero in each single realisation leading to a vanishing dispersion coefficient after ensemble averaging, $D_{11}^{\text{eff}} = 0$.

The results for D_{11}^{ens} and D_{11}^{eff} indicate once more the importance of how the ensemble average is performed for pre-asymptotic transport: Only effective dispersion coefficients yield a realistic description of the system behaviour. Of course, the situation changes, if small-scale dispersion is acting. This is the focus of the next section.

5.2.3 Transport with Finite Peclet Numbers

5.2.3.1 Asymptotic Behaviour

The derivation of the asymptotic behaviour for finite Peclet numbers is possible without any knowledge of the explicit shape of the homogeneous concentration distribution $c_0(\boldsymbol{x},t)$ in (5.12) and (5.11). The crucial point is that for very long times the time integral over the Green's function $g_0(\boldsymbol{x}-\boldsymbol{x}',t-t')$ in (5.12) and (5.11) becomes equivalent to the corresponding steady-state Green's function in the conservative transport case. Accordingly, the ensemble dispersion coefficient reduces to the result for linearly adsorbing transport

$$D_{ii}^{\mathrm{ens}}(\infty,p) \quad = \quad D_{ii}^{\mathrm{ens}}(\infty,p=1)\,. \tag{5.18}$$

The solutions for $D_{ii}^{\mathrm{ens}}(\infty,p=1)$ are well-known [30], [62]. Their explicit form depends on the spatial dimension as well as on the anisotropy of the medium and the Peclet number relating advective and dispersive processes, $\mathrm{Pe} \equiv \bar{u} l_x / D_{11} = l_x / \alpha_{11}$.

Furthermore, for very long times the second term in (5.12) approaches zero. The effective dispersion coefficient becomes equivalent to the ensemble dispersion coefficient

$$D_{ii}^{\mathrm{ens}}(\infty) \quad = \quad D_{ii}^{\mathrm{eff}}(\infty) \tag{5.19}$$

which indicates that the plume has reached its ergodic regime.

5.2.3.2 Transient Results

For transient times one is not aware of any explicit solution for D_{11}^{ens} and D_{11}^{eff} derived rigorously from formulae (5.11) and (5.12). However, in this case one was able to derive explicit results for the ensemble and the effective dispersion coefficients.

It was found out that the ensemble dispersion coefficient (C C.1), rewritten in terms of the travel distance instead of the travel time can be approximated by the ensemble dispersion coefficient of the linearly adsorbing transport. The only difference is that for a non-linearly adsorbing solute the correlation length of the heterogeneous medium appears to be increased

$$l_x \rightarrow \frac{1}{\left(\frac{M_0}{\phi}\right)^{\frac{1-p}{p}}} \cdot l_x = \quad l_x'\,. \tag{5.20}$$

The reason for this difference lies in the extremely large tailing of the concentration. The concentration in the tail needs more time to travel over a correlation length which can effectively be modelled by a larger correlation length.

Following the proposed approximation and using the exact results, derived in linear transport theory [37], transient longitudinal dispersion coefficients for transport with non-linear adsorption can analogously be assumed in two dimensions as

$$D_{11}^{\mathrm{ens}}(x_1 > l_x) = D_{11} + \sigma_f^2 \dot{u} l_x \frac{\sqrt{\pi}}{2}\left(1 - \frac{3}{2}\sqrt{\frac{2}{\pi}}\mathrm{Pe}^{-1}\right) \qquad (5.21)$$

$$D_{11}^{\mathrm{eff}}(x_1 > l_x) = D_{11} + \sigma_f^2 \dot{u} l_x \frac{\sqrt{\pi}}{2}\left(1 - \frac{3}{2}\sqrt{\frac{2}{\pi}}\mathrm{Pe}^{-1}\right) \times \left(1 - \frac{1}{\sqrt{1 + 4\dfrac{\alpha_{22} x_1}{l_x'}}}\right) . \qquad (5.22)$$

This assumption is heuristic and can be proved only by numerical evaluation of formulae (5.11) and (5.12). This is presented at the end of subsection 5.2.4.

5.2.4 Semi-Analytical Results

Considering a non-zero local dispersivity there is no explicit solution of the homogeneous non-linear transport problem which is needed for evaluation of (5.11) and (5.12). Therefore, it is proceeded as follows: Two-dimensional concentration distributions in a homogeneous porous medium are calculated numerically. The numerical solution is used for evaluation of the integral expressions for $\boldsymbol{D}^{\mathrm{eff}}$ and $\boldsymbol{D}^{\mathrm{ens}}$. One aims to quantify the impact of local dispersion on the transient behaviour of $\boldsymbol{D}^{\mathrm{ens}}$ and $\boldsymbol{D}^{\mathrm{eff}}$ as functions of time and prove the validity of the explicit results derived in (5.21) and (5.22).

The numerical code MODFLOW [98] is used for numerical calculation of the Darcy velocity field. Assuming a constant head gradient and constant permeability k_f=10^{-4} m s^{-1} a uniform steady state flow field is modelled with u=$1.2 \cdot 10^{-5}$ m s^{-1} in the x-direction in a two-dimensional domain. The domain is resolved by elements of grid size Δx=0.1 m in x-direction and Δy=0.5 m in y-direction. For solving the transport problem it is chosen the program package MT3DMS [145] with a GCG Jacobi preconditioned solution meth-

od. The advective part is solved by upstream finite differences with a Courant number Co=0.1. Space and time discretisation are specified such that the grid Peclet number is smaller than 2. The dispersion is implemented implicitly. The transverse and longitudinal dispersivities are assumed to be isotropic, α_{11}= α_{22}=0.055 m. The porosity is set to ϕ=0.1.

The non-linear adsorption isotherm is parameterised by a Freundlich exponent p=0.5 and a Freundlich coefficient K_{nl}=0.53 (g m^{-2})$^{1-p}$. One considers a point-like injection of solute with initial concentration c_0=0.05 g m^{-2}. Additionally, for the correlation function of the spatially distributed velocity field isotropic correlation lengths, l_x= l_y = l_0 = 1 m, is used. Thus, the Peclet number is equal to Pe= l_0/α_{11}=18.18. The variance of the $\ln(k_f)$ is σ_f^2=0.1.

5.2.4.1 Transport Parameters with Linear Adsorption

First with a brief discussion of solute transport with linear adsorption, p=1, in heterogeneous velocity fields is performed.

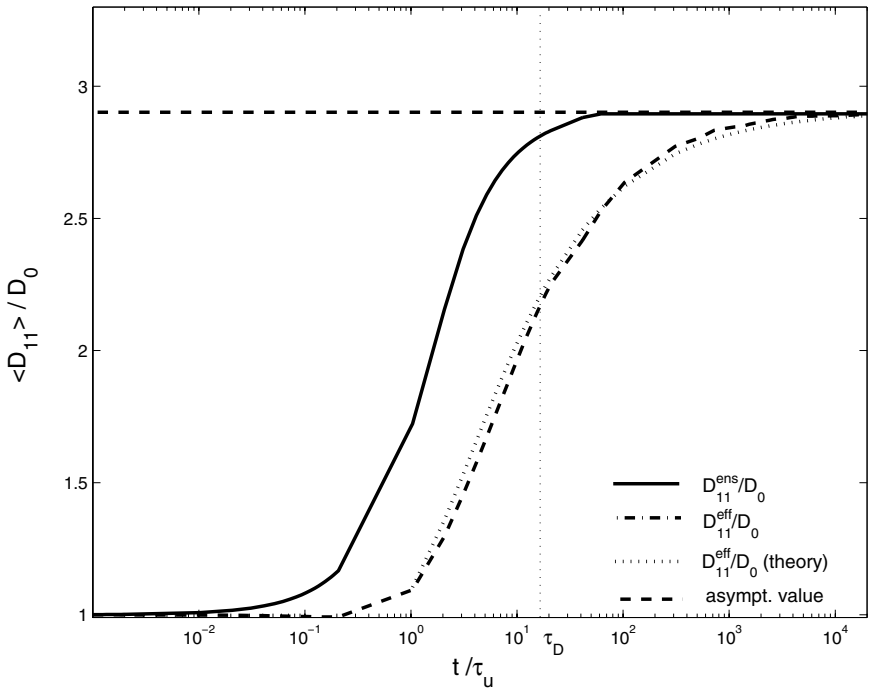

Fig. 5.5 Effective and ensemble longitudinal dispersion coefficient with p=1

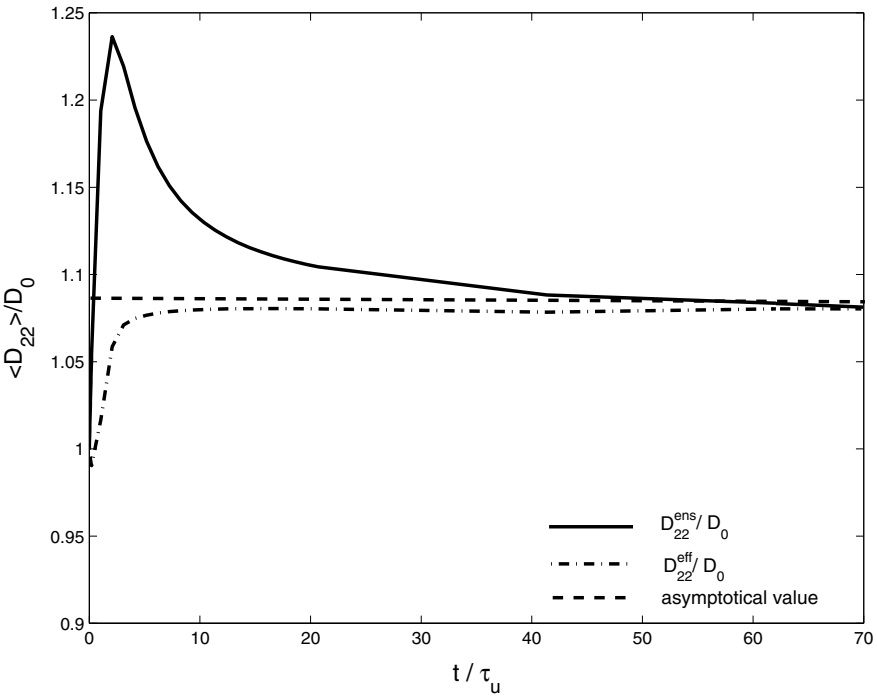

Fig. 5.6 Effective and ensemble transversal dispersion coefficient with p=1

The temporal behaviour of ensemble and effective transport parameters is well known and has been studied both in numerical simulations and theoretical investigations [4], [22], [37], [84], [115], [116]. The explicit results of transport with linear adsorption are used in order to check the reliability of our semi-analytical approach and the precision of the numerical routines. Later on, the numerical results are compared to the results for transport with non-linear adsorption.

In Fig. 5.5 and Fig. 5.6 ensemble and effective dispersion coefficients in longitudinal and transverse directions are plotted as a function of time and compare them with analytical expressions. The impact of numerical dispersion is taken into account.

Studying the temporal behaviour of $D_{11}^{\mathrm{ens}}(t)$ and $D_{11}^{\mathrm{eff}}(t)$ two relevant time scales can be identified: An advective timescale, $\tau_u = l_0 R/\bar{u}$, and a dispersive time scale, $\tau_D = l_0^2 R/D_{22}$. For times smaller than τ_u the solute has only moved over a distance smaller than one correlation length and has not “felt” any heterogeneities. The dispersion coefficients are given more or less by their small scale values. With larger times the longitudinal ensemble dispersion increases continuously but the longitudinal effective dispersion is still very small. For $t >> \tau_u$ the longitudinal ensemble dispersion coefficient

reaches its asymptotic value. However, the effective dispersion coefficient still increases and converges towards the asymptotic value for times $t >> \tau_D$, see Fig. 5.5. For very long times the difference between ensemble and effective dispersion vanishes.

Transversal dispersion coefficients are shown in Fig. 5.6. For small times, ensemble and effective dispersion coefficients approximately are equal to the small scale transversal dispersion value. For $t >> \tau_u$, effective and ensemble dispersion coefficient approach their asymptotic value which is only slightly increased against their small scale values. However, their transient behaviour differs from each other. The ensemble dispersion coefficient increases rapidly reaching a maximum value for times closed to τ_u and decreases for longer times. Again, this phenomenon is an artificial ensemble mixing effect. It can be explained by the fact that ensemble particles on different flowlines can move apart from each other appearing as an increased transversal width of the plume and therefore as an increased transversal dispersion coefficient. However, due to the divergence free velocity field the particles can not separate infinitely far in transverse direction. For times $t >> \tau_u$ the particles move again towards each other, the transversal dispersion decreases and finally approaches the asymptotic value. In contrast, the effective transversal dispersion coefficient does not show a local maximum. It increases continuously from the small-scale value to its asymptotic value.

5.2.4.2 Transport Parameters with Non-Linear Adsorption

In order to obtain effective and ensemble dispersion in the case of transport with non-linear adsorption we numerically evaluate integral expressions (5.11) and (5.12). The results are plotted in Fig. 5.7 and Fig. 5.8.

The asymptotic values of the longitudinal and transverse dispersion coefficients are equivalent to the results for transport with linear adsorption and match the predicted analytical values in section 5.2.3. Differences between linearly and non-linearly adsorbing transport occur only for transient times. The dispersion coefficients start from a small scale value, increase with time and approach their asymptotic value for long times. However, the increase of effective and ensemble dispersion coefficients for non-linearly adsorbing solute is shifted to later times compared to linear transport. This applies for both the longitudinal and the transversal dispersion coefficient, see Fig. 5.7 and Fig. 5.8. It basically means that the transient behaviour of the transport parameters is characterised by time scales different from those in linear transport theory.

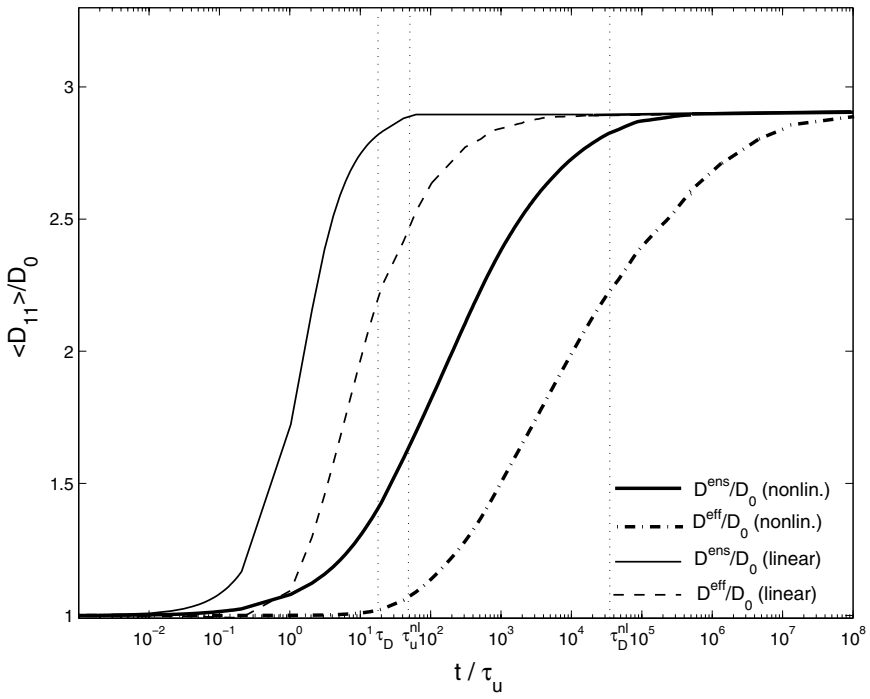

Fig. 5.7 Effective and ensemble longitudinal dispersion coefficients for p=0.5

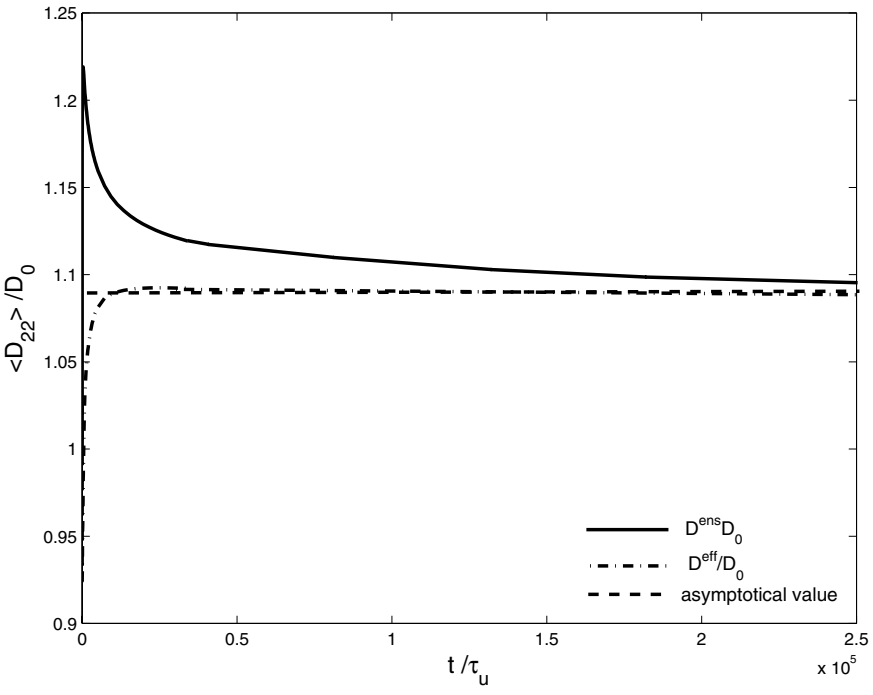

Fig. 5.8 Effective and ensemble transversal dispersion coefficients for p=0.5

If one recalls the way characteristic time scales are introduced in linear transport theory it is consistent to proceed analogously for transport with non-linear adsorption: In linear transport theory the advective time scale is set by the time the centre can be defined by the time the plume needs to spread dispersively over one correlation length in transversal direction.

Following this idea, one uses the center of mass and the squared transversal width of the non-linearly adsorbing plume [17], [33] to derive the typical time scales in the non-linear transport case,

$$\mu_1(t) \approx \left(\frac{M_0}{\phi k_d}\right)^{\frac{2(1-p)}{3-p}} \left(\frac{\dot{u}}{D_{22}}\right)^{\frac{1-p}{3-p}} \left(\frac{\dot{u}t}{k_d}\right)^{\frac{2p}{3-p}} \hat{\mu}_1(p) \geq l_x \qquad (5.23)$$

$$\sigma_{22}^2(t) \approx \left(\frac{M_0}{\phi k_d}\right)^{\frac{2(1-p)}{3-p}} \left(\frac{D_{22}}{\dot{u}}\right)^{\frac{2}{3-p}} \left(\frac{\dot{u}t}{k_d}\right)^{\frac{2p}{3-p}} \hat{\sigma}_{22}^2(p) \geq l_y^2. \qquad (5.24)$$

The p-dependent coefficients $\hat{\mu}_1(p)$ and $\hat{\sigma}_{22}^2(p)$ can be found by numerical integration. For a Freundlich exponent p=0.5 they are $\hat{\mu}_1(p)$ =0.656 and $\hat{\sigma}_{22}^2(p)$ =0.853. Therefore, typical time scales for non-linearly adsorbing solutes can be introduced as:

$$\tau_u^{nl} = \frac{l_x^{\frac{3-p}{2p}} k_d^{\frac{1}{p}} D_{22}^{\frac{1-p}{2p}}}{\dot{u}^{\frac{1+p}{2p}} \left(\frac{M_0}{\phi}\right)^{\frac{1-p}{p}} \hat{\mu}_1(p)^{\frac{3-p}{2p}}} \qquad (5.25)$$

$$\tau_D^{nl} = \frac{l_y^{\frac{3-p}{p}} k_d^{\frac{1}{p}} D_{22}^{-\frac{1}{p}}}{\dot{u}^{-\frac{1-p}{p}} \left(\frac{M_0}{\phi}\right)^{\frac{1-p}{p}} (\hat{\sigma}_{22}^2(p))^{\frac{3-p}{2p}}}. \qquad (5.26)$$

Additionally, the typical transverse Peclet number for transport with non-linear adsorption is introduced as:

$$Pe_{\mathrm{T}} = \frac{\tau_u^{nl}}{\tau_D^{nl}} = \left(\frac{l_y^2 \bar{u}}{l_x D_{22}}\right)^{\frac{3-p}{2p}} \left(\frac{\hat{\mu}_1(p)}{\hat{\sigma}_{22}^2(p)}\right)^{\frac{3-p}{2p}} . \qquad (5.27)$$

As one can see, this Peclet number reflects the non-linear character of the adsorption process. The smaller the p-value is, the bigger the Peclet number appears. In comparison to linear transport, this could be explained by a reduced transverse dispersion coefficient. In fact, a decreasing Freundlich exponent results in a stronger retardation and a smaller dispersion coefficient.

The advective and dispersive time scales depend on the small scale transversal dispersion coefficient D_{22} and the total mass M_0. Especially, the transversal dispersion coefficient not only affects the spreading in transversal direction, but also the center of mass movement of the plume. A large transversal dispersion coefficient causes enhanced mass flow in transversal direction. The local concentration decreases and becomes more strongly retarded due to concentration dependent retardation effects which slow down the center of mass velocity. Moreover, the center of mass movement and the width of the plume are influenced by the total mass. A larger total mass increases the center of mass velocity due to smaller retardation which can decrease the advective time scale τ_u^{nl} against τ_u as well as τ_D^{nl} against τ_D.

As one sees in Fig. 5.7 and Fig. 5.8, the model parameters (M_0,D_{22}) in this special numerical case are chosen in a way, that τ_u^{nl} and τ_D^{nl} are shifted to later times. In general, the time behaviour of the dispersion coefficients in case of linear adsorption does not depend on M_0. Thus, the results for linearly adsorbing transport can always be used in comparison with non-linear results with different total mass and transverse dispersion for analysis of the differences in the typical temporal behaviour of dispersion coefficients due to non-linear adsorption.

The time scales τ_u^{nl} and τ_D^{nl} explain reasonably well the qualitative behaviour of effective and ensemble transport parameters for the non-linearly adsorbing solute. For small times, $t < \tau_u^{nl}$, the ensemble dispersion coefficient grows rapidly. The effective dispersion coef-

ficient is still small because the plume in a single realisation has not yet spread. Due to ensemble averaging effects the ensemble dispersion coefficient reaches its asymptotic values already for times $\tau_u^{nl} \ll t \ll \tau_D^{nl}$. The effective longitudinal dispersion coefficient approaches its asymptotic values for later times, $t \gg \tau_D^{nl}$, after the plume has spread also in transversal direction over several correlation lengths. For comparison, the characteristic time scales τ_u, τ_D, τ_u^{nl} and τ_D^{nl} are plotted in Fig. 5.7 and Fig. 5.8.

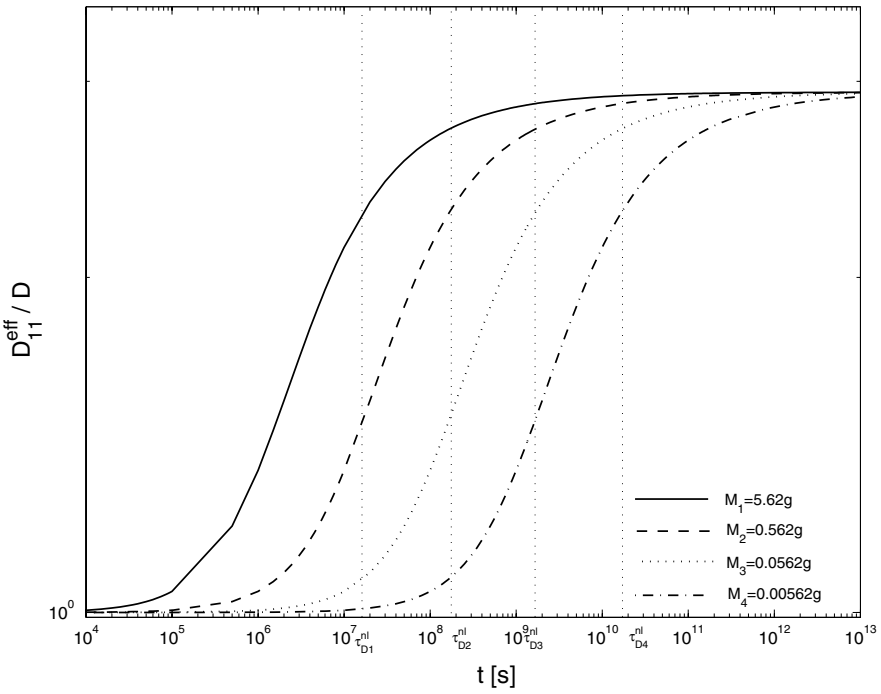

Fig. 5.9 Total mass impact on the effective longitudinal dispersion coefficient

The impact of the total mass on the effective longitudinal dispersion coefficient is separately demonstrated in Fig. 5.9. $D_{11}^{\mathrm{eff}}(t)$ was calculated for four different values of the total mass and otherwise unchanged model parameters. The larger the total mass, the smaller is the dispersive time scale τ_D^{nl} and the faster the asymptotic value is reached.

Moreover, it has to be stressed the point that the semi-analytical approach allows the estimation of transport parameters on large scales by means of the solutions of the homogeneous case only and without performing costly stochastical simulations. This can be very useful for practical applications in the field of risk assessment.

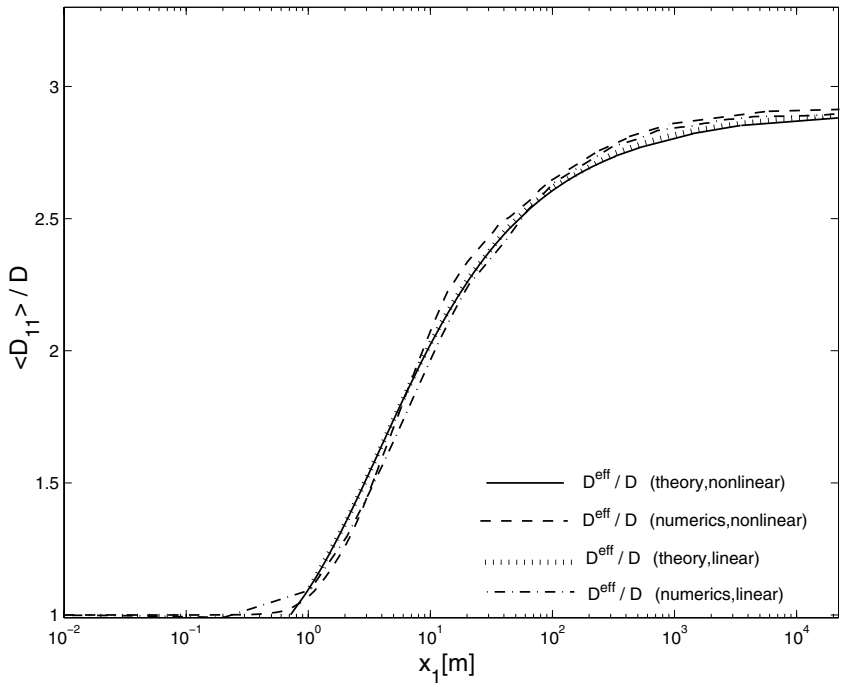

Fig. 5.10 Theoretical and semi-analytical results as function of travel distance for effective longitudinal dispersion coefficients

5.2.4.3 Comparison of Semi-Analytical and Explicit Results for $D^{\mathrm{eff}}(x)$

In (5.22) heuristically an explicit expression for effective dispersion coefficients was derived as a function of travel distance.

In Fig. 5.10 the semi-analytical results are compared with the explicit solution for $D_{11}^{\mathrm{eff}}(x)$. The travel distance is calculated from the center of mass velocity. An excellent agreement was found: $D_{11}^{\mathrm{eff}}(x)$ in the linear and the non-linear case almost overlap. In other words, the explicit formula for $D_{11}^{\mathrm{eff}}(x)$ describes the behaviour of the effective dispersion coefficient adequately.

5.2.5 Relevance of Equivalent Homogeneous Transport Models

The ensemble and effective mixing behaviour in a heterogeneous formation are modelled by using an equivalent homogeneous model. For this reason large-scale transport parameters are proposes to be calculated by means of temporal moments of breakthrough curves because of their high relevance for interpretation of concentration data in the practice. The results from the equivalent homogeneous simulations are compared with the corresponding results from numerical simulations of transport in heterogeneous

domains. One finds that the ensemble averaging procedure causes an additional spreading of the concentration distribution which can only be reproduced if a non local equivalent homogeneous model is used.

Tab. 5.1 Parameters for the two-dimensional heterogeneous problem

Parameter	Value
$\bar{k}_f$ [m s^{-1}]	10^{-4}
σ_f^2 $(\ln(k_f))$	0.12
l_x [m]	1
l_y [m]	0.5
ϕ	0.1
$\bar{u}$ [m s^{-1}]	10^{-5}
α_{11} [m]	0.055
α_{22} [m]	0.0055
c^{in} [g m^{-2}]	1 g m^{-2}
ρ_r [kg m^{-2}]	2 000
p	0.75
K_{nl} [(g m^2)$^{1-p}$]	$7.5 \cdot 10^{-5}$

5.2.5.1 Numerical Computation and Parameter Setup

A two-dimensional log-normally distributed hydraulic conductivity field is considered to represent a sufficiently large sector of a heterogeneous aquifer, covering 36 correlation lengths in longitudinal and 20 correlation lengths in transverse direction. The random field is generated within the code FGEN [117] which uses a fast Fourier method to generate correlated stationary random fields with given mean, variance, correlation length and distribution type. One sample realisation of the stochastically distributed conductivity field is shown in Fig. 5.11 ($\bar{k}_f$=10^{-4} m/s, σ_f^2=0.12, l_x=1 m, l_y=0.5 m). The domain contains 360 by 200 cells of grid size $\Delta x = \Delta y$=0.1 m. The mean of the spatially variable flow field is constructed to align with the x-direction. The solute is released instantaneously in time and uniformly over the whole inflow boundary. The simulation parameters can be found in Tab. 5.1. For comparison two different situations are simulated: conservative transport and transport with non-linear adsorption of Freundlich type.

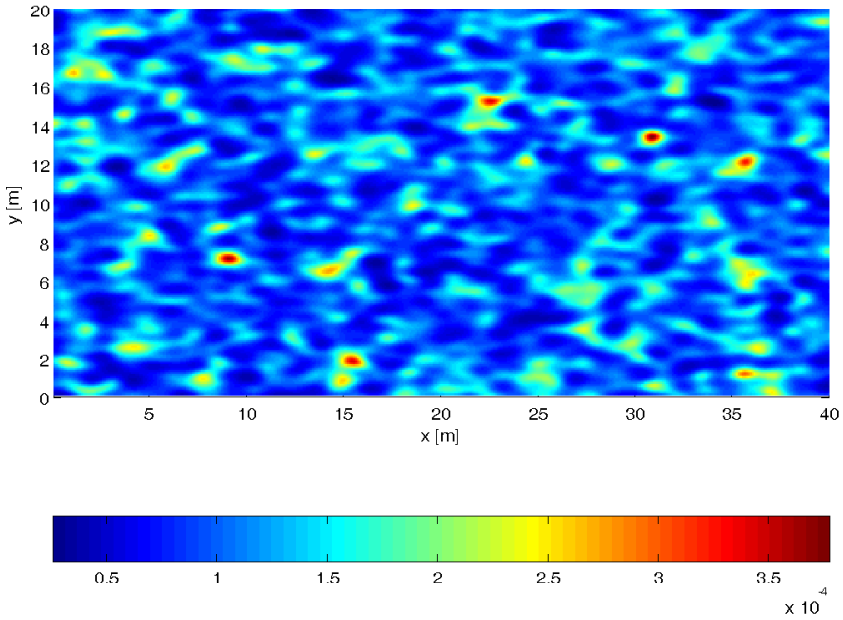

Fig. 5.11 Two-dimensional log-normally distributed hydraulic conductivity field

Fig. 5.14 and Fig. 5.15 show the concentration distribution for conservative transport and transport with Freundlich adsorption at intermediate transport time. In both cases the fluctuating velocity field leads to travel time differences between solute particles on different streamlines. The originally uniformly distributed line source is irregularly deformed. The resulting patterns reflect the typical structure of the velocity field. For conservative transport it is obvious, that the heterogeneity of the velocity field causes an enhancement of the width of the solute distribution. This corresponds to an enlarged longitudinal dispersion coefficient expressed in an increased width of the concentration distribution, cp. Fig. 5.15. For non-linearly adsorbing solute the concentration dependent retardation results in a self-sharpening front with a large tailing behind it. Contrary to conservative transport, the width of the concentration profiles does not give any quantitative information about the magnitude of dispersion coefficients. This is shown in Fig. 5.13 where cross-sectionally integrated breakthrough curves in the heterogeneous medium are compared with breakthrough curves in a homogeneous domain.

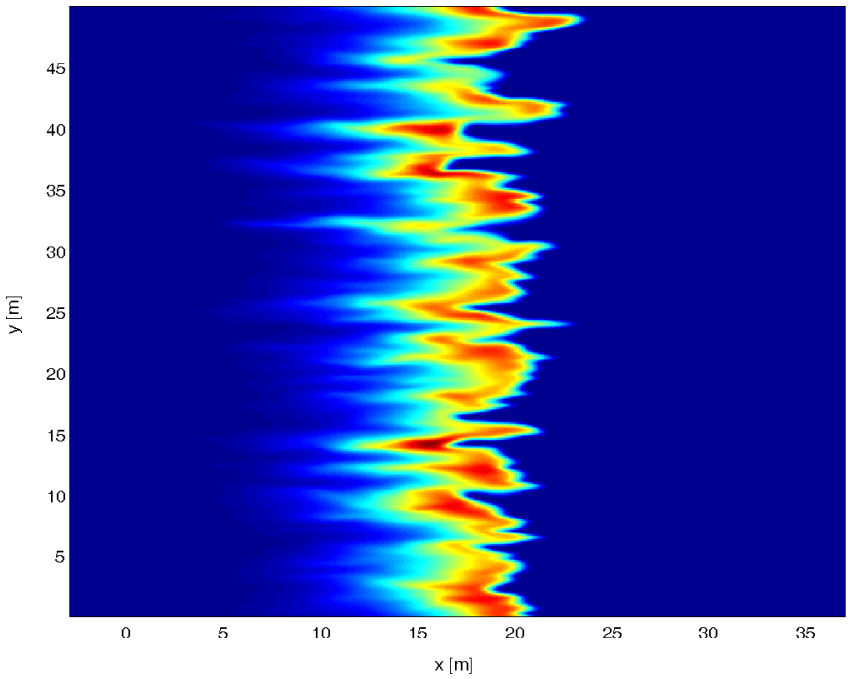

Fig. 5.12 Concentration distribution for non-linear adsorption at t=9.5·10^6 s

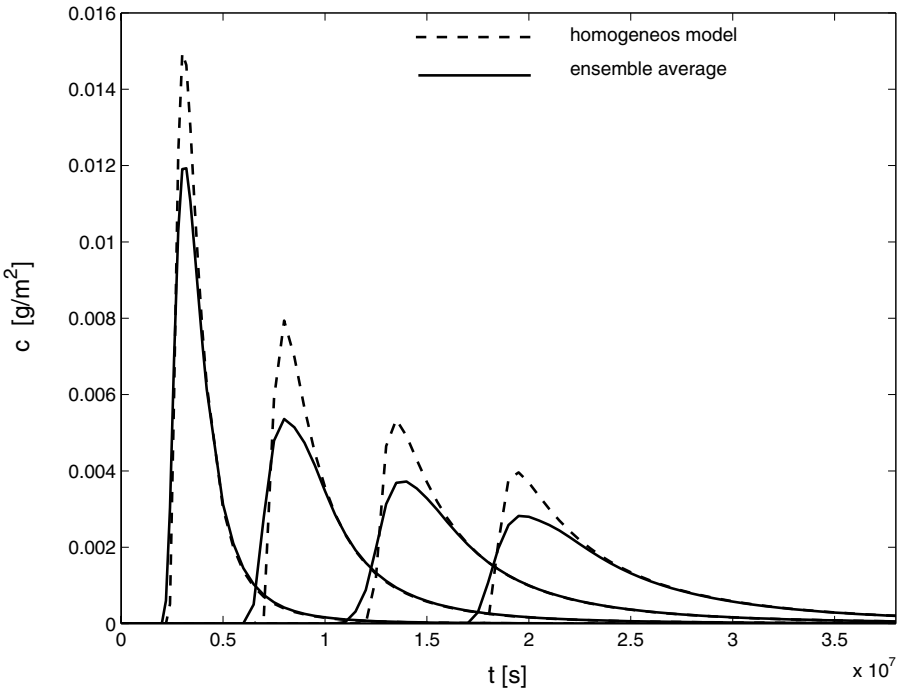

Fig. 5.13 Impact of spatially variable velocities on spreading behaviour of transport with non-linear adsorption

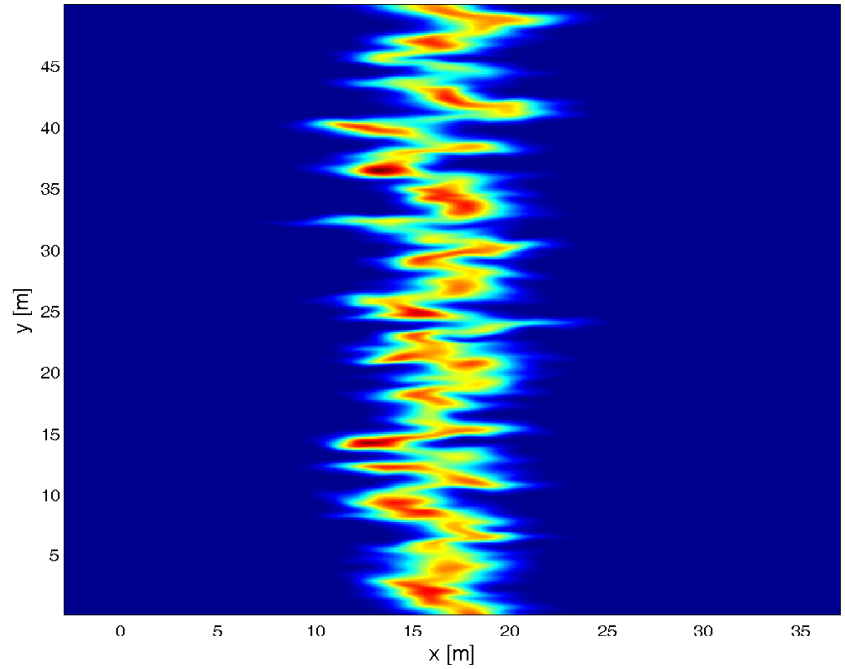

Fig. 5.14 Concentration distribution for conservative transport at t=1.6·10^6 s

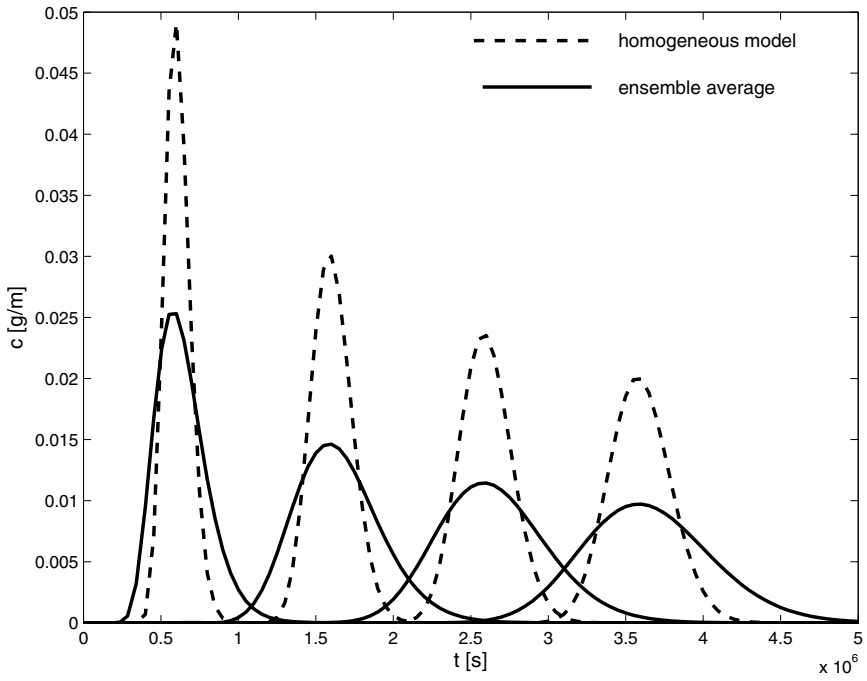

Fig. 5.15 Impact of spatially variable velocities on spreading behaviour on conservative transport

5.2.5.2 Definition of Effective and Ensemble Transport Parameters

If one considers the transport velocity and the dispersion coefficient as random processes one can average them over the ensemble of all realisations. It is proposed to define effective transport parameters as a function of space at location x_i by using expressions (7.20) and (7.21). Consequently, the transport velocity can be written as

$$u_i^{\text{eff}} = \overline{\frac{m_0}{m_1} x_i + k_d \frac{\int_0^{x_i} m_0^{\text{ads}} dx'_i}{m_1}} . \qquad (5.28)$$

The effective dispersion coefficient is given as:

$$D_{ii}^{\text{eff}} = \overline{\frac{m_0 u_i^2}{2} \frac{\left(u_i m_{2c} + 2 k_d \int_0^{x_i} \left(\frac{m_1 m_0^{\text{ads}}}{m_0} - m_1^{\text{ads}} \right) dx'_i \right)}{\int_0^{x_i} (m_0 + k_d m_0^{\text{ads}})^2 dx'_i}} . \qquad (5.29)$$

The equivalent homogeneous model reads

$$R(c) \frac{\partial}{\partial t} c(\boldsymbol{x},t) + \frac{\partial}{\partial x_i} \left(u_i^{\text{eff}} c(\boldsymbol{x},t) - (D_{ij} + D_{ij}^{\text{eff}}) \frac{\partial}{\partial x_j} c(\boldsymbol{x},t) \right) = 0 . \qquad (5.30)$$

The second possibility to calculate large-scale transport parameters is to directly average the heterogeneous transport equation over a stochastic ensemble. By this approach, the ensemble dispersive flux, which arises as a result of center-of-mass fluctuations in different realisations of the heterogeneous medium, is given in a general non local form. Thus, the equivalent homogeneous problem is represented in non local theory by:

$$\begin{aligned} & R(c(\boldsymbol{x},t)) \frac{\partial}{\partial t} c(\boldsymbol{x},t) + \frac{\partial}{\partial x_i} \left(u_i^{\text{ens}} c(\boldsymbol{x},t) - D_{ij} \frac{\partial}{\partial x_j} c(\boldsymbol{x},t) \right) \\ & - \frac{\partial}{\partial x_i} \int_0^t dt' \int d\boldsymbol{x}' g(\boldsymbol{x} - \boldsymbol{x}', t - t') w_{ij}(\boldsymbol{x} - \boldsymbol{x}') \frac{\partial}{\partial x'_j} c(\boldsymbol{x}',t') \end{aligned} . \qquad (5.31)$$

Here, $w_{ij}(\boldsymbol{x}-\boldsymbol{x}')$ denotes the correlation function whose explicit shape is given in the appendix B, and $g(\boldsymbol{x},t)$ is the Green's function of a homogeneous self-adjoint transport problem.

The standard approximation to simplify the non local equation (5.31) is by localizing the ensemble dispersive flux in space and time. This means that $\nabla_{x'}c(\boldsymbol{x}',t')$ does not vary significantly in space and time and can be factored out of the integral

$$\int_0^t dt' \int d\boldsymbol{x}'\, g(\boldsymbol{x}-\boldsymbol{x}',t-t')\, w_{ij}(\boldsymbol{x}-\boldsymbol{x}') \frac{\partial}{\partial x'_j} c(\boldsymbol{x}',t') \approx D_{ij}^{\mathrm{ens}} \frac{\partial}{\partial x'_j} c(\boldsymbol{x},t). \qquad (5.32)$$

The tensor $\boldsymbol{D}^{\mathrm{ens}}$ represents the ensemble dispersion coefficient

$$D_{ij}^{\mathrm{ens}} = \int_0^t dt' \int d\boldsymbol{x}'\, g(\boldsymbol{x}-\boldsymbol{x}',t-t')\, w_{ij}(\boldsymbol{x}-\boldsymbol{x}'). \qquad (5.33)$$

Inserting (5.32) in (5.31) we end up with the equivalent homogeneous equation in local theory:

$$R(c)\frac{\partial}{\partial t}c(\boldsymbol{x},t) + \frac{\partial}{\partial x_i}\left(u_i^{\mathrm{ens}} c(\boldsymbol{x},t) - (D_{ij} + D_{ij}^{\mathrm{ens}})\frac{\partial}{\partial x_j} c(\boldsymbol{x},t)\right) = 0. \qquad (5.34)$$

In the following, it will be discussed the reliability of equivalent homogeneous models in non local (5.31) and local (5.30), (5.34) theory for the reproduction of the ensemble and effective mixing of non-linearly adsorbing solutes.

5.2.5.3 Results for Effective and Ensemble Transport Parameters

As expressed in equations (5.28) and (5.29), effective transport parameters are obtained as an average of transport velocities and dispersion coefficients over the ensemble of all possible realisations. Transferring this idea to the numerical experiment explained before, every single streamline in the heterogeneous domain can be associated with a different one-dimensional realisation of the medium. Accordingly, u_1^{eff} and D_{11}^{eff}

are obtained by calculating the velocity and the dispersion coefficient in each horizontal layer in the heterogeneous domain and subsequently integrating over the transverse direction.

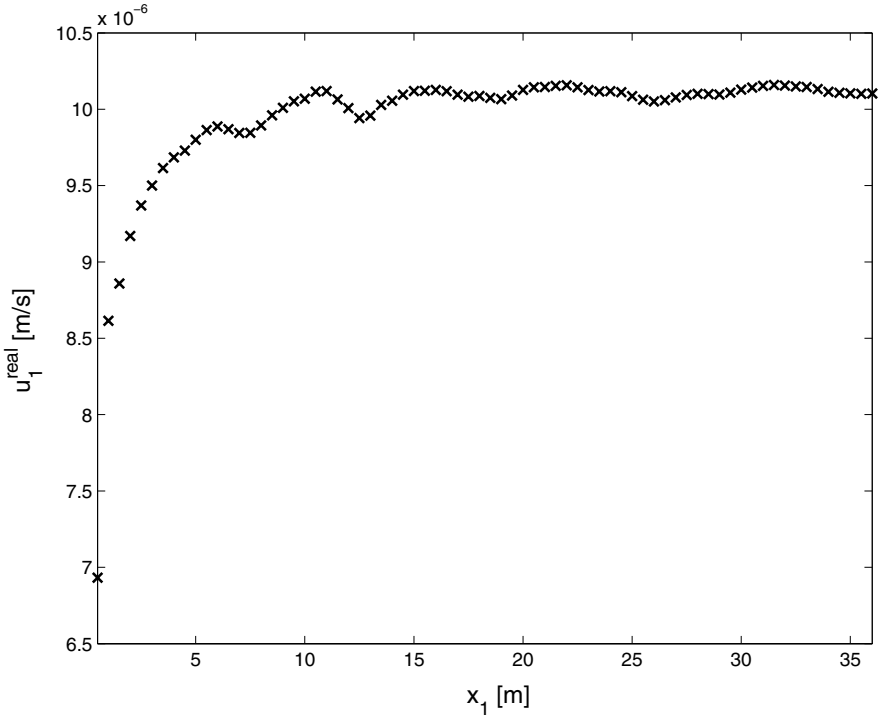

Fig. 5.16 Effective velocity as function of travel distance for p=0.75

In Fig. 5.16 the result for the effective longitudinal velocity is plotted. It increases for small travel distances and converges after about 5 correlation lengths towards the mean transport velocity $\bar{u}$,

$$u_1^{\text{eff}} = \bar{u}\boldsymbol{e}_1 . \qquad (5.35)$$

In Fig. 5.17 the longitudinal effective dispersion coefficient is shown as function of the travel distance. The dispersion coefficients for non-linearly adsorbing (p=0.75) and conservative transport (p=0) are compared. In both cases, D_{11}^{eff} has the same spatial behaviour: It grows quite slowly towards the asymptotic limit. Especially, its behaviour depends on the transverse dispersion which allows solute transfer between different streamlines and smoothes out concentration fluctuations in different streamlines. However, for sufficiently large distances the effective dispersion coefficient approaches the asymptotic limit, see section 5.2.3. For the parameter setup used in the numerical com-

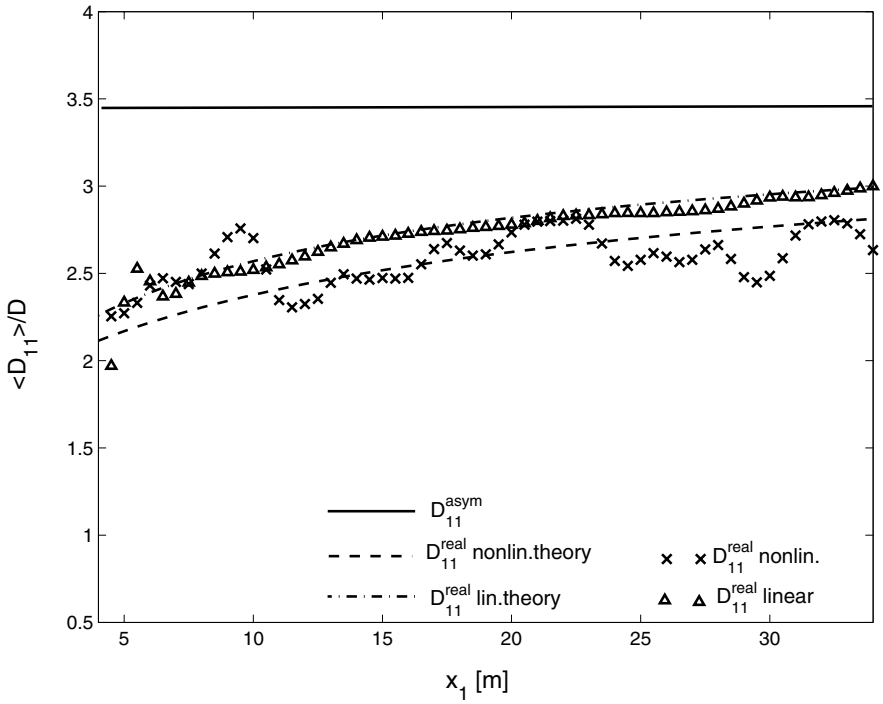

Fig. 5.17 Effective dispersion as function of travel distance
for transport with Freundlich adsorption and conservative transport

putation it is expect that after a travel distance of x=50 m the difference between D_{11}^{asym} and D_{11}^{eff} disappears due to ergodicity. As explicitly shown in subsection 5.2.3, the asymptotic dispersion coefficient for non-linear transport is equivalent to the well-known result for conservative transport

$$D_{11}^{\mathrm{eff}}(x_1 \rightarrow \infty) = \left. D_{11}^{\mathrm{asym}} \right|_{\mathrm{conservative}} . \qquad (5.36)$$

The numerical results are compared with the analytical expressions from section 5.2.3. We find a very good agreement between the theoretical predictions and the numerical calculation.

Ensemble transport parameters are evaluated in local theory using a semi-analytical approach. The ensemble longitudinal velocity is constant and equal to the mean transport velocity, $u_1^{\mathrm{ens}} = \bar{u}\boldsymbol{e_1}$. The longitudinal ensemble dispersion coefficient is calculated from expression (5.33) where a Gaussian correlation function (B.6) is used for the spatially distributed velocity field. The Green's function in (5.33) is solved numerically using translation invariance in space and time.

5.2.5.4 Model of Heterogeneous and Equivalent Homogeneous Media

Using the results derived before, one can answer the question to which extent an equivalent homogeneous medium with large-scale transport parameters can reproduce the effective and ensemble mixing behaviour of a solute in a heterogeneous domain. For this purpose, one proceeds in a twofold way: In order to reproduce the effective mixing behaviour of the solute the one-dimensional equivalent large-scale transport problem (5.30) is solved numerically in local theory with a space-dependent large-scale dispersion coefficients $D_{11}^{\mathrm{eff}}(x)$. Breakthrough curves of the equivalent transport simulation are compared with cross-sectionally averaged local concentration distributions whose center-of-mass positions are superimposed before averaging. In the following, this averaging procedure will be referred to as a “centered average”. Thus, one aims at reproducing the effective mixing of the solute.

The “centered average” has to be distinguished from the “ensemble average” which reflects the ensemble mixing. Ensemble averaged breakthrough curves in the heterogeneous domain are obtained by averaging over the transversal direction without preliminary superposition. For the sake of consistence, they are compared with the results of the equivalent homogeneous simulations reproducing the ensemble mixing which, as shown before, can be solved in localisation approximation (5.34) or in the full non local theory (5.31). Ensemble mixing parameters tend to overestimate the effective mixing process of solutes. Nevertheless, we discuss them as well due to their importance for interpretation of depth-averaged concentrations as they may occur in practical field studies.

Conservative Transport

For the sake of completeness the discussion is started with a short review of conservative solute transport. This case has widely been studied in the last decades [27], [62] and large-scale transport parameters have been calculated using different analytical [31], [32], [115], [116] and numerical [15], [22], [24] techniques. It can be easily shown that the large-scale transport can be reproduced by an equivalent homogeneous equation in local theory with appropriately defined large-scale transport parameters. This applies for the effective as well as for the ensemble mixing transport behaviour.

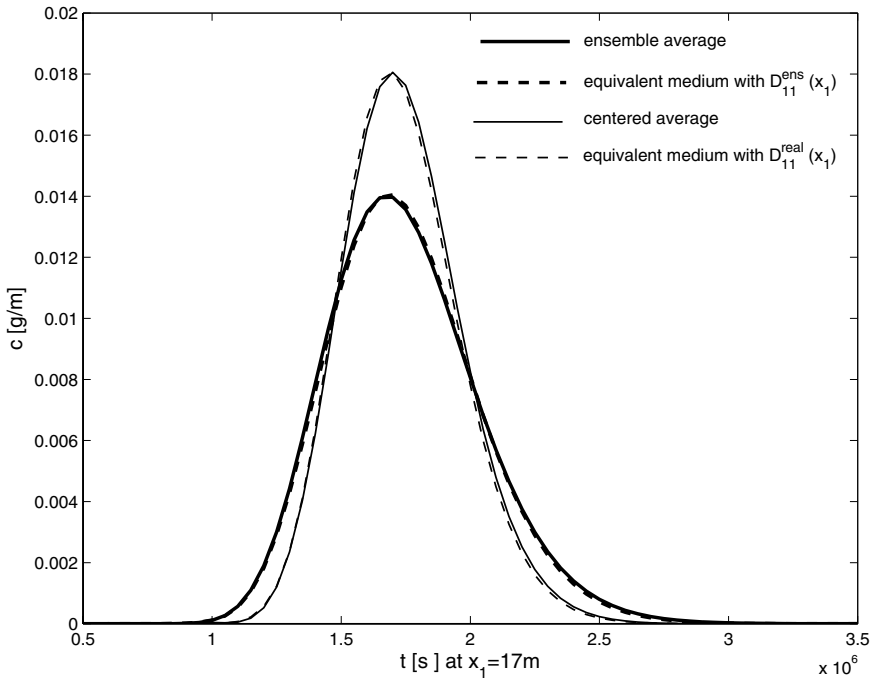

Fig. 5.18 Centered and ensemble averaged breakthrough curves compared with equivalent homogeneous simulations in local theory

The results in Fig. 5.18 confirm the expected behaviour. Here, one reproduces the ensemble and effective mixing behaviour by equivalent homogeneous simulations in local representation (5.34) with $D_{11}^{\mathrm{eff}}(x)$ and $D_{11}^{\mathrm{ens}}(x)$ respectively. In both cases the averaged breakthrough curves in the heterogeneous medium are perfectly reproduced by the equivalent simulation. Especially, the localisation approximation for the ensemble dispersive flux yields reliable results.

Transport with Non-Linear Adsorption

In Fig. 5.19 the breakthrough curves at x=24 m is plotted. The numerical solution of the equivalent transport model (5.30) with the effective dispersion coefficient $D_{11}^{\mathrm{eff}}(x)$ is compared with the centered averaged solution in the heterogeneous formation. Obviously, both breakthrough curves match very well. First of all, this result shows that in order to gain reliable averaged transport parameters the average over the cross section involves a sufficiently large number of different “realisations”. In the simulations this corresponds to a heterogeneous structure covering 40 correlation lengths in transverse direction. Furthermore, effective mixing behaviour can be reproduced by replacing the

heterogeneous medium by an equivalent homogeneous system, as given in equation (5.30), which has the same shape as on mesoscopic scales. Only the effective dispersion coefficient is increased.

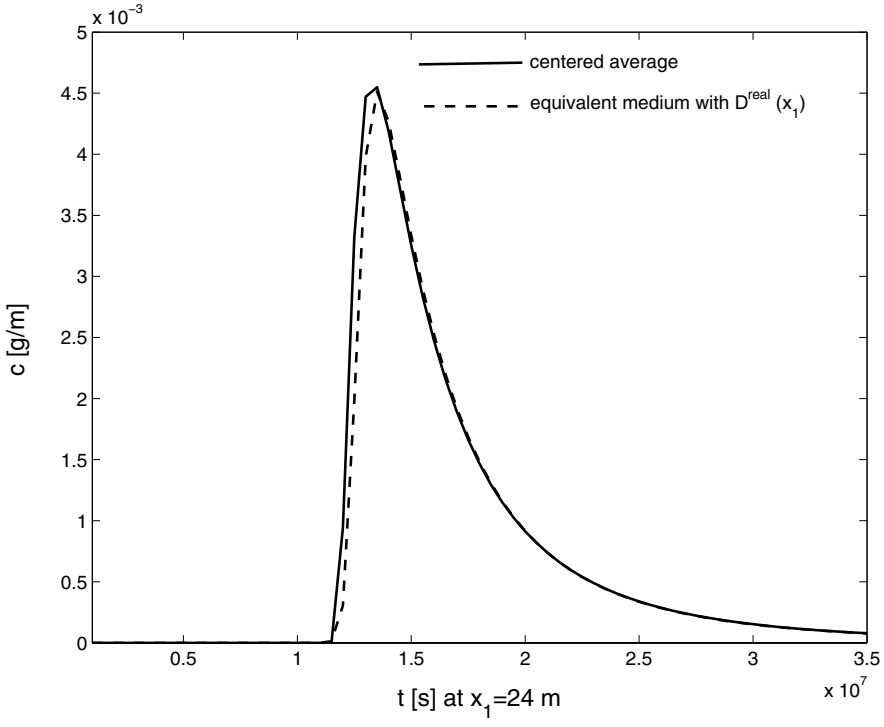

Fig. 5.19 Non-linear adsorbing transport
Comparison of centered averaged breakthrough curves and equivalent homogeneous medium in local theory

The behaviour of ensemble transport is completely different and is illustrated in Fig. 5.20. Here, one plots the ensemble averaged breakthrough curves over the two-dimensional heterogeneous domain at x=24 m and the result of the equivalent homogeneous simulation in localisation approximation with an ensemble dispersion coefficient. The tailing of the concentration distribution is quite well reproduced but the peak concentration and the front steepness fail to be reproduced. The homogeneous large-scale breakthrough curve has a larger maximum peak concentration and a less steep front. It seems as if a larger dispersion coefficient only affecting the concentration distributions at the front has caused an additional spreading by ensemble averaging of the concentration front. On contrary, the solution of the equivalent homogeneous equation is strongly dominated by the non-linear retardation (self-sharpening) and the dispersive spreading is suppressed. Hence,

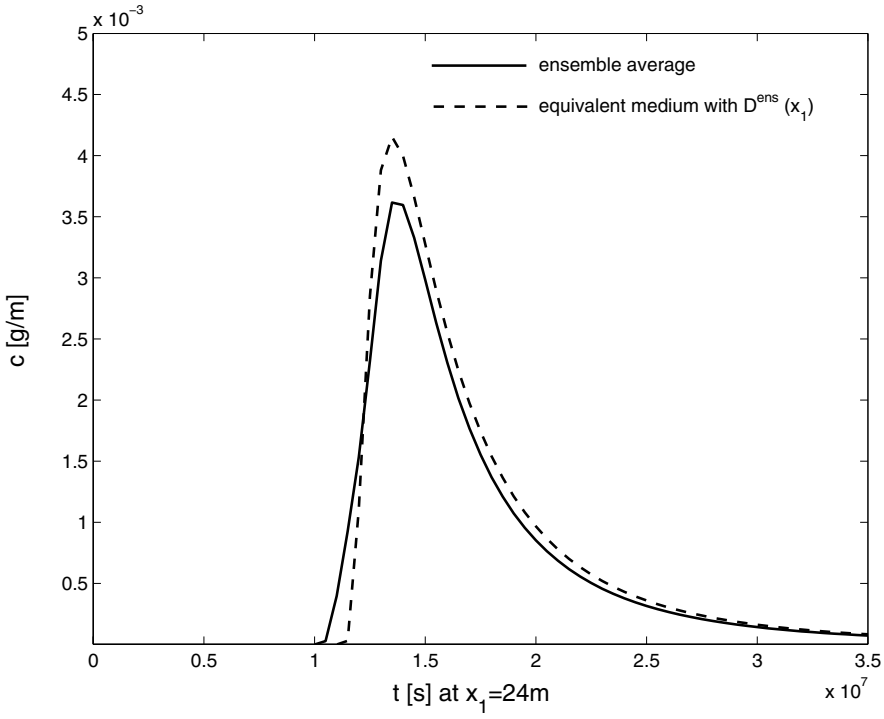

Fig. 5.20 Non-linear adsorbing transport
Comparison of ensemble averaged breakthrough curves and equivalent homogeneous medium in local theory with D_{11}^{ens} at x_1=24 m

the reproduced front is steeper. In contrast, the more pronounced smoothness of the ensemble averaged front in the heterogeneous simulation accounts for the center of mass fluctuations and therefore a stronger influence of dispersive spreading.

To avoid these problems an equivalent homogeneous simulation accounting for a non-local dispersive flux (5.31) is performed. In Fig. 5.21 the result is shown. Here, the ensemble averaged breakthrough curve in the heterogeneous domain is compared with calculations of the equivalent homogeneous model in local and non local theory respectively. Differently from the solution in local theory, the non local equivalent homogeneous simulation exactly reproduces the ensemble mixing transport behaviour. Especially, the front is properly calculated.

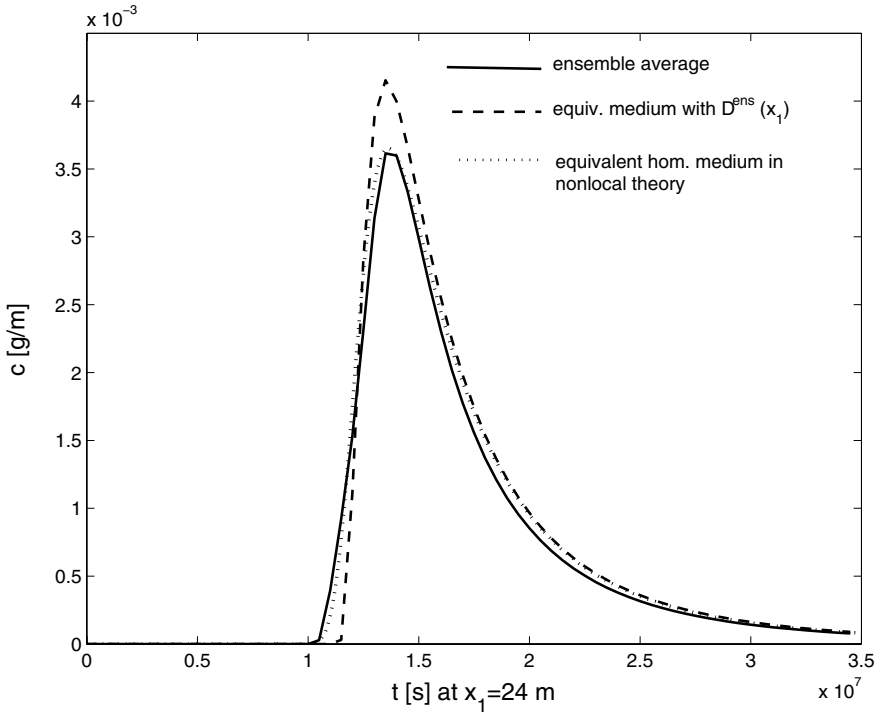

Fig. 5.21 Reproduction of ensemble mixing transport using equivalent homogeneous equation in non local theory

This is the first example where the non-linear character of the adsorption process impacts the large-scale transport behaviour in a way different from linear transport theory. The ensemble mixing behaviour cannot be reproduced by an equivalent homogeneous model of the same type as on the mesoscopic scale. In this case, a non local representation of the ensemble dispersive flux is required.

5.3 Transport in Chemically Heterogeneous Media

In this section it is focused on transport in chemically heterogeneous media and it is assumed that the Freundlich constant or the Freundlich exponent vary in space. The effective large-scale transport behaviour is derived in a homogenisation theory approach. Transient results are obtained in perturbation theory in the case of variable Freundlich constant and numerically for transport in fluctuating Freundlich exponent fields.

5.3.1 Effective Transport Behaviour

The Freundlich constant K_{nl} as well as the Freundlich parameter p are quantities fluctuating on a scale l which is small compared to the overall size of the domain L. In order to investigate the transport behaviour of a solute on the large scale we suppose that the both length scales are strictly separated from each other. This means that only transport processes covering many characteristic correlation lengths of the heterogeneous structure are investigated. The transition from the small to the large scale is asymptotically fulfilled in the limit $\varepsilon := \frac{l}{L} \ll 1$.

The basic idea of homogenisation theory is to construct an expansion of the transport equation in terms of small ε around the large-scale concentration distribution. The asymptotic large-scale transport behaviour is derived in the limit $\varepsilon \to 0$. Additionally, two separated scales are introduced: $\boldsymbol{y}$ accounting for the small-scale variations, and $\boldsymbol{x}$ for the large-scale variations. Both scales are connected by the parameter ε:

$$\varepsilon \;=\; \frac{\boldsymbol{y}}{\boldsymbol{x}}. \tag{5.37}$$

For technical reasons, the transport equation is reformulated in terms of a conserved quantity which in the case of adsorbing transport is the total mass respectively the total concentration:

$$C \equiv c + c^{ad}(c) \;=\; \tilde{F}(c, c^{ad}). \tag{5.38}$$

In particular, the adsorbed concentration is represented by a general adsorption isotherm $c^{ad}(c)$ which includes the small-scale fluctuations. The dissolved concentration c is related to the total concentration by the inverse function of $\tilde{F}(c, c^{ad})$:

$$c \equiv F(C, c^{ad}) \;=\; \tilde{F}^{-1}(c, c^{ad}). \tag{5.39}$$

Thus, the transport equation can be written in terms of C as:

$$\frac{\partial}{\partial t} C(\boldsymbol{x}, t) + \boldsymbol{u} \cdot \nabla_x F(C(\boldsymbol{x}, t)) - \nabla_x \cdot \boldsymbol{D} \nabla_x F(C(\boldsymbol{x}, t)) \;=\; 0. \tag{5.40}$$

For the further development of the homogenisation theory approach one makes the following important ansatz: It is assumed that the adsorption on the large scale is given by an effective adsorption isotherm $\overline{c^{ad}}$ which at this stage is unknown. For linearly adsorbing solutes the effective isotherm is again a linear function of the dissolved concentration with an averaged effective distribution coefficient. However, for non-linearly adsorbing solutes the question is still open what kind of function describes the effective adsorption isotherm $\overline{c^{ad}}$.

Because of conservation of the total concentration C the sum of the new adsorbed concentration $\overline{c^{ad}}$ and the dissolved concentration should remain the same as in equation (5.38):

$$C \equiv c_0 + \overline{c^{ad}}(c_0) = \tilde{F}^*(c_0, \overline{c^{ad}}). \qquad (5.41)$$

The function $\bar{c}$ denotes the dissolved concentration that satisfies the conservation of C. Moreover, c_0 is related to the total concentration by the function $F^*(C, \overline{c^{ad}})$ which is the inverse function of $\tilde{F}^*(c_0, \overline{c^{ad}})$:

$$c_0 \equiv F^*(C, \overline{c^{ad}}) = \tilde{F}^{*-1}(c_0, \overline{c^{ad}}). \qquad (5.42)$$

One includes the effective adsorption into the transport equation (5.40) by adding and subtracting the term $\boldsymbol{u} \cdot \nabla_x F^*(C, \overline{c^{ad}})$.

The next two steps are the following: First, the gradient in equation (5.40) has to be rewritten accordingly to the two-scale approach

$$\nabla_x = \nabla_x + \frac{1}{\varepsilon}\nabla_y. \qquad (5.43)$$

Second, for small ε-values the total concentration can be expanded around the asymptotic large-scale solution C_0:

$$C(\boldsymbol{x}, \boldsymbol{y}, t) = C_0(\boldsymbol{x}, \boldsymbol{y}, t) + \varepsilon C_1(\boldsymbol{x}, \boldsymbol{y}, t) + \varepsilon^2 C_2(\boldsymbol{x}, \boldsymbol{y}, t) + \ldots. \qquad (5.44)$$

Analogously, the functions $F(C,c^{ad})$ and $F^*(C,\overline{c^{ad}})$ have to be expanded around the large-scale limit.

To obtain the large-scale behaviour, the resulting transport equation has to be averaged over the ensemble of all possible realisations of the fluctuating parameter. The final result for the homogenised transport equation on large scales in terms of the total concentration can be expressed as:

$$\frac{\partial C_0}{\partial t} + \boldsymbol{u} \cdot \nabla_x F^*(C_0) - \nabla_x \cdot \left(\boldsymbol{D} + \chi(\boldsymbol{y})\,\xi(\boldsymbol{y},\overline{c^{ad}}) \right) \cdot \nabla_x F^*(C_0) = 0 \quad (5.45)$$

where

$$\xi(\boldsymbol{y},\overline{c^{ad}}) = 1 - \frac{F^{*\prime}(C_0,\overline{c^{ad}})}{F'(C_0,c^{ad})}. \quad (5.46)$$

The prime denotes the derivatives of F^* and F with respect of the total concentration.

The function χ in the last term in (5.45) depends on the solution of an additional equation accounting for the small-scale transport behaviour. Obviously, the functions ξ and χ depend on the explicit shape of the effective isotherm $\overline{c^{ad}}$ which determines the inverse function F^*. Thus, the exact form of the large-scale transport equation can only be evaluated if the effective adsorbing behaviour is known. This is the subject of the following two subsections where transport with variable Freundlich constant and with variable Freundlich exponent is treated separately.

The homogenisation theory analysis presented above is derived for adsorbing transport with a generalised adsorption isotherm. The analysis can easily be extended for every type of reactive transport. The crucial point is to express the transport equation in terms of the total concentration and to find the inverse function with respect to it. The final result will always depend on the shape of the effective reaction term on large scales.

From (5.46) it is obvious that the general shape of the effective reaction term reflects also in the asymptotic dispersion coefficient. In linear transport theory and for non-linearly adsorbing transport in a fluctuating velocity field, the effective dispersion coefficient adopts a constant value for very large times and domains. However, the effective dispersion coefficient in the case of chemically heterogeneous transport is given by

$$\boldsymbol{D}^{\mathrm{eff}} \;=\; \boldsymbol{D} \;+\; \overline{\chi(\boldsymbol{y})\,\xi(\boldsymbol{y},\overline{c^{ad}})}\,. \qquad (5.47)$$

In general, this expression is a function of the dissolved concentration. It becomes concentration-independent only if the following condition is fulfilled:

$$\xi(\boldsymbol{y},\overline{c^{ad}}) \;=\; 1 \;-\; \frac{F^{*}{}'(C_0)}{F'(C_0)} \;=\; K\,, \qquad (5.48)$$

where K is a constant function with respect to C_0. It only depends on the fluctuating parameter and its statistical properties. The solution of (5.48) with respect to F^{*} can be written as

$$F^{*}(C_0) \;=\; (1 \;-\; K)\,F(C_0) \;+\; \Psi \qquad (5.49)$$

with an arbitrary constant function Ψ. The result clearly shows that the effective dispersion does not depend on the dissolved concentration only if the effective reactive term shows the same functional dependence on the concentration field as on the small scale. If the effective reaction on the large scale is reproduced by a function different from the one on the small scale, a concentration-dependent effective dispersion coefficient arises. This is a general result which can be applied to every kind of reactive transport with mass conservation.

5.3.2 Effective Transport with Variable Freundlich Constant

5.3.2.1 Asymptotic Results

The effective transport behaviour of a linearly adsorbing solute in chemically heterogeneous media is given by a linear equivalent homogeneous transport equation by replacing the fluctuating retardation factor by its mean value. The influence of the fluctuating retardation factor is reflected in an increased effective dispersion coefficient [4], [12], [13], [37]. In the case of non-linearly adsorbing solutes it is reasonable to assume that the large-scale transport is also reproduced by a differential equation of the same type as on the mesoscopic scale. This assumption is used to complete the results in homogenisation theory from section 5.3.1.

For very large times one assumes that almost the complete mass is adsorbed at the soil matrix. The total mass can therefore be approximated by:

$$C \equiv c + k_d(\boldsymbol{y})\, c^p \approx k_d(\boldsymbol{y})\, c^p = \tilde{F}(c, k_d(\boldsymbol{y})) . \qquad (5.50)$$

In this case the inverse function of $\tilde{F}$ can be written as

$$F(C, k_d(\boldsymbol{y})) = \left(\frac{C}{k_d(\boldsymbol{y})} \right)^{\frac{1}{p}} . \qquad (5.51)$$

Here, $k_d(\boldsymbol{y})$ denotes the fluctuating Freundlich constant which can be split into a mean part $\overline{k_d}$ and the fluctuations $\mu(\boldsymbol{y})$ around it:

$$k_d(\boldsymbol{y}) = \overline{k_d}\,(1 - \mu(\boldsymbol{y})) . \qquad (5.52)$$

Furthermore, the inverse function with respect to the effective adsorption (5.42) reads as:

$$F^*(C, \overline{k_d}) = \left(\frac{C}{\overline{k_d}} \right)^{\frac{1}{p}} . \qquad (5.53)$$

Inserting (5.51) and (5.53) into (5.46) one obtains:

$$\begin{aligned} \xi(\boldsymbol{y}) &= 1 - \frac{F^{*\prime}(C,\overline{k_d})}{F^{\prime}(C,k_d(\boldsymbol{y}))} = 1 - (1 - \mu(\boldsymbol{y}))^{\frac{1}{p}} \\ &= \frac{1}{p}\mu(\boldsymbol{y}) - \frac{1}{2p^2}\mu^2(\boldsymbol{y}) + \ldots \end{aligned} \qquad (5.54)$$

where the result is expanded in powers of small variations of the fluctuating parameter $\mu(\boldsymbol{y})$. Using this result, the large-scale transport equation in terms of the dissolved concentration (5.45) reads as:

$$\frac{\partial}{\partial t}c_0(\boldsymbol{x},t) + \overline{k_d}\frac{\partial}{\partial t}c_0^p(\boldsymbol{x},t) + \boldsymbol{u} \cdot \nabla c_0(\boldsymbol{x},t) - \boldsymbol{D}^{\text{eff}} \cdot \nabla^2 c_0(\boldsymbol{x},t) = 0 \qquad (5.55)$$

where c_0 denotes the large-scale dissolved concentration. As expected, the large-scale transport behaviour is given by the same type of transport equation as on mesoscopic scales. The effective isotherm corresponds to an averaged Freundlich distribution coefficient $\overline{k_d}$:

$$\overline{k_d} = \int dk_d P(k_d) k_d \qquad (5.56)$$

where $P(k_d)$ is the probability distribution of k_d.

The small-scale variations are incorporated in an increased effective dispersion coefficient $\boldsymbol{D}^{\text{eff}}$:

$$\boldsymbol{D}^{\text{eff}} = \boldsymbol{D} + \overline{\chi(\boldsymbol{y})\mu(\boldsymbol{y})} + \frac{1}{p}\overline{\chi(\boldsymbol{y})\mu^3(\boldsymbol{y})}. \qquad (5.57)$$

First of all, this result shows that explicit results for the effective dispersion coefficient can only be calculated numerically solving the auxiliary small-scale problem for the random field χ. In lowest order the solution of χ does not depend on the non-linear reaction and solves exactly the same equation as in the case of conservative transport. In lowest order also the third term in (5.57) vanishes. Consequently, the asymptotic value of the effective

dispersion in this case is exactly the same as in linear transport theory, $\boldsymbol{D}^{\text{eff}} = \boldsymbol{D}_{\text{lin}}^{\text{eff}}$. This corresponds to the results which we derived for transport with fluctuating velocities in section 5.2. Differently from a physically heterogeneous medium, for large variances the result changes. The asymptotic effective dispersion coefficient is not the same as for conservative transport. The asymptotic value is affected by higher order correction terms which might have a very essential impact on the overall solute migration. Especially, an increased value of the transverse dispersion can considerably slow down the center-of-mass movement of the solute. Moreover, typical times to reach the asymptotic regime can become smaller. In terms of breakthrough curves we expect that they will arrive at later times with a less steep front as compared to transport in fields with heterogeneous conductivities only.

5.3.2.2 Extension to Transient Transport Behaviour

In order to investigate the temporal behaviour of the large-scale dispersion coefficients it is proposed to use the definition of effective transport parameters from section 5.2 and solve the integral expressions in lowest order perturbation theory. The auto-correlation function of the randomly distributed Freundlich constant is given by a Gaussian shaped function, see appendix B. Similarly to transport in physically heterogeneous media one defines the effective velocity as

$$u_i^{\text{eff}} \equiv \left\langle \frac{\partial_t \int d^d x\, x_i \left(c(\boldsymbol{x},t) + \bar{k}_d c^p(\boldsymbol{x},t) \right)}{\int d^d x\, c(\boldsymbol{x},t)} \right\rangle . \qquad (5.58)$$

The effective dispersion coefficients are given by

$$D_{ii}^{\text{eff}} \equiv \left\langle \frac{\partial_t \int d^d x\, x_i^2 \left(c(\boldsymbol{x},t) + \bar{k}_d c^p(\boldsymbol{x},t) \right)}{2 \int d^d x\, c(\boldsymbol{x},t)} \right\rangle - \left\langle u_i \frac{\int d^d x\, x_i c(\boldsymbol{x},t)}{\int d^d x\, c(\boldsymbol{x},t)} \right\rangle . \qquad (5.59)$$

In order to solve (5.58) and (5.59) we expand the heterogeneous concentration field $c(\boldsymbol{x},t)$ in lowest order perturbation theory. The procedure is very similar to the mathematical manipulations in subsection 5.2.1

Our results show that the effective transport velocity is equivalent to the groundwater velocity:

$$u_i^{\mathrm{eff}}(t > \tau_u^{nl}) = u_i \delta_{i,1} . \qquad (5.60)$$

The effective dispersion coefficient is very similar to the effective dispersion coefficient derived in the case of transport in a heterogeneous velocity field:

$$D_{11}^{\mathrm{eff}}(x_1 > l_x) = D_{11} + \sigma_{k_d}^2 u l_x \frac{\sqrt{\pi}}{2} \left(1 - \frac{1}{\left(1 + 4 \frac{\alpha_{22} x_1}{l'_h} \right)^{\frac{1}{2}}} \right) \qquad (5.61)$$

where $\sigma_{k_d}^2$ is the variance of the random k_d-field.

The temporal increase of the effective dispersion coefficient towards the asymptotic value is characterised by the same typical time scales as in the physically heterogeneous transport case. One distinguishes between an advective and a dispersive time scale as introduced in expressions (5.25) and (5.26) in section 5.2.4. For times smaller than τ_u^{nl} the longitudinal effective dispersion coefficient is still equal to the local small-scale dispersion coefficient because the plume is almost unspread. However, it grows as a power law function of time for times $\tau_u^{nl} < t < \tau_D^{nl}$ and approaches after some dispersive time scales the asymptotic regime.

5.3.3 Effective Transport with Variable Freundlich Exponent

The next step in the investigations is concerned with transport of solutes undergoing heterogeneous adsorption of Freundlich type with a fluctuating Freundlich exponent. The transport behaviour is described by a stochastic differential equation where the random

field appears as an exponent. The treatment of such a kind of transport problems is not trivial because the effective adsorption behaviour on the large scale might be completely different from a common Freundlich isotherm. At least, the widely spread approximation to replace the fluctuating parameter by an appropriate mean value has to be checked. Therefore, the efforts in this section aim first at determination of the effective adsorption behaviour and second at the derivation and modelling of the large-scale transport behaviour.

5.3.3.1 Effective Adsorbing Behaviour

To determine the effective adsorbing behaviour the zero-dimensional transport equation is used which expresses the conservation of the total mass with time and represents the adsorption in a well-mixed batch:

$$\partial_t c(\boldsymbol{x},t) + k_d \partial_t c^{p(\boldsymbol{x})}(\boldsymbol{x},t) = 0. \qquad (5.62)$$

The Freundlich exponent $p(\boldsymbol{x})$ is a randomly distributed function with the probability distribution $P(p(\boldsymbol{x}))$ and a vanishing spatial correlation. Consequently, the averaged transport behaviour can be obtained by averaging (5.62) over the probability distribution. In the investigations it is assumed that the Freundlich exponent is log-normally distributed around a mean value μ_x with the variance σ_x^2

$$P(p) = \frac{1}{\sqrt{2\pi\sigma_x^2}} \exp\left(-\frac{(\ln(p) - \mu_x)^2}{2\sigma_x^2}\right). \qquad (5.63)$$

A log-normal distribution guarantees that the Freundlich exponent will strictly be positive. Assuming small variances, one ends up with the effective adsorption isotherm

$$\overline{c^{ad}} = k_d c^{\exp(\mu_x)} \left(1 + \frac{\sigma_x^2}{2} \exp(\mu_x) \left(1 + \ln\left(\frac{c}{c^{in}}\right) \exp(\mu_x) \right) \ln\left(\frac{c}{c^{in}}\right) \right.$$

$$+ \frac{\sigma_x^4}{8} \exp(\mu_x) \left(1 + 7 \exp(\mu_x) \ln\left(\frac{c}{c^{in}}\right) + 6 \exp(2\mu_x) \left(\ln\left(\frac{c}{c^{in}}\right) \right)^2 \right. \quad (5.64)$$

$$\left. \left. + \exp(3\mu_x) \left(\ln\left(\frac{c}{c^{in}}\right) \right)^3 \right) \ln\left(\frac{c}{c^{in}}\right) \right)$$

where c^{in} denotes the initial concentration. This result shows clearly that the effective adsorption behaviour is not given by an adsorption isotherm of Freundlich type. Higher order logarithmic correction terms affect the effective adsorption behaviour of the solute.

For very small variances the correction terms in (5.64) might be negligible. However, still for variances $\sigma_x^2 \sim O(10^{-3})$ the results differ considerably from the adsorption behaviour given by a Freundlich isotherm with a Freundlich exponent equal to a constant value. Moreover, the higher order correction terms $O(\sigma_x^4)$ have a non-negligible effect on the correct transport behaviour and should be taken into account. For comparison, in Fig. 5.22 the effective adsorption isotherm from (5.64) and a Freundlich adsorption isotherm with σ_x^2=0.12, μ_x=-0.32, and $p = \exp(\mu_x)$=0.726 are plotted as a function of the dissolved concentration. As one can see, the two adsorption isotherms differ considerably from each other. The effectively adsorbed concentration is bigger corresponding to a stronger retardation of the transport processes. Indeed, as the dissolved concentration decreases, the difference between the two adsorption isotherms grows. For $c \to 0$ the logarithmic terms increase very rapidly; thus, more mass is adsorbed on the soil matrix. This leads to an infinitely large retardation.

In order to numerically verify the effective transport behaviour in a variable Freundlich exponent field one considers a one-dimensional transport case. First, the transport equation (7.1) is solved numerically. The adsorption term is given by a Freundlich equilibrium isotherm with a log-normally distributed Freundlich exponent around a mean value $\mu_x = -0.32$. One considers two different situations according to two different values of the variance $\sigma_x^2 = 0.02$ and 0.12. Note that the values of the variance are kept small because the calculation of (5.64) is performed only for small variances. The domain is resolved by elements of grid size $\Delta x = 0.1$ and contains 1 000 cells. The dispersivity is

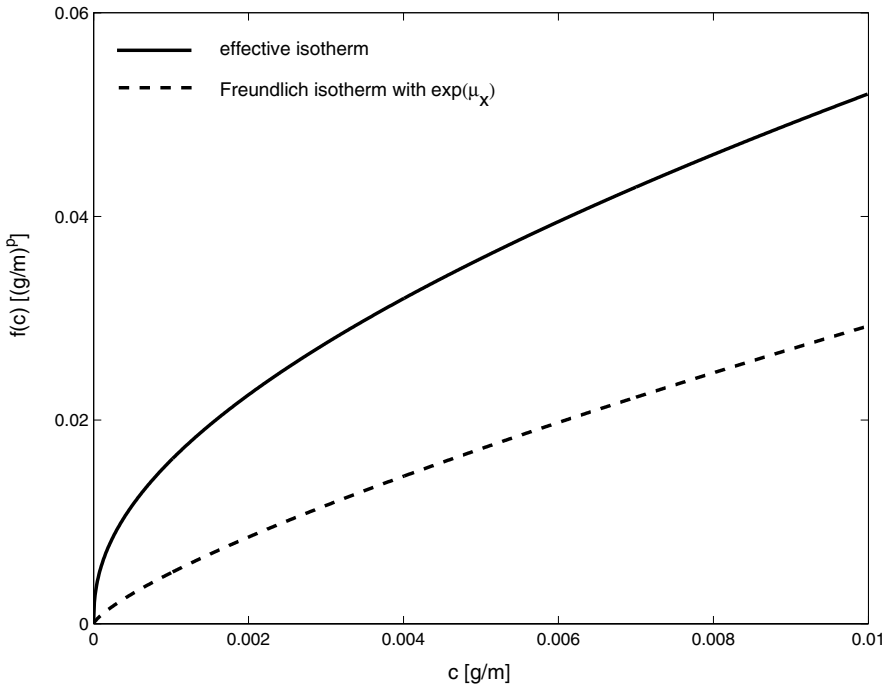

Fig. 5.22 Effective adsorption and Freundlich isotherm

set to $\alpha_{11} = 10^{-4}\,\mathrm{m}$. The tracer is released point-like in space and time with $c^{in} = 1$ g m^{-1}. The advective part is solved by the method of finite differences with a Courant number $Co = 0.9$. The numerical procedure is repeated for an equivalent transport situation with an effective adsorption isotherm as given in (5.64).

In Fig. 5.23 the result of the calculations with $\sigma_x^2 = 0.12$ is plotted. Here, one compares distributions of dissolved concentrations at the transport time $t = 10^{+8}\,\mathrm{s}$. The influence of the fluctuating Freundlich exponents is visible from the concentration tailing which is no longer smooth. As one can see, the heterogeneous concentration profile is very well reproduced by the effective transport. It is not expected to be able to reproduce the whole irregular structure of the tailing. However, the front position as well as the general evolution of the tailing match perfectly. A reasonable match of the two solutions appears still after a sampling of about 100 different p-values and holds as function of time and space.

The center-of-mass movement for transport with variable Freundlich exponent is essentially slowed down compared to a homogeneous transport situation with a Freundlich exponent $p = \exp(\mu_x)$. In Fig. 5.24 the breakthrough curves at x_1 =60 m in the homogeneous transport case and with variable (σ_x^2 =0.12) Freundlich exponent are plotted. As one can see, the concentration front in the heterogeneous transport situation arrives

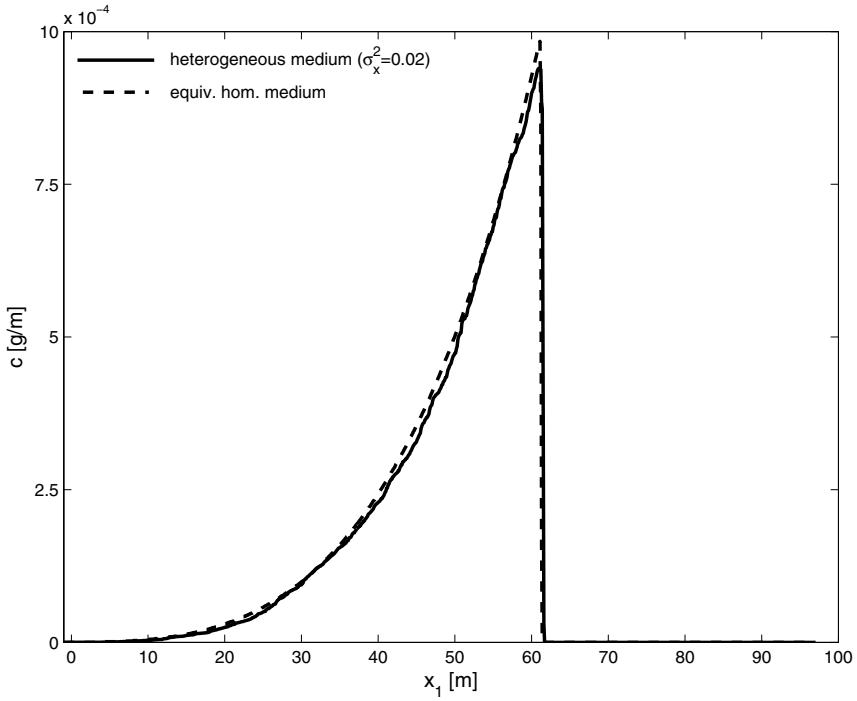

Fig. 5.23 Concentration distribution at t=10^8 s

retarded. This behaviour can be explained by the influence of the logarithmic terms in (5.64) causing a stronger retardation (see figure Fig. 5.22). Moreover, Fig. 5.24 represents again the very good agreement between the solutions with spatially variable Freundlich exponent and the theoretically predicted effective transport with the new isotherm (5.64).

Fig. 5.25 shows a double-logarithmic representation of the breakthrough curves from Fig. 5.24. Since in the homogeneous transport situation the tailing decrease is given by a power law function of time $\sim t^{1/(1-p)}$, see [33], the decrease of the heterogeneous breakthrough curve varies with time. Obviously, the stronger retardation of the heterogeneous transport cannot be reproduced by an effective isotherm of Freundlich type with a constant Freundlich exponent. The adsorbing behaviour depends on the concentration field. Especially, smaller concentration values are more strongly retarded than in the case of Freundlich-type adsorption.

In Fig. 5.26 the solution of the heterogeneous transport with σ_x^2=0.12 at time t=10^{+8} s is plotted. The increased variance is reflected in a stronger “roughness” of the tailing representing the bigger spatial differences in the adsorption behaviour. The concentration distribution fits very well with the simulation result with an effective adsorption isotherm.

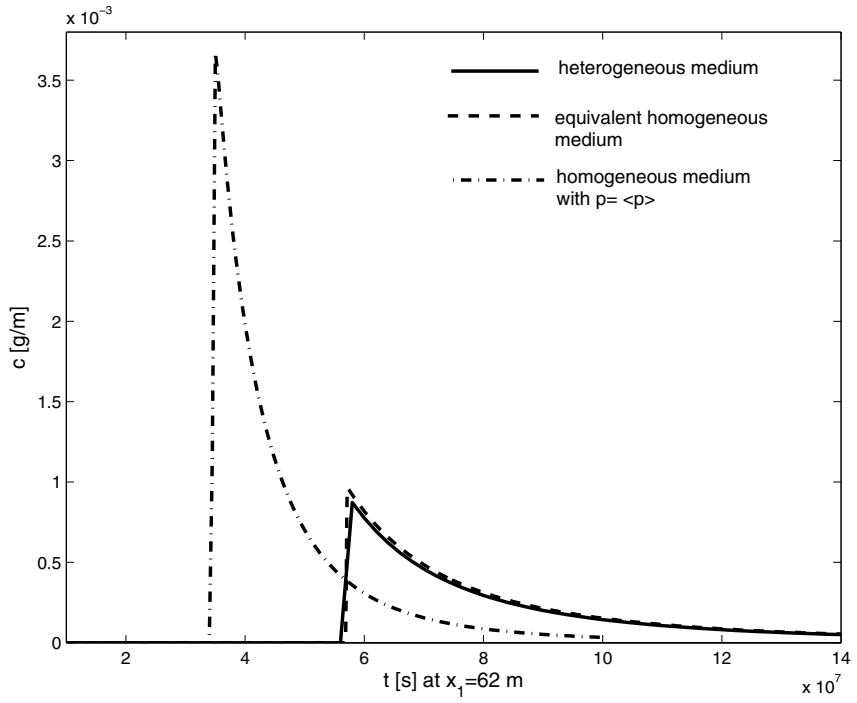

Fig. 5.24 Breakthrough curves in linear representation

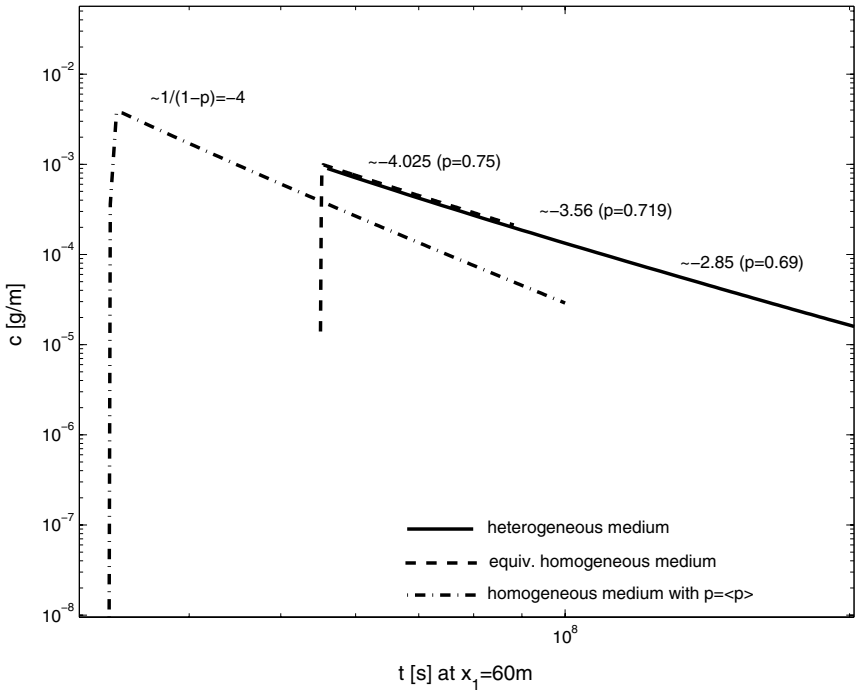

Fig. 5.25 Breakthrough curves in double-logarithmic representation

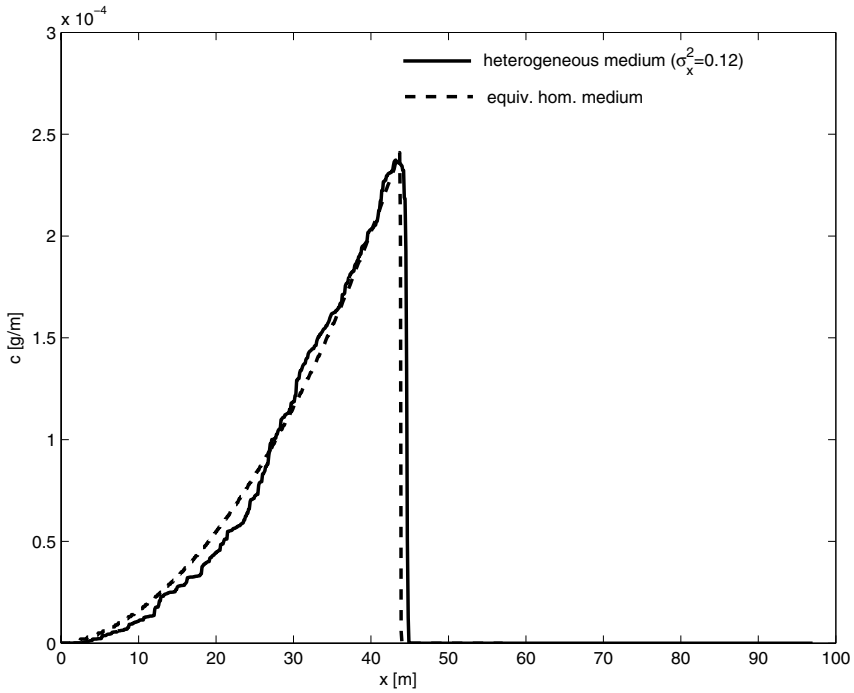

Fig. 5.26 Concentration distribution at t=10^8 s

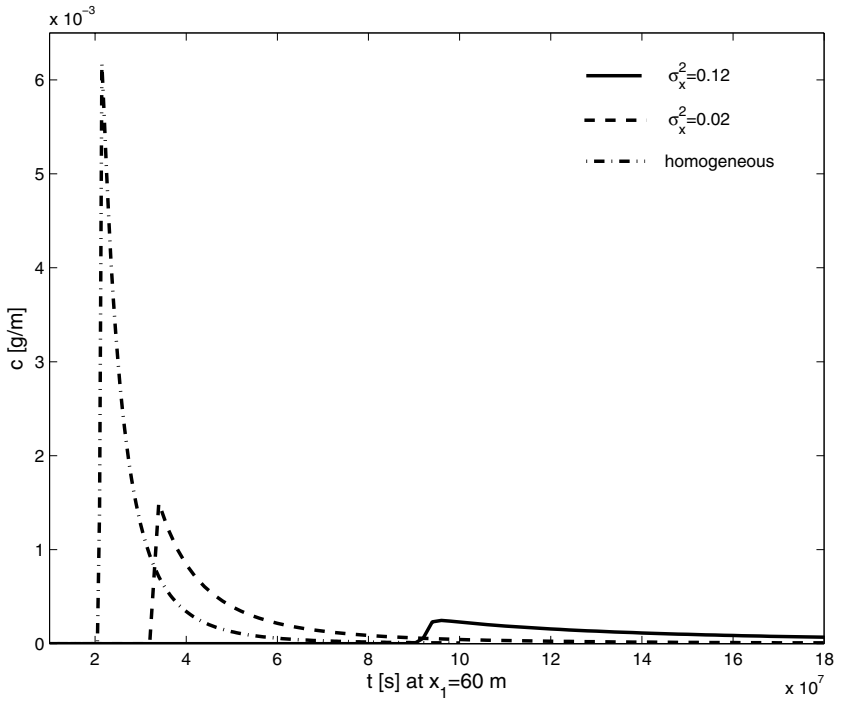

Fig. 5.27 Breakthrough: impact of heterogeneity on the first arrival time

The higher contrasts in the random field influence essentially the solute migration. Compared to the transport situation in Fig. 5.23 the transport is more strongly retarded. As the variance grows, the first arrival time of the heterogeneous breakthrough curves is shifted to later times. As shown in Fig. 5.27, the difference to the homogeneous transport case with $p = \exp(\mu_x)$ at x=60m is essential still for a variance as small as σ_x^2=0.02 and increases for higher values of σ_x^2. This behaviour can be explained by the impact of small values of the variable Freundlich exponent which retard the transport additionally. Especially, the small concentrations at the tail are considerably affected. As a result, more mass gets stuck around the initial position and the tailing is widely spread.

The results of this subsection are very important in understanding upscaling and effective transport behaviour. They show that upscaling of heterogeneous structures does not necessarily lead to upscaled parameters in the macroscopic process but can cause a completely different character of the transport processes involved.

5.3.3.2 Asymptotic Results

In the following, the investigations are extended to the asymptotic behaviour of the transport parameters and the results from homogenisation theory are used to derive the transport equation on large scales.

Again, one starts with the assumption that for very long times the dissolved mass becomes very small compared to the adsorbed mass. Therefore, the total concentration in (5.38) can be approximated by

$$C \equiv k_d c^{p(\boldsymbol{y})} = \tilde{F}(c, p(\boldsymbol{y})) . \qquad (5.65)$$

Here, $p(\boldsymbol{y})$ denotes the spatially fluctuating Freundlich exponent. The inverse function of $\tilde{F}(c, p(\boldsymbol{y}))$ is given by

$$c = F(C,\ p(\boldsymbol{y})) = \left(\frac{C}{k_d}\right)^{\frac{1}{p(\boldsymbol{y})}} . \qquad (5.66)$$

As shown above, the type of the effective adsorption isotherm changes as an ensemble average is performed. Consequently, the total mass in terms of the effective adsorption isotherm (5.41) can be expressed as

$$\begin{aligned} C &\equiv k_d c_0^{\exp(\mu_x)\left(1 + \sigma_x^2 \exp(\mu_x)\left(1 + \ln\left(\frac{c_0}{c^{in}}\right)\exp(\mu_x)\right)\right)} \\ &= \tilde{F}^*(c_0, \exp(\mu_x), \sigma_x^2) \end{aligned} . \qquad (5.67)$$

For simplification, one assumes only lowest order Taylor expansion which allows to rewrite the effective isotherm (5.64) in an exponential form. With this result the function ξ can be written as a function of the total concentration, the variable Freundlich exponent and its statistical moments:

$$\begin{aligned} \xi(\boldsymbol{y}) &= 1 - \frac{F^{*\prime}(C, \exp(\mu_x), \sigma_x^2)}{F'(C, p(\boldsymbol{y}))} \\ &= 1 - \delta D\left(\ln\left(\frac{C}{k_d}\right), \exp(\mu_x), \sigma_x^2\right) p(\boldsymbol{y})\, C^{-\frac{1}{p(\boldsymbol{y})}} \end{aligned} . \qquad (5.68)$$

The expression for ξ is given in appendix D.

Inserting the result for ξ into (5.45), the large-scale transport equation can be written as:

$$\frac{\partial}{\partial t} c_0(\boldsymbol{x}, t) + \frac{\partial}{\partial t} \overline{c^{ad}}(\boldsymbol{x}, t) + \boldsymbol{u} \cdot \nabla c_0(\boldsymbol{x}, t) - \boldsymbol{D}^{\text{eff}}(c_0) \cdot \nabla^2 c_0(\boldsymbol{x}, t) = 0 . \qquad (5.69)$$

The function $\overline{c^{ad}}$ denotes the effective adsorption isotherm given in expression (5.64); c_0 is the large-scale dissolved concentration.

The result in equation (5.69) is a novelty in stochastic groundwater hydrology. It shows clearly that the upscaling of the small-scale inhomogeneities can essentially influence the character of the large-scale transport behaviour. The small-scale heterogeneities are not merely incorporated in large-scale transport parameters, but also the type of transport equation is modified. This behaviour is very different from the treatment of heterogeneous

transport equations where the heterogeneity is contained in a linear term. In the latter case, the effective transport on large scales is given by the same type of differential equation as on the small scale. This applies for linear transport processes as well as for transport with non-linear adsorption with heterogeneous velocities or in a stochastic field with variable Freundlich distribution coefficient.

For the asymptotic effective dispersion we end up with a concentration-dependent result. The effective dispersion coefficient in (5.69) is given by

$$\boldsymbol{D}^{\mathrm{eff}}(c_0) \;=\; \boldsymbol{D} \;+\; \delta D\left(\ln\left(\frac{c_0}{c^{in}}\right),\sigma_x^2,\exp(\mu_x)\right)\overline{\chi(\boldsymbol{y},c_0)\,p(\boldsymbol{y})}\,. \qquad (5.70)$$

The explicit form of $\delta D(\ln(c_0/c^{in}),\sigma_x^2,\exp(\mu_x))$ can be found in appendix D. A closed expression for the effective dispersion coefficient can only be evaluated numerically by solving the auxiliary equation with respect to the random field ξ. In this case, the random field ξ becomes also a function of the concentration field and depends on the explicit shape of the adsorption isotherm. This behaviour also differs from the results for transport with variable velocities or variable Freundlich coefficient. As a consequence, the results for conservative transport can not be used for modelling of the effective dispersion. Especially, for small concentration values the effective dispersion will increase very fast leading to an infinite spreading of the solute cloud (see formula D.4).

5.3.3.3 Modelling of Effective and Ensemble Transport Behaviour

In order to verify the analytical investigations one studies numerically the transport in a spatially variable Freundlich exponent field. The numerical solution of transport with spatially variable Freundlich exponent is performed in a two-dimensional domain with a constant flow velocity u=10^{-5} m/s. The domain includes 36 correlation lengths in longitudinal direction and 40 correlation lengths in transverse direction. In order to ensure only positive values of p, the heterogeneous Freundlich exponent field is assumed by construction to be log-normally distributed with a mean value $\bar{p}$=0.75 and a variance σ_p^2=0.12. The Freundlich constant is defined as ρK_{nl}=0.15 $(\mathrm{g/m^2})^{1-p}$. The solute is injected into the domain as a line over the transverse direction instantaneously in space and time with the initial concentration c^{in} = 1 g $\mathrm{m^{-2}}$. The influence of the transverse mixing

on the mixing behaviour is studied by comparison of simulations with three different values of the transverse dispersivity α_{22} =10^{-4}, 0.0055, 0.055 m. Figures 5.29, 5.30, and 5.31 show the propagation of the initially line-like solute at four different times.

In Fig. 5.29 the results are plotted for very small values of the dispersion coefficients which are of the order of magnitude of the numerical dispersion, α_{11}= α_{22} =10^{-4} m. In this case, the fluctuating Freundlich exponent field deforms the initially uniformly distributed solute front. Moreover, the distributions of the Freundlich exponent vary from streamline to streamline. This results in differently retarded solute transport and therefore different velocities on the single streamlines. In particular, regions with higher p-values ($p \cong 1$) appear as “faster” streamlines. In contrast, small values of the Freundlich exponent cause higher retardation effects. Especially, small concentrations are very strongly retarded. This behaviour becomes apparent for longer travel times (e.g. for t=$2 \cdot 10^{+7}$ s). Here, the small concentration values at the end of the tail are in fact infinitely retarded and remain around their initial positions. A very broad, spatially wide-stretched tailing results. The concentration distribution at every streamline is similar to Fig. 5.26. Moreover, the movement of particles on single streamlines takes place independently from each other. Because of the very small transverse dispersion, there is no effective physical mechanism causing particle exchange and mixing between single streamlines. As a consequence the differences between single streamlines increase with time.

In order to verify the results in homogenisation theory one has to perform the average over an ensemble of possible realisations of the heterogeneous medium. The idea is similar to the idea in section 5.2.5. Every streamline is considered as a single realisation of the stochastic medium. The average over the 200 single streamlines is associated with the averaged transport behaviour. As explained in section 5.2.5 one performs the average over the streamlines according to our definition of ensemble and effective mixing. The average over the concentration distributions at every streamline yields the so-called ensemble average providing information about the ensemble mixing behaviour. The effective mixing is associated with the average of concentration distributions whose maximum positions have been superimposed before averaging. The ensemble and centered average concentration distributions at t=$5 \cdot 10^{+6}$ s and t=$2 \cdot 10^{+7}$ s and the equivalent transport are shown in Fig. 5.28. The ensemble averaged concentration profiles confirm the expectation: They are widely spread over the longitudinal direction. With time the width of the distribution grows because of increasing concentration differences between the single streamlines. As widely discussed in previous sections, the effective mixing

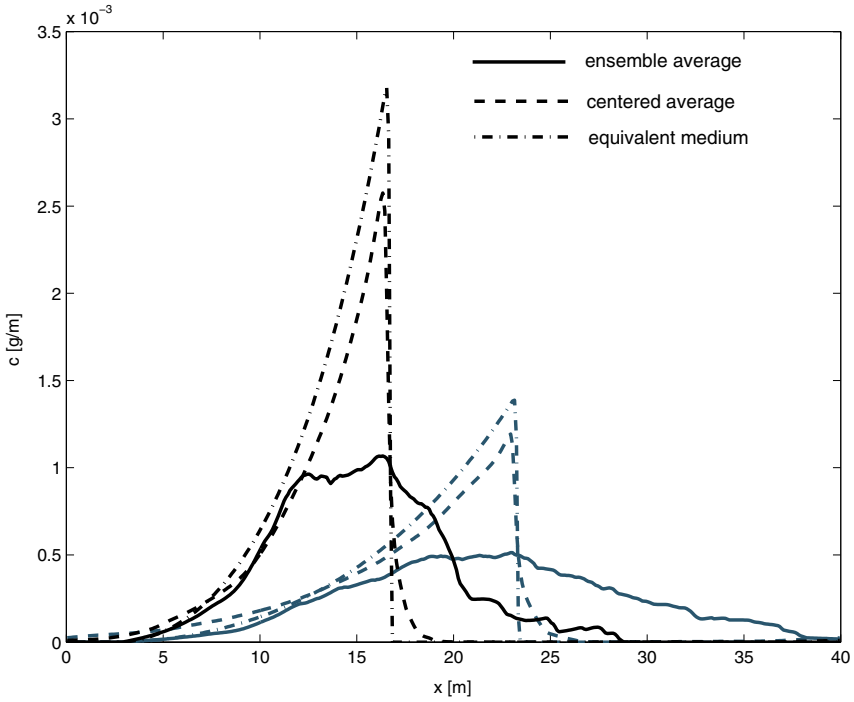

Fig. 5.28 Ensemble and centered average of concentration distributions at t=5·10^{+6} s (black) and t=2·10^{+7} s (blue)

parameters provide a more realistic information about the real mixing behaviour in the stochastic domain. Comparing the ensemble with the centered average concentration profiles this fact becomes much more clear. The centered average concentrations do not contain the center-of-mass fluctuations between the single streamlines. Therefore, they are more regularly shaped and present again the self-sharpening character of the non-linear transport process. The essential impact of the averaging method on the shape of the resulting averaged concentration agrees with the results from subsection 5.2.5 where it was proved that the ensemble averaging procedure in the case of transport with variable velocities leads to an additional broadening of the self-sharpening concentration front that cannot be reproduced in local transport theory. This artificial averaging effect becomes much more obvious in the case of fluctuating Freundlich exponents. Here, the widely spread ensemble averaged concentration profile cannot be modelled by means of an equivalent transport equation in local nor in non local theory. An equivalent ensemble transport simulation can only reproduce the center-of-mass position and give information about the arrival time of the maximum concentration. For other aspects, a fully heterogeneous simulation of the ensemble has to be performed.

The centered average concentration profiles are compared with equivalent homogeneous simulations with an effective adsorption isotherm, as described in subsection 5.3.3. Because one does not know the explicit shape of the effective longitudinal dispersion coefficient one uses only the local dispersion with α_{11} =10^{-4} m. As one can see, the equivalent homogeneous simulations reproduce not only the center of mass position but also the general shape of the centered average concentration profile. The differences are due to the impact of the effective dispersion which was disregarded in the equivalent simulations. Obviously, the effective dispersion coefficient particularly affects the small concentration values. This agrees with the results from homogenisation theory where an increasing dispersion coefficient as function of decreasing concentrations is derived. If one turns back to Fig. 5.28 one sees that especially the small concentration values at the tail and at the concentration front are additionally spread suggesting higher values of the effective dispersion coefficient. It is reasonable to assume that the effective dispersion does not affect the higher concentration values. Here, the difference between the equivalent and the heterogeneous domain reflects the impact of the effective dispersion on the small concentrations and mass conservation. For very large travel distances the additional broadening of the concentration front increases and shows up as a small "tailing" in front of the concentration profile. This reflects again the fact that the effective dispersion becomes very large for small concentrations.

How this "tailing" in front of the concentration profile arises can be observed if we increase the transverse dispersion. In Fig. 5.30 and Fig. 5.31 the results for α_{11} =0.0055 m and α_{22} =0.0055 m and 0.055 m, resp., are plotted. The transverse dispersion smoothes out differences between the single streamlines. As one can see, the contrasts in the domain vanish as α_{22} grows. The transverse dispersion decreases the concentration values at single streamlines. Consequently, the transport is additionally retarded. Moreover, this retardation is stronger than for transport with fluctuating velocities. Comparing Fig. 5.30 with the simulation in section 5.2.5, Fig. 5.12, one recognises that the typical time to cross the middle of the domain has increased by a factor of 2. Moreover, as discussed above, the concentration is widely distributed overall in the domain.

As it is discussed in subsection 5.2.4, the transverse dispersion influences the characteristic dispersive time scale. The bigger D_{22} the shorter the time is to reach the asymptotic regime. Therefore, the bigger transverse dispersion corresponds to a larger "tailing" in front of the centered average concentration profile. This "tailing" grows with time incorporating the concentration dependence of the effective dispersion coefficient. Moreover,

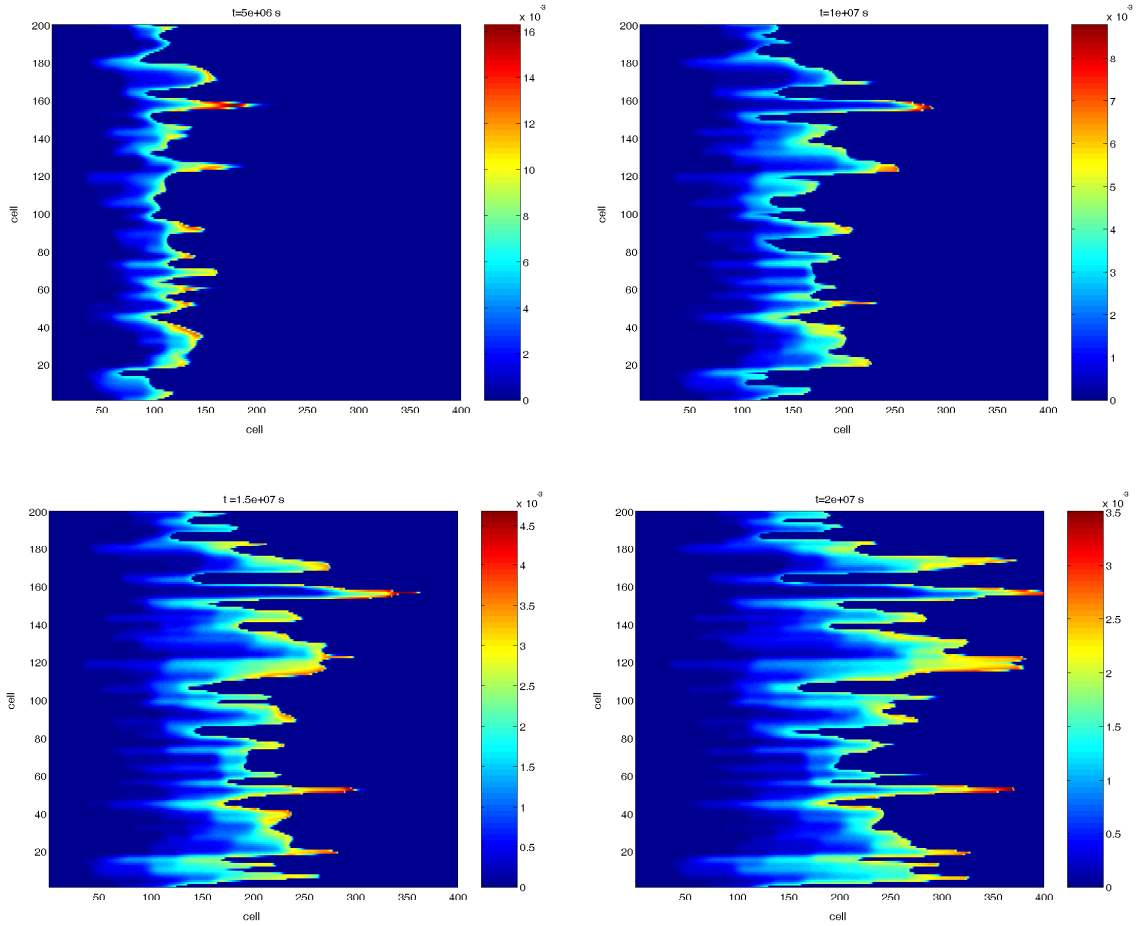

Fig. 5.29 Concentration distribution for fluctuating Freundlich exponent $D_{11}=D_{22}=10^{-9}$ m^2 s^{-1}

different from the case of physical heterogeneity, concentration distributions and breakthrough curves, respectively, cannot be observed to be well localised in space and time. For very long travel times and travel distances the large-scale concentration will disperse infinitely.

5.4 Conclusions

This part of the report was focused on the transport behaviour of non-linearly adsorbing solutes in heterogeneous porous media. In particular, equilibrium adsorption reactions described by a Freundlich-type adsorption isotherm are examined. The heterogeneity of the medium was associated with spatial variability of the underlying formation materials and their physical and chemical properties. Therefore, the influence of three different fluctuating parameters were studied: Spatially variable conductivities were related to a

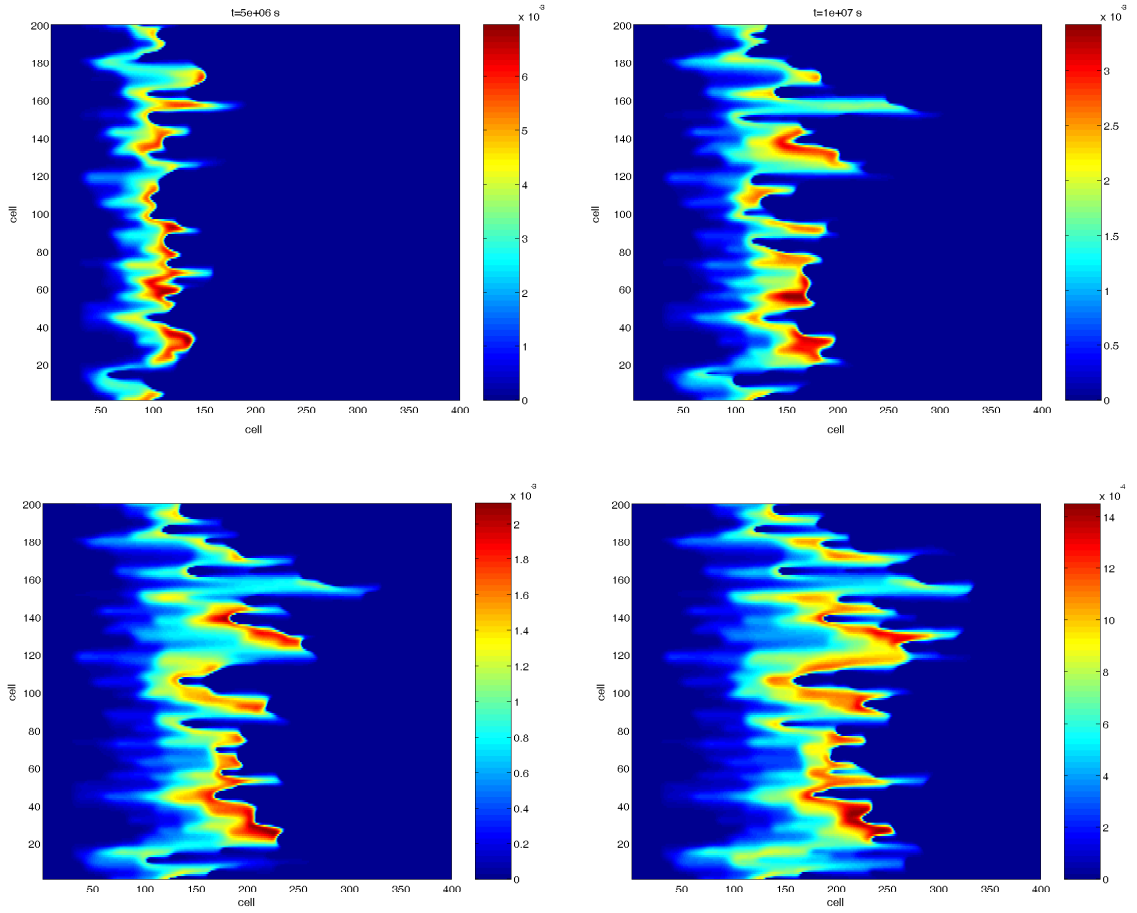

Fig. 5.30 Concentration distribution for fluctuating Freundlich exponent D_{11} =5.5·10^{-7} m^2 s^{-1} and D_{22} =5.5·10^{-8} m^2 s^{-1}

heterogeneous velocity field. The different adsorption affinity of the differently spatially distributed materials appeared in a spatially variable Freundlich distribution coefficient and Freundlich exponent. Moreover, it is assumed that these fluctuations take place on a scale which is small compared to the intrinsic scale of the solute transport.

Especially, it was focused on the impact that the small-scale variability might have on the transport behaviour on large scales. The aim was to develop an effective transport theory presented by a homogeneous equivalent transport equation which incorporate the small-scale variations in ensemble averaged transport parameters. Additionally, formulae for calculation of the averaged transport parameters were derived. Here, two conceptually different averaging methods leading to the so-called ensemble and effective transport parameters were introduced. The difference between the effective and ensemble dispersion is well-known from the linear transport literature: The ensemble dispersion coeffi-

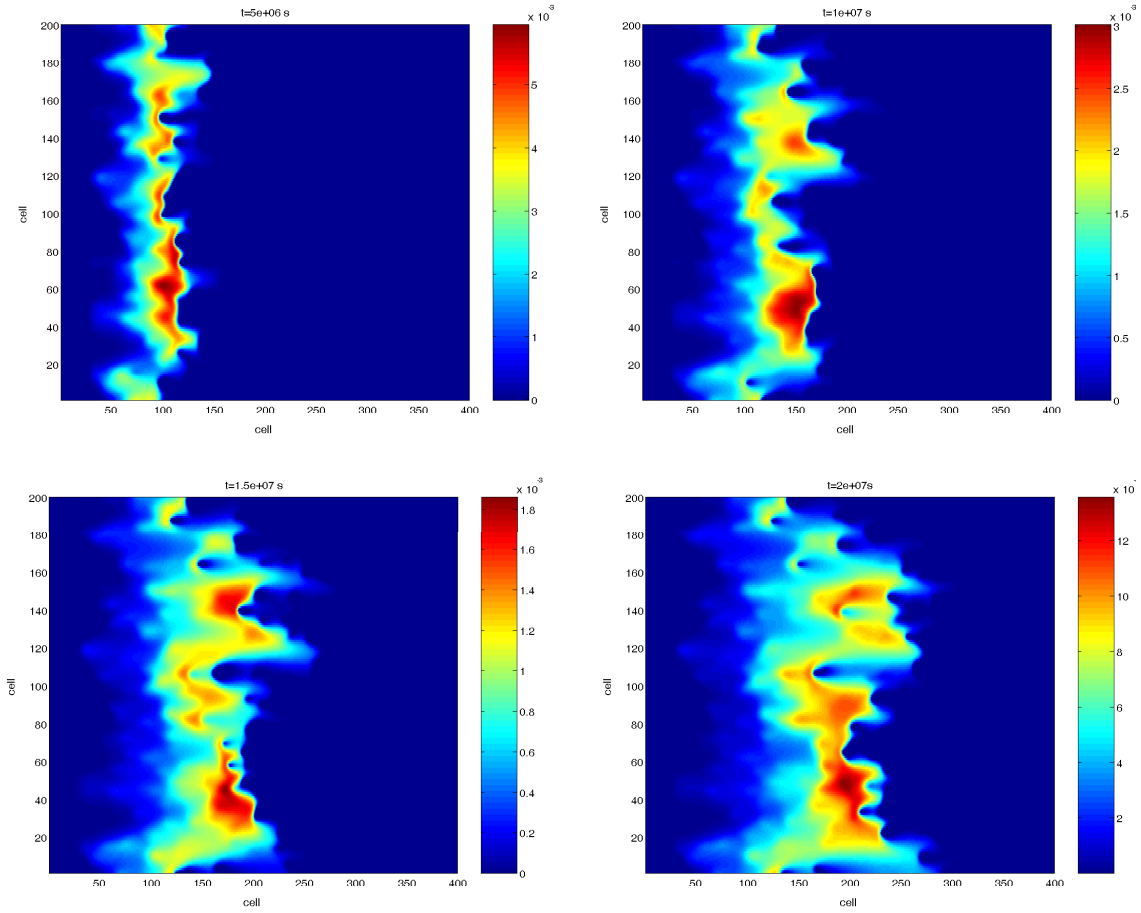

Fig. 5.31 Concentration distribution for fluctuating Freundlich exponent D_{11} =5.5·10^{-7} m^2 s^{-1} and D_{22} =5.5·10^{-7} m^2 s^{-1}

cient takes into account artificial mixing effects due to the sample to sample fluctuations of the centre of mass. This effect is suppressed by the effective dispersion coefficient which is defined as ensemble average over the dispersion coefficients in the single realisations.

In the case of physically heterogeneous media explicit results for the ensemble and effective dispersion coefficients were derived. It was found that the effective mixing behaviour of a solute can be reproduced by an equivalent transport model by replacing the local small-scale dispersion by space- resp. time-dependent effective dispersion coefficient. In contrast, the ensemble mixing transport behaviour cannot be reproduced by an equivalent transport model of the same type as on the small scale. The reason is that the ensemble dispersive flux does not localise in time and space because of the very sharp concentration front. In order to avoid this inaccuracy the transport equation was

solved taking into account a non-local ensemble dispersive flux. Consequently, depth-averaged concentration profiles have to be modelled by means of an equivalent homogeneous transport equation with a non-local dispersive flux. However, one has to be aware of the fact that this non-local dispersive flux does not account for the real dilution process in a heterogeneous formation - neither for transient nor for asymptotic times.

For chemically heterogeneous media the influence of a fluctuating Freundlich constant on the one side and the influence of a variable Freundlich parameter on the other side were investigated. In the case of adsorbing transport with a randomly distributed Freundlich distribution coefficient the resulting upscaled transport equation is of the same type as on the mesoscopic scale. The fluctuating parameter is replaced by its mean value. The effective dispersion coefficient reaches a constant value. In lowest order the result for the effective dispersion coefficient is exactly the same as for conservative transport. However, as the variance increases this result changes. The effective dispersion coefficient is not the same as in linear transport theory and is affected by higher order correction terms. Such behaviour considerably differs from the investigations in linear transport theory and non-linear transport with variable velocities. A larger effective dispersion coefficient can essentially affect the solute migration. For example, a larger dispersion can cause a stronger retardation of the solute and therefore an overestimation of first arrival times and maximum peak concentrations.

In contrast, the transport on macroscopic scales of a solute in a variable Freundlich exponent field differs considerably. It is represented by a transport equation which has a completely different structure as on the mesoscopic scale. First of all, the effective adsorbing behaviour is no longer given by a Freundlich-type isotherm but by a new isotherm which depends in a complicated functional relationship on the dissolved concentration and the statistical properties of the random field distribution. The influence of small values of the randomly distributed Freundlich exponents appears in logarithmic terms which essentially retard the solute migration and affect in particular small concentration values. Consequently, the small concentrations are much stronger retarded as in a homogeneous transport situation with a Freundlich exponent equal to its mean value. A spatially extended tailing results. The additional retardation effects grow as the variance increases. Moreover, the different adsorption behaviour on the mesoscopic and macroscopic scale causes a concentration-dependent effective dispersion coefficient whose explicit form is affected by the effective adsorption isotherm. Consequently, the spreading behaviour of the solute varies with time and at different locations in the domain. It was

found that especially for small concentration values the effective dispersion becomes infinitely large. Thus, the general behaviour of a solute cloud in a heterogeneous domain with spatially variable Freundlich exponents strongly differs from the transport with variable velocity and distribution coefficient. It is mainly influenced by two processes: the very strong retardation leading for very large times and travel distances to an almost vanishing transport velocity and the very large dispersion coefficient as function of the dissolved concentration. Therefore, it can be expected that in the asymptotic regime the solute will disperse infinitely by keeping the centre of mass spatially practically fixed.

The results of the stochastical modelling can be very useful for the correct understanding of field experiments, performing risk assessment and remediation schemes. They can be applied for modelling of non-linearly adsorbing transport by means of equivalent transport models with effective dispersion coefficients as function of time or space. Moreover, they make an important contribution to the general understanding of the method of upscaling and the resulting consequences for modelling of processes on macroscopic scales. In groundwater hydrology it is common practice that small-scale variabilities in the physical and chemical properties of the underlying materials are often smoothed out by spatial averaging over a representative volume or using stochastic modelling. The main assumption in such investigations is that the small-scale dynamics of the processes can correctly be reproduced by an effective law at the large scale. Another assumption concerns the form of the effective law. In general, the flow and transport behaviour on the larger scale is modelled by the same type of equations as on the small scale by incorporating the small-scale variations in appropriately defined, averaged parameters.

In the case of linear processes such as flow in saturated media, conservative solute transport etc. such kind of approximations turned out to successfully reproduce the experimentally observed behaviour on macroscopic scales. However, in a more general case natural processes are not linear. The dynamics of the small-scale heterogeneity can essentially influence the large-scale behaviour. Consequently, the effective law can essentially vary from the small-scale process. Even worse, for a more complicated physical phenomenon an effective law might not exist. This means that for the most general processes simulation of a large realisation or an ensemble of realisations incorporating small-scale heterogeneity is unavoidable. Exactly in this situation a very efficient transport model solver such as r^3t is required.

In this work a very simple case of really non-linear dynamics was considered. However, already in this case it was found that upscaling of the small-scale variability results in a completely different transport equation on the macroscopic scale. Moreover, averaged transport parameters such as the dispersion coefficient are not represented by a constant value, but become a function of the concentration field and thus of time and space.

It is shown that the kind of averaging used can be very important for modelling and understanding of experimental data. In this work, it is distinguished between two different averaging procedures. In linear theory, it is assumed that they become equal as soon as the solute has spread over some longitudinal correlation lengths. In non-linear transport theory, it was proven that already in the very simple case of fluctuating velocities, the ensemble average generates artificial spreading effects which do not vanish even in the asymptotic regime. The difference between ensemble and effective averaging becomes much more pronounced in the case of variable Freundlich exponents. In particular, the ensemble dispersion will never represents the real mixing behaviour. After all, non-linear transport processes should be modelled with care. A kind of “naive” modelling can lead to considerable mistakes in general predictions of concentration peaks, first arrival times, migration and location of contaminants. Possibly the numerical modelling based on small-scale heterogeneous fields and the small-scale transport equation is the only reliable alternative in risk assessment.

6 The Software Package r^{3}t

The software package r^{3}t comprises three almost independent parts: preprocessor, simulator, and postprocessor.

6.1 The Preprocessor

The input data which has to be provided by the user essentially consist of two parts: the data describing the model, and the data controlling the numerical algorithms.

6.1.1 Input Data to Describe the Model

To conduct a simulation with the computer code r^{3}t some special data are needed. This data are written by the preprocessor into various input files which afterwards can be read by the simulator. The data needed comprise results from release calculations for the near field, from flow modelling for the overburden and parameters which define transport and retention for the far field. It is assumed that the sources of radionuclides (pollutants) are given as time-dependent mass fluxes. These distributions of mass fluxes are usually defined by results of near-field modelling with the computer code EMOS[19], [128]. Concerning the flow field data one uses the stationary or transient velocity field generated with the code d^{3}f [45]. For this reason the description of the structure model is given by the d^{3}f input file **geometry**. In future it is planned to provide filters in order to use results from flow simulators other than d^{3}f.

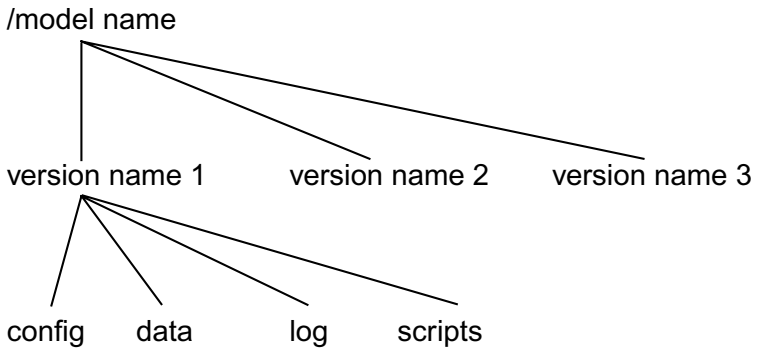

Fig. 6.1 Directory structure of input and output of r^{3}t

In general every input and output data are located in the same directory which has the structure shown in Fig. 6.1.

Principally the mks system is used, i.e. m, kg and s, and derived units, respectively. Particularly time is given in seconds. Possibly one uses the results of simulations with different computer codes. Some of these simulators use different units for time. For example Darcy velocities from d^{3}f are given in m s^{-1}, but mass fluxes from EMOS are in mol y^{-1}. The preprocessor converts this into time units s. The various data are written in different files. In Fig. 6.2 the organisation of the data input is shown. As is depicted in Fig. 6.1 every input file for a simulation has to be in the same directory. To perform a transport simulation seven input files have to be given anyway and additional two files are used optionally for special purposes.

6.1.1.1 The Input File: pollutant

This file comprises the selected radionuclides (pollutants), mother-daughter relations as well as half-lifes $T_{1/2}$ and decay constants λ, respectively. Initially these data are taken from results of near field simulation with EMOS but they can be changed by the preprocessor. It is possible to neglect nuclides simply by omitting or by combining the mass flux with the mass flux of the daughter nuclide. Anyway the neglecting of nuclides should be treated with respect. It is only valid if the half-life of the neglected nuclide is very small in comparison with the half-life of the daughter. To neglect a nuclide it is not sufficient that the initial inventory of that nuclide is zero.

Further on the agents which are transported as well are given. They change the solubility limits and the K_d-values, respectively.

6.1.1.2 The Input File: geometry

The input file **geometry** is identical to the d^{3}f input file of the same name. It contains the geometrical definition of the modelled area and the appropriate hydrogeological units and their names. The file comprises informations about hydrogeolocical units (unit-info), polylines (line-info), surfaces (surface-info), and points (point-info).

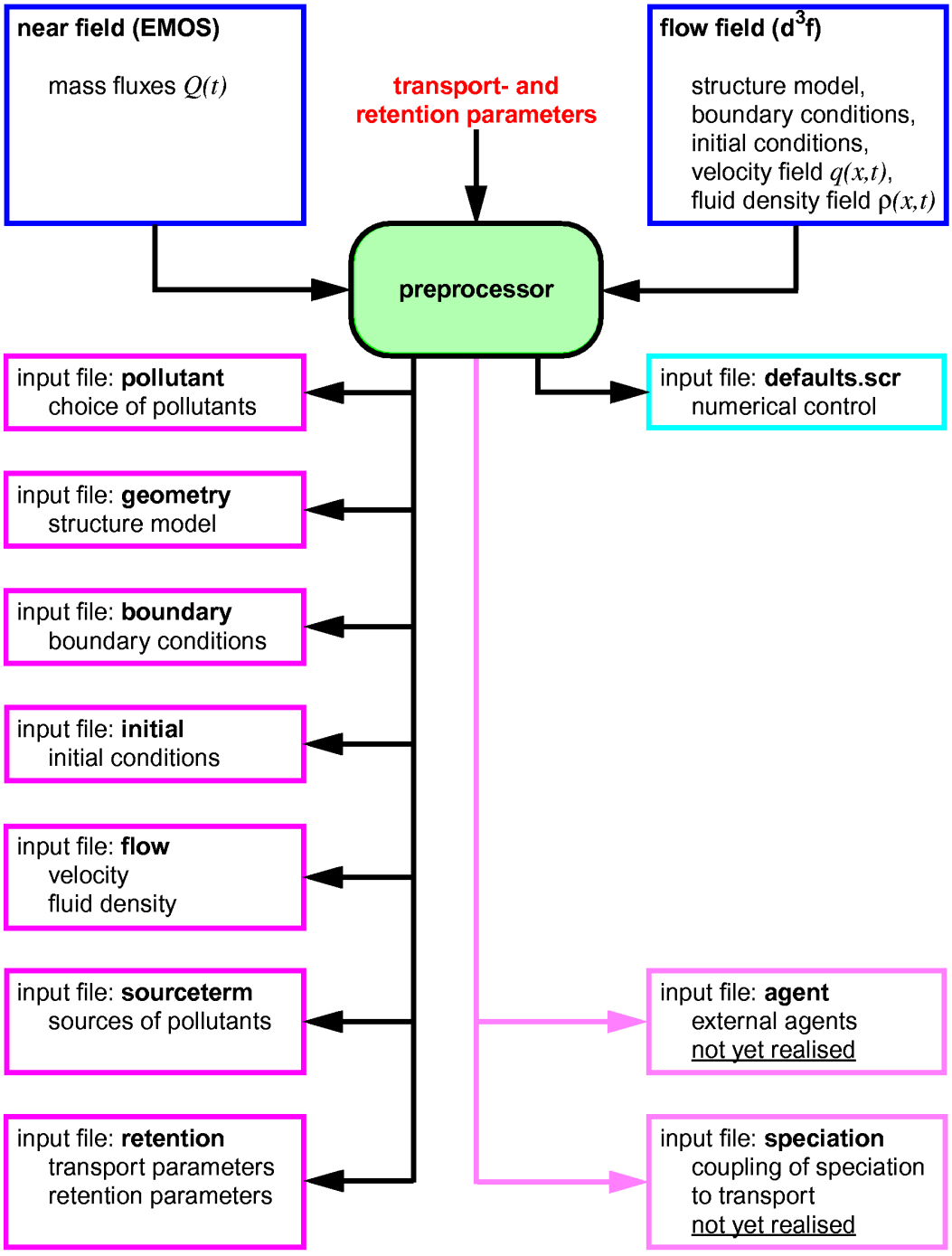

Fig. 6.2 Modelling and numerical input data
seven obligatory and two optional, and one numerical control file

6.1.1.3 The Input File: retention

In the input file **retention** every hydrogeological unit defined in **geometry** is assigned to materials. With the help of materials hydrogeological units which do not differ in transport and retention parameters can be combined. Thus the parameters for the various materi-

als have to be subsequently given once. Apart from transport parameters these are element-specific sorption and solubility limits. It is possible to define the diffusion constant material-specific as well as element-specific. If K_D-values or solubility limits are used as functions of agents one has to define the name of the agent, the name of the function, and the parameters of the functions. If the immobile pore water model is used retention parameters have to be defined for sorption in the immobile area. In that case only equilibrium sorption is accepted.

6.1.1.4 The Input File: boundary

The input file **boundary** contains the total amount of boundary conditions which can be stationary or transient. Since one does not want to give boundary conditions for pollutants and agents, resp., the first given boundary conditions are valid for every pollutant and every agent. After that one can define exceptions for several pollutants and agents. Parts of surface (surface-ids) with identical boundary conditions can be combined and labelled. This label is only used by the preprocessor **pre-mod** and serves for identification of boundary conditions. The following boundary conditions may be chosen:

- **level**
  Dirichlet's condition (fixed concentration). It can be defined as **const** or as **function**.
- **flux**
  Cauchy's condition (total mass flux is fixed). It can be defined as **const** or as **function**.
- **dissolution**
  Total mass flux is fixed to be proportional to the difference in concentration inside and outside the boundary.
- **out**
  Diffusive/dispersive flux is set to zero.
- **trans**
  Diffusive/dispersive flux is fixed to be constant.

- **inout**

  This boundary condition is fixed by flow modelling (i.e. by d^3f simulations). Depending on the direction of flow velocity the domains of inflow and outflow are defined. In inflow domains the concentrations of the inflowing pollutants are fixed as **const** or as **function** while in outflow domains the diffusive/dispersive mass flux vanishes.

If no boundary condition is explicitly defined for any part of boundary it is automatically assumed that this part of boundary is impermeable.

6.1.1.5 The Input File: initial

Initial conditions have to be defined for all pollutants and agents. They are given in the input file **initial** analogously to the input of d^3f. Usually the initial conditions are equal for every substance. Therefore general initial conditions are defined firstly for all substances and occurring exceptions are given afterwards.

Initial conditions can be specified as a global constant or as a spatial function. Again these global parameters can be regionally overwritten by constants or spatial functions for various hydrological units. Another possibility to define global initial conditions is the declaration of a concentration field given on an equidistant rectangular grid. For that purpose the numbers of grid points, the origin, and increments for the directions in space have to be given as well as the concentrations at the grid points. That global declarations are not regionally overwritable.

6.1.1.6 The Input File: flow

The input file **flow** comprises informations about velocity and density field. This information is described by absolute path names of d^3f results. One has the possibility to define a constant velocity field in giving the components. If no density driven flow is modelled the density of the fluid has to be defined.

6.1.1.7 The Input File: sourceterm

The input file **sourceterm** comprises the time behaviour of the pollutant rate which are considered at their entry point to the overburden. Usually these data are taken from an EMOS simulation. If some agents which enter the overburden coming out of the mine workings are modelled, the output file of EMOS has to be enlarged by the appropriate inflow rates of the agents.

It is allowed to model several sources (sinks) which are distinguished by different names. For every source firstly the names of the pollutants which enter the overburden at that source are defined. Subsequently the shape of the source is determined as point-, line-, square-, or cuboid source (sink). Finally the temporal behaviour of the pollutant rate is defined as constant or δ-shaped or is given at discrete time points. If the rates are given at discrete points for each time step and for each pollutant they are linearly interpolated on demand.

6.1.1.8 The Input File: speciation

This input file is provided for future development: coupling of a speciation code to r^3t.

6.1.1.9 The Input File: agents

This input file is not realised, yet.

6.1.2 Input Data to Control Numerical Algorithms

The data which are needed to control numerics are written into the three following files: **defaults.scr** contains any parameter which may be changed by the user. This input file is generated or changed by the preprocessor. The file **advance.scr** contains other parameters which must not be changed by a “standard” user. Only advanced users with large experience are allowed to modify it. Finally the file **r3t.scr** contains the course of execution. This file should never be changed.

The preprocessor of r^3t is platform independently coded in Java. It is equipped with a graphical user interface (GUI).

6.1.3 Using the Preprocessor

When input data for r^{3}t are generated with the preprocessor one has to distinguish two cases: the new development and the modification of model data. In the first case all data have to be fed to the computer while in the latter case only some data have to be changed or completed. Already entered data are shown as default values and can be changed or accepted. After the selection of creating, changing or copying a model and the defining of the appropriate path names one ends up with the window shown in Fig. 6.3. Here one has to decide which of the input files have to be generated or changed. The user is guided to prepare the model data or the numerical control parameters, which have to be provided.

6.2 The Simulator

The efficient numerical simulation of reactive contaminant transport in porous media in large domains has been a major research issue within the last decade. In order to be able to compute such transport phenomena in three dimensions several modern numerical techniques have to be applied to ensure reasonable computation times. Such techniques include higher order discretisations, efficient solvers of the resulting non-linear systems of algebraic equations, and the usage of parallel computers.

Several mathematical models are required to be solved by r^{3}t. Their description can be found in Section 4 on “Conceptual Model and Mathematical Description”. As there are some common features of all of these models, an abstract unique mathematical model is presented later.

Many difficulties arise from the complexity of solving this general mathematical model. First, nontrivial (three-dimensional) computational domains are to be used and very long time simulations are expected. This requires an application of unstructured computational meshes with local grid adaption and some careful control of time discretisation steps.

Second, the mathematical model includes a system of convection dominated transport equations with different (in general non-linear) retardation factors for each transported contaminant and these equations are coupled by decay reactions. To our knowledge, no

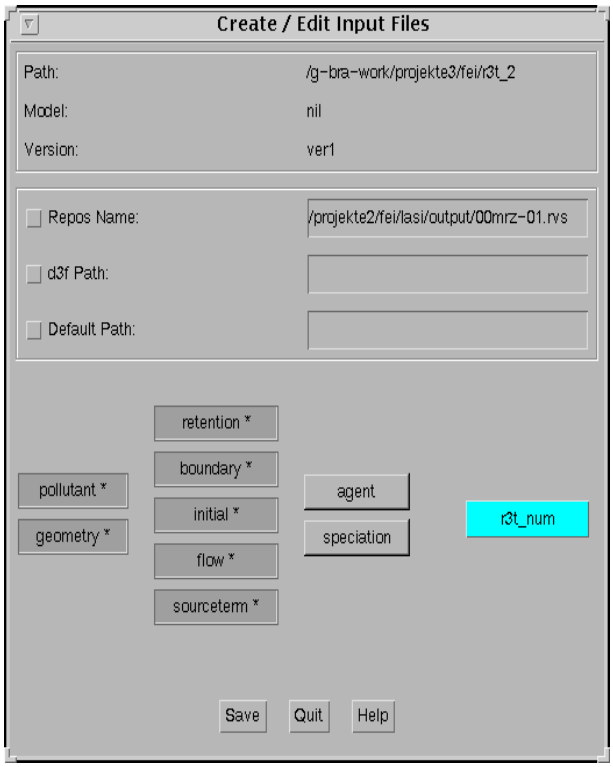

Fig. 6.3 "Create/Edit Input" window of preprocessor with switch to numerical control parameters

satisfactory algorithm for this type of equations was previously developed. The existing algorithms, in general, require very small time steps (i.e., very long simulation times), or, otherwise, they exhibit a large time discretisation error.

Third, the case of fast non-linear sorption with Freundlich isotherms can lead to a development of shocks in the solution and special algorithms must be used to resolve well such situations. If the transport of a single chemical element with several particular nuclides is modelled with non-linear sorption, a nontrivial non-linear coupling of the available transport equations occurs.

Fourth, a very large number of partial differential equations, possibly coupled with an even larger number of ordinary differential equations, must be solved by r^3t. A very efficient memory format for the discretisation matrices is required, otherwise numerical simulations can not be provided in a reasonable computational time.

Finally, for a large number of equations, especially, if one thinks about more complex 3D examples, computations on parallel computer systems will be possible with r^{3}t.

Last but not least, a user-friendly interface is required to enable a straightforward, practically oriented, numerical modelling of typical applications when using the software tool r^{3}t.

6.2.1 Summary of Obtained Results

In next subsections, the results concerning the development of r^{3}t are summarised, especially the implementation of data exchange between r^{3}t and d^{3}f, a user interface, a parallelisation, an adaptivity, and solvers. In sections afterwards, the general mathematical model and discretisation methods that are used in r^{3}t to solve it numerically are described.

The software tool r^{3}t is based on the numerical library UG (Unstructured Grids) [7], in analogy to d^{3}f [45]. In practice this means that only requirements of a specific application based on UG, like the management of input data or the discretisation methods, must be implemented with larger effort. Other parts, like the data management (geometric and algebraic), the solvers, etc., can be used within UG with only slight or no modifications.

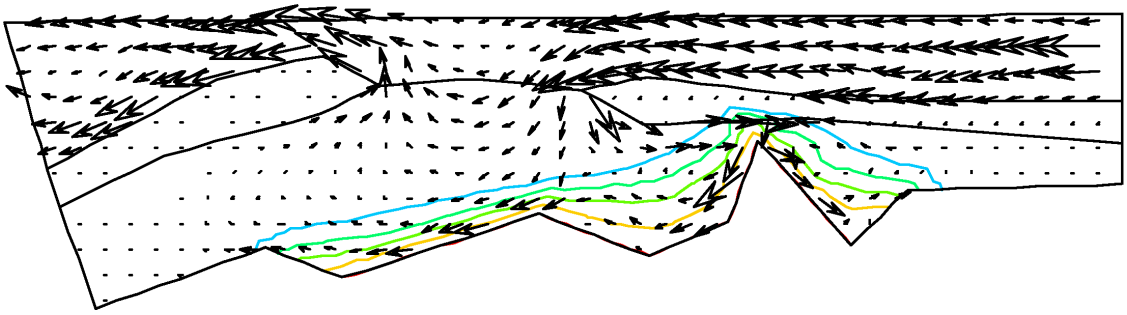

Fig. 6.4 An illustration of velocity and density data from d^{3}f

6.2.1.1 Data Interface Between r^{3}t and d^{3}f

The main purpose of r^{3}t is to realise numerical simulations of radionuclides transport using the results of d^{3}f for the modelling of groundwater flow with variable density. Moreover, the geometrical modelling of computational domains, the grid generation, etc., can be realised with tools available in d^{3}f and used with r^{3}t afterwards.

The computational results of d^3f in the form of data describing the velocity field can be saved directly within d^3f. Afterwards, they can be read by r^3t and used in numerical modelling of the convective transport of radionuclides.

In most of applications, the computational grid that accompanies the velocity data from d^3f can be used directly in r^3t. This has several advantages, especially concerning the modelling of velocity data, that are, in such a way, used in the origin approximation quality from d^3f (a piecewise linear profile in space). The same is valid for the density data that can be saved in d^3f and used in r^3t, if variable density flow is considered.

The main disadvantage of this approach is that the velocity and density data are modified in r^3t with each grid adaption, and, consequently, the origin information can be lost. For instance, if a local grid coarsening is used, the data on a corresponding finer grid will be deleted. Consequently, the grid from d^3f shall be used in r^3t, for instance, if one uses only grid refinement. If a local grid coarsening is applied, later refinement at the same place does not use the origin “finer” data.

To enable also a more flexible grid management, one can save the velocity data from d^3f in a grid independent format that was developed specially for r^3t. In such a way, with each grid adaption the origin data are not lost and they can be reread to fit to the new computational grid.

Due to a complexity of this approach, the velocity data are saved only in a piecewise constant form with respect to the finest grid in d^3f. Consequently, this new format for the velocity data shall be used, if an enough fine grid was used in d^3f, and if some flexible grid readapting is required in r^3t. The disadvantage is that the origin approximation quality of the velocity field in d^3f is lost (i.e., the piecewise linear profile), and the corresponding recalculations of velocity and density data after grid adaption are more time consuming. Fig. 6.4 illustrates a possible modelling of 2D groundwater flow with variable density. The picture of input velocity and density data was plotted using r^3t.

6.2.1.2 Preprocessing and Postprocessing Tools in r^{3}t

The geometrical and physical data, like the description of computational domain, the model parameters, etc., can be defined using a readable format of configurable files. These are **geometry**, **pollutant**, **retention**, **flow**, **sourceterm**, **initial**, and **boundary**. They can be created using a graphical tool developed during this project, see Section 6.1 “The Preprocessor”.

The processing of these input files in r^{3}t is realised using tools of compiler design [2] like FLEX (scanner generator) and BISON (parser generator). These tools help to generate C files that are included in r^{3}t and that are responsible for the reading of input parameters from the configuration files. In such a way, the processing of input files can be realised in an efficient way and (more likely) error free.

To control the parameters of numerical methods, script files with an UG own programming language are used. To make the runs of r^{3}t as simple as possible for typical users, the most important parameters are collected in the single file **defaults.scr**. In fact, only this one file should be modified by an user to control specific requirements of his/her particular example. A graphical interface was implemented again to prepare this file, see section 6.1 “The Preprocessor”.

As there are several other parameters that can be defined for all UG and r^{3}t script commands, the script file **advance.scr** is available. This file is meant only for advanced users or for special research on numerical methods, and the parameters there should not be changed in typical applications of r^{3}t.

A general single run-script file **r3t.scr** was developed. Both script files **advance.scr** and **r3t.scr** must be called at the end of the initialisation file **defaults.scr**. It calls all UG and r^{3}t commands to realise numerical simulation, see [52]. This file is hidden for typical users of r^{3}t. Nevertheless, some special requirements or modifications can be realised in a relatively straightforward way, if it is necessary, because the script files offer very large flexibility in the control of r^{3}t.

Finally, let us note that the results of r^{3}t, if saved in a standard UG format, can be read and used by the powerful graphical postprocessing tool GRAPE, see section 6.3 on “The Postprocessor”. In fact, not only the direct results of r^{3}t can be saved for the visualisation

with GRAPE, like the mole concentration of dissolved contaminant, but also other data that require some postprocessing computations in r^{3}t, e.g., the concentration of adsorbed contaminant for the case of equilibrium sorption.

6.2.1.3 Parallel version of r^{3}t

The numerical library UG is available for several parallel computer platforms. In practice, if standard discretisation methods are implemented for some particular application of UG in a correct way, almost no special implementation is necessary concerning the parallelisation of the code.

In such a way, also the computations with r^{3}t can be realised on parallel computers and large scale simulations with enormous requirements on computer memory and computation times are possible. All important numerical algorithms that are available in r^{3}t are functional also on parallel computers.

In [60], test examples were referred that were realised with r^{3}t during its development. For instance, an example of transport of 26 radionuclides in a three-dimensional complex domain with 5 millions of grid points was realised using 64 processors of the HELICS parallel computer (an AMD-based PC cluster).

The important advantage of UG (that is used also by r^{3}t) is that the problem independent parts, like the grid data management, the solvers, the visualisation, etc., have been implemented also for parallel computer platforms. From this point of view, a further development of UG contributed also to the development of r^{3}t [93], [8], [92].

6.2.1.4 Adaptivity

An important part of any numerical simulations for complex applications is a grid and time adaption. Clearly, if one wish to obtain a numerical solution that approximates well an analytical one, one has to control the discretisation errors resulted from approximations of the exact solution in space and time.

Without any a-priori or a-posteriori estimation of such errors, one has no other chance to obtain a “discretisation independent” numerical solution than to refine uniformly computational grid and to use very small time steps. On the other hand, with some knowledge of discretisation errors, one can refine the computational grid locally and one can use reasonable time steps. Of course, the advantage of this approach concerning the duration of computations is enormous with respect to the first one.

The refinement of computational grids is necessary strictly only to improve the numerical approximation of the convection-diffusion-dispersion differential operator. An effective error indicator of numerical errors for standard discretisation methods of convection-diffusion-dispersion partial differential equations was developed, see section 6.2.11 on “The Error Estimator”.

The estimator is implemented in r^{3}t to mark these elements of computational grid for a further refinement, where large numerical errors from the approximation of convection and diffusion-dispersion are detected. In such a way, in numerical simulations with r^{3}t users can utilise locally adapted computational grids within computations for each time step.

To estimate the time discretisation error, some well-known indicators used like the Courant number, appeared to be appropriate for computations with r^{3}t. As there are several numerical algorithms available in r^{3}t, including some non-standard ones, different error indicators are necessary for the control of time and space discretisation errors.

This report and the User’s Guide for r^{3}t [52] explain in more detail, how one can successfully realise numerical simulations using grid and time automatic adaption in r^{3}t. Together with the possibility to use parallel computations of complex applications, the simulator r^{3}t offers the highest level software tools for realistic computations of problems dealing with radionuclides transport in subsurface.

6.2.1.5 Solvers in r^{3}t

Natural and robust solvers for numerical simulations that are realised on hierarchical grid structures are the multigrid solvers, see, e.g., [142]. In fact, such solvers are the most important part of UG library and they are exploited successfully also in r^{3}t.

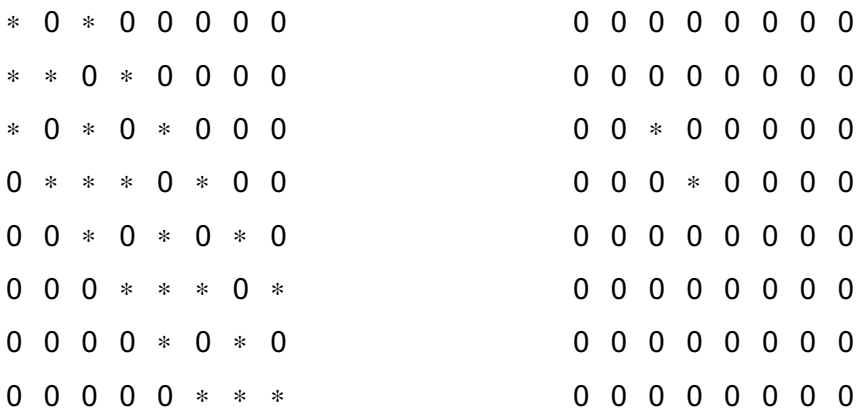

Fig. 6.5 Example of sparse matrix format for transport of eight radionuclides modelled with two partial differential equations and six ordinary differential equations. On the left a diagonal block of the matrix and on the right an off-diagonal block can be seen.

Very large number of partial differential equations coupled with ordinary differential equations has to be solved with r^3t. Such difficult task must be resolved using an optimal format for discretisation matrices, otherwise extreme requirements on the size of computer memory can make the computations impracticable.

In practice, additionally to the sparsity of matrices due to local discretisation methods, the sparsity due to the mathematical model must be utilised. If the number of unknown radionuclide concentrations is, e.g., 26, the standard format would require the block matrices with 26×26 blocks, although, in fact, each off-diagonal block can be represented by a single scalar number (!) instead of the block matrix 26×26. This is the case if all physical parameters for the modelling of convection-diffusion are identical for each of 26 unknown contaminant concentrations.

The matrix format that can resolve the sparsity inside of mathematical models, was proposed and implemented in UG by Neuss [104]. Fig. 6.5 should illustrate this matrix format resulting from some “sparse” coupling of equations in our mathematical model. Using this efficient matrix format, very large systems of equations can be solved by r^3t. A formal test was reported in [60] for an example with 120 components on some coarse computational grid.

6.2.1.6 Numerical Methods

The most important part of the research work at Heidelberg university was the development of specific numerical algorithms that appeared to be necessary for a successful solving of typical applications with r^3t.

All numerical algorithms that can be used in r^3t for solving of radionuclides transport problems are based on finite volume methods. In such a way, every computations realised with r^3t are based on a discrete local mass balance formulation. Together with appropriate discretisation of flux based boundary conditions, all numerical schemes preserve the mass on local and global level, i.e., on a computational cell (the finite volume) and on a whole computational domain. This topic will be explained in next Sections in more details.

The Finite Volume Methods (FVM) are very well-known discretisation algorithms and they were applied to solve many diverse applications. For the problems of convection-diffusion equations, the implicit form of FVM is very popular and it was used also in d^3f [49]. This method is available in r^3t, see later.

Nevertheless, the application of such implicit FVM for the specific mathematical equations to be solved by r^3t can bring in some cases several disadvantages.

First of all, the decay reactions can be described by very large constants of reaction rates that result in impracticable restrictions on the choice of time steps. To overcome this difficulty, the exact solution of ordinary differential equations describing the decay reactions was implemented in r^3t [61].

Furthermore, the so called maximal grid Peclet number can be very large for some computational examples, if grids are used which are not fine enough. As it is shown later, the standard fully implicit FVM (the central difference method), if used with too large time steps, can lead not only to unphysical oscillations in numerical solution, but also to a large artificial longitudinal dispersion. See Fig. 6.6 for a well-known example of rotated Gaussian impulse with zero diffusion.

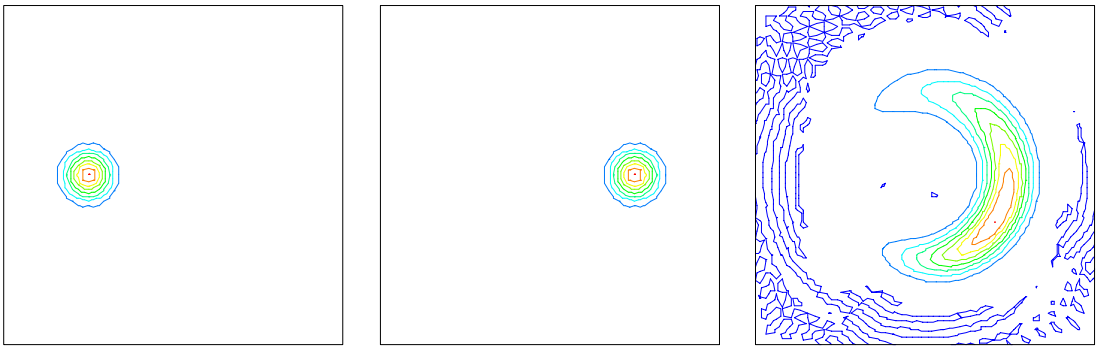

Fig. 6.6 Gaussian impulse rotating in a circle with zero diffusion
Illustration of numerical errors, if fully implicit, central difference discretisation scheme is used with large time steps for purely convective transport. The example is a Gaussian impulse that rotates in a circle with zero diffusion: the initial function (left), the exact solution after the half of rotation cycle (middle), and the corresponding numerical solution (right). Note unphysical oscillations and large artificial longitudinal dispersion in the numerical solution.

To overcome such situations, a new second order explicit discretisation scheme for the convection equation with flux limiter was developed and implemented in r^3t [54], [51]. This method coincides in one-dimensional (1D) case with well-known Lax-Wendroff method for hyperbolic equations, see, e.g., [94], and it was extended, together with a special local flux limiter to avoid unphysical oscillations, for unstructured grids as required by r^3t.

Nevertheless, even if the reaction equations are solved exactly and the convection equations with some higher precision, they can be combined only using the so called operator splitting approach. This works very well, if the two involved operators commute, but otherwise, a large time splitting error can occur.

For the system of convection equations with different retardation factors that are coupled through decay reactions, such large time splitting errors can occur. A novelty second order explicit discretisation method was developed for this type of equations and implemented in r^3t [61], [55]. To our knowledge, up to now, no satisfactory algorithm was

available for such problems, see, e.g., [113]. The new scheme is, in fact, exact for 1D case with constant data, and it is based on the idea of Godunov method [94] for 2D and 3D case.

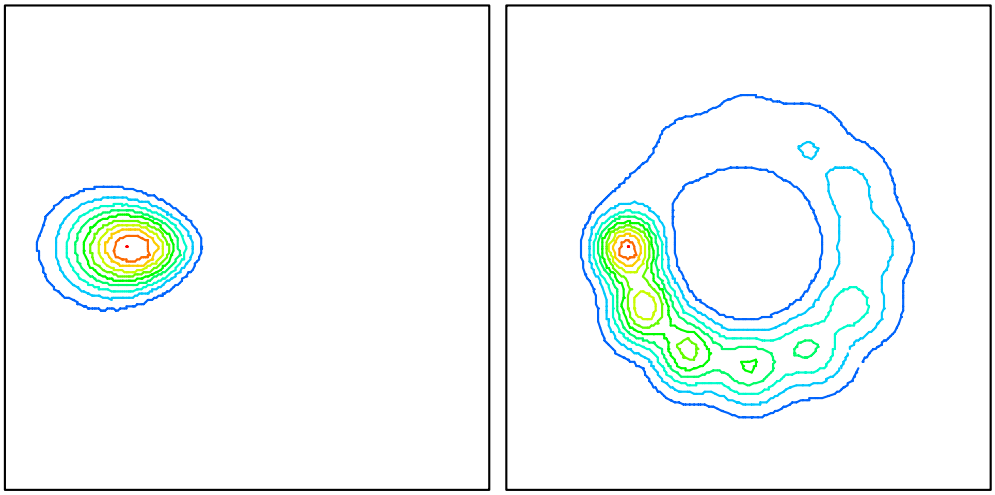

Fig. 6.7 Gaussian with decay rotating in a circle
Illustration of numerical errors, if standard operator splitting method is used with too large time steps for convection-decay equations. Analogously to Fig. 6.6, the example is a rotated Gaussian impulse with decay, where the product of the decay reaction (the second component in the right picture) is transported with almost zero velocity. The solution was obtained with 12 time steps and the large time splitting error of the operator splitting method is clearly visible for the second component.

Of course, the explicit discretisation scheme for convective transport has the well-known CFL restriction for the choice of time steps. This is not very restrictive to some level of grid refinement, but, especially if very fine local grid adaption is used, it can require too small time steps.

For such cases, a new flux-based method of characteristics for the convection-dominated transport [50], and later also for coupled system of convection equation [51] was developed and implemented in r^3t. This numerical algorithm can be seen as an extension of previously mentioned second order explicit discretisation scheme for the case of grid

Courant numbers larger than 1. This method can solve convection-dominated transport without the CFL restriction on time steps, without nonphysical oscillations, and without violation of a local mass balance formulation.

Moreover, the flux-based method of characteristics for a system of transport equations includes in a natural way the treatment of decay reactions, avoiding the time splitting error of standard operator splitting methods. See Fig. 6.7 for an illustration of such errors, where numerical results with standard operator splitting method for the transport of 2 radionuclides are presented. The transport of the second component is very slow due to a very large retardation, and one can clearly see all (large) discrete steps of the sequential solving - first, only the decay was solved, secondly, only the convection was solved. Compare these results later with the results in Fig. 6.12, where the time splitting error is reduced significantly.

Finally, for the case of transport with equilibrium non-linear sorption, appropriate extensions of the previous explicit methods to resolve correctly shock formations in numerical solutions, were implemented in r^{3}t. In [76], very precise numerical solutions for the 1D convection-diffusion equation with Freundlich and Langmuir non-linear sorption isotherms were developed, see Fig. 6.8 for some typical results. The computations with r^{3}t for analogous examples confirmed that numerical solutions of the same approximation quality can be obtained.

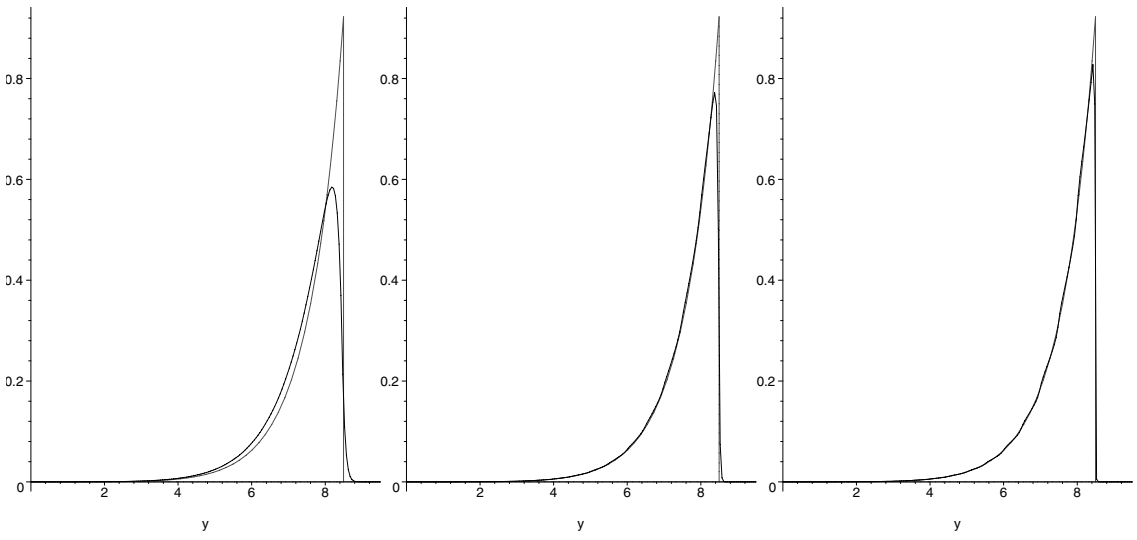

Fig. 6.8 Numerical solutions of the equation $\partial_t(u + u^{3/4}) + \partial_x u + d\partial_{xx} u = 0$ for d=10^{-2}, 10^{-3}, 10^{-4} at some fixed time point (from the left to the right) that are compared with the exact solution for d=0.

In the following section, we describe in more details all important numerical algorithms used in r^{3}t. At the end, we summarise the advantages and disadvantages of each method and we propose general guidelines for the user of r^{3}t concerning his/her decision on applications of particular methods.

6.2.2 General Mathematical Model

In this section we present a representative general mathematical model that includes in an abstract form features of all mathematical models used in r^{3}t, see Section 4 on "Conceptual Model and Mathematical Description". In such a way, we can describe in an unique way all common features of algorithms used in r^{3}t.

6.2.2.1 General Partial Differential Equation

Firstly, the general mathematical model can be given by a partial differential equation for an unknown function $u(\boldsymbol{x},t)$,

$$\partial_t(\theta u) + \nabla \cdot \boldsymbol{J} + ru = q. \qquad (6.1)$$

We prefer to explain each term in (6.1) after formulating an equivalent integral form to (6.1). If $\boldsymbol{J} \equiv \boldsymbol{0}$, the equation (6.1) represents an ordinary differential equation. In general, $\boldsymbol{J} = \boldsymbol{J}(x,u,\nabla u)$, where only a linear dependence on u and ∇u is considered.

For an example, if θ denotes the porosity ϕ, the differential operator $\boldsymbol{J}$ denotes the convection-diffusion term $\boldsymbol{v}u - \boldsymbol{D}\nabla u$, and r denotes the constant decay rate, one obtains

$$\phi\partial_t u + \nabla \cdot (\boldsymbol{v}u - \boldsymbol{D}\nabla u) + \lambda u = 0.$$

If the mathematical model includes several components, i.e., $u = u^l$ for $l = 1,2,\ldots,L$, each component is described by its own differential equation of the form (6.1). In fact, the functions u^l for two different indices l can denote the same contaminant in different phases, e.g., one is dissolved in flowing groundwater, and one is adsorbed to the skeleton of porous media.

In general, the parameters in (6.1) are non-linear and different for each component u^l. In our case, we can summarise it in the form

$$\begin{aligned} \theta^l &= \theta^l(x,u^1,u^2,\ldots,u^L) \\ J &= J^l(x,u^l,\nabla u^l) \\ r^l &= r^l(x,u^1,u^2,\ldots,u^L) \\ q^l &= q^l(t,x,u^1,u^2,\ldots,u^L) \end{aligned} \quad .$$

For concrete forms of these parameters see Section 4. Note that the equation (6.1) is linear in most cases, or, if non-linear, then with the parameters depending only on few components.

Further, we deal with a single equation of the form (6.1), i.e. $L = 1$.

The function u must be considered on some bounded computational domain $\Omega \subset R^d$ (d=2 or d=3) and for some positive time $t > t^0$.

If $\boldsymbol{J} \neq \boldsymbol{0}$, one must define for u some boundary conditions for $x \in \partial\Omega$ and $t \geq t^0$. The first possibility is to explicitly define the values at some part of the boundary (i.e., the so called Dirichlet boundary conditions)

$$u(t,\gamma) = U_1(t,\gamma),\ \gamma \in \partial_1\Omega \subset \partial\Omega,\ t \geq t^0 \qquad (6.2)$$

or the second possibility is to prescribe the values for the flux $\boldsymbol{J}$ (i.e., the so called flux based boundary conditions)

$$\boldsymbol{n} \cdot \boldsymbol{J} = J_0(t,\gamma,u),\ \gamma \in \partial_0\Omega \subset \partial\Omega,\ t \geq t^0. \qquad (6.3)$$

The vector $\boldsymbol{n} = \boldsymbol{n}(\gamma)$ in (6.3) denotes the normal outwards vector at $\gamma \in \partial\Omega$. Of course, the union of the Dirichlet boundary $\partial_1\Omega$ and the flux based boundary $\partial_0\Omega$ must be equal to the total boundary $\partial\Omega$, i.e.,

$$\partial_1\bar{\Omega} \cup \partial_0\bar{\Omega} = \partial\Omega.$$

Finally, the function u must be explicitly defined for $t = t^0$ by initial conditions, i.e.,

$$u(t^0,x) \quad = \quad U^0(x),\ x \in \Omega \cup \partial_0\Omega . \tag{6.4}$$

6.2.2.2 General Integral Formulation

All methods implemented in r^{3}t are of finite volume type. In such a way, the computational domain Ω is covered by finite volumes (FV) that are non intersecting subsets Ω_i of Ω for $i = 1,2,\ldots,I$. The set of finite volumes Ω_i determines the discretisation of spatial computational domain Ω. To discretise the time variable t, we introduce time intervals (t^n,t^{n+1}), for $n = 0, 1,2$, and so on.

In r^{3}t, analogously to d^{3}f, the so called dual mesh of finite volumes is used that is complementary to a finite element mesh, see [49] for all details.

Having the discretisation of the computational domain Ω and of the time variable t, it is now straightforward to formulate an equivalent integral formulation to the partial differential equation (6.1). To do so, one has to integrate (6.1) over Ω_i and (t^n,t^{n+1}), and one obtains

$$\begin{aligned}\int_{\Omega_i} \theta u(t^{n+1},x)\,dx \quad = \quad & \int_{\Omega_i} \theta u(t^n,x)\,dx - \int_{t^n}^{t^{n+1}} \int_{\Omega_i} \boldsymbol{n} \cdot \boldsymbol{J}\,d\gamma\,dt \\ & - \int_{t^n}^{t^{n+1}} \int_{\Omega_i} r\,u(t,x)\,dx\,dt + \int_{t^n}^{t^{n+1}} q\,dx\,dt\end{aligned} \quad . \tag{6.5}$$

Note that if the differential equation (6.1) is valid, the integral formulation (6.5) is fulfilled for arbitrary finite volume mesh (such that is used in r^{3}t) and for an arbitrary time interval (t^n,t^{n+1}).

To simplify our considerations, we suppose next that the integral equation (6.1) describes a *mass balance* formulation for a contaminant in groundwater. Nevertheless, our considerations are valid for any mathematical model represented by the partial differential equation of the form (6.1).

From this point of view, the integral on the left hand side (l.h.s.) of (6.5) will represent the *mass* in the volume Ω_i at time $t = t^{n+1}$. Further, the unknown function $u = u(t,x)$ will represent here a *concentration* of the contaminant, but one can replace this notion, e.g., by a mass fraction. The given function $\theta > 0$ must describe properties of the volume occupied by u in Ω_i (e.g., the water content) like the porosity, the flow density, etc. For particular forms of u and θ, see Section 4.

Analogously, the first integral on the right hand side (r.h.s.) of (6.5) represents the mass in the volume Ω_i at time $t = t^n$. For $n = 0$, this integral can be determined explicitly using the initial conditions (6.4).

Further, the second (double) integral in the r.h.s. represents the mass *fluxes* that describe the mass exchange due to the transport of contaminant during time interval (t^n,t^{n+1}) between the volume Ω_i and some neighbouring volumes Ω_j, or, if $\partial\Omega_i \subset \partial_0\Omega$, the mass exchange due to boundary conditions.

Next, the third integral in the r.h.s. of (6.5) represents the sink of u in the volume Ω_i during the time interval (t^n,t^{n+1}). Here, the given function r describes an effective (total) rate of all sinks. Particularly, for r^{3}t the parameter r is determined by the decay reaction, the kinetic sorption, the immobilisation reaction and/or the external flow sinks (e.g., wells), see Section 4.

Finally, the last integral in the r.h.s. of (6.5) represents the effective source term of u in the volume Ω_i during the time interval (t^n,t^{n+1}). Analogously to the description of r, the parameter q is determined in r^{3}t by decay reactions, the kinetic sorption, the immobilisation reaction and the external flow sources.

6.2.2.3 Principle of Superposition

If the partial differential equation (6.1) is linear, one can use the so called principle of superposition to find the solution by solving (independently) series of simplified problems. For a given finite volume mesh and a time interval, the idea is to define the simplest possible equation to be solved in such a way, that the solution of the origin problem (6.1) is obtained by an appropriate linear combination of solutions of the simplified problems.

Particularly, one has to solve the general differential equation (6.1) with the following three series of different combinations of initial and boundary conditions. Note that the following explanation is valid only for the flux based boundary conditions (6.3) with $J_0 = J_0(t,\gamma)$, but it can be easily extended for the case of a linear dependence of J_0 on u.

Firstly, one has to solve (6.1) for the following series of initial conditions (i.e., for $i = 1,2,\ldots,I$)

$$u(t^n,x) = u_i(t^n,x) = \begin{cases} U^0(x) & x \in \Omega_i \\ 0 & x \notin \Omega_i \end{cases}, \qquad (6.6)$$

with homogeneous boundary conditions on $\partial_1\Omega$ and $\partial_0\Omega$, i.e.,

$$\begin{aligned} u(t,\gamma) &= 0, & \gamma \in \partial_1\Omega,\ t \geq t^0 \\ \boldsymbol{n} \cdot \boldsymbol{J}(t,\gamma) &= 0, & \gamma \in \partial_0\Omega,\ t \geq t^0 \end{aligned}.$$

Further, the same equations have to be solved for zero initial conditions, e.g., $U^0(x) \equiv 0$, and homogeneous boundary conditions on $\partial_0\Omega$, but the nonhomogeneous, locally defined, Dirichlet boundary conditions, (i.e., for j such that $x_j \in \partial_1\Omega$)

$$u(t,\gamma) = u_j(t,\gamma) = \begin{cases} U_1(t,\gamma) & (\gamma \in \partial_1\Omega) \wedge (\gamma \in \partial\Omega_j) \\ & t \geq t^0 \\ 0 & (\gamma \in \partial_1\Omega) \wedge (\gamma \notin \partial\Omega_j) \end{cases}. \qquad (6.7)$$

Finally, the same equations have to be solved with the zero initial conditions, homogeneous boundary conditions on $\partial_1\Omega$ and nonhomogeneous, locally defined, flux-based boundary conditions on $\partial_0\Omega$, (i.e., for k such that $x_k \in \partial_0\Omega$).

$$\boldsymbol{n} \cdot \boldsymbol{J} = \begin{cases} J_0 & (\gamma \in \partial_0\Omega) \wedge (\gamma \in \partial\Omega_k) \\ & t \geq t^0 . \\ 0 & (\gamma \in \partial_0\Omega) \wedge (\gamma \notin \partial\Omega_k) \end{cases} \qquad (6.8)$$

Having the solutions of all above problems, one can define the solution of the differential equation (6.1) with the origin initial conditions (6.4) and boundary conditions (6.2) and (6.3) by

$$u(t,x) = \sum_{i=1}^{I} u_i(t,x) + \sum_j u_j(t,x) + \sum_k u_k(t,x) .$$

The principle of superposition was used very successfully for the implementations of explicit discretisation schemes for convection-decay equations, especially for their extension in the form of flux-based method of characteristics. In fact, this approach can be used even by users of r^{3}t in the mathematical modelling of particular applications, when the origin complex problem can be split to several simpler problems.

Finally, if a system of equations (6.1) has to be solved, i.e., $u = u^l$ for $i = 1,2,\ldots,L$, one has, in general, to solve the whole system at once with the local initial or boundary conditions (6.6) - (6.8). Nevertheless, for the case of decay equations, one can again apply the principle of superposition to split the system of equations (6.1) to several simplified subsystems.

Particularly, one radionuclide (the daughter) can be produced by decays of several radionuclides (the mothers), and some nontrivial decay chains are then produced. Using the principle of superposition, one can easily show that such system can be divided to the problems of simple linear decay chains, where only the radionuclide at the top has some nonzero initial conditions, see Section 6.2.5.1 later.

6.2.3 Numerical Solution

In this section, we introduce how the numerical solution of (6.5) shall be understood. At the same time, we discuss the discrete form of initial conditions (6.4) and the discrete form of boundary conditions (6.2) and (6.3). Using afterwards the same principles for the discretisation of the integral equations (6.5), one obtains at the end the algebraic system that has to be solved by solvers in r^{3}t.

6.2.3.1 Understanding of Numerical Solution

In Section 6.2.2, we defined a finite volume mesh that covers the computational domain Ω. The analytical mass balance formulation (6.5) for time interval (t^n,t^{n+1}) is valid for an arbitrary mesh of this form.

The numerical solution, say $\hat{u}^{n+1} = \hat{u}^{n+1}(x)$, that will approximate the analytical solution $u(t^{n+1},x)$, shall be determined in a sequence at the time points $t = t^{n+1}$, for $n = 0,1,\ldots$ and so on, for a particular finite volume mesh, i.e.,

$$\hat{u}^{n+1} = \hat{u}_I^{n+1}(x) \approx u(t^{n+1},x),\ x \in \Omega = \bigcup_{i=1}^{I} \overline{\Omega}_i,$$

where I is the total number of finite volumes. The numerical solution at $t = t^0$, e.g., $\hat{u}^0 = \hat{u}^0(x)$, can be determined explicitly from initial conditions (6.4), see later.

As the integral equations (6.5) represent a finite number of equations, the numerical solution can be represented by I discrete values, say, u_i^{n+1} for $i = 1,2,\ldots,I$.

From the point of view of finite volume methods (FVM), one can accept very natural piece-wise constant representation of $\hat{u}(t^{n+1},x)$ with respect to finite volume mesh,

$$\hat{u}^{n+1} = \hat{u}^{n+1}(x) = u_i^{n+1}, \qquad x \in \Omega_i. \qquad (6.9)$$

One can describe the numerical solution also in a “finite difference” and “finite element” form as usual for finite difference methods (FDM) or finite element methods (FEM). Due to our special form of finite volumes, each finite volume Ω_i has a representative grid point

$x = x_i \in \Omega_i$, where x_i for $i = 1,2,\ldots,I$ are the vertices of the finite element mesh T^e for $e = 1,2,\ldots,E$, see [49] for details or Figure Fig. 6.9 and Fig. 6.10 later for an illustration. In such a way, one can consider that

$$u_i^{n+1} \approx u(t^{n+1}, x_i), \; i = 1,2,\ldots,I; \; n = 0,1,\ldots, \qquad (6.10)$$

and the standard finite element interpolation

$$\tilde{u}^{n+1} = \tilde{u}^{n+1}(x) = P^e(x), \; x \in \Omega = \bigcup_{e=1}^{E} \bar{T}^e, \qquad (6.11)$$

where the function $\tilde{u}^{n+1}$ is continuous in Ω, and P^e is a polynomial specific to each type of finite element. It is important to note that only the finite element function $\tilde{u}^{n+1}$ has a clearly defined gradient $\nabla \tilde{u}^{n+1}$ for $x \in T^e$.

Next, we shall describe the treatment of initial conditions and boundary conditions for the numerical solution.

Firstly, the values u_i^0 are determined from the initial conditions. This gives us at the same time a clear definition of the mass in the discrete form for numerical solution.

Further, the values u_i^{n+1} for $x_i \in \partial_1 \Omega$ are determined directly from the appropriate Dirichlet boundary conditions (6.2).

Finally, the values of the flux $\boldsymbol{J}$ for $x_i \in \partial_0 \Omega$ must be determined (or approximated) from the flux based boundary conditions (6.3). This determines at the same time, how to discretise $\boldsymbol{J}$ in the integral equations (6.5).

6.2.3.2 Initial Conditions for Numerical Solution

The most natural definition of u_i^0 for $i = 1,2,\ldots,I$, used in finite volume methods, is to determine these values by an averaging procedure

$$u_i^0 := \frac{\int_{\Omega_i} \theta U^0 dx}{\int_{\Omega_i} \theta dx} . \qquad (6.12)$$

Note that, in general, (6.12) is a non-linear equation for the unknown u_i^0, if $\theta = \theta(u)$.

Further, one can denote

$$\theta_i^0 := \frac{1}{|\Omega_i|} \int_{\Omega_i} \theta dx , \qquad (6.13)$$

where $|\Omega_i|$ is the "measure" of $\Omega_i \subset R^d$, i.e., the area of $\Omega_i \subset R^2$, or the volume of $\Omega_i \subset R^3$. If $\theta = \theta(x,u)$ then one has to replace θ in (6.12) and (6.13) by $\theta = \theta(x,u_i^0)$.

If (6.12) and (6.13) are fulfilled exactly, one can express the mass in Ω_i at $t = t^0$ by

$$\int_{\Omega_i} \theta U^0 dx = |\Omega_i| \theta_i^0 u_i^0 . \qquad (6.14)$$

Even if (6.12) and (6.12) are not fulfilled exactly, but only approximately, the r.h.s. of (6.14) will represent the *mass of the contaminant u* at $t = t^0$ in Ω_i in a discrete form.

Analogously, the total mass in Ω at $t = t^0$ can be expressed then by

$$\int_{\Omega} \theta U^0 dx = \sum_{i=1}^{I} |\Omega_i| \theta_i^0 u_i^0 .$$

Another form, how to determine u_i^0, is to use the idea (6.10) of finite difference methods and to consider

$$u_i^0 := U^0(x_i), \qquad i = 1,2,\ldots,I . \qquad (6.15)$$

In general, if one use , the property (6.14) can be fulfilled only very roughly (approximately). On the other hand, the implementation of initial conditions in the form (6.15) is very straightforward and much simpler. Moreover, it preserves the values of U^0 in vertices x_i of the finite element mesh and this needs not to be valid for (6.12).

In r^{3}t, the user can choose between the “value preserving” initial conditions and the “mass preserving” initial conditions (6.12), see [52] for more details.

6.2.3.3 Dirichlet Boundary Conditions for Numerical Solution

If $x_i \in \partial_1 \Omega$ with the Dirichlet boundary conditions (6.2), then one can define

$$u_i^{n+1} := U_1(t^{n+1}, x_i), \qquad x_i \in \partial_1 \Omega .$$

The definition is very natural for finite difference or finite element methods.

Note that for the finite volume representation, as $\hat{u}^{n+1}(x_i)$ is constant per each Ω_i, one obtains that $\hat{u}^{n+1}(x) \equiv u_i^{n+1}$ for $x \in \Omega_i$. Consequently, the Dirichlet boundary conditions describes, in fact, the mass for discrete numerical solution in Ω_i at $t = t^{n+1}$, i.e.,

$$|\Omega_i| \, \theta_i^{n+1} u_i^{n+1} = \int_{\Omega_i} \theta u^{n+1} dx ,$$

where θ_i^{n+1} is defined analogously to (6.13).

From this point of view, one should avoid using the Dirichlet boundary conditions (6.2), if possible. There exist several flux based boundary conditions (6.3) that are more natural for this type of problems, and that have similar property as the Dirichlet boundary conditions. For instance, one can replace (6.2) by the flux based boundary conditions (6.3) with

$$J_0(t, \gamma, u) = \alpha (u(t, \gamma) - U^0(t, \gamma)) , \qquad (6.16)$$

where the constant $\alpha > 0$ must be given. For very large values of α, i.e., if $\alpha^{-1} \approx 0$, one obtains that (6.16) is qualitatively very near to standard Dirichlet boundary conditions (6.2).

Finally, two technical remarks about Dirichlet boundary conditions for FVM. Firstly, the finite volumes Ω_i are excluded from the system of integral equations (6.5), if $x_i \in \partial_1\Omega$.

Secondly, for $x_i \in \partial_1\Omega$ and $t = t^0$, the values u_i^0 are given by the Dirichlet boundary conditions (6.2), and not by the initial conditions (6.4).

6.2.3.4 Flux Based Boundary Conditions for Numerical Solution

First, it is denoted

$$\Gamma_{i0} := \partial\Omega_i \cap \partial_0\Omega . \qquad (6.17)$$

If $\Gamma_{i0} \neq \{\emptyset\}$, then one has to apply the flux based boundary conditions in the integral equation (6.5) by substituting

$$\int_{t^n}^{t^{n+1}} \int_{\Gamma_{i0}} \boldsymbol{n} \cdot \boldsymbol{J}\, d\gamma\, dt = \int_{t^n}^{t^{n+1}} \int_{\Gamma_{i0}} J_0\, d\gamma\, dt . \qquad (6.18)$$

If $J_0 = J_0(t,\gamma)$, i.e., the function J_0 is not depending on the unknown solution u, one can, at least theoretically, compute the integral on the r.h.s. of exactly. In general, one has to apply some numerical integration.

In r^{3}t, the integral on the r.h.s. of is computed exactly, if $J_0(t,\gamma)$ is a piecewise linear function in time and space. In fact, the time intervals that define the time dependence of $J_0 = J_0(t)$ can be different to the time intervals (t^n, t^{n+1}) of the discretisation. Consequently, the time dependent source terms at inflow boundaries, that are defined for discrete set of time points with a linear interpolation in between, see [52], are integrated exactly.

In general, the “middle” point quadrature rule is used and

$$\int_{t^n}^{t^{n+1}} \int_{\Gamma_{i0}} J_0 \, d\gamma \, dt \;=\; \tau^n \left|\Gamma_{i0}\right| J_{i0}^{n+\frac{1}{2}},$$

where $J_{i0}^{n+\frac{1}{2}} := J_0(t^{n+\frac{1}{2}}, x_i)$. Here, the time step τ^n is defined by $\tau^n := t^{n+1} - t^n$, and the middle time point $t^{n+\frac{1}{2}}$ by $t^{n+\frac{1}{2}} := t^n + \frac{\tau^n}{2}$.

In fact, the numerical integration over Γ_{i0} can be realised using the middle point quadrature rule over several segments $\Gamma_{i0}^e \subset \Gamma_{i0}$, where e runs through indices of all finite elements T^e containing the vertex x_i, see [49] for more details.

The approximation can be, formally, applied also in the case of solution-dependant function $J_0 = J_0(t, \gamma, u)$, e.g., in the case of the so called Newton (or Robin) type of flux based boundary conditions by defining

$$J_{i0}^{n+\frac{1}{2}} := J_0(t^{n+\frac{1}{2}}, x_i, u_i^{n+\frac{1}{2}}).$$

Analogously to the treatment in the discretisation of the integral equations (6.5), see next section, one can recognise three basic approximation for $u_i^{n+\frac{1}{2}}$

$$u_i^{n+\frac{1}{2}} := \begin{cases} u_i^n & \text{explicit} \\ u_i^{n+1} & \text{implicit} \\ \dfrac{u_i^n + u_i^{n+1}}{2} & \text{explicit-implicit} \end{cases}.$$

6.2.3.5 General Discretisation Scheme

In the discretisation of integral equations (6.5) one applies the analogous principles that were used for the discretisation of initial and boundary conditions.

Particularly, all the discretisation schemes shall determined the *mass* of u in Ω_i at $t = t^{n+1}$

$$|\Omega_i|\,\theta_i^{n+1}u_i^{n+1} \approx \int_{\Omega_i} \theta u(t^{n+1},x)\,dx\,. \qquad (6.19)$$

In such a way, the mass of u in the whole domain Ω at $t = t^{n+1}$ is given by

$$\sum_{i=1}^{I} |\Omega_i|\,\theta_i^{n+1}u_i^{n+1} \approx \int_{\Omega} \theta u(t^{n+1},x)\,dx\,.$$

The mass defined in (6.19) shall be obtained by solving the system of discrete equations given by the following general discretisation scheme

$$\begin{aligned} |\Omega_i|\,\theta_i^{n+1}u_i^{n+1} \;=\; & |\Omega_i|\,\theta_i^n u_i^n - \tau^n \sum_j |\Gamma_{ij}|\,J_{ij}^{n+\frac{1}{2}} \\ & -\tau^n |\Omega_i|\,r_i^{n+\frac{1}{2}} u_i^{n+\frac{1}{2}} + \tau^n |\Omega_i|\,q_i^{n+\frac{1}{2}} \end{aligned}\,, \qquad (6.20)$$

that is used for the nodes $x_i \in \Omega$ and $x_i \in \partial_0\Omega$ (i.e., the inner nodes and the nodes at boundary with the flux based boundary conditions, but not for the Dirichlet nodes $x_i \in \partial_1\Omega$).

As mentioned before, the first term on the r.h.s. and the l.h.s. of (6.20) represent (in a discrete form) the mass of the contaminant u in Ω_i at the time points $t = t^{n+1}$ and $t = t^n$, respectively. The last three terms in (6.20) can be viewed as an approximation of integrals in (6.5) by middle point quadrature rules.

The "middle point" value $J_{ij}^{n+1/2}$ represents (or approximate) the *flux* between Ω_i and Ω_j during the time interval (t^n, t^{n+1}) through the boundary Γ_{ij}, where

$$\Gamma_{ij} := \partial\Omega_i \cap \partial\Omega_j . \qquad (6.21)$$

The index j runs only through indices of Ω_j for which the measure of Γ_{ij} is nonzero, e.g., the length $|\Gamma_{ij}|$ in 2D or the area $|\Gamma_{ij}|$ in 3D are nonzero.

More precisely, $J_{ij}^{n+1/2} \approx (\boldsymbol{n} \cdot \boldsymbol{J})(t^{n+1/2}, \gamma_{ij})$ with the point $\gamma_{ij} \in \Gamma_{ij}$ given by $\gamma_{ij} = (x_i + x_j)/2$. The dependence $\boldsymbol{J} = \boldsymbol{J}(u, \nabla u)$ is resolved by using the finite element approximation $\tilde{u}^n$ and $\tilde{u}^{n+1}$ given by (6.11). For instance, for $u_{ij}^{n+1/2} := \tilde{u}(t^{n+1/2}, \gamma_{ij})$ one obtains

$$u_{ij}^{n+\frac{1}{2}} = \frac{u_{ij}^n + u_{ij}^{n+1}}{2} = \frac{1}{2}\left(\frac{u_i^n + u_j^n}{2} + \frac{u_i^{n+1} + u_j^{n+1}}{2} \right). \qquad (6.22)$$

Note that even more accurate approximation of $J_{ij}^{n+1/2}$ can be used by considering the middle point quadrature rule for $\Gamma_{ij}^e \subset \Gamma_{ij}$, see Fig. 6.9 for the illustration of notations. This approach is used for the computations of $\nabla\tilde{u}$, because the gradient of finite element interpolation is continuous only in T^e, see [49] for details.

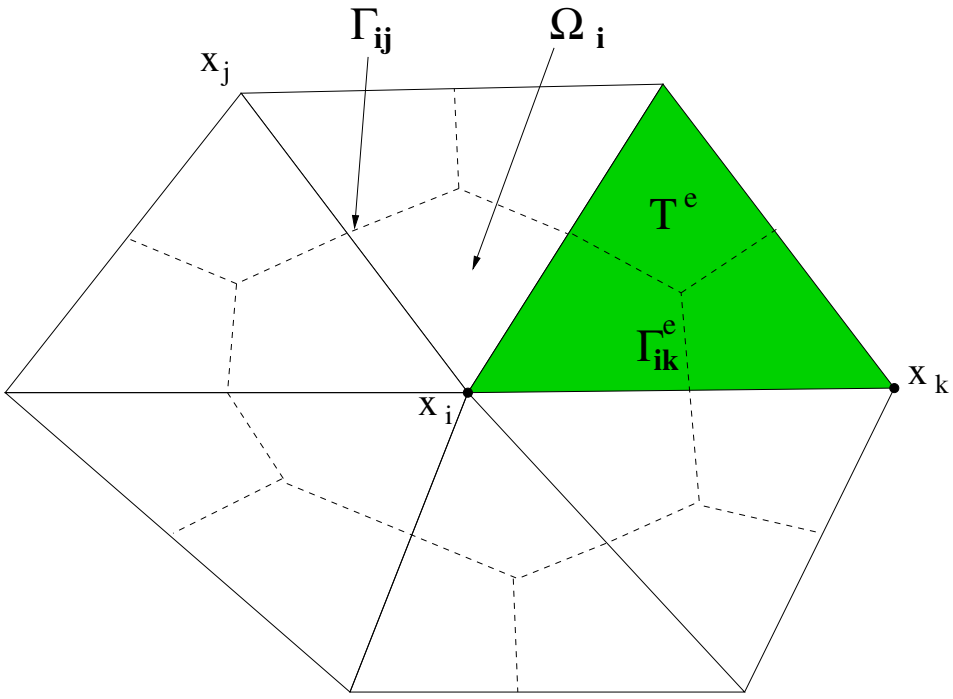

Fig. 6.9 Illustration of notations for a finite volume mesh which is dual to a finite element mesh

Finally, the last two terms represent (or approximate) the effective *sink* and *source* term, respectively, in Ω_i during (t^n,t^{n+1}). Again, this can be viewed as a middle point rule used for the numerical integration of (6.5), e.g., $q_i^{n+1/2} \approx q(x_i,t^{n+1/2})$, where x_i is (in general only approximately) a middle point of Ω_i and $t^{n+1/2}$ is the middle point of (t^n,t^{n+1}).

In such a way, the general discretisation scheme (6.20) can be viewed as an application of *explicit-implicit* time discretisation (the so called Crank-Nicholson scheme) and the *central difference* space discretisation of the differential equation (6.1).

The general scheme (6.20) is available in r^{3}t, see [52]. The main advantage of this universal scheme is that it is applicable for all mathematical models included in r^{3}t, it is based on the local mass balance formulation, and it is a second order scheme (i.e., the numerical error is reduced approximately 4 times by halving the time and space discretisation steps). The latter is valid only for “enough small” time and space discretisation steps and only for the approximation of “enough smooth” analytical solutions.

In next sections, several other algorithms are introduced, that result in a much better approximation quality for some important particular cases of the general model. At the same time, comparing the general scheme (6.20) with other algorithms, one can clearly introduce the advantages and disadvantages of this universal scheme.

6.2.4 Explicit and Implicit Discretisation Schemes

If our mathematical model is linear, one can use the following substitutions in the general discretisation scheme (6.20),

$$J_{ij}^{n+\frac{1}{2}} = \frac{J_{ij}^n + J_{ij}^{n+1}}{2} := \frac{J(\gamma_{ij},u_{ij}^n) + J(\gamma_{ij},u_{ij}^{n+1})}{2} \qquad (6.23)$$

$$r_i^{n+\frac{1}{2}} u_i^{n+\frac{1}{2}} = \frac{r_i^n u_i^n + r_i^{n+1} u_i^{n+1}}{2} := \frac{r(t^n,x_i) u_i^n + r(t^{n+1},x_i) u_i^{n+1}}{2} \qquad (6.24)$$

$$q_i^{n+\frac{1}{2}} = \frac{q_i^n + q_i^{n+1}}{2} := \frac{q(t^n, x_i) + q(t^{n+1}, x_i)}{2}. \qquad (6.25)$$

If the model is non-linear, the substitutions (6.23) - (6.25) must be viewed as approximations.

Using (6.23) - (6.25), one can rewrite the general scheme (6.20) into the following two step scheme. Particularly, the first *explicit* scheme with the time step $\tau^n/2$

$$\begin{aligned} |\Omega_i| \theta_i^{n+\frac{1}{2}} u_i^{n+\frac{1}{2}} &= |\Omega_i| \theta_i^n u_i^n - \frac{\tau^n}{2} \sum_j |\Gamma_{ij}| J_{ij}^n \\ &\quad - \frac{\tau^n}{2} |\Omega_i| r_i^n u_i^n + \frac{\tau^n}{2} |\Omega_i| q_i^n \end{aligned}, \qquad (6.26)$$

and the second *implicit* scheme with the same time step $\tau^n/2$

$$\begin{aligned} |\Omega_i| \theta_i^{n+\frac{1}{2}} u_i^{n+\frac{1}{2}} &= |\Omega_i| \theta_i^{n+1} u_i^{n+1} + \frac{\tau^n}{2} \sum_j |\Gamma_{ij}| J_{ij}^{n+1} \\ &\quad + \frac{\tau^n}{2} |\Omega_i| r_i^{n+1} u_i^{n+1} - \frac{\tau^n}{2} |\Omega_i| q_i^{n+1} \end{aligned}. \qquad (6.27)$$

The right hand side of the explicit scheme (6.26) depends only on the known values of numerical solution at $t = t^n$, opposite to the implicit scheme (6.27), where all terms on the r.h.s. can depend on the unknown values of numerical solution at $t = t^{n+1}$.

This means that the general discretisation scheme (6.20) can be viewed as a two step procedure - first the fully explicit step (6.26) is realised, and afterwards its output is used as the initial condition for the second fully implicit step (6.27).

In following sections, some explicit and implicit discretisation schemes for particular mathematical models and their combinations using an operator splitting approach, are studied.

6.2.4.1 Explicit Discretisation Schemes

For a reference, one introduces the fully explicit version of the general discretisation scheme (6.20), i.e., $u_*^{n+1/2} \equiv u_*^n$ and one obtains

$$\begin{aligned} |\Omega_i| \theta_i^{n+1} u_i^{n+1} &= |\Omega_i| \theta_i^n u_i^n - \tau^n \sum_j |\Gamma_{ij}| J_{ij}^n \\ &\quad -\tau^n |\Omega_i| r_i^n u_i^n + \tau^n |\Omega_i| q_i^n \end{aligned} . \qquad (6.28)$$

Note that this scheme is presented here only formally and it is not used in this form in r^{3}t. The most important advantage of explicit discretisation schemes like (6.28) is that they include the best solving algorithm ever - the exact solutions. Clearly, if the analytical solution is available, it can depend only on “explicit information” like initial conditions, boundary conditions, time-space dependent source terms and so on. In r^{3}t, for instance, the system of purely decay reaction equations can be solved exactly, see later. Of course, for the general partial differential equation (6.1) such solution is not available.

Furthermore, the explicit discretisation schemes have an advantage that they contribute only to the r.h.s. of the resulting algebraic system, i.e., they do not contribute to the matrix of this system. For instance, in (6.28), the matrix has only diagonal entries and it is trivial to invert, if the mathematical model is linear.

At the same time, one must mention the most important disadvantage of explicit discretisation schemes. To do so, one splits the explicit scheme (6.28) into two explicit steps where the first step resolves only the transport term, and the second step only the sink/source term, i.e.,

$$|\Omega_i| \theta_i^{n+\frac{1}{2}} u_i^{n+\frac{1}{2}} = |\Omega_i| \theta_i^n u_i^n - \tau^n \sum_j |\Gamma_{ij}| J_{ij}^n \qquad (6.29)$$

$$|\Omega_i| \theta_i^{n+1} u_i^{n+1} = |\Omega_i| \theta_i^{n+\frac{1}{2}} u_i^{n+\frac{1}{2}} - \tau^n |\Omega_i| (r_i^n u_i^n - q_i^n) . \qquad (6.30)$$

The two step scheme (6.29) - (6.30) is equivalent to the discretisation scheme (6.28). The form (6.29) - (6.30) should illustrate that the explicit schemes, in general, *decouple* each term in the mathematical model. For instance, the first scheme (6.29) for the transport does not influence (couple) the parameters r and q in the second scheme for the sink/source, and vice versa, although this is not the case in the analytical model, i.e., the transport can be immediately influenced by sinks and sources, and vice versa.

In practice, even if the first scheme approximates very well the transport term (e.g., exactly), and the second scheme approximates very well the sink/source term, their combination can be a pure approximation of the transport with sinks and sources, especially if a large time step τ^n is used.

To reduce this disadvantage of fully explicit scheme (6.28), one can use the so called operator splitting approach.

6.2.4.2 Operator Splitting Method

There exists several possibilities how to reduce the decoupling error of explicit schemes. The most simple is the so called *operator splitting* approach (or fractional step method, see, e.g., [94]). Concretely, the fully explicit scheme (6.28), or its equivalent two step form (6.29) - (6.30), can be replaced by two sequential explicit steps

$$\left|\Omega_i\right| \theta_i^{n+1} \tilde{u}_i^{n+1} = \left|\Omega_i\right| \theta_i^n u_i^n - \tau^n \sum_j \left|\Gamma_{ij}\right| J_{ij}^n \qquad (6.31)$$

$$\left|\Omega_i\right| \theta_i^{n+1} u_i^{n+1} = \left|\Omega_i\right| \theta_i^n u_i^n - \tau^n \left|\Omega_i\right| (r_i^n u_i^n - q_i^n) \qquad (6.32)$$

$$u_i^n \equiv \tilde{u}_i^{n+1}$$

The two-step scheme (6.31) - (6.32) can be interpreted as follows - first, only the transport is solved for given initial conditions, and, afterwards, the solution is used as initial conditions for the second step, where only the sink/source is solved. Opposite to the splitting (6.29) - (6.30), the parameters r and q in the second step (6.32) are influenced by the results of the first step (6.31), i.e., the two step scheme (6.31) - (6.32) is coupled in one direction.

Of course, the order of these two steps can be exchanged in general. If the both obtained numerical solutions u^{n+1} are identical for both cases (i.e., the two operators “commute”), the operator splitting procedure exhibits no *time splitting error* [129]. Otherwise, if these two orders of operator splitting method bring different results, the discretisation scheme (6.31) - (6.32) has a *time splitting error* of the order $O(\tau^n)$, it means, the overall time discretisation scheme can be only of the first order approximation.

For example, if a mathematical model of the transport of several radionuclides is solved in the case of no retardation, the transport operator and the reaction operator commute and the operator splitting procedure works very well. On the other hand, if each radionuclide has different retardation factor, these two operators do not commute and the standard operator splitting method can result in a large numerical error. For the latter case, a new numerical method was developed in r^{3}t that exhibits no splitting error between the convective and reactive step in such case, see later.

Finally, the disadvantage of explicit discretisation schemes is that they require constraints on the choice of time step τ^n. This is, e.g., very famous Courant number restriction for explicit discretisations of convective transport, see, e.g., [94]. The reason for this can be easily understood by noting the fact that the discretisation schemes like (6.28) are *local* schemes. This means, they determine the value u_i^{n+1} only by using the immediate neighbours of u with respect to x_i evaluated at the time $t = t^n$. Such approximation of differential or integral equations is reasonable for enough small time steps, but for larger time steps the influence of non-immediate neighbours become more important. Consequently, the explicit discretisation schemes become instable, this means, they produce physically non-acceptable numerical solutions.

6.2.4.3 Implicit Discretisation Schemes

Again, for a reference, we present here the fully implicit version of the general discretisation scheme (6.20), i.e., $u_*^{n+1/2} \equiv u_*^{n+1}$ and one obtains

$$\begin{aligned} &|\Omega_i|\,\theta_i^{n+1}u_i^{n+1} + \tau^n \sum_j |\Gamma_{ij}|\,J_{ij}^{n+1} \\ &+ \tau^n |\Omega_i|\,r_i^{n+1}u_i^{n+1} - \tau^n |\Omega_i|\,q_i^{n+1} = |\Omega_i|\,\theta_i^n u_i^n \end{aligned} \quad . \qquad (6.33)$$

This scheme is, in fact, available in r^{3}t.

The main advantage of the implicit discretisation schemes like (6.33) is that all terms in the differential (or integral) equation remain *coupled*. In such a way, no time splitting error occurs, opposite to explicit discretisation schemes.

Consequently, the implicit discretisation schemes do not require constraints on the choice of time step τ^n due to stability reasons. This means that these schemes usually produce numerical solutions without non-physical oscillations, even if larger time steps are used. Of course, the implicit schemes are also local, i.e. only immediate neighbours of u_i^{n+1} are involved in local mass balance formulation (6.33), but, opposite to explicit discretisation schemes, this involves, if $\boldsymbol{J} \neq \boldsymbol{0}$, also immediate neighbours Ω_j of Ω_i at time $t = t^{n+1}$. In such a way, all unknown values u_i^{n+1} for $i = 1,2,\ldots,I$ are indirectly coupled and some non local approximations can be realised.

The very well-known example where the implicit discretisation schemes work very well, are the time dependent (parabolic) diffusion equations. On the other hand, for the case of convection-dominated transport, the implicit discretisation scheme should be used with enough small time steps to respect the local character of discretisation scheme, otherwise unrealistic results can be obtained, see Fig. 6.6 for an illustration.

The disadvantage of implicit schemes with respect to explicit schemes is that they contribute to the matrix of the algebraic system to be solved after the discretisation. Especially the discretisation of transport term contributes also to the off-diagonal terms in this matrix, and the solving of (linear or non-linear) system of equations is required.

The implicit schemes are only very rarely exact schemes, it means, they produce approximations of analytical solutions even for simple examples.

6.2.5 Special Numerical Algorithms

In this section, special numerical algorithms are described in more details that are implemented in r^{3}t additionally to the general discretisation scheme (6.20) or (6.33).

6.2.5.1 Explicit Exact Scheme for System of Decay Equations

If the general mathematical model (6.1) describes decay reactions only, one obtains the following system of ordinary differential equations (ODEs)

$$\begin{aligned} \partial_t(\theta^{(l)}u^{(l)}) + \lambda^{(l)}\theta^{(l)}u^{(l)} &= \sum_k \lambda^{(k)}\theta^{(k)}u^{(k)} \\ l &= 1,\ldots,L \end{aligned} \quad . \qquad (6.34)$$

In (6.34), the index k runs over all “mothers” of the l-th radionuclide, and $\lambda^{(k)}$ are constant reaction rates. The initial conditions are given analogous to (6.4), concretely,

$$u^{(l)}(t^0,x) = U^{(l),0}(x), \qquad x \in \Omega \cup \partial_0\Omega. \qquad (6.35)$$

One can apply the principle of superposition, described in Section 6.2.2.3, and replace the single system with L subsystems of simplified ODEs

$$\begin{aligned} \partial_t\left(\theta^{(l_1)}u^{(l_1)}\right) + \lambda^{(l_1)}\theta^{(l_1)}u^{(l_1)} &= 0 \\ u^{(l_1)}(t^0,x) &= U^{(l_1),0}(x) \end{aligned} \qquad (6.36)$$

$$\begin{aligned} \partial_t\left(\theta^{(l_k)}u^{(l_k)}\right) + \lambda^{(l_k)}\theta^{(l_k)}u^{(l_k)} &= \lambda^{(l_{k-1})}\theta^{(l_{k-1})}u^{(l_{k-1})} \\ u^{(l_k)}(t^0,x) = 0, \qquad k &= 2,\ldots,l_K \end{aligned} \qquad (6.37)$$

This means that instead of a single general decay chain with general initial conditions 6.35, one can solve several linear chains of radionuclides with nonzero initial conditions only for the component $u^{(l_1)}$. The index l_{k-1} denotes the index of the mother for l_k, and the index l_K denotes the last included component of the linear decay chain that starts with l_1.

The system 6.34 can be solved exactly, see, e.g., [9], [60]. This is realised in r^{3}t by implementation of exact solution for (6.36) - (6.37) for each vertex $x = x_i$, $i = 1,2,\ldots,I$. This exact solution can be then used for general mathematical model (6.1) using the operator splitting approach described in Section 6.2.4.2.

Concretely, the values $u^{(l_1),n}$ in r^{3}t, that are given by computations of previous time step (or, for $n = 0$, from the initial conditions (6.35)), are *replaced* by the exact solution $u^{(l_1),n+1} = u^{(l_1)}(t^{n+1})$ of (6.36) - (6.37). In such a way, the results of this exact solving procedure are used as initial conditions for the numerical solution of integral equations (6.5) without sinks/decays due to the decay, but with all other terms in the mathematical model.

If $\theta^{(l)} = \theta^{(l)}(u^{(1)},\ldots,u^{(L)})$, e.g. in the case of non-linear sorption in equilibrium, one has firstly to solve the simplified system of linear ordinary differential equations for $l_1 = 1,\ldots,L$ and for $i = 1,\ldots,I$

$$
\begin{aligned}
\partial_t c_i^{(l_1)} + \lambda^{(l_1)} c_i^{(l_1)} &= 0, \\
c_i^{(l_1)}(t^n) &= \theta_1^{(l_1)}(u_i^{(1),n},\ldots,u_i^{(L),n})\, u_i^{(l_1),n}, \\
\partial_t c_i^{(l_k)} + \lambda^{(l_k)} c_i^{(l_k)} &= \lambda^{(l_{k-1})} c_i^{(l_{k-1})}, \\
c_i^{(l_k)}(t^n) &= 0,
\end{aligned}
$$

and afterwards to solve the non-linear algebraic system for L unknowns $u^{(l),(n+1)}$

$$
\begin{aligned}
\theta_i^{(l)}(u^{(1),n+1},\ldots,u^{(L),n+1})\, u^{(l),n+1} &= c_i^{(l),n+1}, \\
l &= 1,\ldots,L
\end{aligned}
\qquad (6.38)
$$

Note that very often $\theta^{(l)} = \theta^{(l)}(u^{(l)})$, and then (6.38) represents L decoupled scalar non-linear equations. In r^{3}t, such equations are solved by standard Newton solver with analytical linearisation. In a general case, when (6.38) includes two or more coupled scalar equations, these are solved by an iterative solver, where only diagonal terms are linearised analytically.

6.2.5.2 Explicit Discretisation Scheme for 1D Convection Equation

In this and following section, it is dealt with the purely convective transport modelled by the linear partial differential equation

$$\theta(x)\,\partial_t u(t,x) \;+\; \nabla \cdot (\boldsymbol{v}(x)\,u(t,x)) \;=\; 0\,, \qquad (6.39)$$

with the initial conditions (6.4) and the (flux based) inflow boundary conditions

$$\boldsymbol{n}(\gamma) \cdot \boldsymbol{v}(\gamma)\,u(t,\gamma) \;=\; \boldsymbol{n}(\gamma) \cdot \boldsymbol{v}(\gamma)\,U_1(t,\gamma)$$

$$\gamma \in \partial_{in}\Omega := \{\gamma \in \partial\Omega,\ \boldsymbol{n}(\gamma) \cdot \boldsymbol{v}(\gamma) > 0\}, \qquad t \in (t^n, t^{n+1})\,.$$

Applying the fully explicit step (6.28), one obtains

$$|\Omega_i|\,\theta_i^{n+1}\,u_i^{n+1} \;=\; |\Omega_i|\,\theta_i^n\,u_i^n \;-\; \tau^n \sum_j |\Gamma_{ij}|\,\boldsymbol{n}_{ij} \cdot \boldsymbol{v}_{ij}\,u_{ij}^n\,, \qquad (6.40)$$

where the values u_{ij}^n are defined using only two values u_i^n and u_j^n, see later.

If one uses (6.22) for the definition of values u_{ij}^n in (6.40), one obtains an explicit, central difference discretisation method that is not suitable for purely convective transport, see, e.g., [94]. It can be shown that for one-dimensional (1D) problems (i.e., $\Omega \subset R$ with piecewise linear initial conditions, with piecewise constant $\theta(x)$ and with a constant velocity $v(x) = v$, the values u_{ij}^n in (6.40) can be redefined in such a way that for time steps τ^n smaller than some maximal time step τ_{CFL}^n, see later, (6.40) corresponds to the exact integration of integral equation (6.5).

This method is described in details. To do so, one writes the 1D case of (6.39) with $v \equiv const > 0$, because the case $v < 0$ can be treated analogously,

$$\theta(x)\,\partial_t u(t,x) \;+\; v\,\partial_x u(t,x) \;=\; 0$$

$$u(t^n,x) \;=\; u^n(x), \qquad x \in [0,H]\,.$$

The finite volume mesh consists of $I+1$ intervals $(x_{i-1/2},x_{i+1/2})$ for $i = 0,1,\ldots,I$, where we formally define $x_{-1/2} \equiv x_0$ and $x_{I+1/2} \equiv x_I$. The length of each interval is $h_i = x_{i+1/2} - x_{i-1/2}$ and the middle points x_i for $i = 1,2,\ldots,I$ are defined by $x_i := x_{i-1/2} + h_i/2$.

The initial function for $u(t^n,x)$ is considered in the form

$$u(t^n,x) = u_i^n + (u_{i+1/2}^n - u_i^n)\frac{2}{h_i}(x - x_i), \qquad x \in (x_{i-1/2},x_{i+1/2}] \tag{6.41}$$

This means that for two nodes x_i and $x_{i+1/2}$, one has $u(t^n,x_{i-1/2}) = u_i^n$ and $u(t^n,x_{i+1/2}) = u_{i+1/2}^n$, and otherwise one interpolates linearly for $x \in (x_{i-1/2},x_{i+1/2}]$. Furthermore,

$$\theta(x) \equiv \theta_i, \qquad x \in (x_{i-1/2},x_{i+1/2}]. \tag{6.42}$$

For such initial conditions (6.41) and the parameter θ from (6.42), one obtains that the integral equation (6.5), i.e.,

$$\theta_i \int_{x_{i-1/2}}^{x_{i+1/2}} u(t^{n+1},x)dx = \theta_i \int_{x_{i-1/2}}^{x_{i+1/2}} u(t^n,x)dx + \nu \int_{t^n}^{t^{n+1}} (u(t,x_{i-1/2}) - u(t,x_{i+1/2}))dt$$

is equivalent to

$$\theta_i \int_{x_{i-1/2}}^{x_{i+1/2}} u(t^{n+1},x)dx = \theta_i h_i u_i^n + \nu\tau^n(u_{i-1/2}^{n+1/2} - u_{i+1/2}^{n+1/2}), \tag{6.43}$$

where $u_{-1/2} = U_1(0,t^{n+1/2})$ and for $i = 0,1,\ldots,I$ one has

$$u_{i+1/2}^{n+1/2} := u_{i+1/2}^{n} + \frac{\tau^n}{\tau_i}(u_i^n - u_{i+1/2}^n). \qquad (6.44)$$

Here, τ_i is the *critical time step* for *i*-th finite volume $(x_{i-1/2},x_{i+1/2})$, i.e.,

$$\tau_i := \frac{h_i\theta_i}{v}, \qquad (6.45)$$

and the "global" time step τ^n must fulfil the CFL condition (Courant-Friedrichs-Lewy condition, see, e.g., [94])

$$\tau^n \le \tau_{\mathrm{CFL}} := \min\{\tau_i,\ i=0,1,\ldots,I\}. \qquad (6.46)$$

The notion "critical time step" for τ_i comes from the fact that the time step τ^n can be chosen at most equal to $\tau_i = \tau_{CFL}$, when the equation (6.43) turns to

$$\theta_i \int_{x_{i-1/2}}^{x_{i+1/2}} u(t^n + \tau_i,x)\,dx = v\tau_i u_{i-1}^n. \qquad (6.47)$$

This means that for $\tau^n = \tau_i$ one obtains that the mass in Ω_i at $t = t^n + \tau_i$ is completely determined by the concentration u_{i-1}^n from the neighbour Ω_{i-1} and the definition $u_{i+1/2}^{n+1/2}$ in (6.43) is no more valid for larger time steps.

If one uses the piecewise constant form of $u(t^n,x)$ given in (6.9) instead of piecewise linear form (6.35), i.e., $u_{i+1/2}^n \equiv u_i^n$, the scheme (6.43) is then equal to the well-known explicit upstreaming scheme

$$\theta_i \int_{x_{i-1/2}}^{x_{i+1/2}} u(t^{n+1},x)\,dx = \theta_i h_i u_i^n + v\tau^n(u_{i-1}^n - u_i^n). \qquad (6.48)$$

For the equations (6.48), the discrete minimum and maximum principle is fulfilled, if (6.46) is valid, i.e., no unphysical oscillations can occur in numerical solution [48], [51].

For a general form of $u(t^n,x)$, one has to determine a piecewise linear form (6.41). The values u_i^n are given in a standard way, e.g. by (6.12), and to compute $u_{i+1/2}^n$, one can determine them by defining a constant gradient in Ω_i using the values $u_{i-1/2}^n$, u_i^n and $u_{i+1/2}^n$. Particularly,

$$\partial_x u(t^n,x) \;=\; \frac{2}{h_i}(u_{i+1/2}^n - u_i^n) := \frac{u_{i+1}^n - u_{i-1}^n}{x_{i+1} - x_{i-1}}. \qquad (6.49)$$

In general, the computations of $u_{i+1/2}^n$ from (6.49) can lead to nonphysical oscillations. To obtain the discrete minimum and maximum property for (6.43) with (6.49), analogously to (6.48), one has to apply for some Ω_i the so called flux limiter that replaces the value $u_{i+1/2}^{n+1/2}$ in (6.43) by some limited value $\bar{u}_{i+1/2}^{n+1/2} \in [u_i^n, u_{i+1/2}^{n+1/2}]$, or $\bar{u}_{i+1/2}^{n+1/2} \in [u_{i+1/2}^{n+1/2}, u_i^n]$, see [51] for more details.

Finally, let us note that the values u_i^{n+1} are obtained from (6.43) analogously to (6.12), i.e., by computing the piecewise constant form of numerical solution $\hat{u}^{n+1}$ using

$$u_i^{n+1} \;=\; \frac{1}{\theta_i h_i}(\theta_i h_i u_i^n + v\tau^n(u_{i-1/2}^{n+1/2} - u_{i+1/2}^{n+1/2})).$$

6.2.5.3 Explicit Discretisation Scheme for 2D/3D Convective Transport

The explicit scheme (6.43) for 1D convective transport can be extended to several dimensional case (6.39) using the idea of Godunov method, see, e.g., [94]. This means that at each Γ_{ij}, see (6.21), an appropriate one-dimensional problem in the normal direction $\boldsymbol{n}_{ij}$ between Ω_i and Ω_j is solved.

At the end, one obtains

$$\begin{aligned} |\Omega_i|\,\theta_i u_i^{n+1} \;=\; & |\Omega_i|\,\theta_i^n u_i^n - \tau^n \sum_{j \in out(i)} v_{ij} u_{ij}^{n+1/2} \\ & + \tau^n \sum_{k \in out^{-1}(i)} v_{ki} u_{ki}^{n+1/2} \end{aligned} \qquad (6.50)$$

where

$$v_{ij} := \int_{\Gamma_{ij}} \boldsymbol{n}(\gamma) \cdot \boldsymbol{v}(\gamma)\, d\gamma \;\approx\; |\Gamma_{ij}|\, \boldsymbol{n}(\gamma_{ij}) \cdot \boldsymbol{v}(\gamma_{ij}). \qquad (6.51)$$

The set $out(i)$ contains the indices j of neighbours Ω_j for Ω_i such that $v_{ij} > 0$, i.e., all neighbours at outflow boundaries of Ω_i. Further, $k \in out^{-1}(i)$, when $i \in out(i)$, and, of course, $v_{ki} = -v_{ik}$.

The values $u_{ij}^{n+1/2}$ in (6.50) are defined by

$$u_{ij}^{n+1/2} := u_{ij}^n + \frac{\tau^n}{\tau_i}(u_i^n - u_{ij}^n), \qquad (6.52)$$

where the critical time step τ_i is defined by

$$\tau_i := \frac{|\Omega_i|\,\theta_i}{v_i}, \qquad (6.53)$$

and v_i denotes the total integrated outflow flux

$$v_i := \sum_{j \in out(i)} v_{ij}. \qquad (6.54)$$

The values u_{ij}^{n} are reconstructed from the piecewise constant form of $\hat{u}^{n}$, see [54], [51]. To obtain no unphysical oscillations, the new local limiter [51] is used that replaces the value $u_{ij}^{n+1/2}$ in (6.50) by a limited value $\bar{u}_{i+1/2}^{n+1/2} \in (u_i^n, u_{ij}^{n+1/2})$, or $\bar{u}_{i+1/2}^{n+1/2} \in (u_{ij}^{n+1/2}, u_i^n)$.

Again, the choice of time step τ^n is restricted by the CFL condition (6.46).

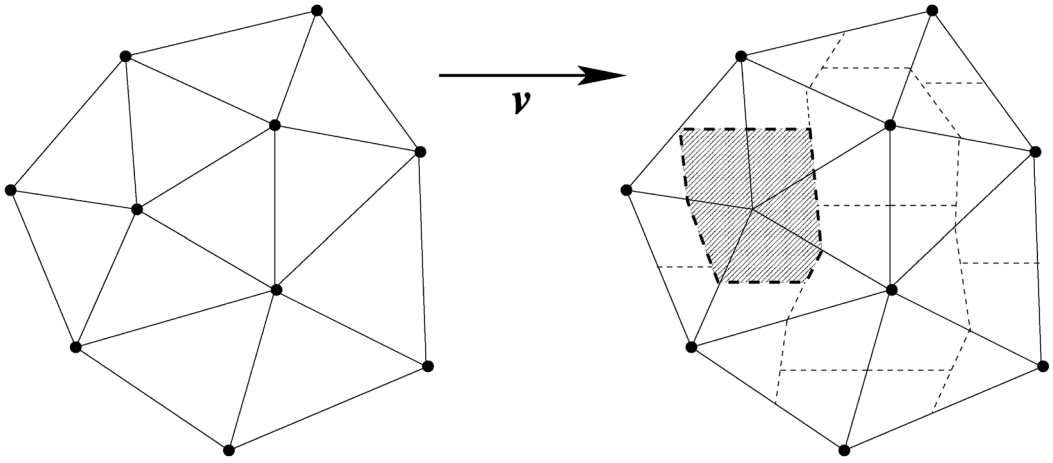

Fig. 6.10 Illustration of an aligned finite volume mesh for a constant velocity: primary finite element mesh (left) and dual aligned finite volume mesh (right).

The discrete scheme (6.50) approximates the convective transport described by a general velocity function $v \in R^d$ with several 1D transport problems with velocities v_{ij} in the normal directions n_{ij}. In general, the "real" direction of the transport, given by $\boldsymbol{v}$, can be very different to directions given by normal vectors, and the application of the scheme (6.50) can lead to unrealistic results known as "grid" effect. This is the case especially if coarse grids are used. This problem was resolved already in d^{3}f by using the so called "aligned" finite volumes, see [67], and Fig. 6.10 for an illustration, and the aligned finite volumes are used in r^{3}t, too.

6.2.5.4 Convective Transport for General Flow Equation

It can be proved, see, e.g., [48], [51], that numerical solutions obtained from the discretisation scheme (6.50), fulfil the discrete minimum and maximum principle (i.e., they exhibit no unphysical oscillations), when

$$\sum_{j \in out(i)} v_{ij} = \sum_{k \in out^{-1}(i)} v_{ki}. \qquad (6.55)$$

The equality (6.55) represents in a discrete form the analytical property

$$\nabla \cdot \boldsymbol{v}(x) = 0, \qquad x \in \Omega_i.$$

If the groundwater velocity $\boldsymbol{v}$ is given from a variable density flow, like in d^{3}f, the flow and the convective transport are described by

$$\begin{aligned} \phi \partial_t \rho + \nabla \cdot (\rho \boldsymbol{v}) &= 0 \\ \phi \partial_t (\rho u) + \nabla \cdot (\rho u \boldsymbol{v}) &= 0 \end{aligned} \qquad x \in \Omega, \quad t \geq t^0, \qquad (6.56)$$

where ϕ is the porosity of the medium. The groundwater velocity $\boldsymbol{v}$ is in this case time and space dependent, i.e., $\boldsymbol{v} = \boldsymbol{v}(t,x)$.

After simple algebraic manipulations, one obtains an equivalent “non-divergent” form of the transport equation in (6.56), namely,

$$\phi \partial_t u + \boldsymbol{v} \cdot \nabla u = 0. \qquad (6.57)$$

Note that the convective transport equation (6.57) does not represent any more a mass balance formulation for u, the mass is conserved only for values ρu in (6.56).

The transport equation (6.57) in the non-divergent form can be viewed as a “value preserving” formulation, opposite to the “mass preserving” formulation (6.56). Clearly, one obtains from (6.57) that u is constant along the characteristics, i.e., $u(t^0,x_0) = u(t,X(t))$ for $t \geq t^0$, see, e.g., [50], where

$$X(t) = X(t;t^0,x_0) = x_0 + \int_{t^0}^{t} \boldsymbol{v}(s,X(s))\,d\boldsymbol{s}.$$

As it was shown in [56], the finite volume discretisation can be applied also to (6.57). One obtains the discretisation scheme identical to (6.50) with the only difference that v_i is given as the total integrated *inflow* flux, i.e.,

$$v_i := \sum_{k \in out^{-1}(i)} v_{ki}. \qquad (6.58)$$

Clearly, if (6.55) is fulfilled, the both definitions for v_i, i.e., (6.58) and (6.54), are identical. If this is not the case, the form (6.54) prescribes the “mass preserving” form of the discretisation scheme (6.50), and (6.58) prescribes the “value preserving” form of (6.50).

In general, the velocity field $\boldsymbol{v}$ obtained from d^{3}f fulfils the equation (6.56), consequently, the transport in r^{3}t is computed by default using the definition (6.58). Note that in the numerical approximation of v_{ij} in (6.51), the time dependence of $\boldsymbol{v}$ is resolved by fixing the time variable t at the single time point for which is the velocity from d^{3}f in r^{3}t available.

6.2.5.5 Convective Transport with Non-Linear Retardation

For the case of non-linear sorption in r^{3}t, one obtains a non-linear transport equation with the parameter θ depending on the solution u, i.e.,

$$\partial_t(\theta(u)u) + \nabla \cdot (\boldsymbol{v}u) = 0. \qquad (6.59)$$

The idea of Godunov method can be used also here. In this case, one can show that for piecewise constant $\hat{u}^n$ from (6.9), the following first order scheme is an exact integration of integral equations (6.5) in 1D case for enough small time step τ^n,

$$\begin{aligned} |\Omega_i|\,\theta_i(u_i^{n+1})u_i^{n+1} &= |\Omega_i|\,\theta_i^n(u_i^n)u_i^n \\ &\quad + \tau^n \sum_{k \in out^{-1}(i)} v_{ki}(u_k^n - u_i^n). \end{aligned} \qquad (6.60)$$

In fact, this scheme is identical (at least, formally) to the previous discretisation scheme (6.50), if $u_{ij}^n \equiv u_i^n$, i.e., if the first order scheme is used also in (6.50).

The very important difference is in the definition of the total inflow flux v_i, that is given now, instead of (6.58), by

$$v_i := \theta_i(u_i^n) \sum_{k \in out^{-1}(i)} \frac{u_k^n - u_i^n}{\theta_i(u_k^n) u_k^n - \theta_i(u_i^n) u_i^n} v_{ki}. \qquad (6.61)$$

Consequently, the critical time step $\tau_i = \tau_i^n$ must be defined by using (6.61) in (6.45), and, analogously, the CFL restriction (6.46) on the choice of time step τ^n must be given by a minimal value of τ_i^n for $i = 1,\ldots,I$. Note that if θ does not depend on u, then (6.61) is identical to (6.58).

The correct computation of the CFL restriction for the time step τ^n in the case of non-linear retardation was implemented in r^{3}t. Note that, although the scheme (6.60) is only the first order approximation, due to the “self sharpening” effect of non-linear convection equations, this scheme approximates well the analytical model (6.59). For instance, if one computes with the time step $\tau^n \approx \tau_{CFL}^n$, the sharp fronts are well resolved. Moreover, the Godunov method is not known to us, if the piecewise linear form of $\hat{u}^n$ is used.

In [76], exact 1D solution of (6.59) for the case of Freundlich and Langmuir isotherms were described. These solutions were tested with r^{3}t and satisfactory results were obtained, see Fig. 6.8.

6.2.5.6 Explicit Discretisation for System of Convection-Decay Equations

The system of equations for the convective transport with decay reactions takes the form

$$\begin{aligned} &\partial_t(\theta^{(l)} u^{(l)}) + \nabla \cdot (\boldsymbol{v} u^{(l)}) + \lambda^{(l)} \theta^{(l)} u^{(l)} \\ &\quad = \lambda^{(l-1)} \theta^{(l-1)} u^{(l-1)} \end{aligned} \qquad (6.62)$$

In general, one can use the exact scheme (6.50) for the decay part of (6.62) and the explicit discretisation scheme (6.50) for the transport part. If the parameters $\theta^{(l)}$ for each component are not very different, i.e., $\theta^{(l)} \approx \theta$ for $l = 1,\ldots,L$, then the operator splitting approach, described in Section 6.2.4.2, has only small time splitting error, and it can be successfully used for (6.62).

On the other hand, in general, e.g., if the retardation factors are different, the convective and the reaction operator do not commute, and one obtains very different results, if the first step in the two-step operator splitting method is the convective step or the reaction step. In both cases, the standard operator splitting method can have a large time splitting error.

In r^{3}t, a novelty algorithm for the computations of (6.62) was developed and implemented [60], [55]. The idea is based, again, on Godunov method.

Concretely, for each Ω_i and $j \in out(i)$, the following system of 1D convection-reaction equations for $l = 1,\ldots,L$

$$\theta_i^{(l)} \partial_t u_i^{(l)} + v_{ij} \partial_x u_i^{(l)} + \lambda^{(l)} \theta_i^{(l)} u_i^{(l)} = \lambda^{(l-1)} \theta_i^{(l-1)} u_i^{(l-1)} \qquad (6.63)$$

is solved exactly [60]. In (6.63), the space variable x is considered for $x \in (0,\infty)$, and the velocity $v_{ij} > 0$ is given by (6.51). Using the principle of superposition, it is enough to consider the basic initial conditions of the form

$$\begin{aligned} u^{(1)}(t^n,x) &= u_i^{(1),n} + \frac{2}{L}(u_{ij}^{(1),n} - u_i^{(1),n})\left(x - \frac{L}{2}\right), \quad x \in (0,L] \\ u^{(1)}(t^n,x) &= 0, \qquad\qquad x \in (L,\infty) \\ u^{(l)}(t^n,x) &= 0, \qquad\qquad x \in (0,\infty),\ l = 2,\ldots,L \end{aligned} \quad ,$$

with $L = |\Omega_i|$.

This system can be integrated exactly and the result of the integration for two cells $\Omega_i := (0,L)$ and $\Omega_j := (L,\tilde{L})$, $L \ll \tilde{L}$, can be written as follows [55], [60],

$$|\Omega_i|\,\theta_i^{(l)}\,u_i^{(l),n+1} = |\Omega_i|\,\theta_i^{(l)}\,u_i^{(l),n} - \tau^n v_{ij} u_{ij}^{(l),n+1/2}$$

$$|\Omega_j|\,\theta_j^{(l)}\,u_j^{(l),n+1} = \tau^n v_{ij} u_{ij}^{(l),n+1/2}$$

The definitions of values $u_{ij}^{(l),n+1/2}$ can be found in [61]. Using these definitions of

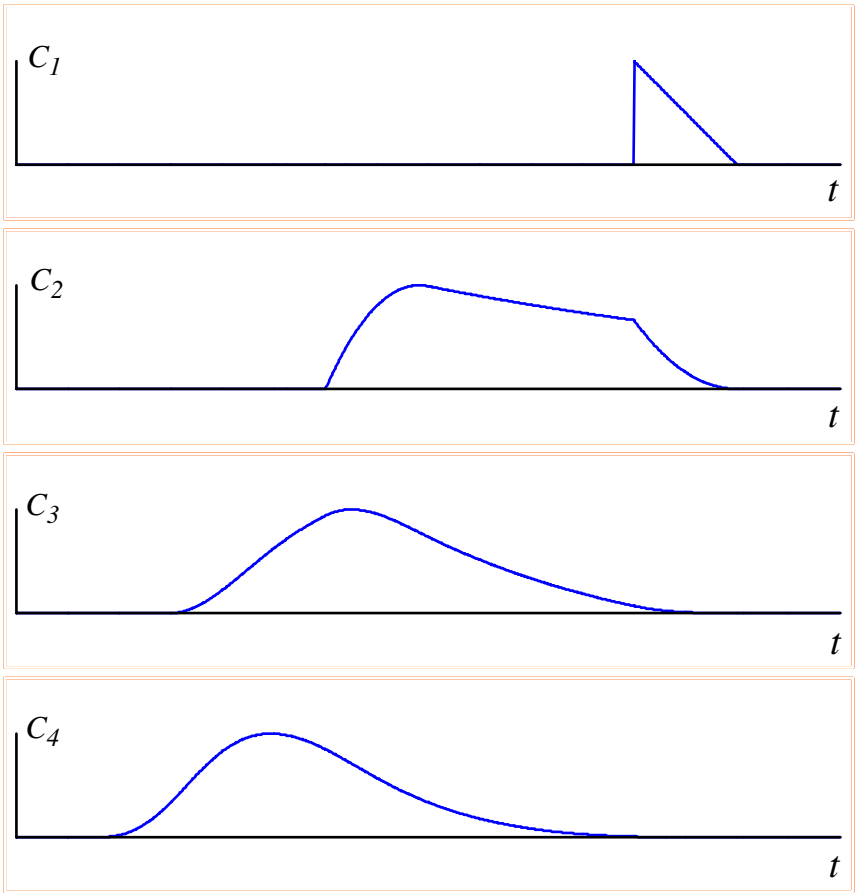

Fig. 6.11 Four components of the numerical solution for *t*=6 with the retardation factors R_1=1 (top), R_2=2, R_3=4 and R_4=8 (bottom). The velocity is $v \equiv 1$ and the domain is $(0,8) \subset R$.

$u_{ij}^{(l),n+1/2}$ in (6.50), one obtains the discretisation scheme for 2D/3D case. Note that if no decay reaction is presented, the values $u_{ij}^{(l),n+1/2}$ are identical to ones given by (6.52).

This method on a simple 1D example with 4 components is illustrated, where $\theta^{(l)} = R_l \phi$ and the retardation factors have the values $R_1 = 1$, $R_2 = 2$, $R_3 = 4$ and $R_4 = 8$. The numerical solution at the last computation time $t = 6$ is presented in Fig. 6.11 and it can not be distinguished from the exact solution. The computations were realised with $\tau^n = \tau^n_{CFL}/2$, i.e., with the Courant number 0.5, the domain Ω is the interval $(0,8) \subset R$.

In the Tab. 6.1, one compares the absolute error E_1 for the standard operator splitting approach (the second column) and the equivalently defined error E_2 for the new algorithm (the fourth column). The results are presented for several uniformly refined grids and the numerical convergence rates are presented for the operator splitting algorithm (the third column) and the new algorithm (the fifth column). As expected, for the operator splitting method, the convergence rate is approximately 1, i.e., the absolute error is halved for one grid refinement, and the convergence rate for the new algorithm is approximately 2, i.e., the absolute error is 4 times smaller after one grid refinement.

Tab. 6.1 The absolute errors E_1 (operator splitting method) and E_2 (the new algorithm) for the 4th component of the numerical solution. The third and fifth column contain the corresponding convergence rates.

h	$E_1 \cdot 10^{-4}$	α_1	$E_2 \cdot 10^{-4}$	α_2
1/16	413.2		23.76	
1/32	201.3	1.04	5.573	2.09
1/64	99.25	1.02	1.374	2.02
1/128	49,25	1.01	0.344	1.99

6.2.5.7 Flux-Based Method of Characteristics

All explicit discretisation schemes for convective transport equations, presented so far, have the CFL restriction on the choice of time step. This restriction is very well supported also by “physical” arguments, nevertheless, this means in practice that for each grid refinement also the time step must be decreased. Consequently, for very fine grids this can be computationally impracticable.

If the time step τ^n is chosen such that $\tau^n = \tau_i$, i.e., $t^{n+1} = t^n + \tau_i$, the *i*-th discrete equation (6.50) takes the form

$$|\Omega_i| \, \theta_i u_i^{n+1} = \tau_i \sum_{k \in out^{-1}(i)} v_{ki} u_k^n .$$

Using (6.58), one obtains

$$\begin{aligned} |\Omega_i| \, \theta_i u_i^{n+1} &= |\Omega_i| \, \theta_i \sum_{k \in out^{-1}(i)} \frac{v_{ki}}{v_i} u_k^n \\ \Rightarrow u_i^{n+1} &= \sum_{k \in out^{-1}(i)} \frac{v_{ki}}{v_i} u_k^n \end{aligned} \quad . \qquad (6.64)$$

This means that, roughly speaking, at the time point $t = t^n + \tau_i$ the new concentration in Ω_i is equal to u_i^{n+1} given by the last equality in (6.64).

Consequently, for a “little” bit larger time step τ^n such that $\tau^n > \tau_i$, but $\tau^n \leq \tau_j^n$ for $j = 1,\ldots,I$ and $j \neq i$, one can still easily derive a correct form of the discretisation, although the CFL restriction is no more valid. In fact, the only discrete equations to be changed are those for $j \in out(i)$ where the function u for the flux at Γ_{ij} shall be approximated in two steps - firstly, for $t \in (t^n, t^n + \tau_i)$ by $u \approx u_i^n$, and, secondly, for $t \in (t^n + \tau_i, t^n + \tau^n)$ by the last right hand side of (6.64), see [56], [50], [51] for details.

Following such approach, one can extend the explicit discretisation scheme for the convective transport equations coupled through decay reactions with no CFL restriction, at least theoretically, see [51]. It is important to note that such extension is based on the first order scheme, analogous to (6.60).

The decay reactions are solved using the operator splitting approach. If it would be realised in a standard form, the time splitting error can be large, if large time steps are used. This was illustrated in Fig. 6.7, where the convection-decay equations of two components was computed for the case of large retardation for the second component.

In r^{3}t, a novelty operator splitting approach was used that reduces the time splitting error to the order of the maximal critical time step τ_i, opposite to the standard operator splitting method, where the time splitting error is of order of τ^n. See Fig. 6.12 for significantly improved results concerning the same example as presented in Fig. 6.7, see also [51] for more details.

Due to a large complexity, the flux-based method of characteristics is available for parallel computers only for time steps τ^n restricted by the CFL condition (6.46).

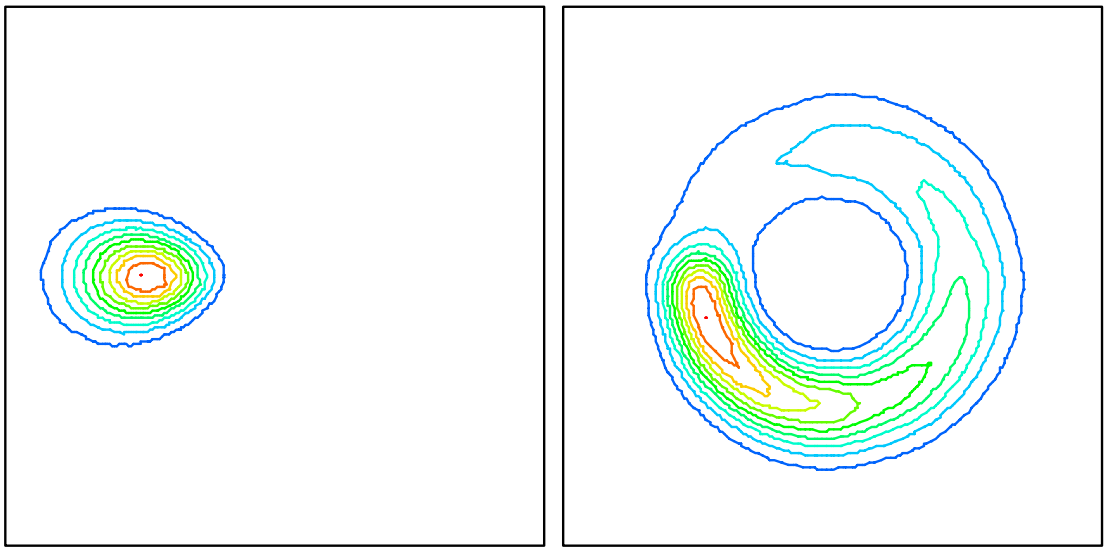

Fig. 6.12 Flux-based method of characteristics
Numerical solution of analogous example to Fig. 6.7 computed here with the flux-based method of characteristics. The solution was obtained with 12 large time steps, but the time splitting error is for the second component significantly smaller than in Fig. 6.7.

6.2.6 Time Discretisation Errors

In this and next section, in more details the two most important numerical errors are discussed - the time discretisation error and the space discretisation error, and how they can be controlled by the user of r^{3}t to obtain satisfactory numerical results.

Considering the integral equations (6.5), one has to compute (or, in fact, approximate) the time integration of the transport term (represented by $\boldsymbol{J}$) and of the source/sink term (represented by $ru - q$), see (6.5). In fact, the flux based boundary conditions (6.3) must be integrated analogously to the sink/source terms, see Section 6.2.3.4, so they can be treated identically.

As this time integration can not be realised exactly, one has to apply numerical integration and the numerical solution $\hat{u}^{n+1}$ from (6.9) differs from the exact solution of (6.5), among others, due to the time discretisation error.

In r^{3}t, several algorithms to reduce time discretisation error and to enable relatively large time steps were developed.

First of all, if possible, an exact integration in time is used. This is the case for all time dependent source terms that are explicitly described in the configurable file `source-term`, [52].

Furthermore, the system of ordinary differential equations for decay reactions can be solved exactly, see Section 6.2.5.1.

In all other cases, one can use the first or second order time integration (discretisation) method. The first order discretisation method means, roughly speaking, that starting from some $\tau < \tau^1$ by halving the time step τ, one can expect almost halving of the numerical error. Unfortunately, the value τ^1 is unknown and given only theoretically, and in practice, i.e., if $\tau > \tau^1$, the halving of time steps can result in much slower reduction of the numerical error. The first order time discretisation error is usually denoted by $O(\tau)$, and the error depends not only on τ, but also on some (unknown) “leading term” constant, say C.

Analogously, the second order schemes should asymptotically exhibit four times smaller numerical error after halving a time step. Such behaviour of numerical solution can be expected only for enough smooth analytical solutions and enough small time steps, and the error is denoted by $O(\tau^2)$.

In r^{3}t, two universal discretisation schemes are available, the fully implicit, first order, backward Euler scheme (6.33), and the explicit-implicit, second order, Crank-Nicholson scheme (6.20).

The first one is unconditionally stable for arbitrary time steps, it has no time splitting (uncoupling) error, but it is a first order scheme.

The second can be viewed as a two-step operator splitting method and it has all disadvantages (and advantages) of explicit discretisations schemes.

It is important to note that in practice it is enough to apply a second order discretisation only to the single term in integral equation (6.5) that would otherwise results in the largest error, if the first order scheme is used. This means that all other terms can be discretised using a first order scheme, because the overall time discretisation error is still dominated by the discretisation error $O(\tau^2)$ of the single term in (6.5).

For instance, see the description in next section, it is enough to use the second order scheme (6.50) for the system of convection-decay equations and to couple it with the first order fully implicit discretisation (6.33) for the diffusion, especially for much coarser computational grids. Of course, for the second order time discretisation scheme, the numerical error is reduced much faster than for the first order schemes, and, at some time refinement level, the numerical errors caused by the latter will start to dominate.

Several useful indicators are available in r^{3}t, that can help users to decide about the influence of time discretisation error on numerical solution. In Section 6.2.8, it is summarised how these information can help the users of r^{3}t in the choice and control of numerical algorithms. A general idea is that all the following time errors indicator should be smaller than 1, if possible, see discussions later.

6.2.6.1 Courant Number

Typical applications of r^{3}t are the *convection dominated* problems, so the most important indicator of time discretisation error is the *Courant number* Co that is in an abstract form defined by

$$Co := \frac{V \Delta T}{\Delta L}. \qquad (6.65)$$

In (6.65), the parameters are “representative” velocity V, the time length ΔT and the space length ΔL. In such a way, the condition $Co < 1$ means that a point moving with the velocity V does not travel more than ΔL during the time length ΔT.

In r^{3}t, the grid Courant number $Co_i^{(l),n}$ is used that is defined as an *exact* analogous to (6.65) for the discretisation scheme (6.50).

To define it, one has to introduce the critical time step $\tau_i^{(l),n}$ first, that is given by (6.45) or (6.53), or, in general, for system of l equations by

$$\tau_i^{(l),n} := \frac{|\Omega_i| \, \theta_i^{(l),n}}{v_i} \qquad (6.66)$$

where v_i is the total (integrated) inflow flux, see (6.58).

One can again see in (6.66) a “physical” interpretation of the local critical time step $\tau_i^{(l),n}$ - it denotes the time length in which the volume Ω_i will be completely filled through the inflow boundary of $\partial\Omega_i$ by the groundwater flowing into Ω_i with the given (retarded) velocity.

Having the definition of local critical time steps $\tau_i^{(l),n}$, one can easily introduce the grid Courant number $Co_i^{(l),n}$ as the ratio of actual time step and the critical time step, i.e.,

$$Co_i^{(l),n} := \frac{\tau^n}{\tau_i^{(l),n}}.$$

The grid Courant number $Co_i^{(l),n}$ is a very important indicator for the explicit discretisation scheme of convective transport. For instance, the explicit first order scheme (6.50) for one component, i.e., $L = 1$, can be written as

$$|\Omega_i| \, \theta_i u_i^{n+1} = |\Omega_i| \, \theta_i u_i^n (1 - Co_i^n) + \tau^n \sum_{k \in out^{-1}(i)} v_{ki} u_k^n.$$

The standard theory for the discrete minimum and maximum principle, see [66], [48], [51], requires that the coefficient before u_i^{n+1} is positive and the coefficients before u_i^n and u_k^n are non-negative. Clearly, this can be fulfilled only if the grid Courant number Co_i^n is not greater than 1.

In such a way, the maximal grid Courant number

$$Co_I^{L,n} := \max\left\{ Co_i^{(l),n},\ i = 1,\ldots,I,\ l = 1,\ldots,L \right\} \qquad (6.67)$$

is the most important indicator that is printed during the computations in r^{3}t, see [52].

An automatic time control is implemented in r^{3}t that suggests a new time step according to the user definition of the smallest and largest $Co_I^{L,n}$, see [52].

The discussion of how large time steps can be taken with which discretisation schemes to use, will follow later. Nevertheless, one can say already here that if time steps are not too much restricted by the CFL condition (6.67), one shall prefer computations for *all* numerical algorithms in r^{3}t using the automatic time control to have $Co_I^{L,n} \approx < 1$.

6.2.6.2 Neumann Number

The restriction on the choice of time step due to the explicit discretisation of diffusion-dispersion term can be expressed by the so called Neumann number. An abstract definition is given by

$$Ne := \frac{D\Delta T}{(\Delta L)^2}, \qquad (6.68)$$

where the parameters are “representative” diffusion D, time length ΔT and the space length ΔL.

The grid Neumann number for (6.26) can be derived analogously to the definition of grid Courant number in Section 6.2.6.1. It means, by requiring the positivity of coefficients in (6.26) before u_i^n, one can obtain the corresponding definition of $Ne_i^{(l),n}$, that is not presented here due to its complex form. Nevertheless, the maximal grid Neumann number, analogous to (6.67), can be printed during computations in r^{3}t.

Opposite to the case with the Courant number, the maximal grid Neumann number $Ne_I^{(L),n}$ is not very suitable indicator for an estimation of time discretisation error, if a fully implicit discretisation scheme (6.27) is used for the diffusion-dispersion term. Roughly speaking, the restriction $Ne_I^{(L),n} \leq 1$ can be too pessimistic. Nevertheless, $Ne_I^{(L),n}$ is introduced here for completeness and because of the definition of the so called Peclet number later.

6.2.6.3 Reaction Number

Finally, one can derive the restriction on the choice of time step due to the time integration of the (total, effective) sink term in (6.1). This is very simple and straightforward, one can define $R_i^{(l),n}$ by

$$R_i^{(l),n} := \frac{\tau^n r^{(l),n}}{\theta^{(l),n}}, \qquad (6.69)$$

and the maximal grid “Reaction” number $R_I^{(L),n}$, defined analogously to (6.67), must be smaller or equal to 1. For instance, if $r \equiv \theta^{(l)} \lambda^{(l)}$, one obtains the well-known restriction for the half-times of the decay.

Of course, if decay equations in general mathematical model (6.1) are solved exactly using the methods from Section 6.2.5.1 or 6.2.5.6, there is no time restriction due to sinks given by decay. It is required only by kinetic reactions of sorption and/or immobilisation, if presented.

6.2.7 Space Discretisation Errors

The most important tool to reduce space discretisation error is the grid refinement in space. Of course, every grid refinement makes the algebraic system much larger and the solving procedure more costly.

The first reason for a grid refinement is to reduce the interpolation error. This can be clearly explained already on the treatment of initial conditions. If the analytical initial conditions are given by some function $U^0 = U^0(x)$, for $x \in \Omega$, the initial conditions for some particular mesh of I number of finite volumes Ω_i are given by a piecewise constant interpolation (6.12). Clearly, if such interpolation is not a good approximation of the exact initial function U^0, one introduces a large discretisation error at the very beginning of numerical simulations.

In general, one can easier approximate (interpolate) smooth functions $U^0(x)$ than functions with discontinuous data. From this point of view, it is much preferable to use such initial function $U^0(x)$ that is, at least, continuous, and it has well defined first derivative almost everywhere in Ω. In an ideal case, if $U^0(x)$ is a piecewise constant function with respect to finite volume mesh, then no interpolation error is introduced.

On the other hand, if initial data with jumps are used, these require very fine (local) grid refinement.

Analogous arguments about interpolation error can be used for other data in the mathematical model. For instance, if the velocity $\boldsymbol{v}(x)$ is given from d^{3}f, it is defined as a piecewise linear function with respect to the finite element mesh. If a different grid is used in r^{3}t, a piecewise constant interpolation of $\boldsymbol{v}$ can be used on the grid used in r^{3}t, see section 6.2.1.1.

The second most important reason to refine computational grids is to improve the approximation of solution gradient, and, consequently, the approximation of convection, diffusion and dispersion. This is a standard topic and it will not be discussed here, see also section 6.2.11 on “The Error Estimator”.

A very important reason for the grid refinement is due to the relation between convection and diffusion. For the fully implicit discretisation schemes, the second order discretisation scheme (the central difference scheme) is the preferable method if diffusion dominates the convection locally. This can be monitored at the grid level by the maximal grid Peclet number.

6.2.7.1 Peclet Number

In an abstract form, the Peclet number is defined by

$$Pe := \frac{V \Delta L}{D}, \qquad (6.70)$$

where the parameters are a representative velocity V, length ΔL and diffusion D. If the Peclet number is much larger than 1, one denotes the corresponding convection-diffusion equation to be convection dominated.

The grid Peclet number can be defined very conveniently (although a little bit formally) as the ratio between the grid Courant and Neumann number

$$Pe_i^n := \frac{Co_i^n}{Ne_i^n}. \qquad (6.71)$$

Note that although the Courant and Neumann number depend on τ^n (and, in general, on l), the grid Peclet number depends only on local discretisation of the velocity and of the diffusion-dispersion parameter. The concrete form of (6.71) is analogous to (6.70), if ΔL in (6.71) is replaced by some representative discretisation step h.

For the fully implicit general discretisation scheme (6.27), one can show that if the maximal grid Peclet number Pe_I^n, defined analogously to (6.67), is smaller than 1, no unphysical oscillations should occur in numerical solutions if the central difference method is used, and larger time steps, e.g., with the Courant number larger than 1, can be used with reasonable results in numerical simulations.

6.2.8 Conclusions Concerning the Discretisation Methods

6.2.8.1 Input Parameters of the Mathematical Model

Several discretisation methods that are available in r^{3}t are designed to be of the second order in space and time. The second order discretisation schemes are appropriate if a priori knowledge about the analytical solution $u = u(t,x)$ is available concerning its smoothness. This means, roughly speaking, that such methods can work very well, if $u(t,x)$ is a continuous function for $t \geq 0$ and $x \in \overline{\Omega}$, and the partial derivatives exist for almost all $t > 0$ and $x \in \Omega$.

In fact, these (unknown) properties can be influenced by the user of r^{3}t by an appropriate form of input parameters. Particularly, one can prefer initial conditions, if possible, with smooth function $U^0(x)$ for $x \in \overline{\Omega}$, the explicit source terms given by smooth functions $q = q(t,x)$ and so on.

Nevertheless, the discretisation methods implemented in r^{3}t are robust to treat general examples with reasonable physical input data.

6.2.8.2 Computational Grids

The methods used in r^{3}t are proposed in such a way that they can produce a reasonable (or physically acceptable) approximation of the exact solution even on coarse computational grids.

This means that the user of r^{3}t can start his/her computations on some (finite element) grid with as less elements as possible. Such grid is determined by the possibilities of a grid generator to resolve the computational domain with less finite elements of “good geometrical” properties.

Furthermore, the initial computational grid shall resolve reasonably the initial data. This means, for instance, that the interpolation $\hat{u}^0(x)$ of exact initial data $U^0(x)$ by (6.12) on a given initial computational grid (i.e., the grid level 0, see [52]) must be roughly appropriate. Analogously, the approximation of explicit source terms $q = q(t,x)$ must be reasonable.

In practice, for instance, if the shape of $U^0(x)$ or $q(0,x)$ is a circle in 2D, one should use an initial computational grid that covers this circle with at least few elements. Otherwise, for instance, if such circle lies inside of a single element, it needs not to be recognised by the discretisation on the initial computational grid.

If the convective transport is given by the velocity data from d^{3}f, the accompanying grid data from d^{3}f are the most suitable initially also for r^{3}t.

The important point is that computations on the initial computational grid *need not* to produce numerical solution that approximates the analytical solution very precisely.

Using enough coarse initial computational grid, one has the possibility to refine this grid several times, and, in such a way, one can decide about the numerical *grid convergence* for the particular example. This means, roughly speaking, that if one compares the numerical solutions of the same example on sequently refined grids and at same time points, the differences must be smaller with finer grids and finer time steps.

In general, on coarser grids one can expect larger “numerical” (un-physical) diffusion and larger interpolation error for finer structures of the analytical solution. With finer grids, the numerical diffusion must diminish, i.e. the diffusive spreading shall be slower, and finer structures (e.g., shapes of contour lines) can be visible in numerical solutions.

6.2.8.3 Numerical Methods

From previous considerations, one can suggest the following choice of appropriate numerical methods in r^{3}t. Note that in general, *all* numerical methods implemented in r^{3}t are convergent, and so, asymptotically (i.e., for enough small time and space discretisation steps), all methods must converge to the same analytical solution. Of course, one wants to prefer the methods that converge faster.

In general, the following rules are applicable.

If the problem (example) is convection dominant, the automatic choice of time steps available in r^{3}t shall be used to hold the maximal grid Courant number Co_I in (6.67) within some prescribed interval.

If smaller time steps with the grid Courant numbers bellow 1 are possible, e.g., within the interval $(COURANT\_MIN, COURANT\_MAX) = (0.5, 1.)$, see [52], one shall prefer the explicit discretisation scheme for the convection and decay, e.g. `MOC=1`, see [52]. This scheme is very precise for reaction equations, it offers the second order approximation for the convection, and the time splitting error with respect to diffusion-dispersion (and, for instance, with respect to kinetic sorption) from the operator splitting approach is acceptable. Consequently, this means that for the initial computational grid (i.e., the grid level 0) one shall start with `MOC=1`.

With further grid refinements, the fixed maximal grid Courant number means that with each grid refinement one has to use smaller time steps. In practice, one grid refinement can mean one halving of the time step. Consequently, for very fine grids, especially, if high local adaptive refinement is used, the time steps become too small and impracticable.

If a grid convergent numerical solution was not achieved with previous approach, and the CFL restriction is impracticable for further computations, one can switch to fully implicit central difference scheme. If the maximal grid Peclet number is smaller than (or approximately around) 1, this is clearly the best choice for numerical methods, if one wish to use large time steps.

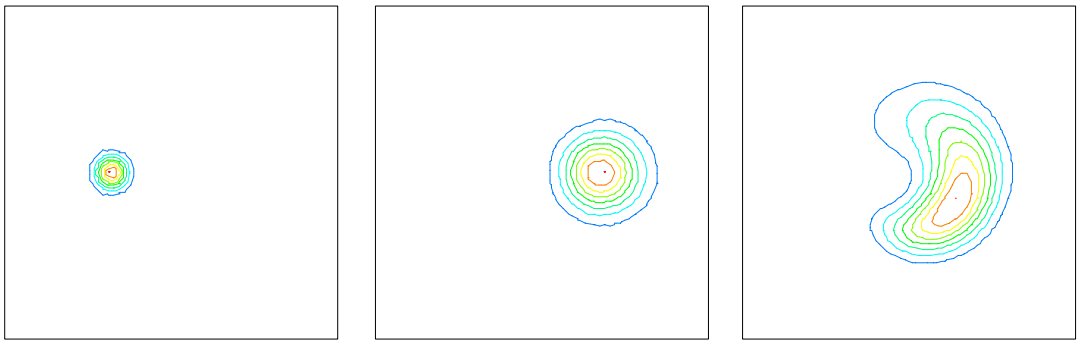

Fig. 6.13 Initial function (l), solutions with `MOC=1` (m) with `MOC=0` (r) after half period, the numerical solutions at the same time point. Due to large Courant and Peclet numbers, the numerical solution with `MOC=0` is corrupted due to artificial longitudinal dispersion.

Nevertheless, as it is illustrated with the next example, one should be aware that the fully implicit central difference scheme with the maximal grid Peclet number larger than 1 can introduce a non-physical, numerical longitudinal dispersion, if one uses time steps with maximal grid Courant number than 1.

The Fig. 6.13 shows again the example of rotated impulse with relatively small (molecular) diffusion where the exact solution is known, see, e.g., [50]. The left picture shows the initial conditions, the middle picture the results of the explicit scheme `MOC=1` after half rotation, and the analogous results with `MOC=0` in the right picture. Note that the contour lines (i.e., their colours) in each picture do not correspond each other. The spreading of the initial circle in the middle picture is due to the physical diffusion.

The absolute error for the numerical solution with `MOC=1` is $2.12 \cdot 10^{-3}$ in L_1 discrete norm and for the fully implicit scheme `MOC=0` it is $1.18 \cdot 10^{-2}$. The both numerical solutions were computed with the maximal grid Courant number equals approximately 20, and the maximal grid Peclet number was approximately 7. Clearly, the numerical solution for the fully implicit scheme is corrupted by some artificial longitudinal dispersion, see also Fig. 6.6. Note that no upwinding algorithms were applied in the fully implicit scheme.

Nevertheless, if the computational grid is further refined, and, consequently, the maximal grid Peclet number is smaller than 1, the fully implicit central difference method can be applied for this example even with the grid Courant numbers significantly larger than 1.

6.2.9 Tutorial

In this last section, a typical application of r^{3}t for complex applications is described. To preserve a simplicity of the explanation, we present only a 2D example and results only for one component. For other examples, see [52], [44].

The domain is presented in Figure Fig. 6.14, together with the coarse grid level $l = 0$.

The velocity field is plotted in Fig. 6.15, concretely, a zoom to the middle part of the domain. This velocity data were saved from d^{3}f in the grid independent data format after computing some stationary groundwater flow problem.

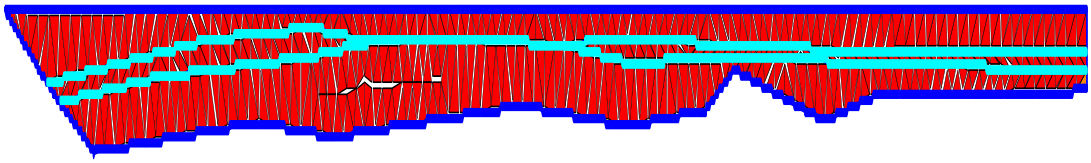

Fig. 6.14 The computational domain and the initial grid.

This velocity data and the coarsest grid from d^{3}f were read by r^{3}t. In the file **sourceterm**, a time dependent source of contaminant was defined that is concentrated to a single point on the bottom boundary of the domain.

As mentioned before, there are several advantages to start the computations on the coarsest grid level $l = 0$. Particularly, first preliminary results can be obtained very fast and the time development of numerical solution can be guessed. Furthermore, the sources of numerical errors can be recognised.

This can be clearly illustrated with two following Figures. In Fig. 6.16, a zoom of the initial coarse grid is plotted together with contour lines of numerical solution after the very first time step. Due to interpolation, although the source is located only in a single point in the domain, very coarse grid in vertical direction causes enormous spreading of concentration to the top of domain. This is clearly the first source of numerical error.

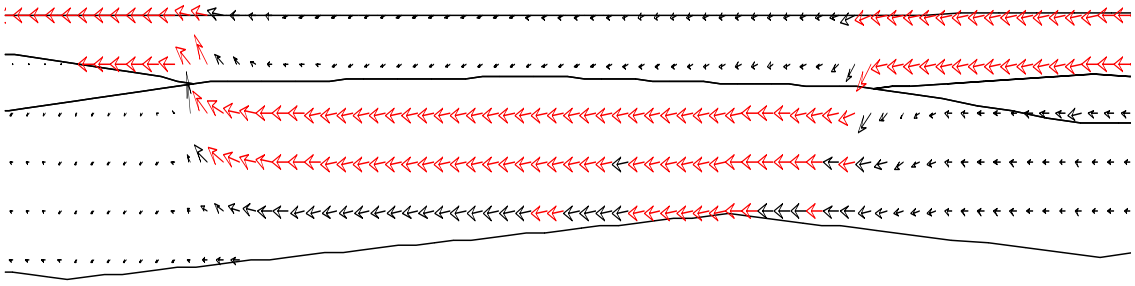

Fig. 6.15 The zoom of velocity field

In Fig. 6.17, the numerical solution at $t = 200$ years is presented that was computed on the coarsest grid. Comparing with the initial concentration profile in Fig. 6.16, the spreading of contaminant along flow lines can be observed, as expected. Clearly, the grid

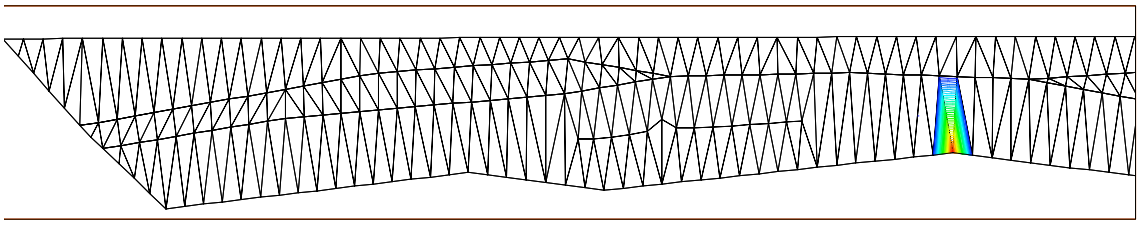

Fig. 6.16 The zoom of initial coarsest grid
and the numerical solution after the very first time step.

refinement along these flow lines is required. Finally, another possible source of numerical error can be guessed near the “turning” point over the narrow, almost impermeable, geological layer on the left.

As the second step, it is very convenient to use adaptive local grid refinement to obtain the next grid level. The error indicator was called after each time step and the elements at the coarsest grid level were refined. The obtained grid after 200 years of simulation time is plotted in Fig. 6.18 and the corresponding numerical solution in Fig. 6.19.

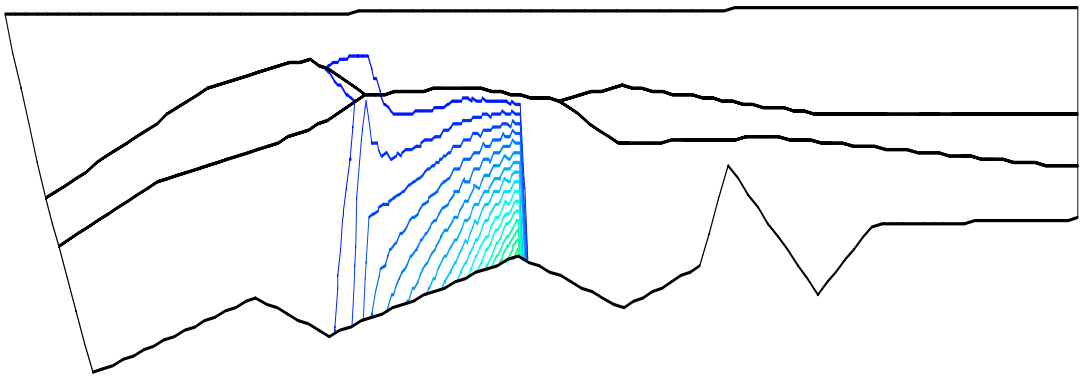

Fig. 6.17 Concentration isolines at t=200 a computed on the coarsest grid.

Because of very large maximal grid Peclet number, the computations were realised with explicit scheme for transport and decay, i.e., `MOC=1`, and with the Courant number below 1. The error indicator marked, as expected, the elements along the flow lines starting at (or near to) the source term. When comparing the numerical results for the grid level 0 and 1, i.e., the Fig. 6.17 and Fig. 6.19, one can see clearly that they differ too much,

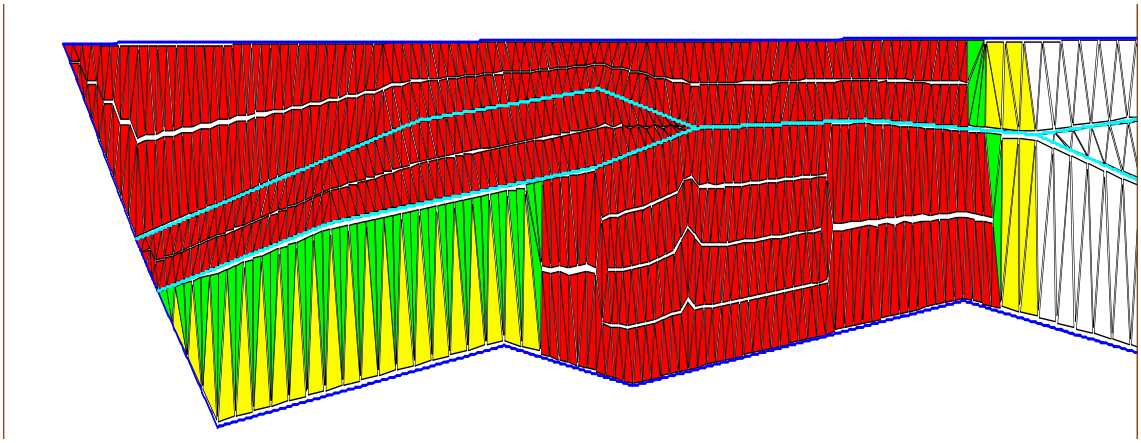

Fig. 6.18 The zoom of locally adapted grid at t=200 a.

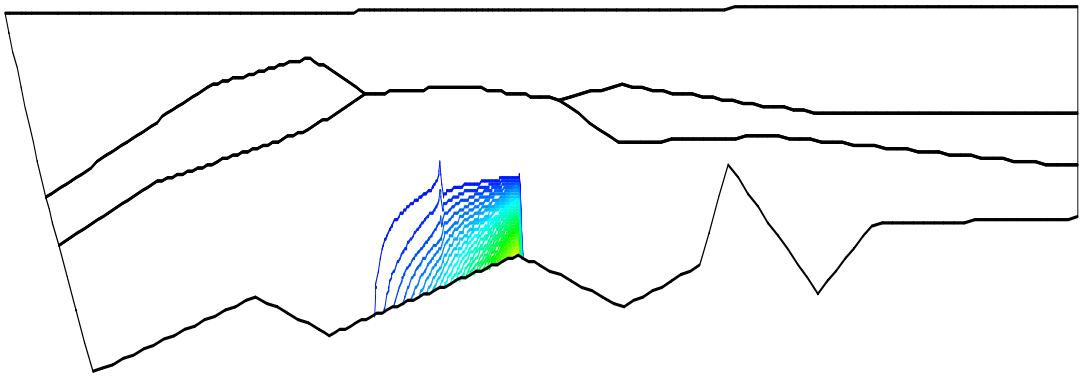

Fig. 6.19 Concentration isolines on locally adapted grid at t=200 a.

especially due to large interpolation error and large numerical dispersion for computations on the grid level $l=0$. Moreover, some “grid dependence” can be still clearly seen also in the numerical solution for grid level $l=1$.

This approach was applied further. The grid from the last time step for the grid level $l=1$, see Fig. 6.18, was taken as the starting grid for the computations with the grid level $l=2$. For the grid level $l=2$, the local adaptive refinement was used again.

In Fig. 6.20, the numerical solutions for grid level $l=5$ and $l=6$ at $t=200$ y are presented. Comparing the both numerical solutions, one can see that a nearly “grid independent” numerical solution was obtained for the grid level $l=6$.

The grid refinement was uniform, starting with $l=3$ and until $l=5$, and only the grid level $l=6$ was again obtained by a local adaptive refinement. As the maximal grid Peclet number for $l=6$ was below 1, computations for $l=5$ and $l=6$ were realised with fully implicit discretisation scheme and with the maximal grid Courant number equals approximately 10.

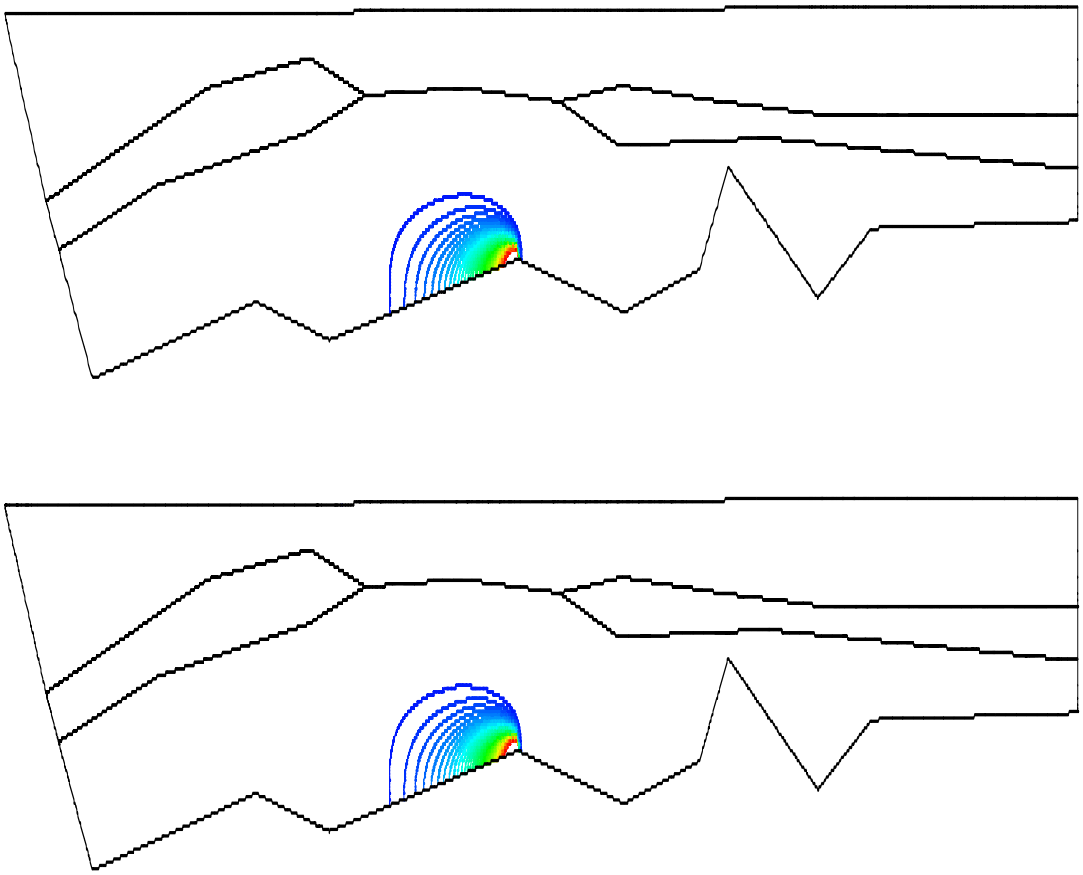

Fig. 6.20 The results on the two finest grids.

6.2.10 Conclusions

The simulator r^{3}t is well prepared to produce (physically reasonable) numerical solutions on sequence of (locally or globally refined) computational grids with appropriate automatic control of time discretisation steps. In such a way, by comparing numerical results between a coarser and a finer grid at given time points, one can easier judge the approximation quality of particular numerical solutions.

The most appropriate method to be used in r^{3}t is the explicit, second order, discretisation of the system of convection-decay equations, coupled with the implicit discretisation for all other terms (like the dispersion), and with the automatic time step control to have the maximal grid Courant number near (but below) 1. This is certainly the best method to start with for coarser grids.

The only disadvantages of this method is that it can not be, in general, used with larger time steps, i.e., with the maximal grid Courant number significantly larger than 1. The only reason for that is that a large operator splitting errors can occur for other terms, i.e., for diffusion, dispersion, kinetic sorption, and/or the immobilisation. Analogously, non-linear problems can exhibit large errors, if explicit discretisation is used with the Courant number larger than 1.

Summarising, the first simple rule is that if the automatic time control of time steps is not too much restricted by the condition that the Courant number remains below 1, one shall use the explicit discretisation method.

If this condition restrict the time step too much, the second choice of numerical method is the implicit discretisation of all terms that exhibits no time splitting error. If the maximal grid Peclet number is smaller than 1, one can use this method for convection-diffusion problems with larger time steps, i.e., with the Courant number larger than 1. Consequently, this method is the best choice for finer computational grids.

If some very fast decay reactions occur in the example computed with the fully implicit discretisation scheme, the time step can be restricted very much by the maximal Reaction number due to the large time discretisation errors. In such a case, the exact solver for decay reactions can be used that is combined then with the implicit discretisation for all other terms using the standard operator splitting method.

All discretisation methods used in r^{3}t must converge to the analytical solution. In such a way, numerical results with different methods can be compared on sequence of computational grids to judge the discretisation errors of numerical solution for particular examples and to obtain grid convergent numerical solutions.

6.2.11 The Error Estimator

In this part of the project one deals with highly accurate discretisations that are based on self-adaptive methods.

The main goal of self-adaptive methods is to minimise the computational costs for the approximate solution in order to achieve a given tolerance for the error between the exact and the numerical solution. One way to do this, is the method of local mesh refinement, which is controlled by the numerical solution itself on the basis of a-posteriori error estimates. They measure the error between the exact and the numerical solution in terms of the numerical solution which is known.

For convection dominated partial differential equations with small diffusion one derives such a-posteriori error estimates that are uniform with respect to the diffusion coefficient and thus hold even through in the limit where the diffusion coefficient might be zero. Such a result was not available up to now and is of great importance for the use of this theoretical result in the grid adaptation strategy.

In more detail, within several steps (see [88], [59], [75], [21], [6], [35], [77], [53], [85], [54], [78]) we finally managed to deal with systems of transport equations of the following general form in $\Pi_T := \Re^2 \times [0,T]$:

$$R^i(x,\ c^i)_t + \nabla \cdot (\boldsymbol{F}^i(x,\ t,\ c^i)) - \nabla \cdot (D^i(x,\ t)\nabla c^i) + \lambda^i(x,\ t,\ \boldsymbol{c}) = 0 \quad \text{in} \quad \Pi_T \qquad (6.72)$$

$$c^i(.\ ,\ 0) = c_0^i \quad \text{in} \quad \Re^2 \qquad (6.73)$$

Here $\boldsymbol{c} = (c^1, \ldots, c^M)^T : \Pi_T \to \Re^M$ denotes the vector valued function of mass concentrations of M species. Furthermore, for $i = 1, \ldots, M$, $R^i : \Pi \times \Re \to \Re$ denotes the accumulation term including the adsorbed part of the species, $\boldsymbol{F}^i : \Pi_T \times \Re \to \Re^2$ the convective flux function, $D^i : \Pi_T \to \Re_{\geq 0}$ a generalised diffusion-dispersion coefficient, and $\lambda^i : \Pi_T \times \Re^M \to \Re$ the species reaction and source term. Note that (6.72) is only weakly coupled since coupling is solely due to zero-order terms λ^i.

Equations of type (6.72) are of special interest if they model phenomena in which the effect of the convective fluxes dominates the diffusive-dispersive terms. In a unit space-time reference frame this effect occurs in the case

$$0 \leq D^i(x,\ t) \ll \left| \boldsymbol{F}_c^i(x,\ t,\ c^i(x,\ t)) \right| \qquad i \in \{1,\ldots,\ M\},\ (x,\ t) \in \bar{\Pi}_T$$

A possible degeneracy in $\Re$ (i.e. $\partial_c R$ very small or very large) and the dominance of the convective term makes the numerical approximation and the numerical analysis of problem (6.72), (6.73) very difficult. There are mainly two numerical approaches to handle these difficulties: the method of characteristics and upwind methods. In the project it is focused on upwind finite volume methods, as they are easier to implement and more universal in their application than the method of characteristics. For recent results on the method of characteristics it is referred to [35], [6], [75], [77], [139] and the references therein. In the context of upwind discretisations it is referred to [54], [35], [78] and the references therein.

One particular scalar example of (6.72) is the following advection-dispersion equation in porous media, including non-linear adsorption modelled by the Freundlich isotherm:

$$(\Phi c + \rho K c^p)_t + \nabla \cdot (\boldsymbol{u} c) - \nabla \cdot (\Phi \tilde{D} \nabla c) = 0 \qquad (6.74)$$

Here Φ denotes the porosity of the medium, ρ the bulk density, K the adsorption coefficient, p the Freundlich exponent, $\boldsymbol{u}$ the Darcy velocity, and $\tilde{D}$ the diffusion-dispersion tensor.

6.2.11.1 The Final Theoretical Result and its Usage for the Implementation

The finite volume approximation of c is denoted by c_h. Then the main result of the analysis is an a-posteriori error estimate of the form:

$$\left\| \left| \boldsymbol{c} - \boldsymbol{c}_h \right| \right\| \leq \sum_n \sum_T \eta_T^n(\boldsymbol{c}_h) \qquad (6.75)$$

where $|||.|||$ denotes an L^1-norm in time and space and the right hand side only depends on the approximate solution c_h. The sums on the right hand side thereby denote summations of local quantities η_T^n over all elements T of the computational grid, and all discrete time steps t^n.

Having derived the a-posteriori error estimate, one was able to derive an efficient adaption strategy for the finite volume method which is based on an equal distribution of the error to the elements of the computational grid (see for instance [75] for a detailed description of the algorithm).

One can now state the main theoretical result of this part of the project in detail (for the definition of the finite volume scheme and the proof of the theorem is referred to [75], [85], [78]).

A-posteriori error estimate for the first order method

Let $R^i(x, c^i) \equiv R^i(c^i)$, $\left\|R^{i'}\right\|_{L^\infty(\Re)} \leq \bar{R}^i$, and let c be the entropy weak solution of (6.72), (6.73) and c_h the approximate solution, defined by the implicit vertex centred finite volume scheme. With some further assumptions on the data, the numerical fluxes and the grid the following a-posteriori error estimate holds:

$$\sum_{i = 1, \ldots, M} \left\| c_h^i - c^i \right\|_{L^1(\Re^2 \times [0, T])}$$

$$\leq k_1(\eta_0 + \eta_\lambda + \eta_t + \eta_c + \eta_d) + k_2 \sqrt{\eta_{\bar{U}}} + k_3 \sqrt{\eta_t + \eta_c + \eta_d}$$

The constants k_1-k_3 are computable (for more details see [85]) and the error estimator terms η_l are given as

$$\eta_0 = \sum_{i = 1}^{M} \left\{ \int_{\Re^2} \left| R^i(c_h^i(x, 0)) - R^i(c_0^i(x)) \right| dx \right\},$$

$$\eta_t = \sum_{i=1}^{M} \left\{ \sum_{n=0}^{N} \sum_{j \in J} \left(\left| R^i(c_j^{n+1,i}) - R^i(c_j^{n,i}) \right| \Delta t^n |\Omega_j| \right. \right.$$

$$\left. \left. + h_j \Delta t^n \int_{\Omega_j} \bar{R}^i \left| \nabla c_h^i(x, t^{n+1}) dx \right| \right) \right\},$$

$$\eta_c = \sum_{i=1}^{M} \left\{ \sum_{n=0}^{N} \sum_{(j,l,.) \in D} (h_{jl} + \Delta t^n) \Delta t^n Q_{jl}^{*,n+1,i}(c_j^{n+1,i}, c_l^{n+1,i}) \left| c_j^{n+1,i} - c_l^{n+1,i} \right| \right.$$

$$+ \sum_{n=0}^{N} \sum_{(j,l,.) \in D} \sup_{v \in [A,B]} \left\| \partial_v \boldsymbol{F}(.,.,v) \right\|_{c^1(s_{jl}^* \times (t^n, t^{n+1}))}$$

$$\left| c_j^{n+1,i} - c_l^{n+1,i} \right| (h_{jl} + \Delta t^n)^2 \times \Delta t^n \left| S_{jl}^* \right|$$

$$\left. + \left(\sum_{n=0}^{N} \sum_{j \in J} \sup_{v \in [A,B]} \left\| \partial_v \boldsymbol{F}(.,.,v) \right\|_{L^\infty(\Omega_j \times (t^n, t^{n+1}])} h_j \Delta t^n \right) \int_{\Omega_j} \left| \nabla c_h^i(x, t^{n+1}) \right| dx \right\}$$

$$\eta_d = \sum_{i=1}^{M} \left\{ \sum_{n=0}^{N} \sum_{(j,l) \in \varepsilon} \left[\overline{D_{jl}^{n+1,i}} \nabla c_h^{n+1,i} \cdot \boldsymbol{m}_{jl} \right]_{\Gamma_{jl}} \Delta t^n |\Gamma_{jl}| (h_{jl}^n + \Delta t^n) \right.$$

$$\left. + \sum_{n=0}^{N} \sum_{j \in J} \sum_{l \in N(j)} \int_{t^n}^{t^{n+1}} \int_{T_{jl}^a} \left| D^i(x,t) - \overline{D_{jl}^{a,n+1,i}} \right| \left| \nabla c_h^i(x,t) \right| dx dt \right\},$$

$$\eta_\lambda = \sum_{i=1}^{M} \left\{ \sum_{n=0}^{N} \sum_{j \in J} \int_{t^n}^{t^{n+1}} \int_{\Omega_j} \left| \lambda^i(x, t, \boldsymbol{c}_h^{n+1}(x)) - \lambda_j^{n+1,i}(\boldsymbol{c}_j^{n+1}) \right| dx dt \right\},$$

$$\eta_{\overline{U}} = 2 \sum_{i=1}^{M} \Bigg\{ \sum_{n=0}^{N} \sum_{(j,l) \in \varepsilon} \left[\overline{D_{jl}^{n+1,i}} \nabla c_h^{n+1,i} \cdot \boldsymbol{m}_{jl} \right]_{\Gamma_{jl}}$$

$$\left| c_j^{n+1,i} - c_l^{n+1,i} \right| \Delta t^n \left| \Gamma_{jl} \right|$$

$$+ \sum_{n=0}^{N} \sum_{j \in J} \sum_{l \in N(j)} \int_{t^n}^{t^{n+1}} \int_{T_{jl}^a} \left| D^i(x,t) - \overline{D_{jl}^{a,n+1,i}} \right| \left| \nabla c_h^i(x,t) \right|^2 dx dt \quad .$$

$$+ \sum_{n=0}^{N} \sum_{j \in J} \left\| \lambda^i(.,.,c_h^{n+1}) \right\|_{L^\infty(\Omega_j \times (t^n, t^{n+1}])} \int_{t^n}^{t^{n+1}} \int_{\Omega_j} \left| \nabla c_h^{n+1,i}(x) \right| dx dt \Bigg\}$$

Here $Q_{jl}^{*,n+1,i}$ is defined as

$$Q_{jl}^{*,n+1,i}(v,w) := \frac{2 g_{jl}^{*,n+1,i}(v,w) - g_{jl}^{*,n+1,i}(v,v) - g_{jl}^{*,n+1,i}(w,w)}{(v-w)}$$

6.2.11.2 Going to Higher Order Finite Volume Schemes

So far one has always dealt with so called first order finite volume approximations of the transport problem. For linear advection equations it is well known that these first order finite volume schemes are only of order $h^{1/2}$, if h denotes the mesh size. In addition, those methods introduce some artificial numerical viscosity which is proportional to the local mesh size. Due to this drawbacks, such first order schemes on uniform computational grids are not very accurate in the prediction of the propagation of contaminants in the subsoil. The situation gets even worse, if non-linear reactions are also taken into account. In this situation the physical balance between reaction, advection and dispersion may be completely destroyed by the artificial numerical viscosity. In order to cope with an more accurate and efficient simulation of such transport phenomena we then proposed an higher order finite volume scheme on self-adaptive computational grids, where the adaptivity is steered by the rigorous a-posteriori error estimate which was derived for the first order scheme.

Now the final gain in performance of the research in this project is demonstrated by the following example (see also [35], [78]).

6.2.11.3 Numerical Experiment: Transport and Decay of Radionuclides

As a first relevant application in environmental sciences one now introduces a simplified model for subsurface transport and decay of radionuclides (cf. [53], [59], [85]).

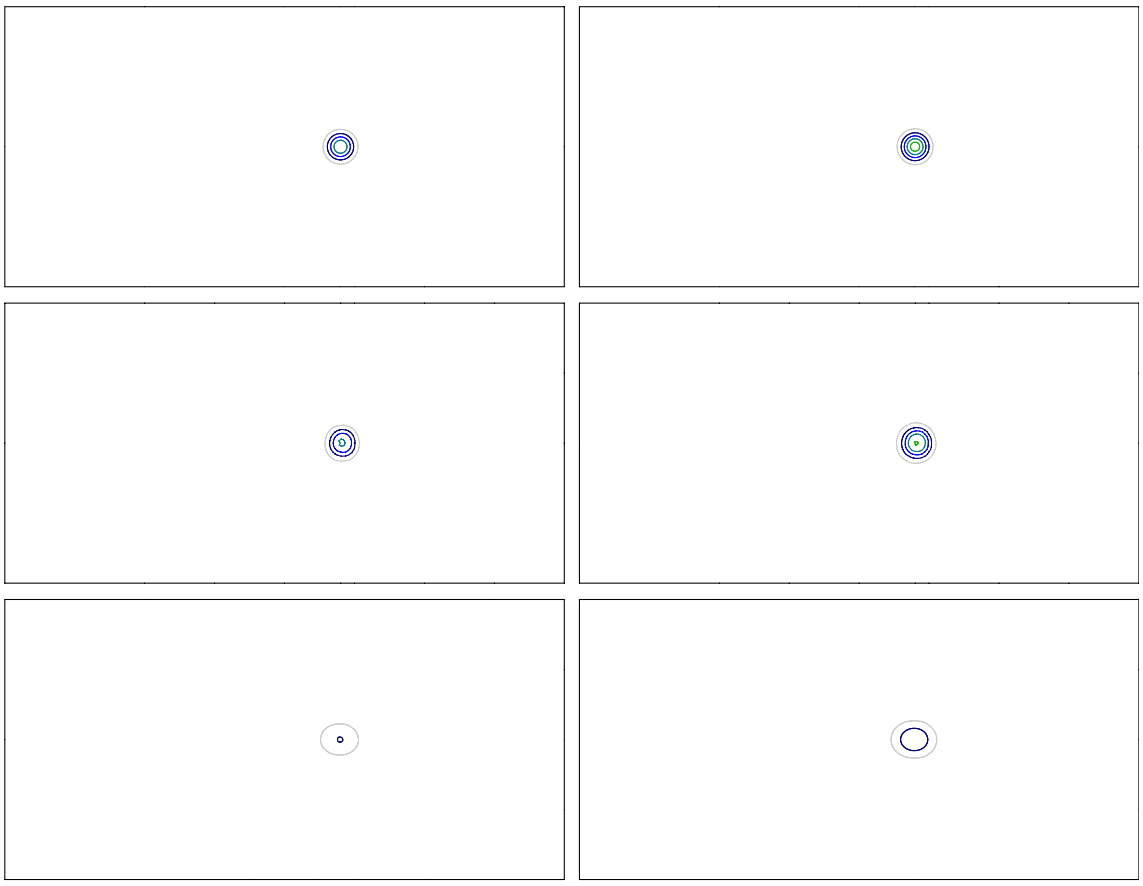

Fig. 6.21 Comparison of exact, higher and first order adaptive solutions
Exact solution at $t = 150$ (first row) in comparison with the solution of an adaptive higher order computation (774 cells, 70 seconds CPU-time) in the second and a corresponding adaptive first order computation (7739 cells, 1411 seconds CPU-time) in the third row. The concentration distribution of nuclide 1 is shown in the left column and of nuclide 2 in the right column.

Let $\Omega \subset \Re^2$ be a bounded computational domain which represents a horizontal cut through the aquifer. The mathematical model for the transport and decay of two radionuclides with concentrations c^1, and c^2 writes

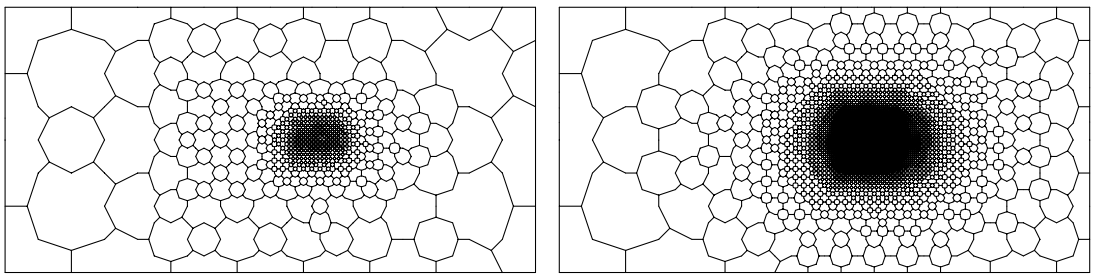

Fig. 6.22 Adaptive grids for the higher (left) and the first order method (right) corresponding to the adaptive solutions shown in Fig. 6.21.

$$\partial_t c^i + \operatorname{div}(\boldsymbol{u} c^i - D\nabla c^i) = -\lambda^i c^i + \lambda^{i-1} c^{i-1} \quad \text{in } \Omega \times (0, T)$$
$$(i = 1, 2)$$

with $\lambda^0 = 0$. Here λ^i denote the decay rates of the radionuclides. This linear weakly coupled system can be solved in the whole space analytically if one prescribes as initial condition $c^1(.,0) = m\delta_{(0,0)}$, $c^2(.,0) \equiv 0$, where $m \in \Re_{>0}$ denotes the mass and $\delta_{(0,0)}$ the Dirac distribution with support in the point $(0,0)$. Taking the analytical solution at $t = 100$ as initial condition for the numerical computations, one is thus able to compare the approximated solutions with the exact one. In the following we will study uniform and adaptive computations for the following data.

$$m = 10 \qquad \lambda^1 = 0.005$$
$$\Omega = (-25, 25) \times (90, 190) \qquad \lambda^2 = 0.0$$
$$u = (1, 0)^T \qquad D = 0.01$$

The spot of the concentrations c^1 and c^2 are transported through the domain, widened by a small diffusion, and the nuclide c^1 decays into nuclide c^2. The exact solution at $t = 150$ is shown in the upper row of Fig. 6.21.

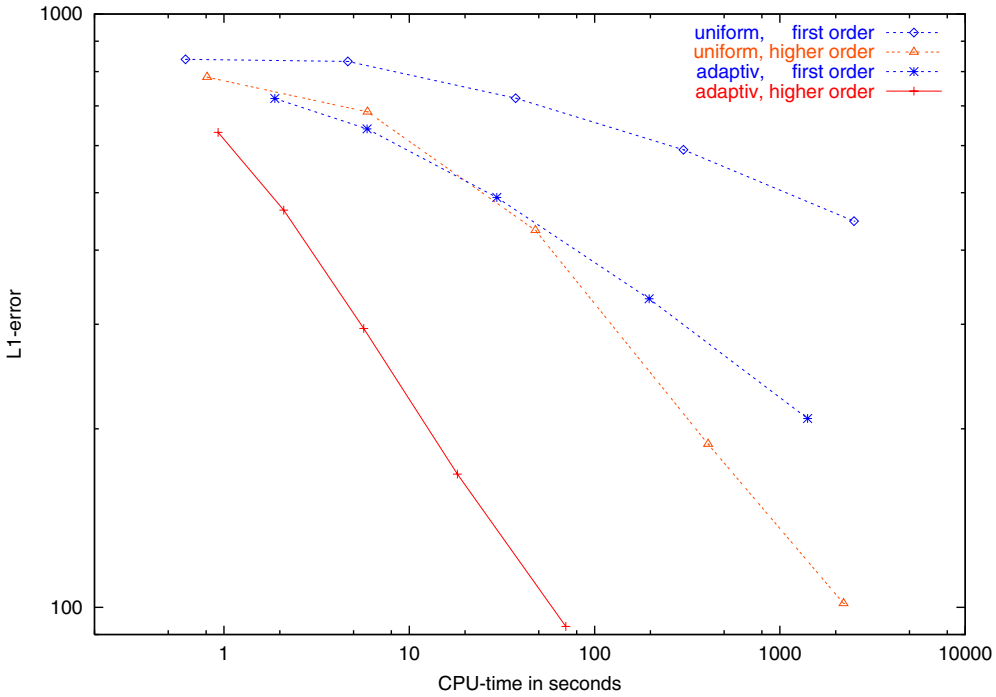

Fig. 6.23 L^1-error versus CPU-time for uniform and adaptive calculations for the first and higher order scheme for the nuclide transport problem in logarithmic scale.

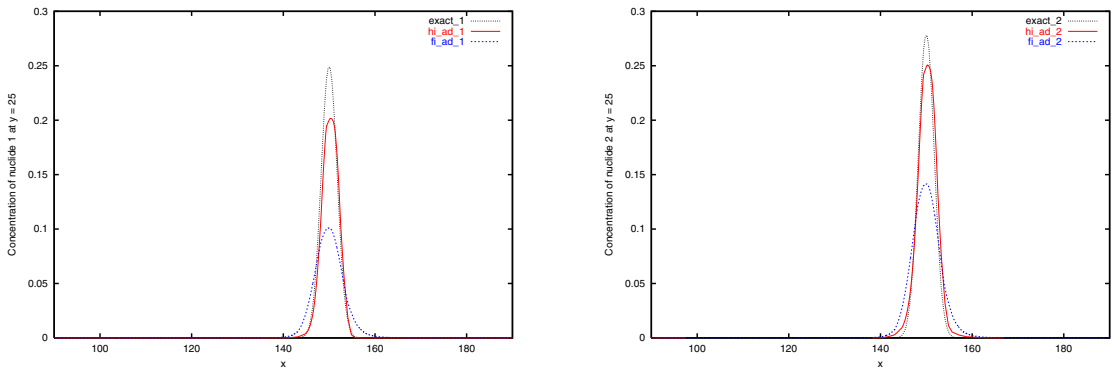

Fig. 6.24 Profiles of the exact, higher order and first order adaptive solutions Comparison at $y = 25$ of the exact solution in black, higher order adaptive approximation in red (70 seconds CPU-time), and first order adaptive approximation in blue (1411 seconds CPU-time). The concentration profile of nuclide 1 is shown on the left, while nuclide 2 is displayed on the right.

The uniform and adaptive first order scheme for this model problem has already been studied in [85]. It was shown that the first order scheme and the error estimator converges with approximately the same rate on uniform grids. Thus, for the first order scheme the error estimator is efficient. In addition to the convergence study, the speed up in CPU-time was demonstrated for the adaptive first order scheme.

By the presentation here, the gain in performance of the higher order scheme, both on uniform and adaptive grids (see Fig. 6.23) will be demonstrated. While the adaptive first order method performs better than the uniform second order method on rather coarse grids, this situation changes on finer grids where higher order beats adaptivity. As expected, the adaptive version of the higher order method is by far the most efficient algorithm. In order to see the advantage of the adaptive higher order method in terms of CPU-time, we plotted in Fig. 6.23 the L^1-error versus runtime.

Finally, for a visual comparison of the adaptive higher order and first order method, the numerical solutions at $t = 150$ are given in Fig. 6.21. The computational grids at $t = 150$ of the adaptive solutions are shown in Fig. 6.22. It is quite evident that the adaptive higher order method needs far less grid cells than the adaptive first order method. In Fig. 6.24 the profile of the solution at $y = 25$ is plotted. Here one recognises the tremendous benefit of the higher order method. Whereas the first order method smears out the solution very much, the higher order method captures the exact solution very well.

6.2.11.4 Conclusion

Within the context of this project an efficient and reliable adaptive strategy for a first order finite volume approximation was derived. In several steps an a posteriori error estimate for the full complexity of weakly coupled systems of non-linear convection-diffusion-reaction equations, including non-linear retardation, was finally rigorously derived. This theoretical result then was the key in deriving an efficient adaption strategy for the finite volume scheme, both in time and space.

Finally, a self-adaptive higher order finite volume method was proposed, where the adaptivity is also based on the results of the first order method. Numerical experiments demonstrated the enormous gain in efficiency by using both, adaptivity and higher order accuracy.

The implementation and testing of the derived adaptive concepts was done on the basis of an other code development called GFLOW and finally these concepts were implemented into the r^3t environment.

6.3 The Postprocessor

The focus of the work of our group in this projects was to extend the postprocessor developed for the program package d^3f and to adapt it to the requirements of r^3t. This includes the enhancement of existing methods as well as the development of new ones, with a special emphasis on the processing and visualising large ensembles of scalar functions, as they occur when exploring sets of radio nuclides, possibly also in different phases, and on the inspection of features inherent to pollutant transport problems.

The focus was on the methods for data import and handling and on tools to understand complex flow fields along which pollutants are transported, to display traces of pollutants in the domain, evaluate and balance nuclide concentration, to handle and visualise large sets of concentrations and focus on subdomains of special interest. In what follows, an overview of the newly developed postprocessing methods will be given.

6.3.1 Anisotropic Diffusion and Transport in Flow Visualisation

Vector field visualisation is an important topic in scientific visualisation. Its aim is to graphically represent field data in an intuitively understandable and precise way. Here a new approach based on anisotropic non-linear diffusion is introduced. It enables an easy perception of flow data and serves as an appropriate scale space method for the visualisation of complicated flow pattern. The approach used for r^3t is closely related to non-linear diffusion methods in image analysis where images are smoothed while still retaining and enhancing edges. An initial noisy image is smoothed along streamlines, whereas the image is sharpened in the orthogonal direction. The method is based on a continuous model and requires the solution of a parabolic PDE problem, remarkably similar to the problems to be solved for the actual simulation processes. The methods have been applied in 2D and 3D for data arising in d^3f and r^3t.

In case of time-dependent flow data this technique has been expanded. The aim has been represent transport phenomena governed by time-dependent vector fields in an intuitively understandable way, using images as well as animations. Here the method for steady flow fields was picked up, expanded and generalised to allow a multiscale visualisation of long-time, complex transport problems. Instead of streamline type patterns generated by the original method now streakline patterns are generated and advected. This process obeys a non-linear transport diffusion equation with typically dominant transport. Starting from some noisy initial image, the diffusion actually generates and enhances patterns which are then transported in the direction of the flow field. Simultaneously the image is again sharpened in the direction orthogonal to the flow field. A careful adjustment of the model's parameters is derived to balance diffusion and transport effects in a reasonable way, as is shown in Fig. 6.25. The numerical scheme is based on an efficient upwind finite element discretisation.

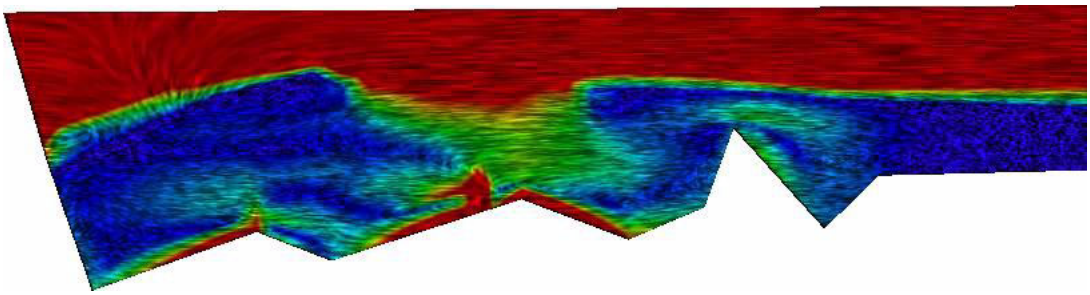

Fig. 6.25 Visualisation of a complex flow field
The absolute value of the velocity is colour coded.

6.3.2 Algebraic Multigrid Approach for Multiscale Visualisation of Flow

To support the understanding and the analysis of 3D flow fields the extraction respectively visualisation of flow pattern and "features" on different scales is an indispensable tool. One observes that a clear and unique definition of "flow feature" has not been achieved so far. This depends significantly on the application and in particular on the different scales of the complex flow. Moreover during our research it has become evident that one-level analysis of feature-defining quantities is not capable of resolving the flow structures adequately, even not with moderate user interaction. Hence, a multilevel analysis of the flow is considered. A natural operator connected with the flow is the streamline diffusion operator [68], [96]. Here we consider the following special anisotropic version

$$
\begin{aligned}
& TD_v[u] \\
& := \varepsilon \Delta_A u + v \cdot \nabla v \\
& := \varepsilon \mathrm{div}\,(A(v, \nabla u_\rho)\nabla u) + \mathrm{v} \cdot \nabla v
\end{aligned}
\qquad (6.76)
$$

which is closely related to our transport diffusion operator. Thereby the anisotropic Laplace-operator Δ_A, which prefers diffusion of u in direction of the flow, is considered together with the corresponding advection term $v \cdot \nabla u$. Performing a multilevel analysis of the operator TD_v in terms of an algebraic multigrid method, one obtains an identification of features of the flow.

6.3.3 Data Import

The r^{3}t data format experienced only slight changes in comparison to the d^{3}f project, so that the changes on the import module concentrate on details of special importance in the setting of radionuclide transport. This mainly involves the possibility to handle data sets with a large number of scalar functions (i.e. pollutant concentrations) that are extracted from the concentration vector that is written by the numerics module. For ease of handling, subsets of this functions can be reassembled as components of a vector-valued `multi-vector` function, that can be subject to a number of special presentation methods for high-dimensional data, see below.

6.3.4 Clipping Planes

Drawing isolines or colorshading of function values on clipping planes through three-dimensional domains is one of the principal visualisation methods for the display of scalar functions. Because of the special setting in our project, a set of additional tools that are adapted to the r^{3}t aims have been developed.

First, this includes a general class, called `clipmesh`, that allows to generate a two-dimensional object from a three-dimensional data set by clipping with a plane. Elements of the clipped grid are generated temporarily at runtime from their three-dimensional counterparts during the traversal of the 2D grid without actually storing them. In this way, one is able to generate any number of slices of a 3D data set and work on them with the full set of display and analysis methods that is available for two-dimensional objects. The

performance of this scheme, if compared to a specialised clip display method for 3D objects decreases only by a constant factor in the range of about two to eight. In addition, fast methods for the display of a set of clip planes in one traversal of the three dimensional element tree were developed. In this case, the advantage of treating several planes in one pass greatly increases the performance advantage to the general concept described above. Further, these methods have a special interface to the data analysis tool (see below) that allows to restrict the domain that is displayed to the area of interest.

The methods `clip-isoline-multi` works on a set of parallel clipping planes. Here the interface to the data analysis tool (DAT) developed in cooperation with AG Kröner is of great importance, as it allows to restrict the part of each plane that is drawn, in this way freeing the line of sight to the next plane behind. The method `spades` or `leporello` draws function values on the cuts of a blade: First one defines the ground plane, on which one marks a number of consecutive lines. The function is then drawn on the plane orthogonal to the ground plane through each of this lines (i.e. a cut of the spade). Additionally, one can unfold this depiction into one plane like a leporello (c.p. Fig. 6.26).

6.3.5 Function Evaluation and Time-Variation Graphs

The function evaluation methods (as well as the integration methods described below) are based on a hierarchical search algorithm in the element tree. Thus they exploit data locality when evaluating function values on nearby points, which is especially useful when evaluating along lines, planes, or subsets of the domain. All methods include the possibility to evaluate the function only at a specific time or to plot a function graph over the time axis. Results of evaluation or balancing methods are additionally stored as a plain ASCII text file that allows easy storage, reference and further processing of the data.

Primarily this includes the evaluation of functions at a specified point or along a line or curve. The time dependent variant of this methods generates a graph over time of the concentration at a given point, line or curve. If the function is vector-valued (as in a assembled set of different concentration in a `multi-vector`), multiple time-variation graphs are automatically generated. Additionally, one can sample function values on an equidistant Cartesian grid and write them to a plain text file, which can usually be easily imported into other program packages, e.g. for comparison or further processing.

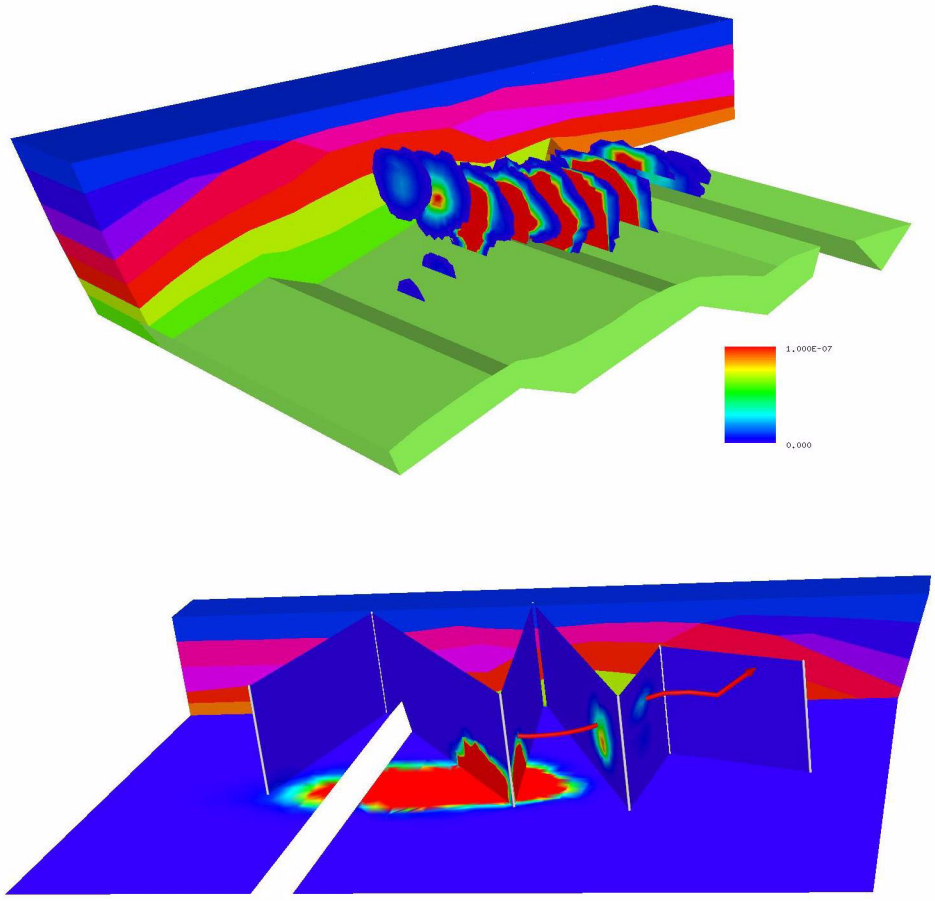

Fig. 6.26 Concentration of pollutant on clipping planes and on a leporello

6.3.6 Mass Balancing

Also a new set of balancing methods is provided mainly for integrating concentrations over subsets of the computational domain. This includes the possibility to integrate the mass contained in a “thick” subset of the domain, as in a cuboid or a subdomain given by the geology. Further methods allow to compute the flow through a n-1-dimensional subset of the domain, given a velocity and a concentration density function. In this case planes, planes intersected with subdomains and subdomain boundaries are useful candidates for such an integration.

6.3.7 Simplified User Interface

In debt of the experiences from the previous project, a version of the postprocessor with a simplified user interface was also developed. This includes controls for some basic visualisation and analysis tools that were selected in collaboration with users of the program into a reduced interface that hides the full complexity of the postprocessing tool. Additionally, this tool integrates functions that aid the user in finding sensible parameter values for the included display methods.

6.3.8 Additional Methods

For debugging purposes, a display method was added that shows the elements of the grid and allows to inspect nearly all properties of elements and functions that are known to the postprocessor, as global and local node numbers, local coordinates, function values, error estimators and so on.

To simplify correlating computational results with e.g. geographical information, image files like aerial photographs, maps etc. can be superimposed onto objects in the postprocessor (cp. Fig. 6.27). They are placed appropriately if you can identify three points of the image and their coordinaters in the computational domain.

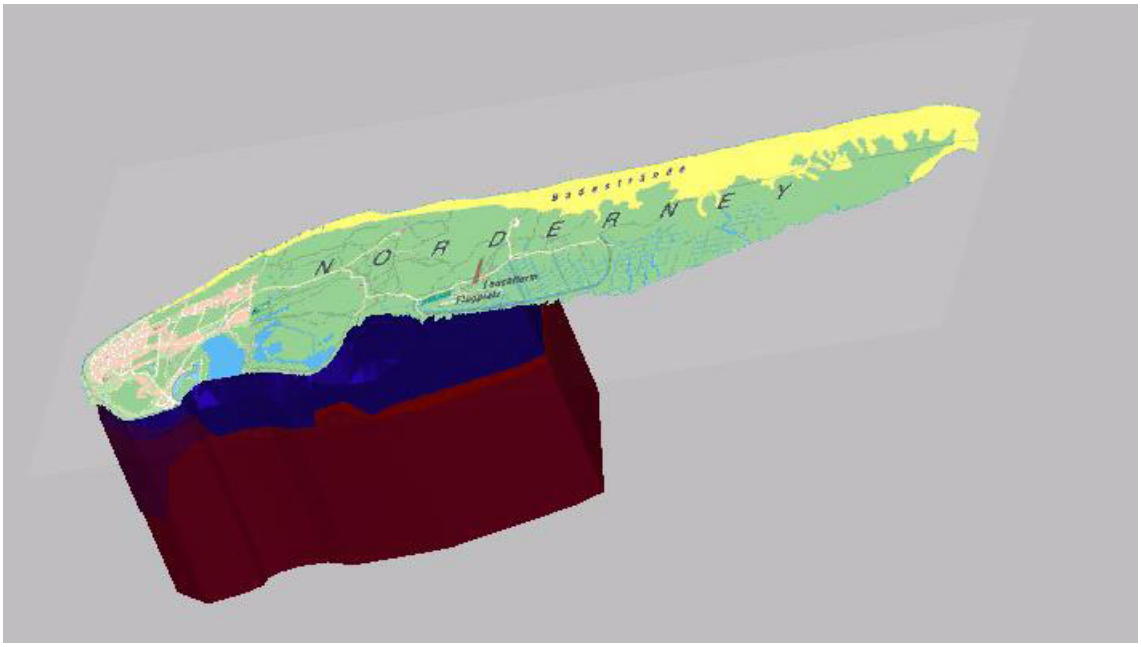

Fig. 6.27 Map texture overlaying the geometry of the computational domain

6.3.9 The Data Analysis Tool (DAT)

The data analysis tool (DAT) allows the definition of new functions by arithmetic operations on existing ones, and to define subsets of the domain (that are to be taken into account for visualisation or analysis purposes, see above). Furthermore, a method for the rendering of massive sets of shaded particles has been developed to support the simultaneous visualisation of multiple species.

7 The Verification of r^{3}t

In this chapter first various methods for verification are introduced while in the latter part of the chapter explicit calculations to verify r^{3}t are shown in one-, two, and three dimensions.

7.1 Methods for Verification of the Simulator r^{3}t

The aim of this chapter is to provide an overview of verification methods for the simulation code r^{3}t. Moreover, the proposed methods can be used for a-posteriori check of any other numerical codes for simulating solute transport. In order to prove the accuracy of the numerical code we propose the following tests:

- re-identification of transport parameters, e.g. transport velocity and dispersion coefficients
- check of total mass conservation and mass reduction in the case of radionuclide decay (both for linear and non-linear models)
- check of the front velocity for transport with a continuous solute injection (for the case of non-linear adsorption with an equilibrium adsorption isotherm)
- comparison with analytical solutions (for linear transport)

Tab. 7.1 Parameters for a two-dimensional homogeneous problem

parameter	value
discretisation level	7
max. edge [m]	0.7912
min. edge [m]	0.125
ϕ	0.1
D_{11}	variable
D_{22} [m^{2}s^{-1}]	$6.5 \cdot 10^{-8}$
c^{in} [g m^{-2}]	1
ρK_{nl} (ρK_d) [(g m^{-2})$^{p-1}$]	0.15

For every test case we proceed as follows: First, the theoretical background is introduced. Second, the application of the current test on the basis of significant examples for transport in homogeneous media is show.

The calculation of the numerical examples is performed by means of the simulation tool r^{3}t, using the upwind finite volume method with a Courant number $Co \leq 1$ for solution of the transport with finite Peclet numbers and the method of characteristics with $0.9 \leq Co \leq 1$ in the purely advective transport case. The homogeneous transport model is solved in a two-dimensional domain of 100 m by 16 m. One models a uniform steady-state flow field aligned with the x-direction. The initial condition for the solute is considered as a Dirac pulse in space, which is released into the domain instantaneously or as a continuous point injection of mass. The necessary simulation parameters can be found in Tab. 7.1.

7.1.1 Governing Equations and Boundary Conditions

On mesoscopic scales, the time evolution of radionuclides which are dissolved in the groundwater and which are coupled by first-order decay processes is given by an advection-dispersion equation. Additionally, the nuclides are adsorbed on the soil matrix. Thus, the transport equation of the i^{th} member of the decay chain results in the following system of differential equations:

$$\begin{aligned} &\phi \frac{\partial}{\partial t} c_1^l(\boldsymbol{x}, t) + (1-\phi)\rho \frac{\partial}{\partial t} c_1^{ad}(\boldsymbol{x}, t) + \nabla \cdot (\boldsymbol{q} - \phi \boldsymbol{D} \nabla) c_1^l(\boldsymbol{x}, t) \\ &\quad = -\lambda_1 (\phi c_1^l + (1-\phi)\rho c_1^{ad}(\boldsymbol{x}, t)) \end{aligned} \tag{7.1}$$

$$\begin{aligned} &\phi \frac{\partial}{\partial t} c_i^l(\boldsymbol{x}, t) + (1-\phi)\rho \frac{\partial}{\partial t} c_i^{ad}(\boldsymbol{x}, t) + \nabla \cdot (\boldsymbol{q} - \phi \boldsymbol{D} \nabla) c_i^l(\boldsymbol{x}, t) \\ &\quad = -\lambda_i (\phi c_i^l + (1-\phi)\rho c_i^{ad}(\boldsymbol{x}, t)) \\ &\qquad - \lambda_{i-1} (\phi c_{i-1}^l + (1-\phi)\rho c_{i-1}^{ad}(\boldsymbol{x}, t)) \end{aligned} \tag{7.2}$$

Here, t is the time, ϕ is the constant porosity of the fully saturated medium, ρ_r is the dry matrix density, $c(\boldsymbol{x}, t)$ the dissolved concentration and $c_i^{ad}(\boldsymbol{x}, t)$ the equilibrium adsorption isotherm. The vector $\boldsymbol{q}$ denotes the Darcy velocity which follows directly from the local hydraulic conductivity of the medium, $\boldsymbol{k}_f$, by Darcy's law

$$\boldsymbol{q} = \boldsymbol{k}_f \cdot \nabla h \qquad (7.3)$$

where h stands for the piezometric head.

Dividing (7.1) - (7.2) by ϕ and performing the time derivative, the system of transport equations can be rewritten as:

$$\begin{aligned} & R(c_1^l)\frac{\partial}{\partial t}c_1^l(\boldsymbol{x}, t) + \nabla \cdot (\boldsymbol{u} - \boldsymbol{D} \cdot \nabla)c_1^l(\boldsymbol{x}, t) \\ = \; & -\lambda_1\left(c_1^l + \frac{(1-\phi)}{\phi}\rho_r c_1^{ad}(\boldsymbol{x}, t)\right) \end{aligned} \qquad (7.4)$$

$$\begin{aligned} & R(c_i^l)\frac{\partial}{\partial t}c_i^l(\boldsymbol{x}, t) + \nabla \cdot (\boldsymbol{u} - \boldsymbol{D} \cdot \nabla)c_i^l(\boldsymbol{x}, t) \\ = \; & -\lambda_i\left(c_i^l + \frac{(1-\phi)}{\phi}\rho_r c_i^{ad}(\boldsymbol{x}, t)\right) \\ & + \lambda_{i-1}\left(c_{i-1}^l + \frac{(1-\phi)}{\phi}\rho_r c_{i-1}^{ad}(\boldsymbol{x}, t)\right) \end{aligned} \quad . \qquad (7.5)$$

Here, the vector $\boldsymbol{u} = \frac{\boldsymbol{q}}{\phi}$ denotes the pore velocity. The tensor $\boldsymbol{D}$ characterises the local dispersion. It is assumed to be diagonal in a Cartesian coordinate system and contains the diffusion coefficient D_m and the dispersivities α_{ii}:

$$\boldsymbol{D} = \begin{bmatrix} D_m + \alpha_{11}|\boldsymbol{u}| & 0 & 0 \\ 0 & D_m + \alpha_{22}|\boldsymbol{u}| & 0 \\ 0 & 0 & D_m + \alpha_{33}|\boldsymbol{u}| \end{bmatrix} \qquad (7.6)$$

$R(c_i^l)$ is the so-called retardation factor which is defined as

$$R(c_i^l) = \left(1 + \frac{(1 - \phi)}{\phi} \rho_r \frac{\mathrm{d}c_i^{ad}}{\mathrm{d}c_i^l} \right). \qquad (7.7)$$

In many cases, linear adsorption models are employed to approximate experimental sorption data. For linearly adsorbing solutes a linear relation between the dissolved and the adsorbed concentrations holds

$$c_i^{ad}(\boldsymbol{x}, t) = K_d^{e(i)} c_i^l(\boldsymbol{x}, t) \qquad (7.8)$$

where $K_d^{e(i)}$ is a positive, element-specific distribution coefficient in units of [m^d kg^{-1}] in d spatial dimensions. However, there is mounting evidence of isotherm non linearity in subsurface soils [80], [140], [141]. Non linearity should in fact be expected for surface adsorption phenomena that extend over a range of significant solution concentrations and may be exhibited if interactions between sorbed solute molecules increase or decrease their affinity for the sorbent.

A variety of conceptual and empirical equilibrium models for representation of non-linear sorption processes exists in the literature [70], [79], [80], [124]. The Langmuir model is based on an asymptotic approach to a maximum sorption capacity κ, and the affinity b of the surface for the solute:

$$c_i^{ad}(\boldsymbol{x}, t) = \frac{\kappa b c_i^l(\boldsymbol{x}, t)}{1 + b c_{e(i)}^l(\boldsymbol{x}, t)}. \qquad (7.9)$$

Here, $c_{e(i)}^l$ denotes the dissolved concentration of the element to which the i^{th} radionuclide belongs.

Equilibrium data are often better described by a general concentration-dependent relationship which does not assume limited levels of sorption. In the following, the special interest and investigations are focused on transport with an equilibrium isotherm of Freundlich type:

$$c_i^{ad}(\boldsymbol{x},\ t) \quad = \quad \frac{K_{nl}^{e(i)}\left(c_{e(i)}^{l}(\boldsymbol{x},\ t)\right)^{p}}{c_{e(i)}^{l}(\boldsymbol{x},\ t)} \tag{7.10}$$

Here, p is the Freundlich exponent and $K_{nl}^{e(i)}$ the element-specific sorption constant in units of [mass^{-p} length^{pd}] in d spatial dimensions.

Neumann boundary condition is defined as

$$c_i^{l}(x_j \rightarrow \pm\infty,\ t) \quad = \quad 0 \qquad\qquad t > 0,\ j \quad = \quad 1,\ 2,\ 3\,. \tag{7.11}$$

Alternatively, a tracer was introduced uniformly distributed along the transverse direction into a finite domain with the flux concentration c_i^{in}. In this case, one assumes a Cauchy boundary condition at the inflow boundary and a vanishing concentration gradient normal to the outflow boundary:

$$\begin{aligned} n_i u_i c_i^{l}(\boldsymbol{x},\ t) - n_i\left(D_{ij}\frac{\partial}{\partial x_j}c_i^{l}(\boldsymbol{x},\ t)\right) & \\ = \quad n_i u_i c_i^{in}(\boldsymbol{x},\ t)\delta(t) & \qquad \text{at } \Gamma_{in} \end{aligned} \tag{7.12}$$

$$n_i D_{ij}\frac{\partial}{\partial x_j}c_i^{l}(\boldsymbol{x},\ t) \quad = \quad 0 \qquad\qquad \text{at } \Gamma_{out} \tag{7.13}$$

The normal vector, n_i, is oriented towards the outside of the domain.

7.1.2 Identification of Transport Parameters

7.1.2.1 Transport with no Decay

Transport processes with linear adsorption are characterised by a constant retardation factor, $R = 1 + \frac{1-\phi}{\phi}\rho_r K_d$. Assuming a point-like instantaneous injection of solute, the transport equation (7.4) is solved by a Gaussian concentration distribution. The distribution is completely described by its centre of mass and its width. The centre of mass is defined as the first spatial moment of the concentration distribution

$$\kappa_i^1(t) \equiv \frac{\int x_i c^l(\boldsymbol{x},\ t)\, d^d x}{\int c^l(\boldsymbol{x},\ t)\, d^d x}, \qquad (7.14)$$

whereas the width is the square root of the second central moment defined as

$$\kappa_{ii}^2(t) \equiv \frac{\int x_i^2 c^l(\boldsymbol{x},\ t)\, d^d x}{\int c^l(\boldsymbol{x},\ t)\, d^d x} - \left(\frac{\int x_i c^l(\boldsymbol{x},\ t)\, d^d x}{\int c^l(\boldsymbol{x},\ t)\, d^d x} \right)^2 . \qquad (7.15)$$

All higher spatial cumulants vanish. By time derivation the transport parameters follow as

$$\begin{aligned} \frac{u}{R} &= \partial_t \kappa_1^1(t) & \frac{D_{11}}{R} &= \frac{1}{2}\partial_t \kappa_{11}^2(t) \\ \frac{D_{22}}{R} &= \frac{1}{2}\partial_t \kappa_{22}^2(t) & \frac{D_{33}}{R} &= \frac{1}{2}\partial_t \kappa_{33}^2(t) \end{aligned} . \qquad (7.16)$$

Hence, a unique relation between spatial moments on one hand and transport parameters on the other exists: The first moment determines the transport velocity, the second the dispersion coefficients. In transport simulations this relation is used in order to identify transport parameters from concentration data, especially for transport in heterogeneous media where no analytical solution of the concentration is known.

Transport with non-linear adsorption is characterised by a concentration-dependent retardation. If the adsorption is given by an isotherm of Freundlich type, the retardation factor reads as:

$$R(c^l) = \left(1 + \frac{(1-\phi)}{\phi} p \rho_r K_{nl} (c^l(\boldsymbol{x}, t))^{p-1}\right). \qquad (7.17)$$

For $p < 1$ equation (7.17) implies that smaller concentration values are stronger retarded than larger ones leading to an asymmetric concentration profile. For an instantaneous point-like injection of solute the self-sharpening concentration profile results in a steep front and an extremely broad concentration tail behind the front. A numerical solution of (7.4) for p=0.5 is shown in Fig. 7.1 after t=2·10^{+6} s (p=0.5, D_{11}=6.6·10^{-6} m^2 s^{-1}) where a typical concentration profile is plotted along the longitudinal x-axis. At the front, self-sharpening and longitudinal dispersion effects balance out. For continuously injected solute the width of the front does not grow with time but reaches a fixed value which essentially depends on the longitudinal dispersion coefficient [136]. For a point-like

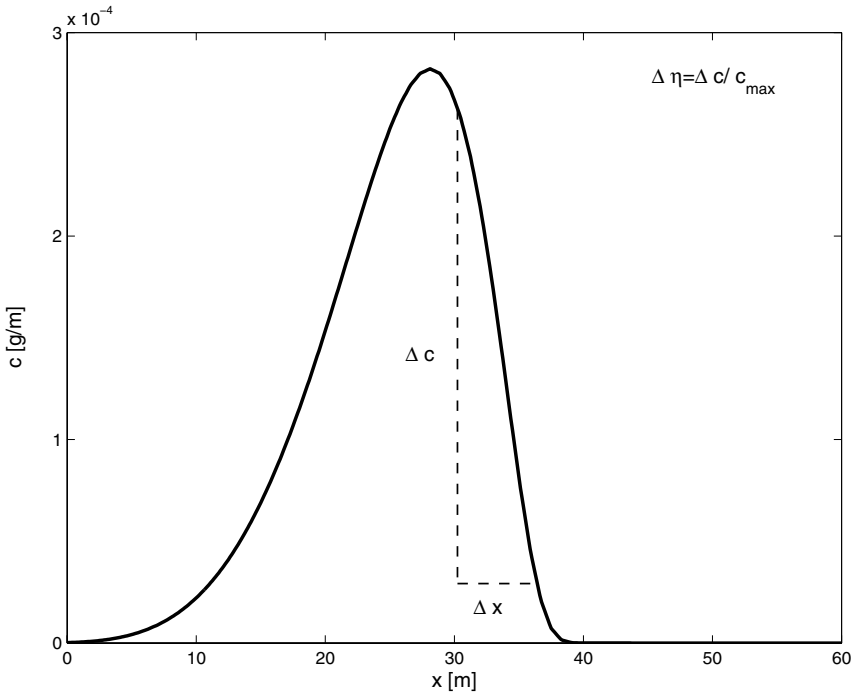

Fig. 7.1 Concentration distribution for Freundlich adsorption
illustration of the relative concentration decrease per cell $\Delta\eta$

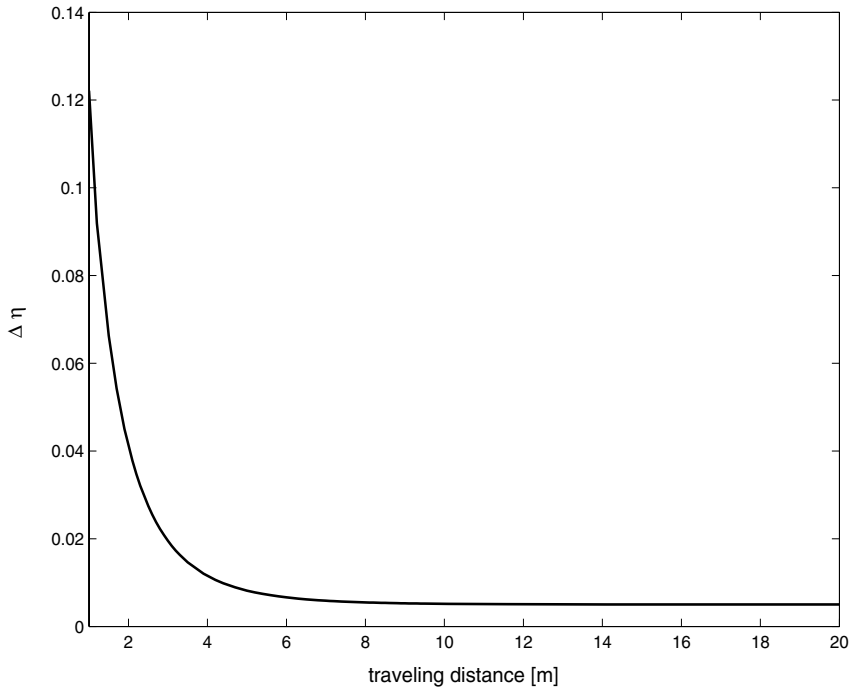

Fig. 7.2 Relative concentration decrease per cell as a function of the travelling distance

injection one calculates the steepness at the front as the relative concentration decrease at the front edge, see Fig. 7.1. For small travel distances dispersive spreading and self-sharpening compete with each other. With travel distance the influence of the non-linear retardation increases. Finally, dispersive spreading and self-sharpening balance out and a constant front angle results, see Fig. 7.2.

The strong asymmetry of the profile is shown in the spatial moments as well. In contrast to linear transport theory, higher cumulants do not vanish and no moment becomes irrelevant with large times. In other words, all cumulants are necessary in order to describe the shape of the profile properly which clearly is a consequence of the extremely asymmetric concentration distribution. Therefore, standard spatial moment analysis cannot be used for a unique identification of the transport parameters. In Fig. 7.3 the second central longitudinal moment divided by t^p is shown against time for two different longitudinal dispersion coefficients both for transport with linear and non-linear adsorption (p=0.5). The longitudinal dispersion coefficients differ by a factor 10. However, in the case of non-linear adsorption the second central spatial moments do not quantitatively show the difference. It implies that standard spatial moments should not be used to infer dispersion coefficients.

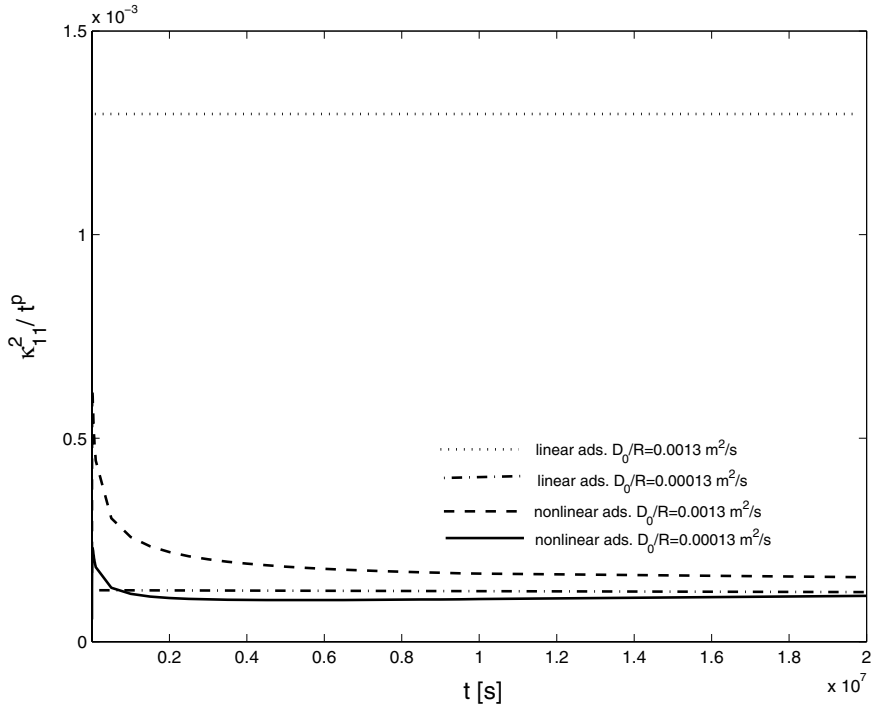

Fig. 7.3 Longitudinal second spatial moment divided by t^p against time for two different longitudinal dispersion coefficients for transport with linear and non-linear adsorption

Therefore, one proposes to identify transport parameters directly from the homogeneous advection-dispersion equation (7.1) with $\lambda_i = 0, \quad i = 1, 2, \ldots n$ by multiplying it with powers of the space vector $\boldsymbol{x}^k$ or time t^k and consecutive integration over space or time. Consequently, the identification method leads to expressions which depend on dissolved as well as adsorbed concentrations.

Definition of Transport Parameters by Means of General Spatial Moments

To obtain the transport velocity in the i-direction one multiplies the transport equation (7.1) by x_i, the i^{th} component of the space vector, and integrate over space:

$$u_i \equiv \frac{\partial_t \int d^d x x_i (c^l(\boldsymbol{x}, t) + k_d (c^l(\boldsymbol{x}, t)^p))}{\int d^d x c^l(\boldsymbol{x}, t)}. \qquad (7.18)$$

For shorter notation one defines $k_d = (1-\phi)\rho_r K_{nl}/\phi$. Analogously, one obtains the dispersion coefficient by multiplication with x_i^2 and integrating over space. One ends up with

$$D_{ii} \equiv \frac{\partial_t \int d^d x x_i^2 (c^l(\boldsymbol{x},\ t) + k_d (c^l(\boldsymbol{x},\ t)^p))}{2\int d^d x c^l(\boldsymbol{x},\ t)} - u_i \frac{\int d^d x x_i c^l(\boldsymbol{x},\ t)}{\int d^d x c^l(\boldsymbol{x},\ t)}. \qquad (7.19)$$

The difference between standard spatial moment analysis and the above definition is that in (7.18) and (7.19) the spatial moments of the total concentration normalised by the mobile mass instead of normalised spatial moments of the mobile concentration were used.

At first glance, the difference might appear minor. But if one applies the new identification rule to the same dissolved solute concentration data as used in Fig. 7.3 one becomes aware of the important difference. The result is plotted in Fig. 7.4 and Fig. 7.5. In both cases, the simulation results for the groundwater velocity and the dispersion coefficient are compared with theoretical parameters. In contrast to Fig. 7.3, the longitudinal dispersion coefficients are now identified very precisely. It demonstrates that the rules (7.18) and (7.19) are appropriate to quantify the transport velocity and the dispersion coefficients correctly. Note that for p=1, (7.18) and (7.19) reduce to the usual identification of transport parameters for transport in uniform flow fields.

Furthermore, the method of general spatial moments can be used for estimation of the numerical dispersion and therefore for a validation of numerical codes and simulations. In Fig. 7.6 the calculated and the actual longitudinal dispersion is shown. The difference between both allows to quantify numerical effects, which later have to be taken into account in the interpretation of the general spreading behaviour of a solute.

Definition of Transport Parameters by Means of General Temporal Moments

The method presented above can be extended for identification of transport parameters from temporal moments of breakthrough curves characterised by the inflow-outflow boundary conditions as given in (7.12) - (7.13).

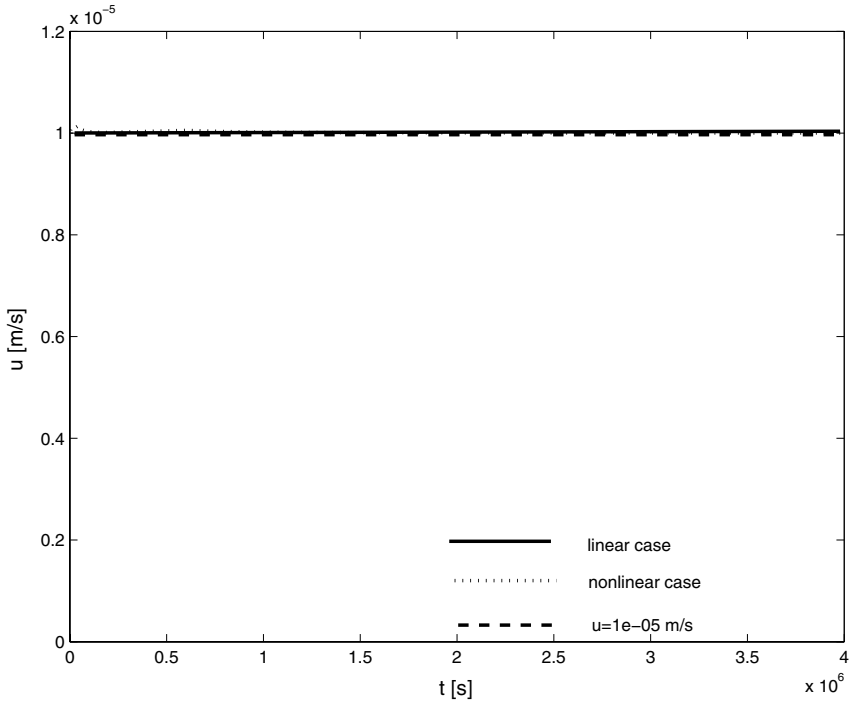

Fig. 7.4 Comparison between calculated and simulated velocity for transport with linear and non-linear adsorption

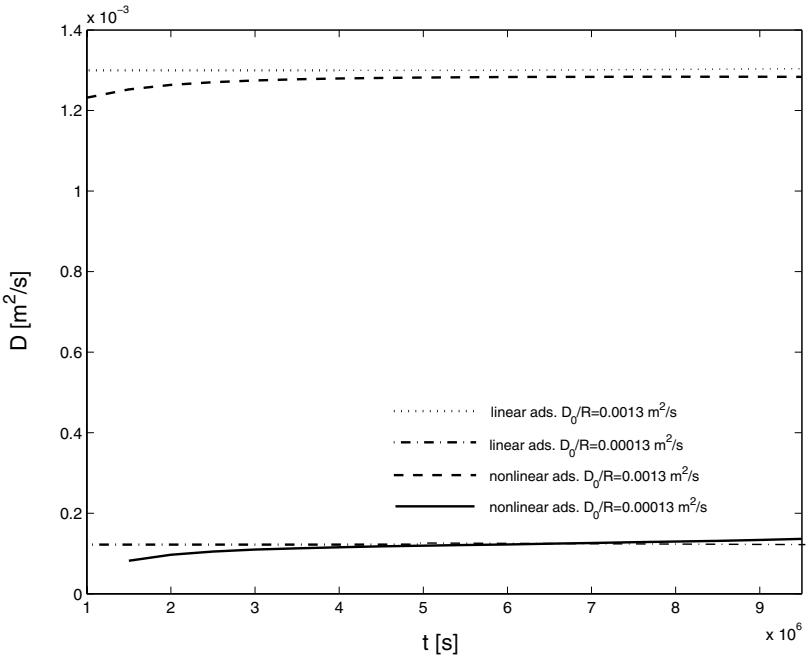

Fig. 7.5 Calculated and simulated dispersion coefficient for transport with linear and non-linear adsorption and two different longitudinal coefficients

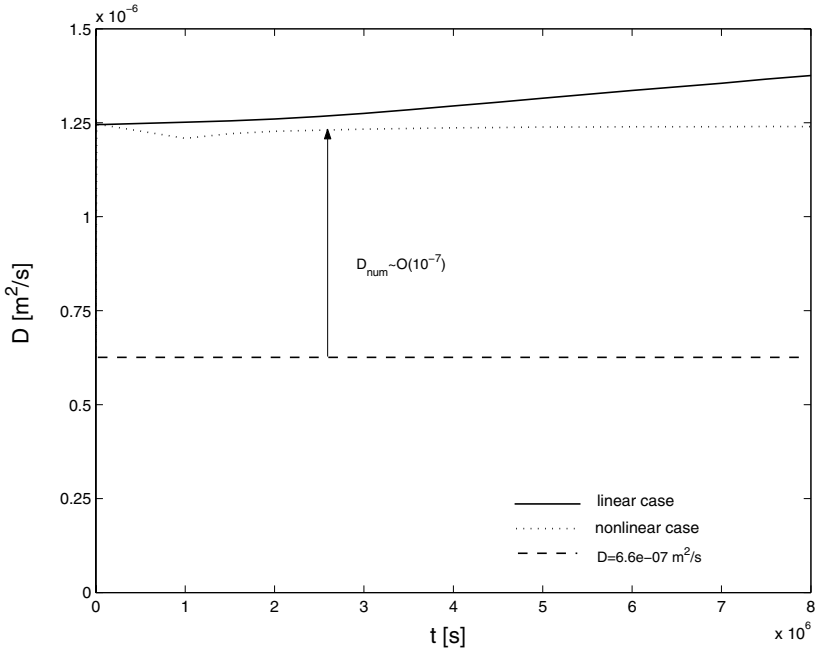

Fig. 7.6 Numerical dispersion with linear and non-linear adsorption
Estimation for p = 0.5 and Co = 0.1

For this reason, one multiplies (7.1) and (7.12) - (7.13) by powers of time t^k and integrate over time. For the transport velocity at location x_i in the domain we end up with:

$$u_i \equiv \frac{m_0}{m_1} x_i + k_d \frac{\int_0^{x_i} dx'_i m_0^{ads}}{m_1} . \qquad (7.20)$$

The dispersion coefficient is given as:

$$D_{ii} = \frac{m_0 u_i^2}{2} \frac{u_i m_{2c}^d + 2k_d \int_0^{x_i} \left(\frac{m_1 m_0^a}{m_0} - m_1^a \right) dx'_i}{\int_0^{x_i} dx'_i \left(m_0 + k_d m_0^{ads} \right)^2} . \qquad (7.21)$$

In the expressions above m_k, k=0,1,2 denotes the k^{th} temporal moment of dissolved concentrations

$$m_k = \int_0^\infty t^k c^l(x_i, t)\,dt. \qquad (7.22)$$

and m_k^{ads} the k^{th} temporal moment of adsorbed concentrations:

$$m_k^{ads} = \int_0^\infty t^k (c^l)^p(x_i, t)\,dt. \qquad (7.23)$$

7.1.2.2 General Transport Case

Expressions (7.18) and (7.19) can easily be extended to a general transport case with radioactive decay and different adsorption isotherms. Accordingly, the groundwater velocity and the dispersion coefficient for the i^{th} nuclide read as:

$$u_j^i \equiv \frac{\partial_t \int d^d x x_j (c_i^l(\boldsymbol{x}, t) + c_i^{ad}(\boldsymbol{x}, t))}{\int d^d x c_i^l(\boldsymbol{x}, t)} + \lambda_i \frac{\int d^d x x_j (c_i^l(\boldsymbol{x}, t) + c_i^{ad}(\boldsymbol{x}, t))}{\int d^d x c_i^l(\boldsymbol{x}, t)} - \lambda_{i-1} \frac{\int d^d x x_j (c_{i-1}^l(\boldsymbol{x}, t) + c_{i-1}^{ad}(\boldsymbol{x}, t))}{\int d^d x c_i^l(\boldsymbol{x}, t)} \qquad (7.24)$$

and

$$D^i_{jj} \equiv \frac{\partial_t \int d^d x x_j^2 (c_i^l(\boldsymbol{x},\, t) + c_i^{ad}(\boldsymbol{x},\, t))}{2\int d^d x c_i^l(\boldsymbol{x},\, t)} - u_i \frac{\partial_t \int d^d x x_j c_i^l(\boldsymbol{x},\, t)}{\int d^d x c_i^l(\boldsymbol{x},\, t)}$$

$$+ \lambda_i \frac{\int d^d x x_j^2 (c_i^l(\boldsymbol{x},\, t) + c_i^{ad}(\boldsymbol{x},\, t))}{2\int d^d x c_i^l(\boldsymbol{x},\, t)} \qquad (7.25)$$

$$-\lambda_{i-1} \frac{\int d^d x x_j^2 (c_{i-1}^l(\boldsymbol{x},\, t) + c_{i-1}^{ad}(\boldsymbol{x},\, t))}{2\int d^d x c_i^l(\boldsymbol{x},\, t)}$$

The isotherm c_i^{ad} may describe Langmuir type sorption processes or first-order kinetic sorption. In the latter case, the isotherm is an integral expression of the mobile concentration and therefore non local in time. However, the general definitions (7.24) and (7.25) also hold in these cases.

In Fig. 7.7 one plots the dispersion coefficient for adsorbing transport with no decay and with a Langmuir isotherm calculated by using equation (7.25) on the one hand and the second central moment on the other hand (the second central moment $\kappa = 7.5 \cdot 10^{-3}$, b=50 $(\mathrm{g\ m^{-1}})^{-1}$). As one can see, the second central moment fails to reproduce the correct dispersion value for short travel times. In contrast, the identification by means of (7.25) reproduces very well the dispersion coefficient at any time. The same behaviour can be observed for transport with first order kinetic adsorption plotted in Fig. 7.8. Obviously, the standard spatial moment analysis overestimates the theoretical value of the dispersion coefficient, quite contrary to the identification by using equation (7.25).

7.1.3 Check of the Total Mass

For an instantaneous solute injection the total amount of the i^{th} nuclide present in the soil system at time $t > 0$ is given as the sum of the dissolved and adsorbed mass

$$M_i(t) = \phi \int_\Omega c_i^l(\boldsymbol{x},\, t)\, dV + (1-\phi)\rho \int_\Omega c_i^{ad}(\boldsymbol{x},\, t)\, dV\,. \qquad (7.26)$$

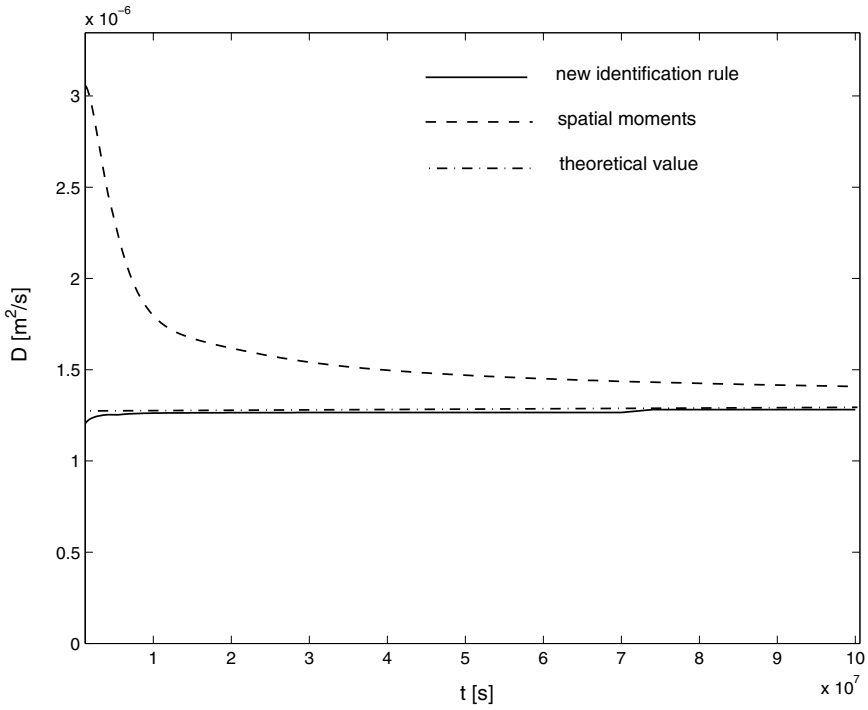

Fig. 7.7 Evaluation of the dispersion coefficient
for a transport with Langmuir adsorption using formula (7.25)

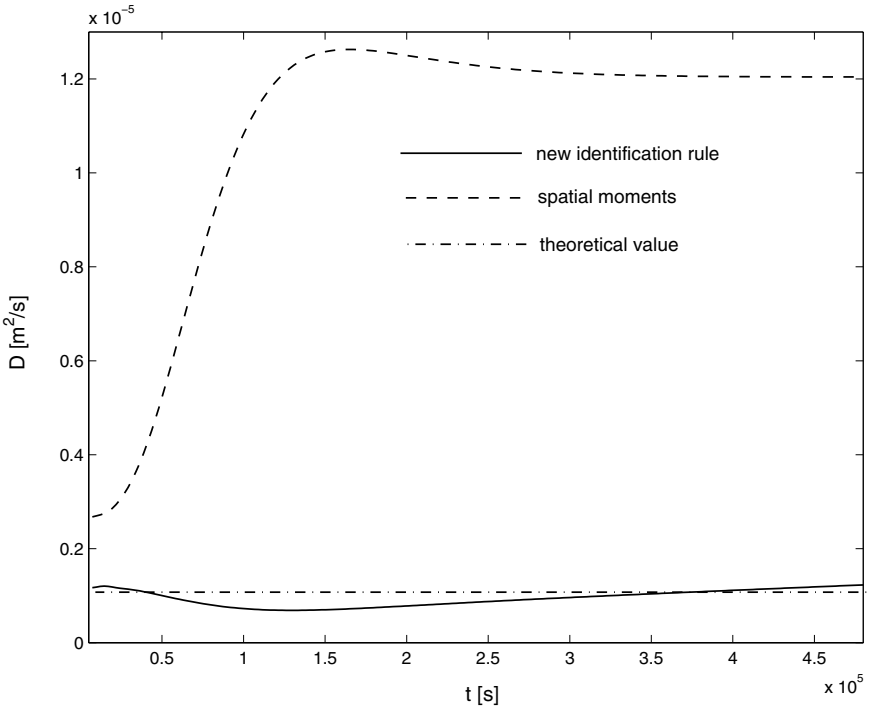

Fig. 7.8 Evaluation of the dispersion coefficient
for a transport with first order kinetic adsorption using formula (7.25)

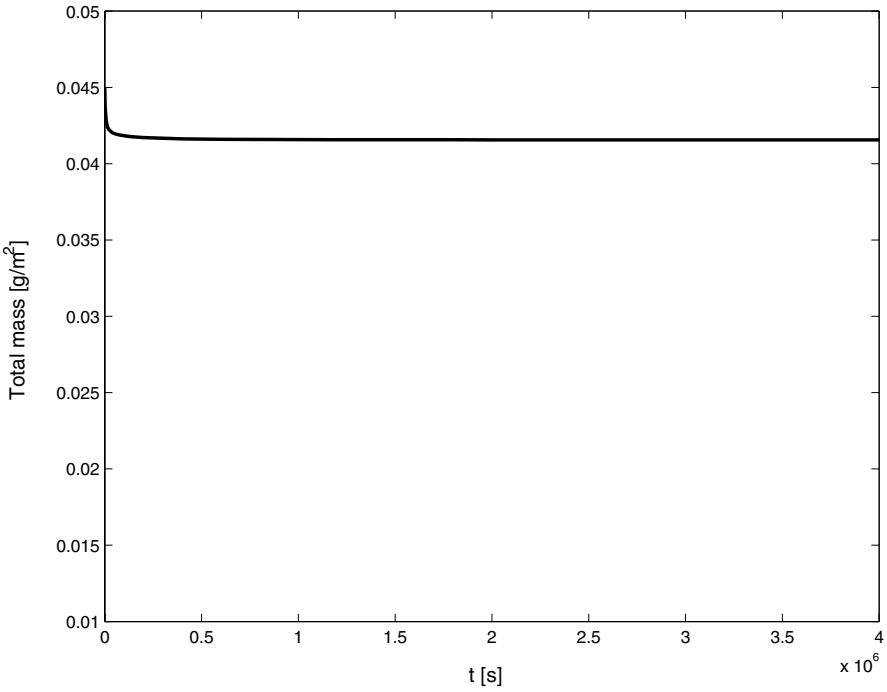

Fig. 7.9 Total mass conservation for transport with non-linear adsorption

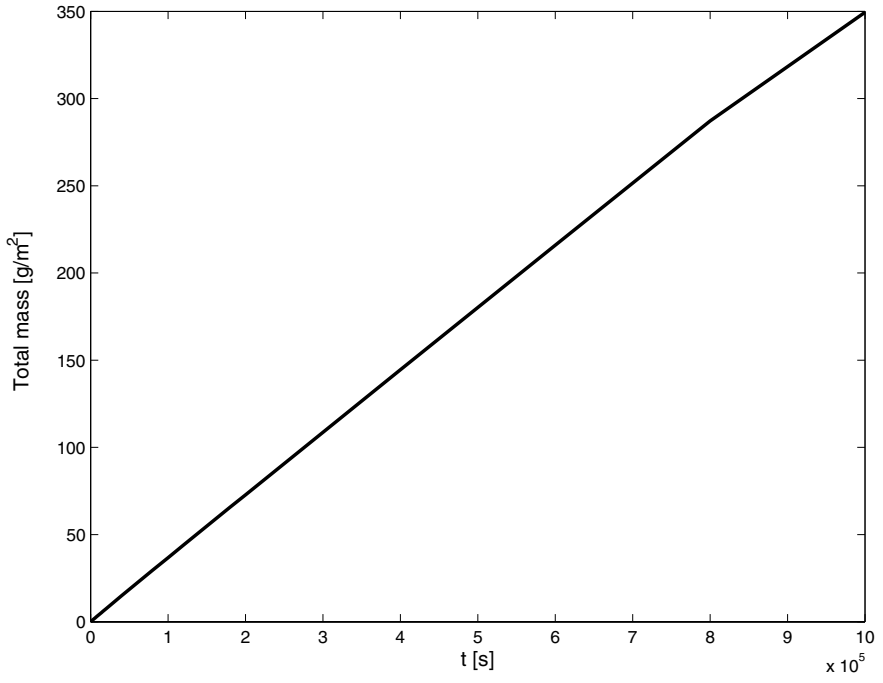

Fig. 7.10 Increase of the total mass as function of time
for transport with non-linear adsorption and continuous solute injection

Moreover, the total mass $M_i(t)$ satisfies

$$\frac{\partial}{\partial t} M_1(t) + \lambda_q M_1(t) = (-\boldsymbol{q}\, c_i^l(\boldsymbol{x}, t) - \phi \boldsymbol{D} \cdot \nabla c_i^l(\boldsymbol{x}, t)) \cdot \boldsymbol{n} \qquad (7.27)$$

$$\frac{\partial}{\partial t} M_i(t) + \lambda_i M_i(t) - \lambda_{i-1} M_{i-1}(t) = (-\boldsymbol{q}\, c_i^l(\boldsymbol{x}, t) - \phi \boldsymbol{D} \cdot \nabla c_i^l(\boldsymbol{x}, t)) \cdot \boldsymbol{n} \qquad (7.28)$$

The terms on the r.h.s. in (7.27) and (7.28) denote the total mass flow over the boundaries.

It is easy to deduce that the total mass of the first nuclide decays exponentially in time if no mass flows over the boundaries

$$M_1(t) = M_1^0 \exp(-\lambda_1 t). \qquad (7.29)$$

Here, M_1^0 is the initial mass of the first nuclide.

If no radioactive decay is considered and no mass abandons the domain, the total mass remains a constant. This is illustrated in Fig. 7.9 where the total mass conservation as a function of time for transport with non-linear adsorption (p=0.75, D_{11}=6.5·10^{-6} m^2 s^{-1})is shown. If the solute is injected continuously in time and undergoes no radioactive decay, its total mass presented in the domain increases continuously with the injection time t:

$$M(t) = M^0(t). \qquad (7.30)$$

This behaviour is illustrated in Fig. 7.10 where the slope of the graph is equivalent to the initial mass M^0 = 0.042 g m^{-2}

7.1.4 Verification of the Front Velocity

The homogeneous transport case with a continuous solute injection can explicitly be solved. The concentration is characterised by a travelling-wave solution [136]. The front moves through the homogeneous medium with a constant wave velocity:

$$a = \frac{u}{r} \qquad (7.31)$$

where r is the a retardation factor defined by the concentration at the inflow boundary c^{in} and the adsorption isotherm c^{ad}

$$r = 1 + \frac{1 - \phi}{\phi} \frac{\mathrm{d}c^{ad}}{\mathrm{d}c} \Bigg|_{c = c^{in}} . \qquad (7.32)$$

In Fig. 7.11 the transport behaviour for a non-linearly adsorbing solute is presented for different times (p = 0.75, D_{11} = 6.5 $\cdot 10^{-6}$ m^2 s^{-1}). Obviously, the solute appears like a travelling wave which moves through the domain with the expected constant velocity (7.32), a = 9.4$\cdot 10^{-5}$ m s^{-1}.

7.1.5 Comparison with Analytical Solutions

7.1.5.1 Analytical Solution for the Linear Transport Case

As already discussed in subsection 7.1.2.1, transport processes with linear adsorption lead to a constant retardation factor R. In this case, the transport equation can easily be solved by means of the Fourier transform method. The resulting solution depends on the initial and the boundary conditions. If one considers the transport of an instantaneously injected nuclide which additionally decays with a decay rate λ, the solution is given by a Gaussian-shaped concentration profile:

$$c(\boldsymbol{x},\ t) \quad = \quad \frac{c^{in}}{8\left(\frac{\pi t}{R}\right)^{\frac{3}{2}}\sqrt{D_{11}D_{22}}} \times$$

$$\exp\left(-\frac{\left(x - \frac{v}{R}t\right)}{4\frac{D_{11}}{R}t}\right)\exp\left(-\frac{y^2 + z^2}{4\frac{D_{22}}{R}t}\right)\exp\left(-\lambda t\right) \qquad (7.33)$$

where c^{in} represents the initial concentration. In the limit $D_{11} = D_{22} = 0$, the solution becomes a Delta distribution:

$$c(\boldsymbol{x},\ t) \quad = \quad c^{in}\delta\left(x - \frac{u}{R}t\right). \qquad (7.34)$$

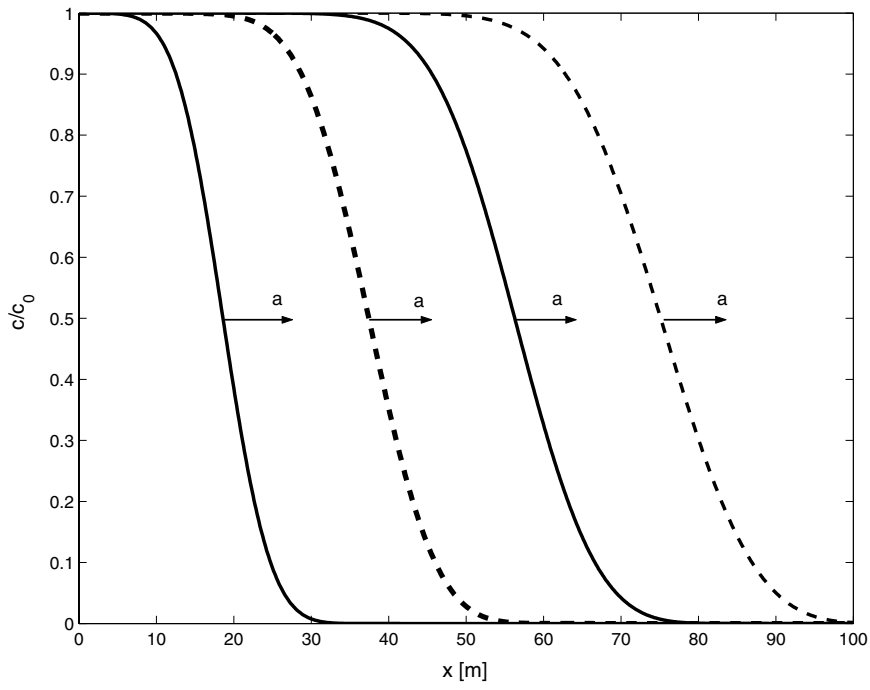

Fig. 7.11 Concentration profiles at different times for non-linear adsorption
The solute is injected continuously.

In Fig. 7.12 and Fig. 7.13 a comparison between the theoretical solution from (7.34) and (7.33) and the numerical calculation by means of r^3t at different times is plotted. In both cases, the numerically calculated concentration profiles agree excellently with the expected concentrations. The numerical dispersion is practically kept at zero because the Courant number used in the calculations is very closed to one ($Co \in [0.99,1]$). The numerical solution for the purely advective case differs slightly from a Delta pulse. This can be explained by the fact that the initially defined concentration profile has to be a smooth function. Accordingly, the default initial concentration is distributed over the neighbouring finite volumes. However, the initial concentration is transported through the domain with a constant velocity and a constant shape. .

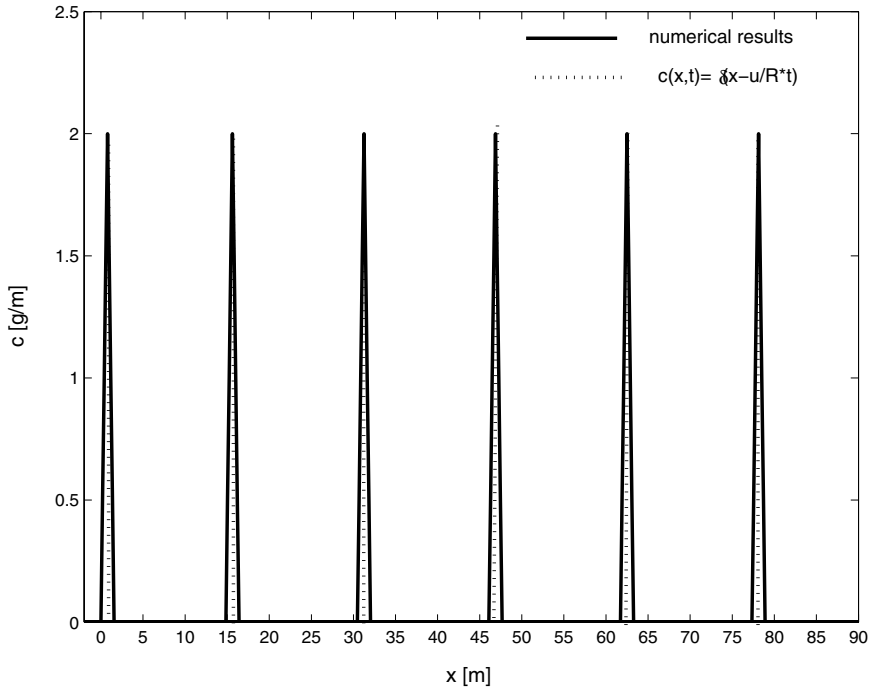

Fig. 7.12 Comparison between the analytical and the numerical solution for purely advective transport (method of characteristics)

7.1.5.2 Analytical Solutions for Pure Advection with Non-Linear Adsorption

In general, the homogeneous transport problem (7.1) with non-linear adsorption has no explicit solution. Only scaling solutions have been investigated so far [33], [65], [137]. However, if we consider only advection dominated transport processes (D_{11}=D_{22}=0) in the x-direction, an asymptotic solution of (7.1) can be found in a closed form.

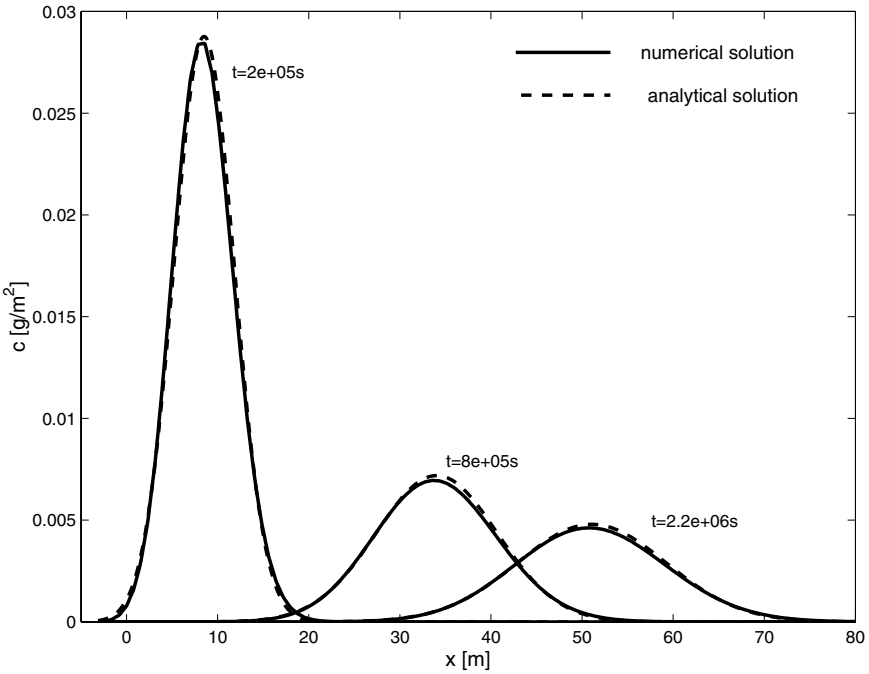

Fig. 7.13 Comparison between the analytical and the numerical solution for transport with linear adsorption, λ = 0

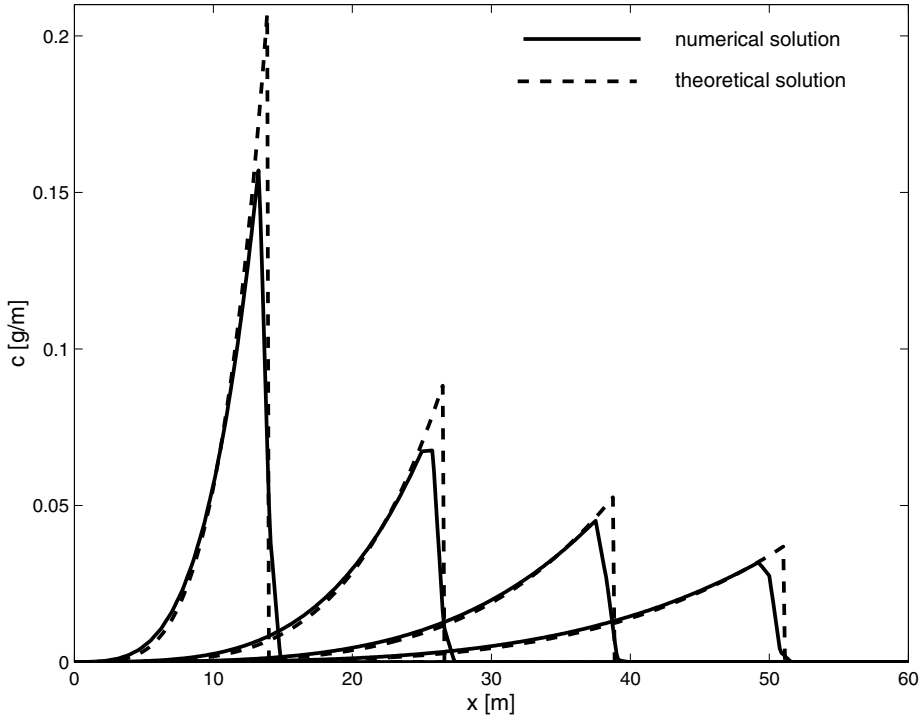

Fig. 7.14 Comparison between numerical and analytical solution for homogeneous, purely advective, non-linear transport

For very large times, the dissolved mass becomes negligible compared to the adsorbed mass. Thus, the total concentration in (7.1) can be replaced by the adsorbed concentration:

$$c(\boldsymbol{x},\ t)\ +\ k_d c^p(\boldsymbol{x},\ t)\ \rightarrow\ k_d c^p(\boldsymbol{x},\ t)\,. \qquad (7.35)$$

The solution of this problem is given as:

$$c(\eta,\ y,\ z)\ =\ \frac{v_0(p\,\eta)}{ut}\delta(y)\delta(z) \quad \text{with} \quad \eta\ =\ \frac{k_d}{t^p \phi^{p-1} u^p M_0^{1-p}}\,x\,. \qquad (7.36)$$

Here, v_0 is the algebraic function

$$v_0\ =\ \begin{cases} (p\,\eta)^{\frac{1}{1-p}} & 0 < \eta < \eta_2\ =\ p^{-1}(1-p)^{-(1-p)} \\ 0 & else \end{cases} \qquad (7.37)$$

and M_0 is the total mass. The last condition follows from the requirement of total solute mass conservation

$$\int v_0^p(p\,\eta)\,d\eta\ =\ 1\,. \qquad (7.38)$$

In order to compare successfully the asymptotic analytical and the numerical solutions, the asymptotic condition (7.35) has to be fulfilled. In the numerical implementation there are two possibilities to achieve the asymptotic regime. On the one hand, one can perform simulations over a very large time period. A disadvantage of this method is that the numerical solution contains information about pre-asymptotic time behaviour and is therefore stronger retarded than the pure asymptotic solution. A second possibility is to start the simulations directly in the asymptotic regime. This can be fulfilled by parameterising the porosity by a very small value $\phi \rightarrow 0$. Under this condition, the numerical and analytical solutions are fully comparable. Thus, in the numerical test case one sets the porosity to $\phi=10^{-6}$, (p = 0.75, u = 10 m s^{-1}). Fig. 7.14 shows the results. As one can see,

at every time the tailing of the numerical and analytical solutions fit very well. The slight difference at the front edge is due to numerical dispersion and the chosen discretisation level.

7.1.5.3 Analytical Solutions for Transport of a Decay Chain

In this subsection one considers the transport of a decay chain in homogeneous media with linear adsorption. Using Laplace transform, one obtains analytical expressions for the transport in a unidirectional steady-state flow field as well as in a radial steady-state flow field in single and multiple porosity media. At least in Laplace domain, all solutions can be written in closed analytical formulae.

7.1.5.4 General Solution of the Transport Model

The system of differential equation (7.4) - (7.5) can be solved by applying Laplace transformation. The solution for the Laplace transform of the dissolved concentrations $\bar{c}_i$ can therefore be written as a linear combination of the fundamental solutions $\overline{\Omega}_i$:

$$\bar{c}_i(\boldsymbol{x}, s) = \sum_{j=1}^{i} A_j^i(s)\overline{\Omega}_j(\boldsymbol{x}, s) \qquad (7.39)$$

with s denoting the Laplace variable. The fundamental solutions $\overline{\Omega}_i$ depend on the flow configuration and solve the single species transport model of the i^{th} species without decay. The solution for the coefficients $A_j^i(s)$ can be obtained in a recursive way by using the relation

$$A_j^i = \frac{R_{i-1}\lambda_{i-1}}{R_i(s+\lambda_i) - R_j(s+\lambda_j)} A_j^{i-1} \qquad \begin{array}{c} j < i \\ R_i \neq R_j \\ R_i\lambda_i \neq R_j\lambda_j \end{array}$$

$$A_j^i = \frac{R_{i-1}\lambda_{i-1}}{R_i\lambda_i - R_j\lambda_j} A_j^{i-1} \qquad \begin{array}{c} j < i \\ R_i = R_j \\ R_i\lambda_i \neq R_j\lambda_j \end{array} \qquad (7.40)$$

$$A_j^i = \frac{R_{i-1}\lambda_{i-1}}{(R_i - R_j)s} A_j^{i-1} \qquad \begin{array}{c} j < i \\ R_i \neq R_j \\ R_i\lambda_i = R_j\lambda_j \end{array}$$

To fully solve the transport problem of an arbitrary length decay chain in porous media, three things have to be done: First, one has to find the basic solutions $\bar{\Omega}_i$ for all flow geometries one is interested in. Second, one has to determine the unknown coefficients $A_j^i(s)$. All other coefficients for the linear combination are given through the recursive formula . The coefficient A_i^i depends on the boundary conditions and will be derived in subsequent sections for some simple cases. Third, one has to find formulae for inverting the Laplace domain solutions to the time domain. Analytical inversion is only possible in some cases of homogenous unidirectional steady-state flow. No inversion formulae were found for radial flow.

7.1.5.5 Transport in Homogeneous Unidirectional Steady-State Flow

One-Dimensional Transport

In this case, the solution of the transport problem can be found in a closed form. The basic solutions in Laplace domain take the form [69]:

$$\begin{array}{lll} \bar{\Omega}_i s,\ x = \exp\left(\frac{x}{2\alpha_{11}}\left(1 - \sqrt{1 + \frac{4\alpha_{11}R_i(s+\lambda_i)}{u}}\right)\right) & x > 0 & \\ & i = 1 \ldots N & \\ \bar{\Omega}_i s,\ x = \exp\left(\frac{x}{2\alpha_{11}}\left(1 + \sqrt{1 + \frac{4\alpha_{11}R_i(s+\lambda_i)}{u}}\right)\right) & x < 0 & \\ & i = 1 \ldots N & \end{array} \qquad (7.41)$$

One considers flow in the infinite half space with a fixed concentration boundary condition at the origin. In the case of a constant Dirichlet boundary condition, $c_i(0,t) = c_i^0$, the Laplace transformed boundary condition takes the form $\bar{c}_i(0,s) = c_i^0/s$. For the delta-type Dirichlet boundary condition

$$c_i(0,t) = \frac{M_i^0}{uR_iA}\delta(t + \Delta t_0),$$

Laplace transform yields $\bar{c}_i(0,t) = M_i^0/(uR_iA)$ (M_i^0 are the masses injected during the Delta-pulse and A is the cross-sectional area of the aquifer). We get the coefficient A_i^i by simply evaluating (7.39) at x=0. Tab. A.1 in appendix A shows the resulting coefficients A_i^i for constant Dirichlet boundary condition (transient and steady-state case) as well as for Delta-type boundary condition. Formulae for the corresponding Cauchy boundary conditions are also included in Tab. A.1. Analytical inverse Laplace transform is possible in this case. All solutions $\bar{c}_i$ can be written as linear combinations of the terms in the left column of table Tab. A.2 in appendix A and can be inverted with the aid of the right column's formulae.

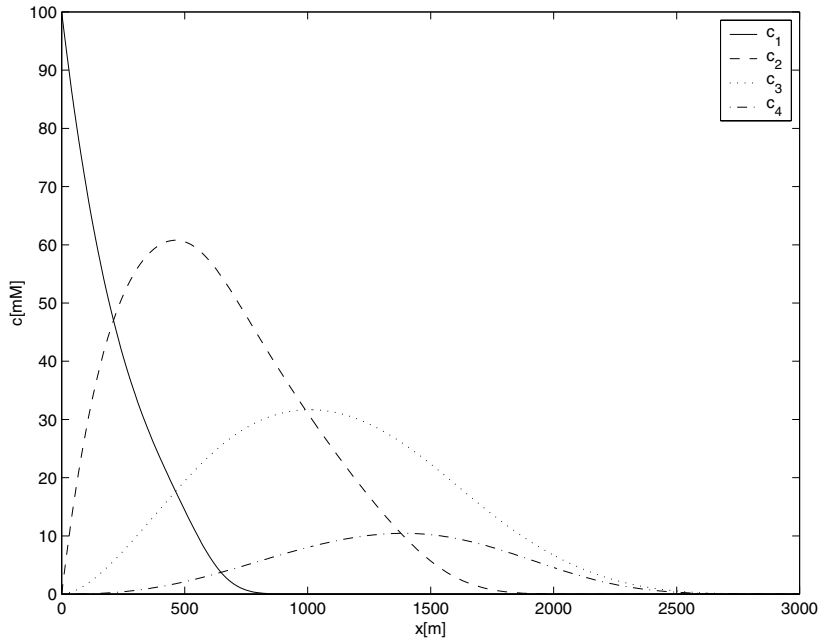

Fig. 7.15 1D transient concentration distribution (constant b.c.)
c_0=(100,0,0,0) mol

Figures Fig. 7.15 - Fig. 7.17 show the resulting concentration distributions for the four-member decay chain at t=3000 d with λ=(7,5,4.5,3.8)·10^{-4} d^{-1}, R=(5.3,1.9,1.2,1.3), u=1 m d^{-1}, α_{11}=10 m, and F=1 m^2. One can see the different chain members successively coming up to the maximum and then vanishing again. Note the long tailing of the concentration distributions in the stationary case. Also note the shape of the second chain member's concentration distribution in Fig. 7.17, which is due to the big difference between R_1 and R_2: the first member acts as a kind of exponentially decaying, nearly non moving source for the second member.

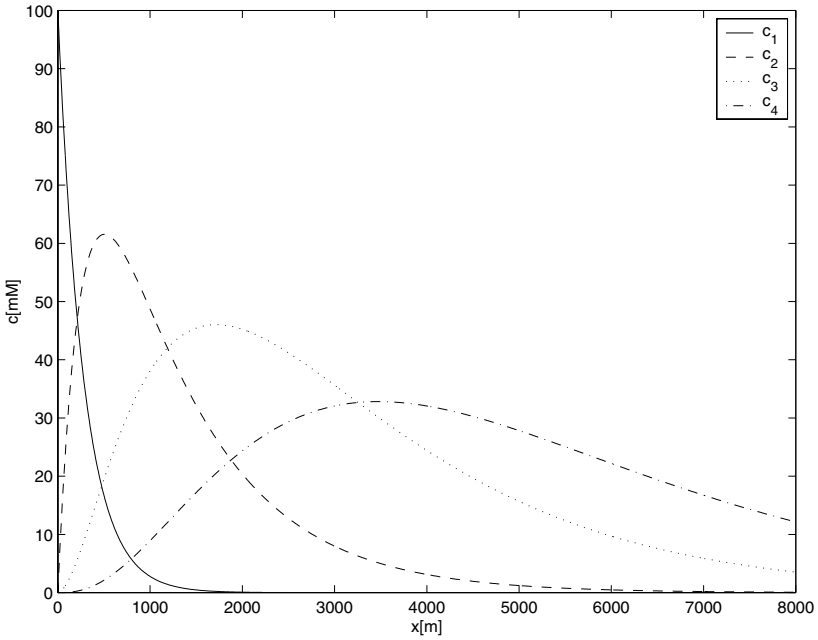

Fig. 7.16 1D stationary concentration distribution (constant b. c.)
c_0 =(100,0,0,0) mol

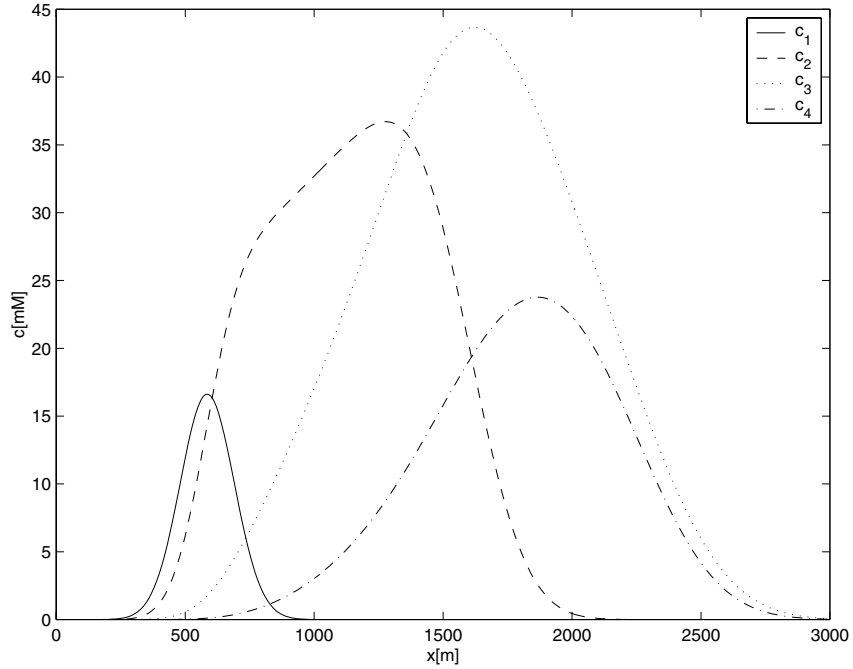

Fig. 7.17 1D transient concentration distribution (d-type b. c.)
c_0 =(1000,0,0,0) mol

Two-Dimensional Transport

Without restriction of generality, one can choose a coordinate system with flow direction parallel to the x-axis. In this case, the basic solutions in Laplace domain are given as:

$$\bar{\Omega}_i(s,\ x,\ y) = \exp\left(\frac{x}{2\alpha_{11}}\right) K_0\left(\frac{\sqrt{\left(1 + \frac{4\alpha_{11}R_i(s + \lambda_i)}{u}\right)\left(x^2 + \frac{\alpha_{11}}{\alpha_{22}}y^2\right)}}{2\alpha_{11}}\right) \qquad (7.42)$$

$$-\infty < x,\ y < \infty,\ i = 1,\ \ldots N$$

K_0 denotes the first-order modified Bessel function of the second kind.

One considers flow in the infinite 2D space with a point source at the origin. Dirichlet boundary conditions can no longer be applied because the concentration distribution diverges at the origin. The point source can have a constant or Delta-type profile in time. Determination of the coefficient $A_i^i(s)$ now requires mass balance conditions instead of boundary conditions. Results for the coefficients $A_i^i(s)$ are shown in Tab. A.3 in appendix A. Analytical inverse Laplace transform is also possible in this case. All solutions $\bar{c}_i$ can be written as linear combinations of the terms in the left column of Tab. A.4 in appendix A and can be inverted with the aid of the right column's formulae.

Fig. 7.18 shows results for the Delta-type point source and for the four-member chain at t=3 000 d, with λ=(7,5,4.5,3.8)·10^{-4} m d^{-1}, R=(5.3,1.9,1.2,1.3), u=1 m d^{-1}, α_{11}=10 m, α_{22}=1 m, M^0=(1000,0,0,0) mol, ϕ=0.15, d=1 m. Note again the shape of the second member's distribution which is highly asymmetric due to the big difference in retardation factors.

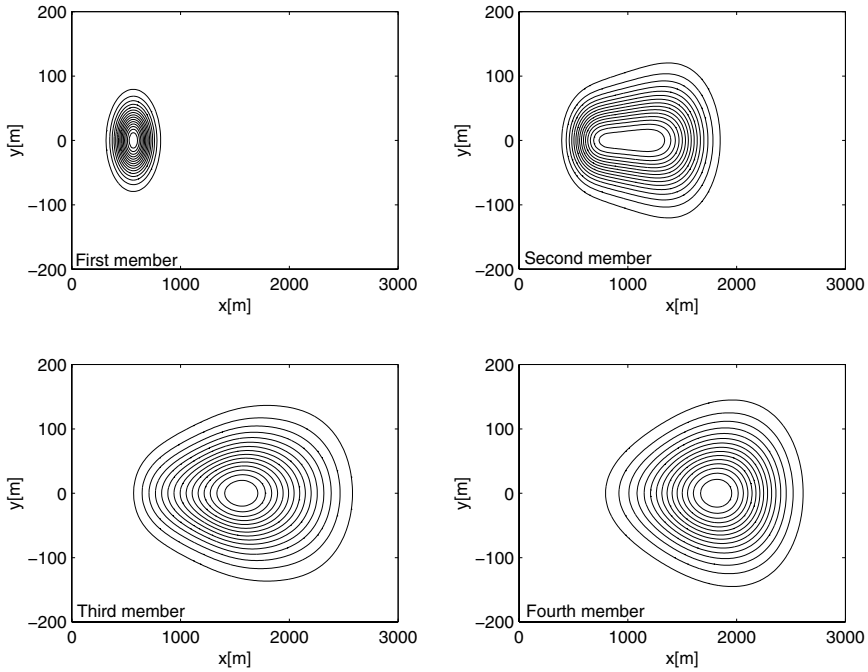

Fig. 7.18 2D transient concentration distribution (δ-type boundary condition)
The outer isolines denote different concentrations in every plot.

Three-Dimensional Transport

Again, one chooses a coordinate system with flow direction parallel to the x-axis. The basic solutions in Laplace domain take the form [69]:

$$\bar{\Omega}_i(s,\ x,\ y,\ z) = \frac{\sqrt{\alpha_{11}u}}{\sqrt{x^2 + \frac{\alpha_{11}}{\alpha_{22}}y^2 + \frac{\alpha_{11}}{\alpha_{33}}z^2}} \times \exp\left(\frac{x + \sqrt{\left(1 + \frac{4\alpha_{11}R_i(s + \lambda_i)}{u}\right)\left(x^2 + \frac{\alpha_{11}}{\alpha_{22}}y^2 + \frac{\alpha_{11}}{\alpha_{33}}z^2\right)}}{2\alpha_{11}}\right) \qquad (7.43)$$

One again considers flow in infinite 3D space with a point source at the origin. This point source can have a constant or Delta-type profile in time. Determination of the coefficient $A_i^i(s)$ is done exactly as in the 2D case. Results are shown in Tab. A.3 in appendix A. Formulae for analytical Laplace inversion are given in Tab. A.4 in appendix A. Application and restrictions are exactly the same as in the 2D case.

Fig. 7.19 shows results for the Delta-type point source and for the four-member chain at t=3000 d with λ =(7,5,4.5,3.8)·10^{-4} d^{-1}, R=(5.3,1.9,1.2,1.3), u=1 m d^{-1}, α_{11} =10 m, α_{22} =1 m α_{33} =1 m, M_0 =(1000,0,0,0) mol, ϕ =0.15. A profile at y=0 and z=0 is shown. Note the shape of the second chain member: It is now decreasing in the plateau region, whereas in the 1D case it was increasing in this region. This fact is due to increased dispersive losses into the two other space directions in 3D compared to 1D.

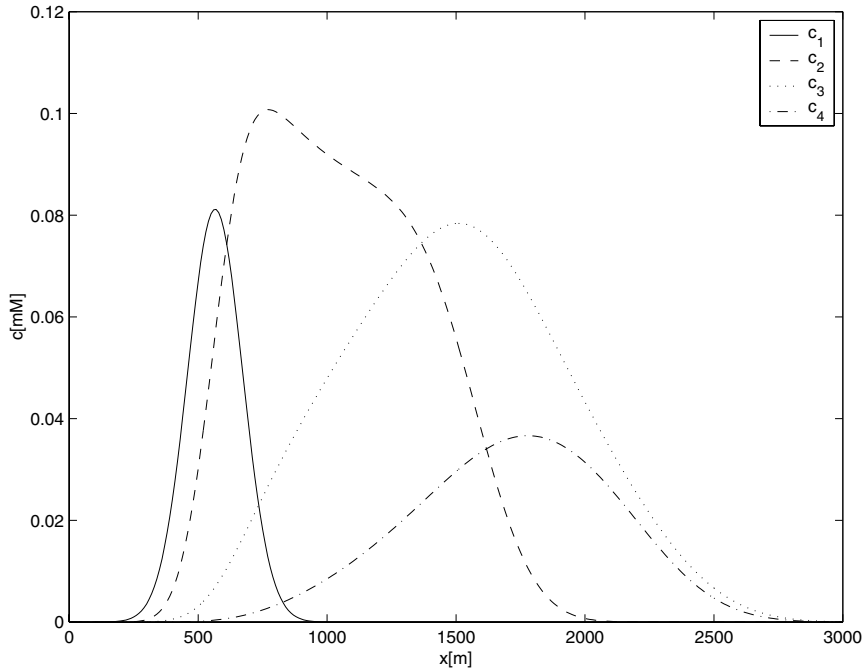

Fig. 7.19 3D transient concentration distribution at y=0 and z=0 for δ-type boundary condition.

Transport in Radial Steady-State Flow

One considers a radially diverging flow field created by an injection well. Concentration gradients in φ- and θ-directions are zero and dispersive terms in these directions can therefore be neglected. Once more, we assume constant dispersivity and neglect molecular diffusion. Then, the governing equation takes the form:

$$R_1 \frac{\partial c_1}{\partial t} = \alpha_r u(r) \frac{\partial^2 c_1}{\partial r^2} - u(r) \frac{\partial c_1}{\partial r} - R_1 \lambda_1 c_1 \qquad (7.44)$$

$$R_i \frac{\partial c_i}{\partial t} = \alpha_r u(r) \frac{\partial^2 c_i}{\partial r^2} - u(r) \frac{\partial c_i}{\partial r} - R_i \lambda_i c_i + R_{i-1} \lambda_{i-1} c_{i-1} \qquad (7.45)$$

α_r is the dispersivity in r-direction. $u(r) = Q/(2\pi d \phi r)$ for 2D radial flow and $u(r) = Q/(4\pi\phi r^2)$ for flow from a point source in 3D infinite space. Q denotes the inflow rate of water at the origin and d the thickness of the aquifer.

Neglecting molecular diffusion is a valid assumption only near the origin. As the flow velocity declines hyperbolically with 1/r, also the dispersive effects become weaker and weaker as r is increasing. Therefore, molecular diffusion should be included in the equation, but for this case, one does not find analytical solutions for the governing equation in Laplace domain.

The basic solutions for 2D radial flow are:

$$\bar{\Omega}_i = \exp\left(\frac{r}{2\alpha_r}\right) \mathrm{Ai}\left(\frac{\left(\frac{R_i(s+\lambda_i)}{\alpha_r G}\right)^{\frac{1}{3}} (4r\alpha_r R_i(s+\lambda_i) + G)}{4\alpha_r R_i(s+\lambda_i)} \right) \qquad (7.46)$$

$$0 < r < \infty, \qquad i = 1, \ldots N$$

Ai is the Airy-Ai function and $G = Q/(2\pi d\phi)$. For 3D radial flow, the basic solutions read:

$$\bar{\Omega}_i = \frac{\exp\left(\frac{r}{2\alpha_r}\right)}{\sqrt{r}} \mathrm{W}\left(-\frac{1}{16} \sqrt{\frac{G}{\alpha_r^3 R_i s + \lambda_i}}, \frac{1}{4}, \sqrt{\frac{R_i(s+\lambda_i)}{\alpha_r G}} r^2 \right) \qquad (7.47)$$

$$0 < r < \infty, \qquad i = 1, \ldots N$$

W is the Whittaker W function and $G = Q/(4\pi\phi)$.

In the case of radial flow, we consider constant and Delta-type concentration boundary conditions at the origin. The only complication is the fact that for all basic solutions $\overline{\Omega}_i(s, 0) \neq 1$. Therefore results are slightly different from 1D unidirectional flow case (Tab. A.7, appendix A).

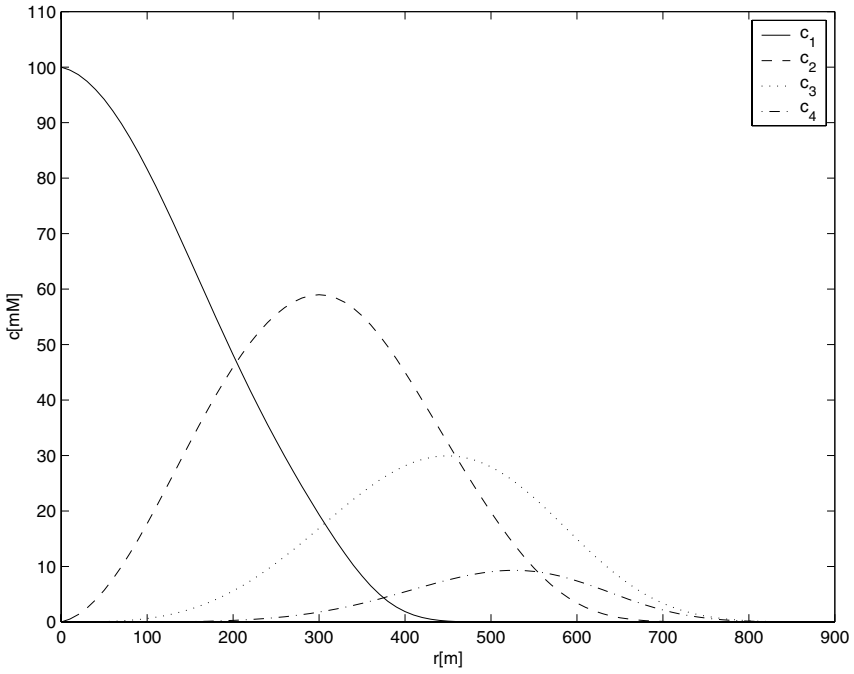

Fig. 7.20 Transient concentration distributions in 2D radial flow for constant boundary condition.

Results for transient concentration distributions with constant boundary conditions in 2D radial flow at t=3000 d with λ=(7,5,4.5,3.8)·10^{-4} d^{-1}, R=(5.3,1.9,1.2,1.3), Q=100 m^3d^{-1}, α_r=10 m, M_0=(100,0,0,0) mol, ϕ=0.15, d=1 m are shown in Fig. 7.20. It is not easy to compare them to the results for unidirectional flow because the flow velocity is decreasing hyperbolically. Thus, the substances do not get so far away from the origin as in unidirectional flow.

Extension to Multiple Porosity Media

One can extend the analysis so far carried out for simple porous media to multiple porous media. In this case, the aquifer contains several overlapping media, in the following called regions, with different retardation and decay coefficients. In one region, the substances are mobile and in the others, they are immobile. Exchange between the regions is governed by a first order law. The immobile region can be arranged parallelly or serially, i.e. exchange can take place between the mobile region and all other regions or between the mobile region and the first immobile region, the first and second immobile region and so on.

The solutions $\bar{c}_i$ can again be written as linear combinations of the basic solutions, see (7.39). The basic solutions are the same as in the simple porous case. The only difference is that $R_i(s+\lambda_i)$ is replaced by $\kappa_i(s)$, which can be an arbitrary function of s, depending on the structure of the medium. The recursive formula for the coefficients is determined as:

$$A_j^i = \frac{\sum_{q=1}^{i-1} a_q(s) A_j^q}{\kappa_i(s) - \kappa_j(s)}, \qquad j < i \qquad (7.48)$$

The coefficient A_i^i can directly be taken from the simple porous case, replacing $R_i(s+\lambda_i)$ by $\kappa_i(s)$.

Although this method in principle allows the description of arbitrarily complex multiple porous media, the formulae soon become extremely complicated. We therefore illustrate the method taking the example of a dual porosity medium, which only contains one immobile region.

In this case, the recursive formula takes the following form:

$$A_j^i = \frac{K_{i-1}A_j^{i-1}}{\kappa_i - \kappa_j} - \frac{\omega_i^*/(\beta_i + \omega_i^*)}{\kappa_i - \kappa_j}\sum_{s=1}^{i-1}\left(\prod_{p=s}^{i-1}\frac{R_p^*\lambda_p^*}{\beta_p + \omega_p^*}\right)\beta_j A_j^s$$

$$j = i-1$$

$$A_j^i = \frac{K_{i-1}A_j^{i-1}}{\kappa_i - \kappa_j} - \frac{\omega_i^*/(\beta_i + \omega_i^*)}{\kappa_i - \kappa_j}\sum_{s=1}^{i-1}\left(\prod_{p=s}^{i-1}\frac{R_p^*\lambda_p^*}{\beta_p + \omega_p^*}\right)\beta_j A_j^s \qquad (7.49)$$

$$+ \frac{R_{i-1}^*\lambda_{i-1}^*/(\beta_{i-1} + \omega_{i-1}^*)}{\kappa_i - \kappa_j}\sum_{s=1}^{i-2}\left(\prod_{p=s}^{i-2}\frac{R_p^*\lambda_p^*}{\beta_p + \omega_p^*}\right)\beta_j A_j^s$$

$$j < i-1$$

with $\omega_i^* = R_i^*(s + \lambda_i^*)$ and κ_i and K_i defined as

$$\kappa_i = R_i(s + \lambda_i) + R_i^*(s + \lambda_i^*)\frac{\beta_i}{\beta_i + R_i^*(s + \lambda_i^*)}$$

$$K_i = R_i\lambda_i + R_i^*\lambda_i^*\frac{\beta_i}{\beta_i + R_i^*(s + \lambda_i^*)} \qquad (7.50)$$

The quantities marked by an asterisk refer to the immobile region. R_i^* is defined as $R_i^* = 1 + ((1 - n^*)/n)\rho K_{d,i}$ and β_i is the first order exchange coefficient between the regions, which can be different for the members of the chain. Figures 7.21 and 7.22 show some results for the double porous case at x=500 m, $\lambda = \lambda^* = 7.5 \cdot 10^{-4}$ d^{-1}, $R = R^* = (5.3, 1.9)$, u=1 m d^{-1}, α_{11}=10 m, c_0=(1,0) mol, $n = n^*$=0.15, A=1 m^2 . For very fast and very slow exchange between the two regions, we can approximate the dual porosity medium by a simple porous medium. For very slow exchange, one can completely neglect the immobile region and for very fast exchange, there is a simple porous substitute with the effective parameters $R_i^e = R_i + R_i^*$ and $\lambda_i^e = (R_i\lambda_i + R_i^*\lambda_i^*)/(R_i + R_i^*)$. The breakthrough curves in the two simple porous substitutes are indicated in the figures together with the breakthrough curve in a dual porosity medium with intermediate exchange.

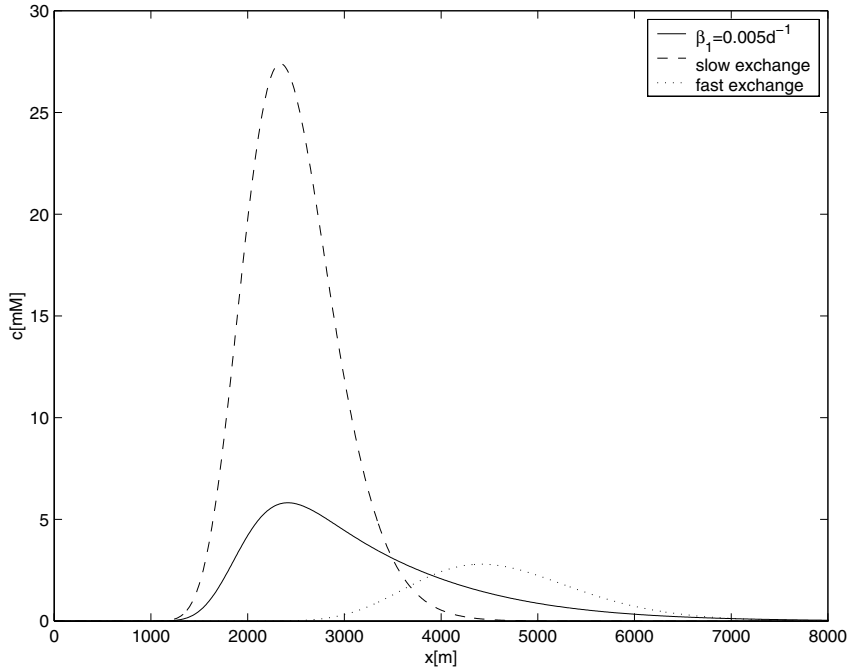

Fig. 7.21 Breakthrough curve of first member in 1D double porous media δ-type boundary condition.

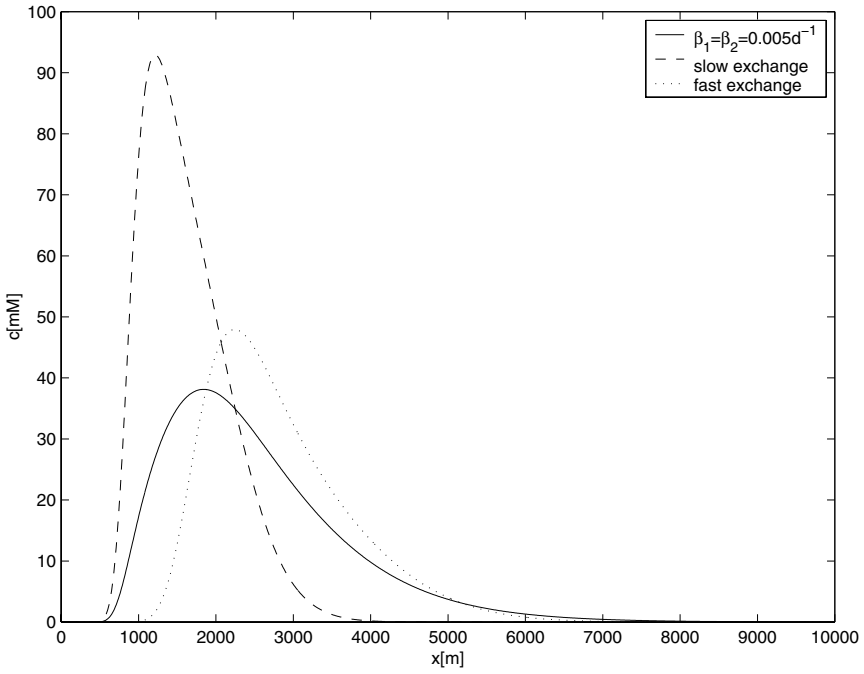

Fig. 7.22 Breakthrough curve of second member in 1D double porous media δ-type boundary condition.

7.1.6 Conclusion

Several tests for verification of r^3t are presented. Moreover, the proposed methods can be used for a-posteriori check of any other numerical codes for simulating solute transport. Adequate checks of numerical routines are very helpful in order to assess numerical effects such as numerical dispersion as well as influence of grid refinement, space and time discretisation or the choice of an appropriate solver for the specific transport problem. For this reason, it is recommended to start with simulations on a very simple level and perform the necessary checks before simulating more complicated flow and transport systems.

In order to verify the reliability of the numerical code the following checks are proposed: back identification of the transport parameters, e.g. transport velocity and dispersion coefficients; check of the total mass; check of the front velocity for transport with a continuous solute injection and comparison with analytical solutions. These checks were used for verification of homogeneous solute transport. The presented results are performed by using the final version of r^3t which uses a second order solver in the advective part. The numerical results are in very good agreement with the expected theoretical values. Especially, the sharpness of the concentration front in the case of non-linear adsorption of Freundlich type is excellently resolved.

7.2 Comparison with Analytical Solutions

To verify the computer code r^3t for linear transport the results of various modellings are compared with analytical solutions. This test cases are described in detail in "r^3t - A Program Suite to Model Transport and Retention of Radionuclides. Test Case Library" [44]. The tests are performed for one-, two-, and thee-dimensional cases. In one- and two-dimensional cases the analytical solutions are calculated with MATHCAD [97].

7.2.1 One-Dimensional Test Cases

In Fig. 7.23 the model for the one-dimensional test case is shown. The model extends to 100 m in length and 10 m in breadth. The right face of the modelled area serves as outflow boundary while the other fronts are impermeable. In the case of continuous injection

the left face serves as inflow boundary, whereas in the case of a pulse like injection it is started with an initial concentration distribution. A parallel flow with constant Darcy velocity is presumed. The parameters used are given in Tab. 7.2.

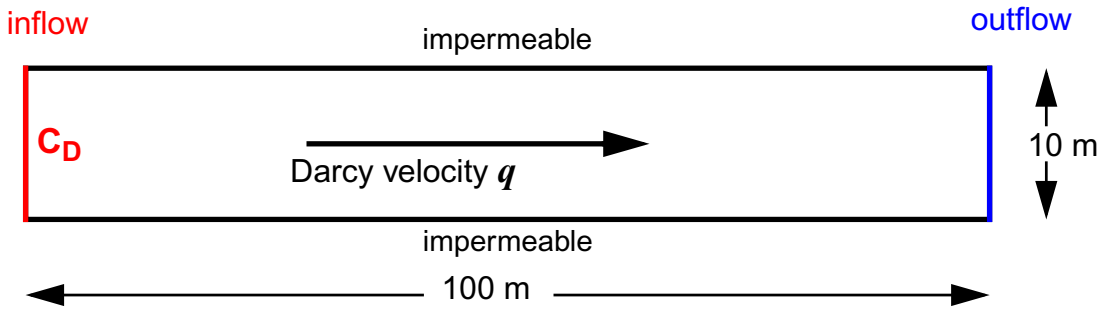

Fig. 7.23 Model of one-dimensional test case

Tab. 7.2 Parameters for one-dimensional models

Darcy velocity q	$3.1689 \cdot 10^{-8}$ m s^{-1}	diffusivity D_m	0.0 m^2 s^{-1}
porosity ϕ	0.2	dispersion α_L	1.0 m
half-life $T_{1/2}$	5 730 y	dispersion α_T	0.0 m
distribution coefficient K_d	0.01 m^3 kg^{-1}		
pulse:		continuous:	
initial distribution (cp. Fig. 7.24)		boundary condition: Dirichlet	
mass M = 1 mol		concentration C_D = 1.0 mol m^{-3}	

7.2.1.1 Pulse Injection

To start with an appropriate initial state the analytical solution is used itself. Therefore the concentration distribution which is shown in Fig. 7.24 is used as initial state. It is a concentration distribution of the pollutant resulting from a δ-shaped injection at the location 10 m which occurred $3.1557 \cdot 10^6$ s before, i.e. 0.1 years. In accordance to the analytical solution the initial concentration depends on half-life, longitudinal dispersion and sorption. The analytical solution reads (cp. section 7.1.5 and [81]):

$$C_\delta(x,\ t) \quad = \quad \frac{C_0}{2nR\pi\sqrt{\alpha_L \frac{ut}{R}}} e^{-\frac{\left(x - \frac{ut}{R}\right)^2}{4\alpha_L \frac{ut}{R}}} e^{-\lambda t} \qquad (7.51)$$

In Fig. 7.24 a cross section of the initial state in x-direction is displayed, whereas in Fig. 7.25 the distribution of the initial concentration is shown as isolines.

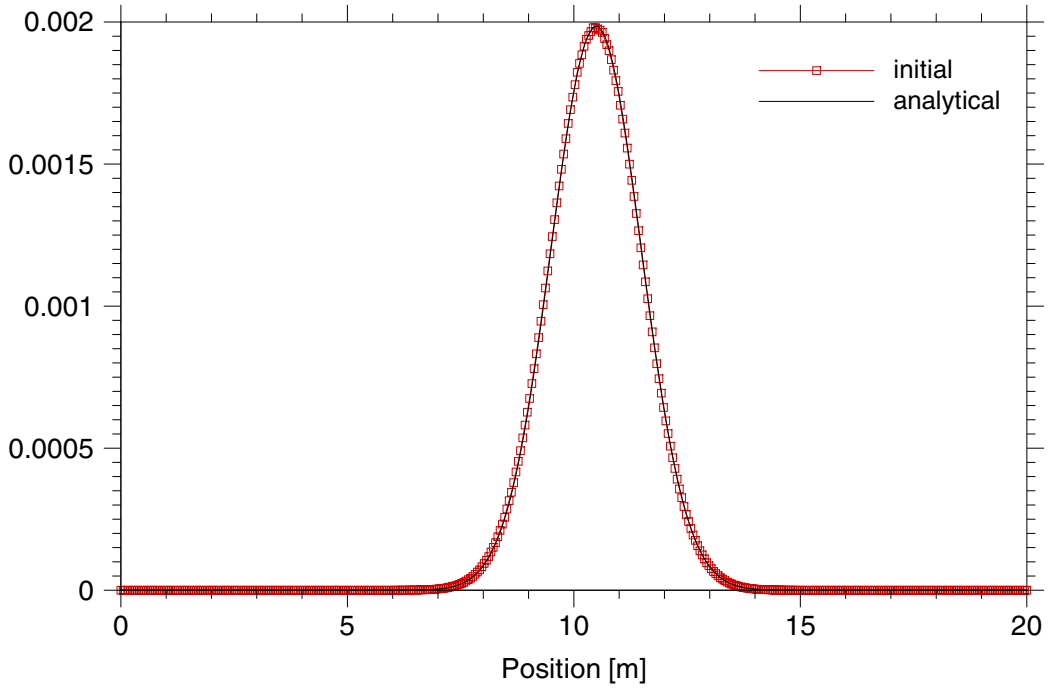

Fig. 7.24 Initial distribution of concentration for a pulse injection in comparison with the analytical solution

Fig. 7.25 Initial concentration distribution for a pulse injection.

Here advection, dispersion, decay, and sorption are simultaneously taken into account. For that purpose the migration of C-14 is modelled with half-life $T_{1/2}$ = 5 730 a and distribution coefficient K_d = 0.01 m^3 kg^{-1}. Longitudinal dispersion length is kept constant at α_L = 1 m. Figures 7.26 and 7.27 show the temporal and spatial concentration development, respectively.

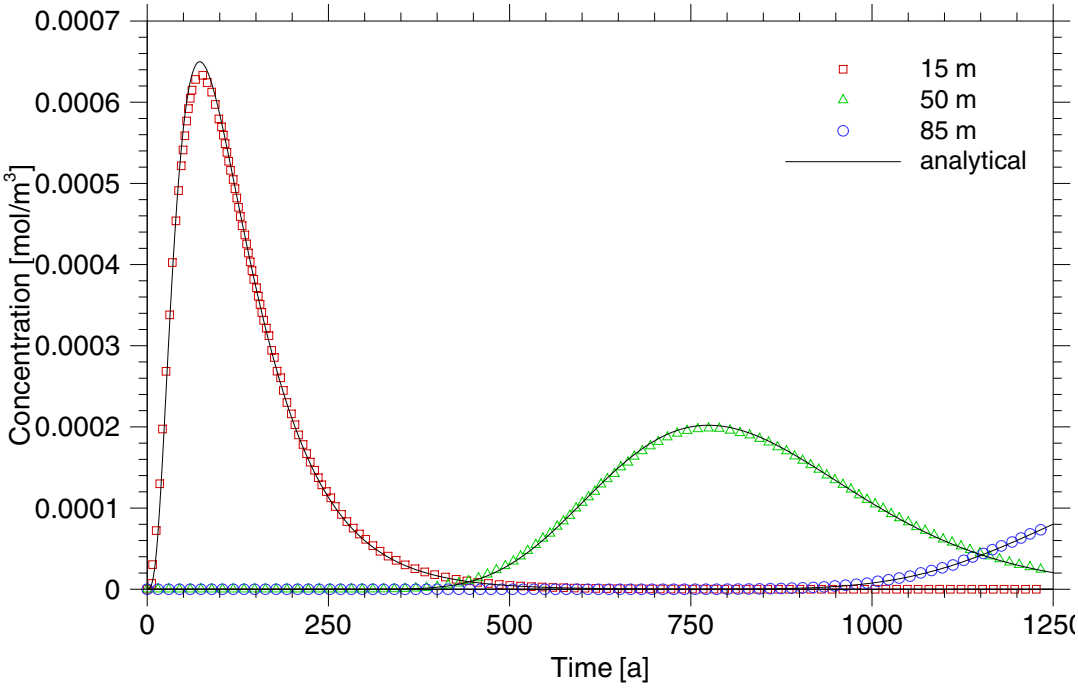

Fig. 7.26 Breakthrough curves considering decay and sorption of C-14
In addition analytical solutions are shown.

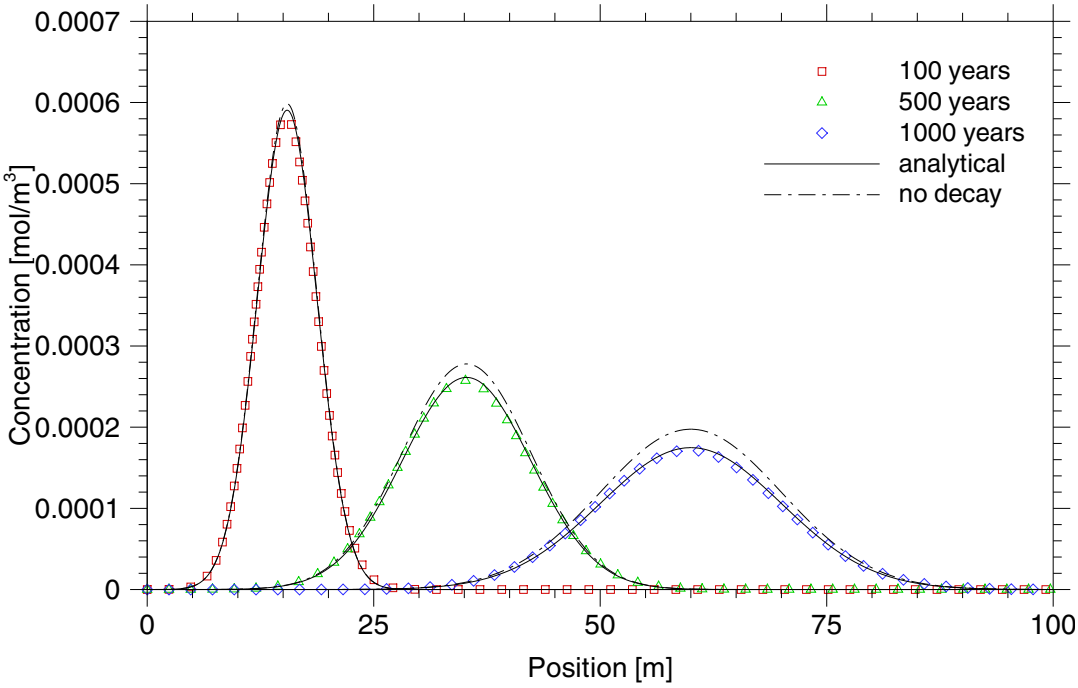

Fig. 7.27 Concentration distribution of C-14 with decay and sorption
In addition analytical solutions are shown.

To show independence of grid alignment the model area is rotated 45 degrees anticlockwise in the x-y-plane as shown in Fig. 7.28. The input data given in Tab. 7.2 are used. Fig. 7.29 and 7.30 show the concentration behaviour with time and in space. There is no influence of the grid orientation recognisable.

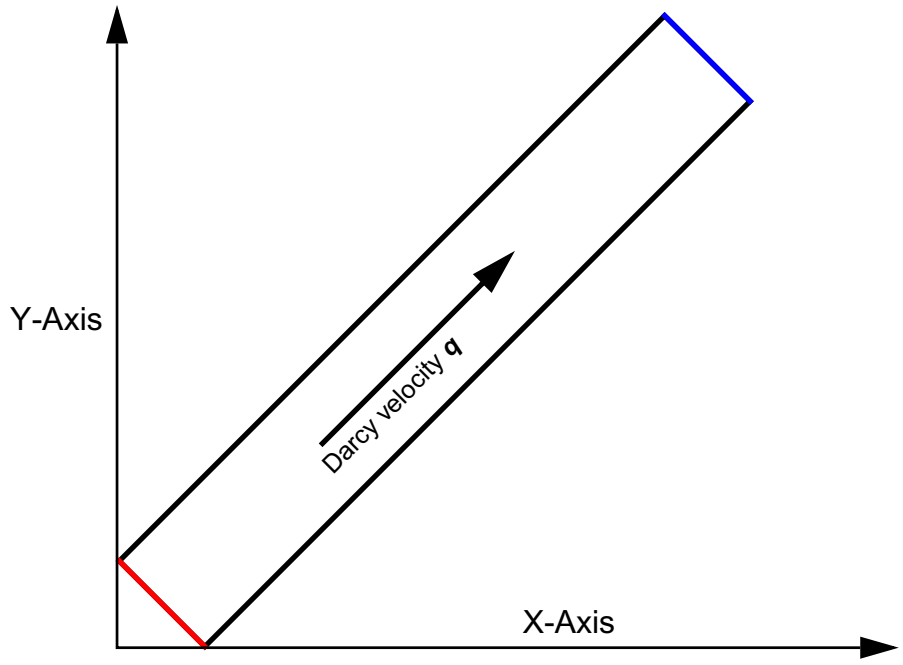

Fig. 7.28 One-dimensional model with rotated model area

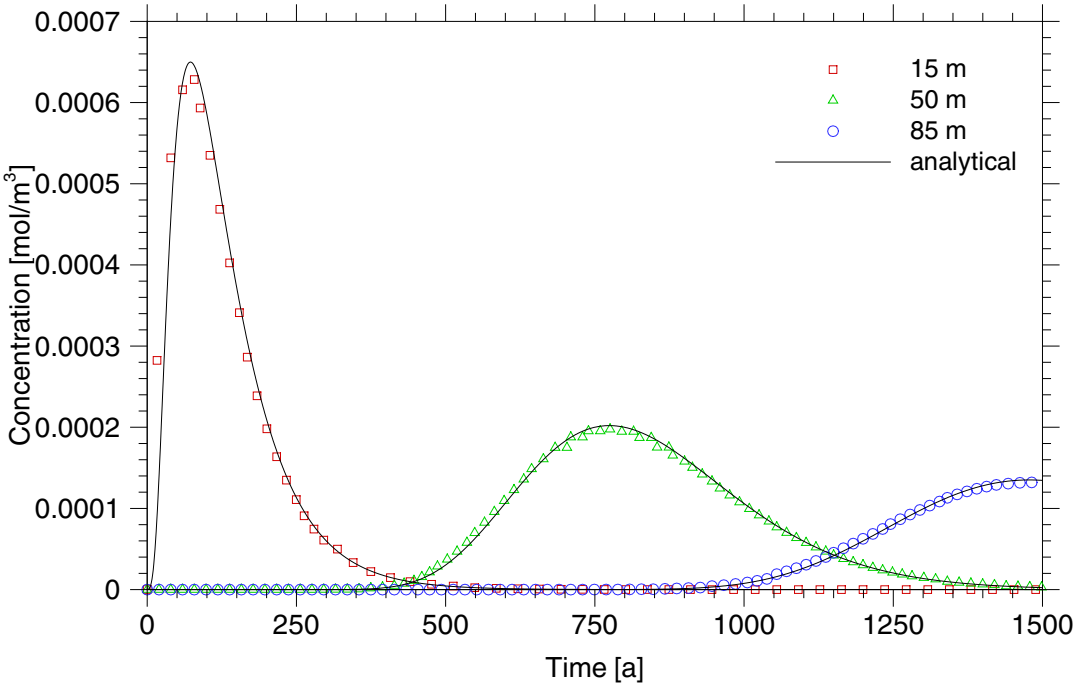

Fig. 7.29 Breakthrough curves considering decay and sorption of C-14 with model area rotated by 45 degrees anticlockwise

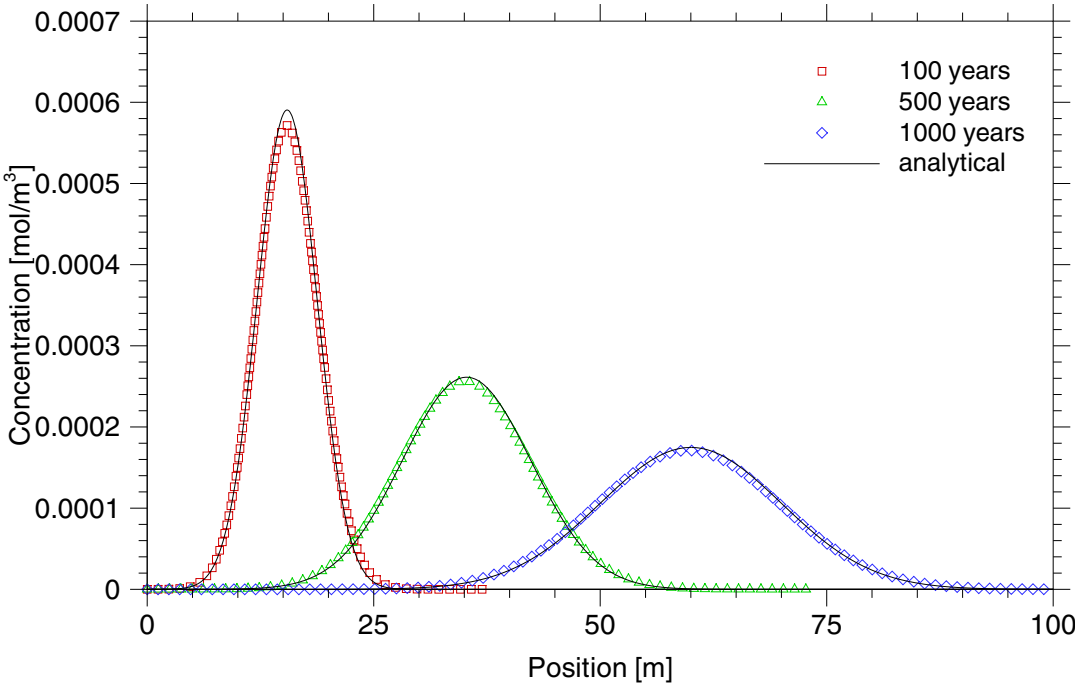

Fig. 7.30 Model rotated by 45°
C-14 with half-life $T_{1/2}$ = 5 730 a and K_d = 0.01 m^3 kg^{-1}

7.2.1.2 Continuous Injection

The one-dimensional analytical solution for continuous injection reads (cp. section 7.1.5 and [81]):

$$C(x,t) = \frac{C_0}{2} e^{\frac{x}{2\alpha_L}} \left(e^{-\frac{x\gamma}{2\alpha_L}} erfc\left(\frac{x - u\gamma\frac{t}{R}}{2\sqrt{\alpha_L u \frac{t}{R}}} \right) - e^{\frac{x\gamma}{2\alpha_L}} erfc\left(\frac{x + u\gamma\frac{t}{R}}{2\sqrt{\alpha_L u \frac{t}{R}}} \right) \right) \quad (7.52)$$

This test case is essentially the same as introduced in Fig. 7.23 except of the continuous inflow. For this case the Darcy velocity is minimally altered to $3.0 \cdot 10^{-8}$ m s^{-1}. The continuous injection is realised by Dirichlet boundary condition at the left face of the model. The concentration is set to C_D= 1 mol m^{-3}. In Fig. 7.31 and 7.32 breakthrough curves and spatial distribution of concentration are depicted. The agreement is very well. Again modellings are performed using a rotated grid, and again no influence of the grid alignment is observed.

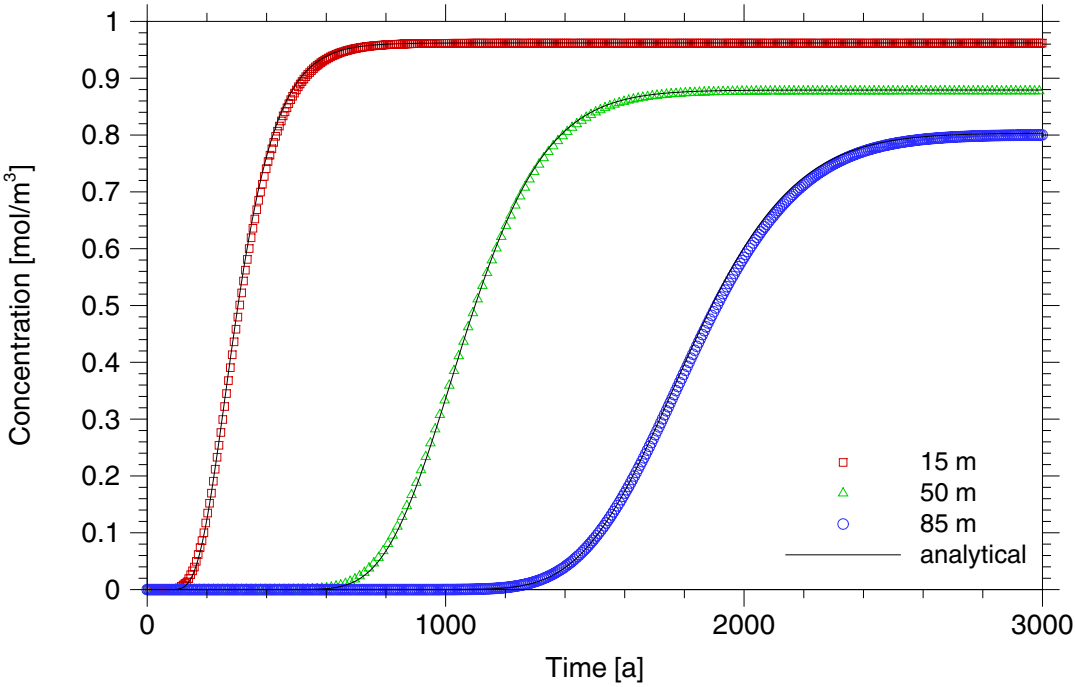

Fig. 7.31 Concentration considering decay and sorption of C-14 versus time ($T_{1/2}$ = 5 730 a, and K_d = 0.01 m^3 kg^{-1}) in model area at 15 m, 50 m and 85 m

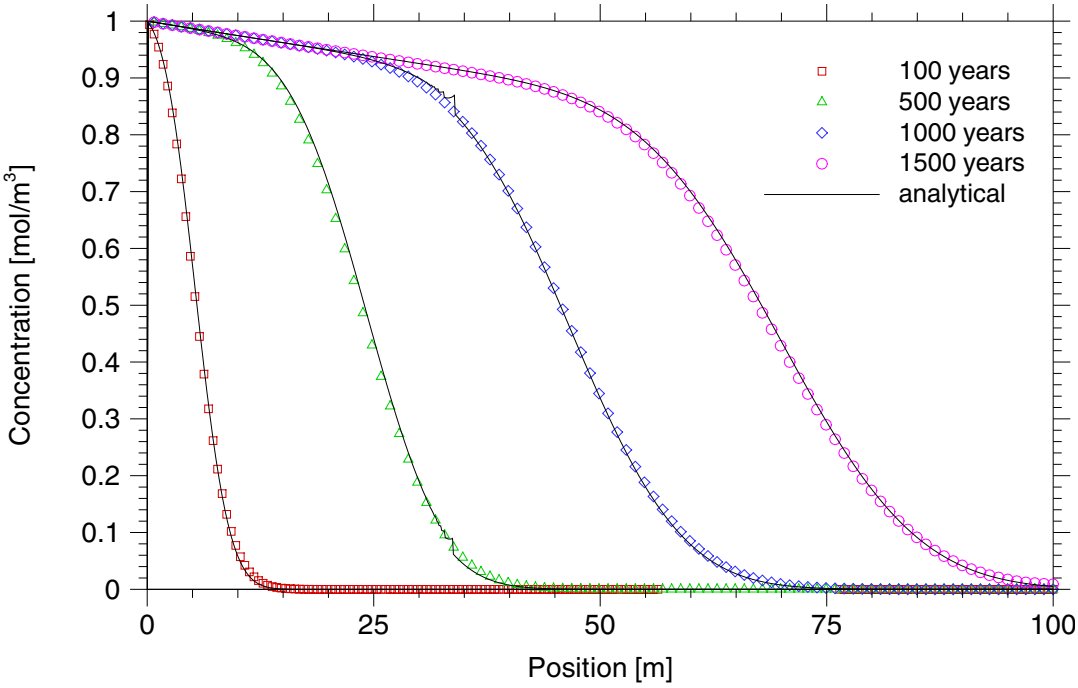

Fig. 7.32 Concentration considering decay and sorption of C-14 ($T_{1/2}$ = 5 730 a, and K_d = 0.01 m^3 kg^{-1}). Comparison with analytical solution.

7.2.2 Two-Dimensional Test Cases

The model for the two-dimensional case is shown in figure 7.33. The model extends to 100 m in length and 50 m in breadth. The right face of the modelling area serves as outflow boundary. The other fronts are impermeable. In the case of continuous injection the point (10,25) serves as inflow point, whereas in the case of a pulse like injection it is started with an initial concentration distribution at that point. A parallel flow with constant Darcy velocity is presumed.

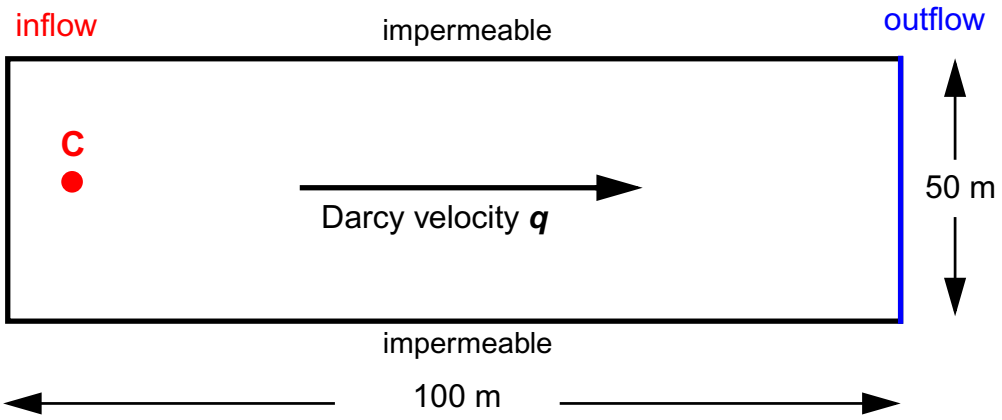

Fig. 7.33 Model of the two-dimensional test cases

Tab. 7.3 Parameters for pulse injection and for continuous inflow

Darcy velocity $\boldsymbol{q}$	$3.1689 \cdot 10^{-8}$ m s^{-1}	diffusivity D_m	$1.0 \cdot 10^{-9}$ m^2 s^{-1}
porosity ϕ	0.2	dispersion α_L	1.0 m
half-life $T_{1/2}$	$1.3639 \cdot 10^{10}$ a	dispersion α_T	0.1 m
distribution coefficient K_d	$1.0 \cdot 10^{-2}$ m^3 kg^{-1}		
location of pollutant source: x = 10 m, y = 25 m			
pulse:		continuous:	
j_m = 10 mol a^{-1}		j_m = 1 mol a^{-1}	
$0 \le t \le 0.1$ a		$0 \le t \le 5000$ a	

7.2.2.1 Point-Like Pulse Injection

The two-dimensional analytical solution for pulse injection reads (cp. section 7.1.5 and [81]):

$$C_\delta(x,\ y,\ t) \quad = \quad \frac{C_0}{4nR\pi\sqrt{\alpha_L\alpha_T}\frac{ut}{R}} e^{-\frac{\left(x-\frac{ut}{R}\right)^2}{4\alpha_L\frac{ut}{R}} - \frac{y^2}{4\alpha_T\frac{ut}{R}}} e^{-\lambda t} \qquad (7.53)$$

The numerical results are compared with the appropriate analytical solutions. Subsequently the Darcy flow is rotated by 26 degree anticlockwise around the z-axis. The left corner at the bottom of the model is set to (0,0) of the coordinate system. All borders of the model area are parallel to the coordinate axes.

In this test case simultaneously advection, dispersion, decay, and sorption are taken into account. The migration of the radionuclide Am-241 with half-life $T_{1/2}$ = 432 a is modelled. The initial pulse is located at the point with x-y-coordinates (10,25). Linear equilibrium sorption is considered by a distribution coefficient set to K_d = 0.01 m^3 kg^{-1}, i.e. the retardation factor amounts to 101. Longitudinal and transversal dispersion length are kept at α_L = 1 m and α_T = 0.1 m.

Fig. 7.34 Initial concentration for a pulse injection at point (10, 25)

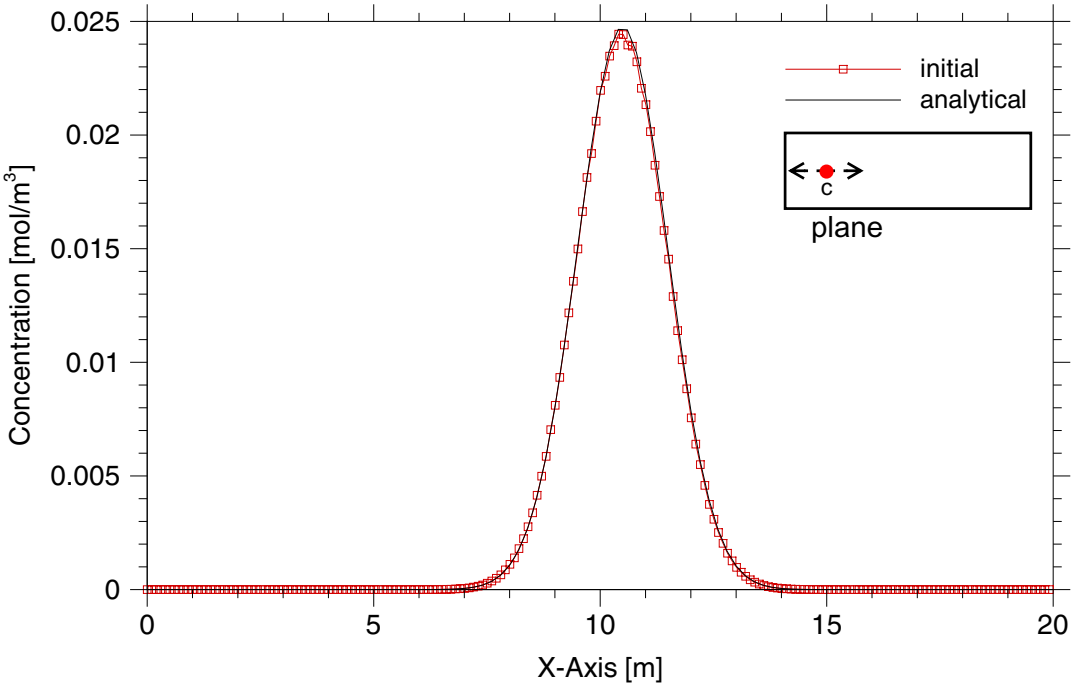

Fig. 7.35 Initial concentration along plane y=25 m at t=0 a

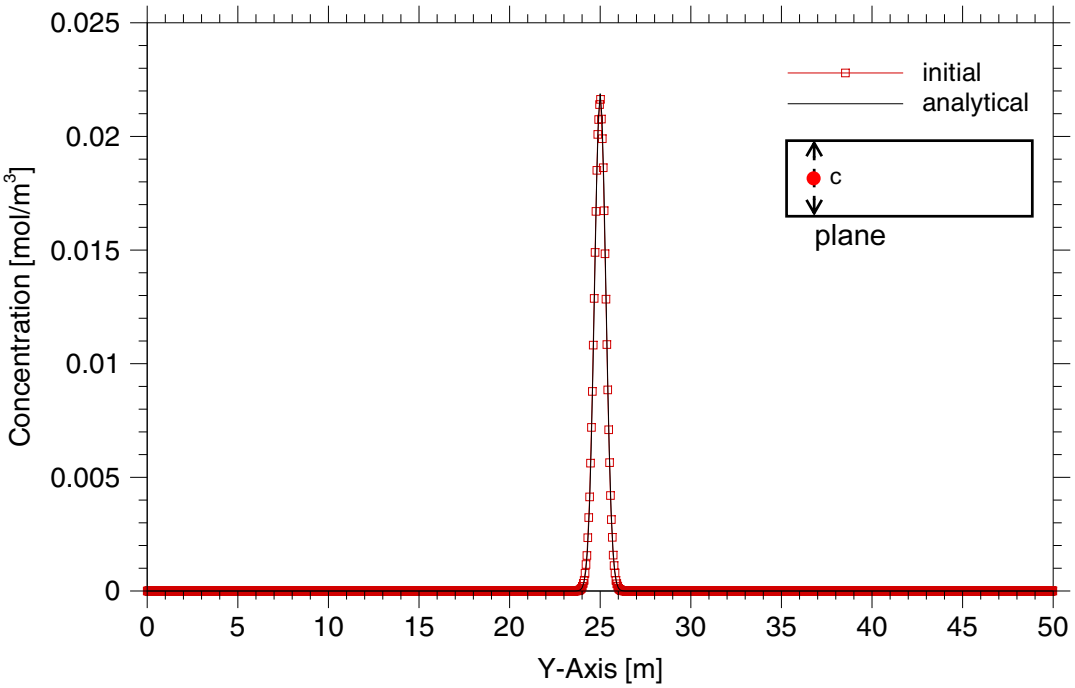

Fig. 7.36 Initial concentration along plane x=10 m at t=0 a

In Figs. 7.34 to 7.36 the initial concentration distribution is shown as a two-dimensional isoline plot in patch mode, as a concentration distribution along x-axis, and as a concentration distribution along y-axis, respectively. One easily recognises that the initial concentration distribution is centred around the point (10,25). In Fig. 7.37 and Fig. 7.38 the analytical and numerical solutions are given at the time of 100 a and 500 a as distributions along the x-axis at y=25 m and along the y-axis at x=15 m and x=35 m. In every test case an excellent agreement can be found.

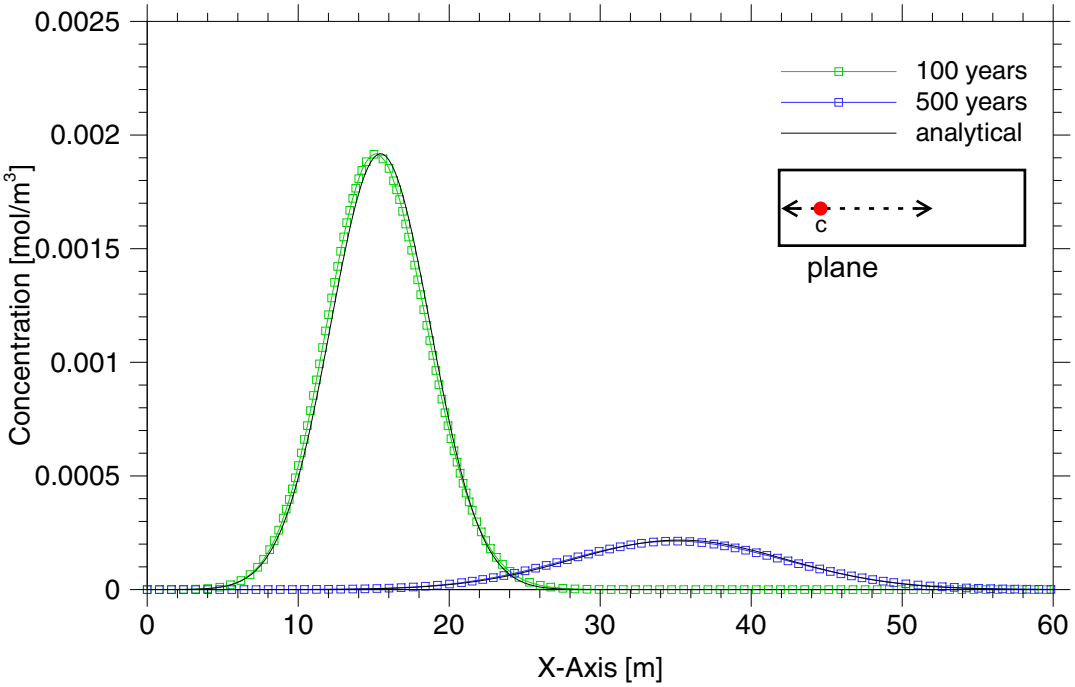

Fig. 7.37 Concentration at two times along plane y=25 m

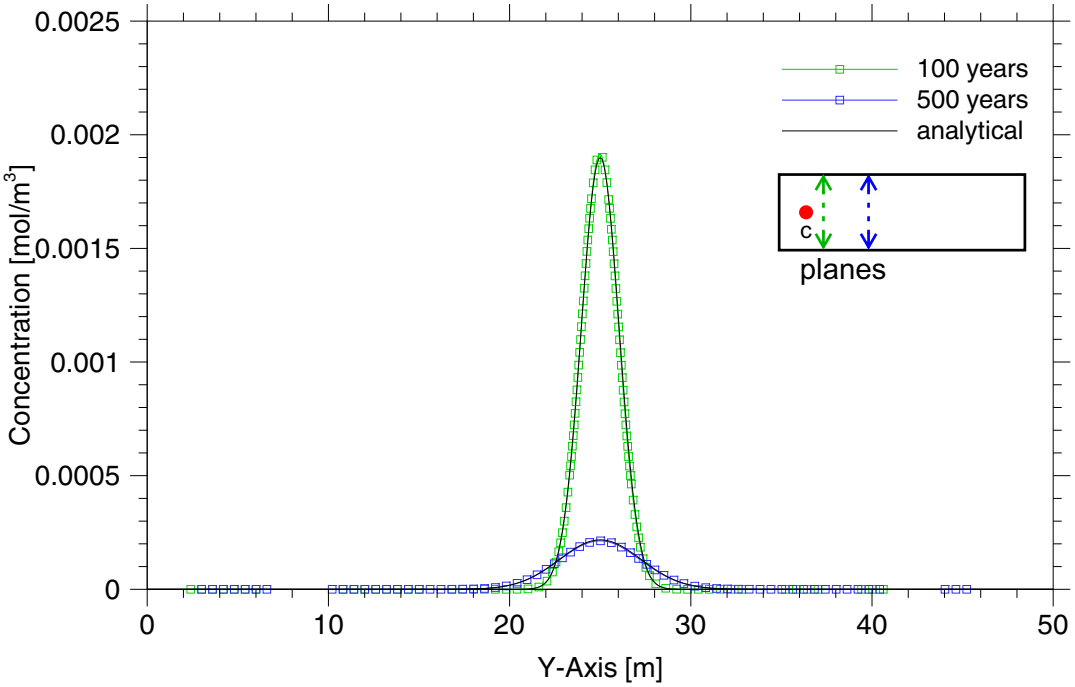

Fig. 7.38 Concentration for two times and at two planes

Planes at x=15 m and x=35 m, close to maxima of Fig. 7.37

Diagonal Model

In this test case again advection, dispersion, decay, and sorption are simultaneously taken into account. In contrast to the model area shown in Fig. 7.33, the flow direction is rotated by an angle of 26.6° (realisation 1). Hence Darcy velocity occurs diagonally to the model area. In the second case the coordinate system is rotated by the same angle (realisation 2). Now the Darcy velocity is diagonal to the model area but still parallel to the x-axis. In both cases right and top sides of the area serve as outflow boundaries, while the left and the bottom sides are kept impermeable. Both realisations are depicted in Fig. 7.39. The results of both realisations are given in Figs. 7.40, 7.41, and in Figs. 7.42, 7.43, respectively. No evidence for dependence on grid alignment is to be found.

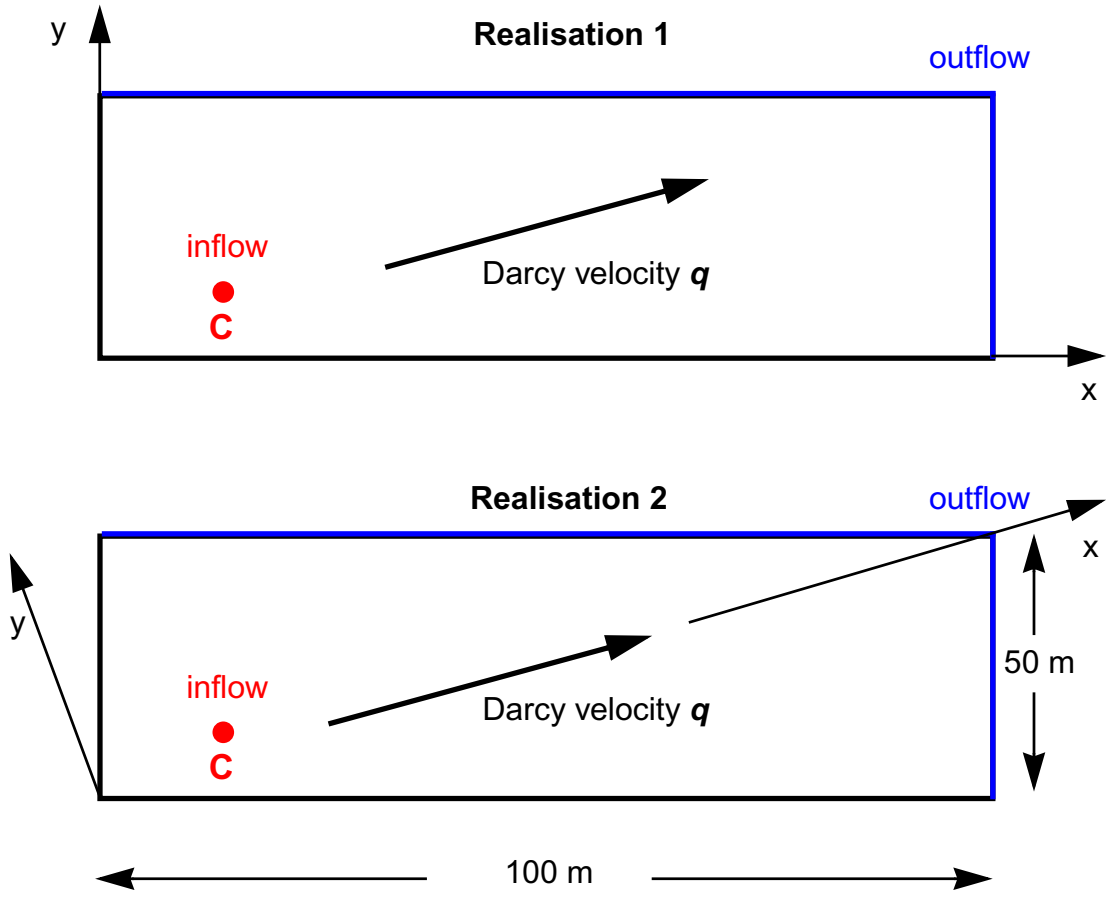

Fig. 7.39 Models of two-dimensional test cases with pulse injection. Realisations with rotated flow and rotated model area

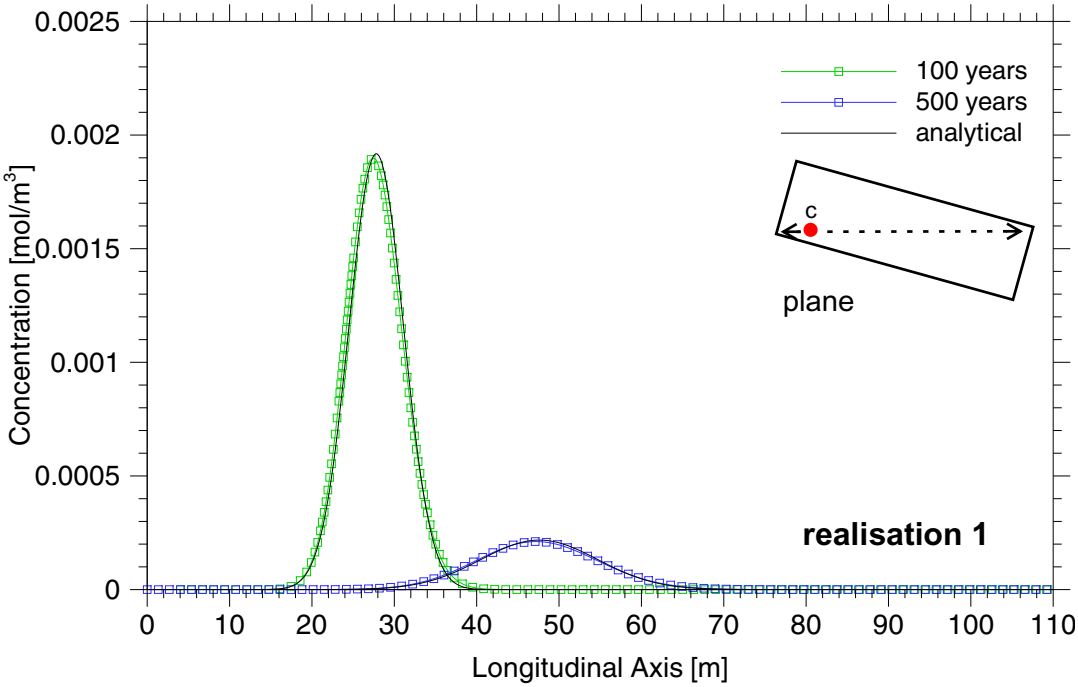

Fig. 7.40 Concentration at two times along longitudinal plane

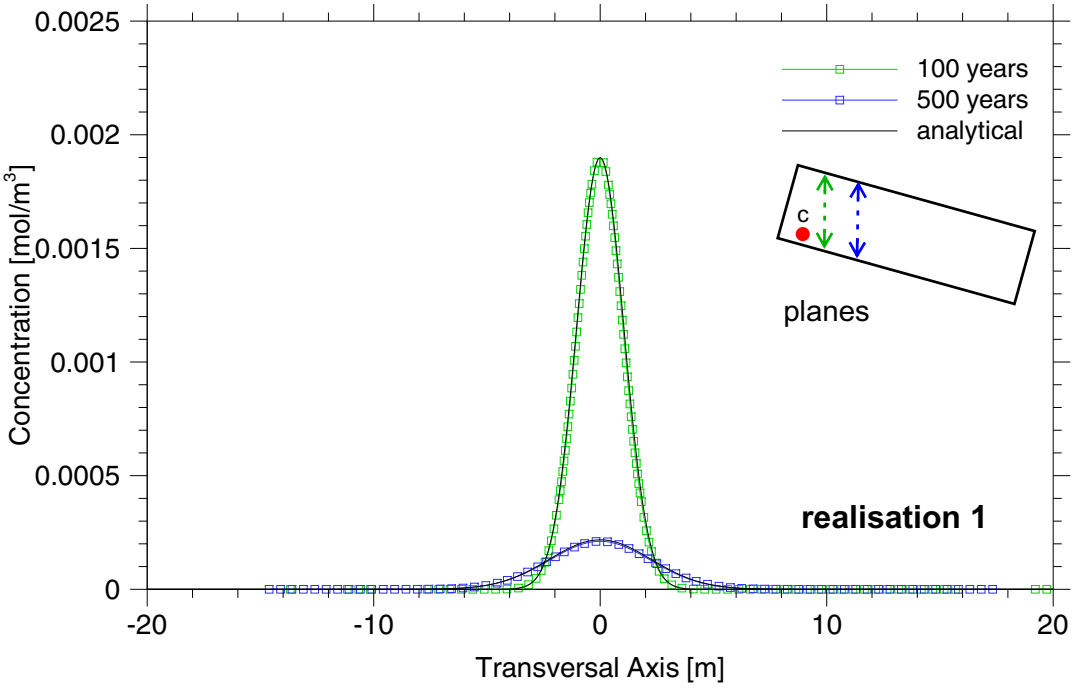

Fig. 7.41 Concentration at two times along two transversal planes

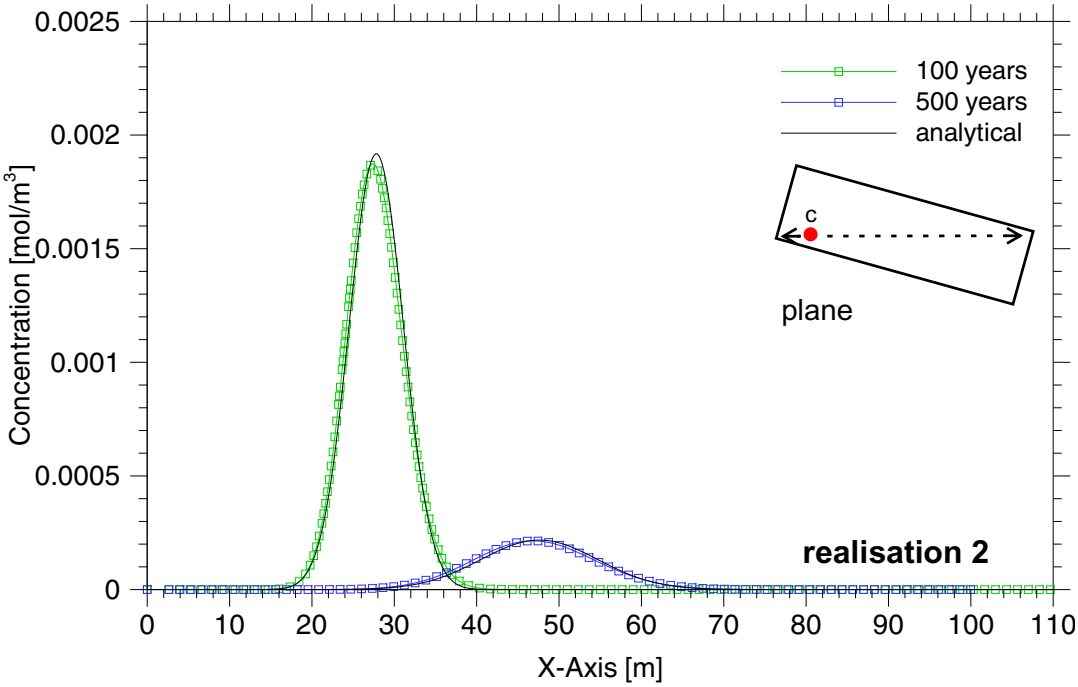

Fig. 7.42 Concentration at two times along longitudinal plane

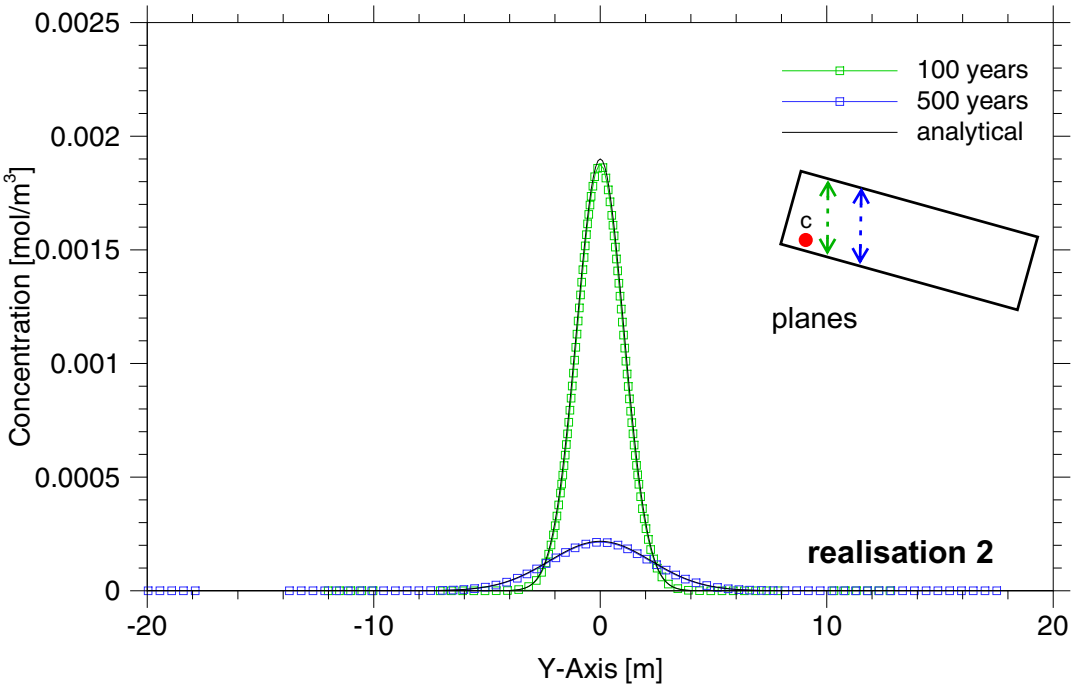

Fig. 7.43 Concentration at two times along two transversal planes

7.2.2.2 Point-Like Continuous Inflow

In this test case two-dimensional transport calculations for a point-like inflow with continuous injection are examined. The two-dimensional analytical solution (cp. section 7.1.5 and [81]) for continuous injection reads:

$$C(x,\ y,\ t) = \frac{C_0}{4\pi\sqrt{\alpha_L \alpha_T}} e^{\frac{x}{2\alpha_L}} W\left(\frac{r^2 R}{4\alpha_L u t}, \frac{r\gamma}{2\alpha_L}\right)$$

with Hantush's function

$$W(a_1, a_2) = \int_{a_1}^{\infty} \frac{1}{\varsigma} e^{-\varsigma - \frac{a_2^2}{4\varsigma}} d\varsigma \quad \text{and} \qquad (7.54)$$

$$\gamma = \sqrt{1 + 4\alpha_L \lambda \frac{R}{u}} \quad \text{and}$$

$$r = \sqrt{x^2 + \frac{\alpha_L}{\alpha_T} y^2}$$

The model for the point-like inflow with continuous injection is equal to the model for point-like inflow with pulse injection except the chosen radionuclide. The model extends to 100 m in length and 50 m in breadth. The right face of the modelled area serves as outflow boundary while the other fronts are impermeable. A parallel flow with constant Darcy velocity is presumed.

Advection, dispersion, decay, and sorption are simultaneously taken into account. Instead of Am-241 this time C-14 with half-life $T_{1/2}$=5730 a is examined. Other parameters are not changed and are given in Tab. 7.3. The model is shown in figure 7.33. The point (10,25) serves as an inflow point. Linear equilibrium sorption is considered by a distribution coefficient set to K_d = 0.01 m^3 kg^{-1}, i.e. the retardation factor amounts to 101. Longitudinal and transversal dispersion length are kept at α_L = 1 m and α_T = 0.1 m. Fig. 7.44 to Fig. 7.46 show the concentration distributions at four times along and transverse with respect to the flow direction and the breakthrough curves at four points.

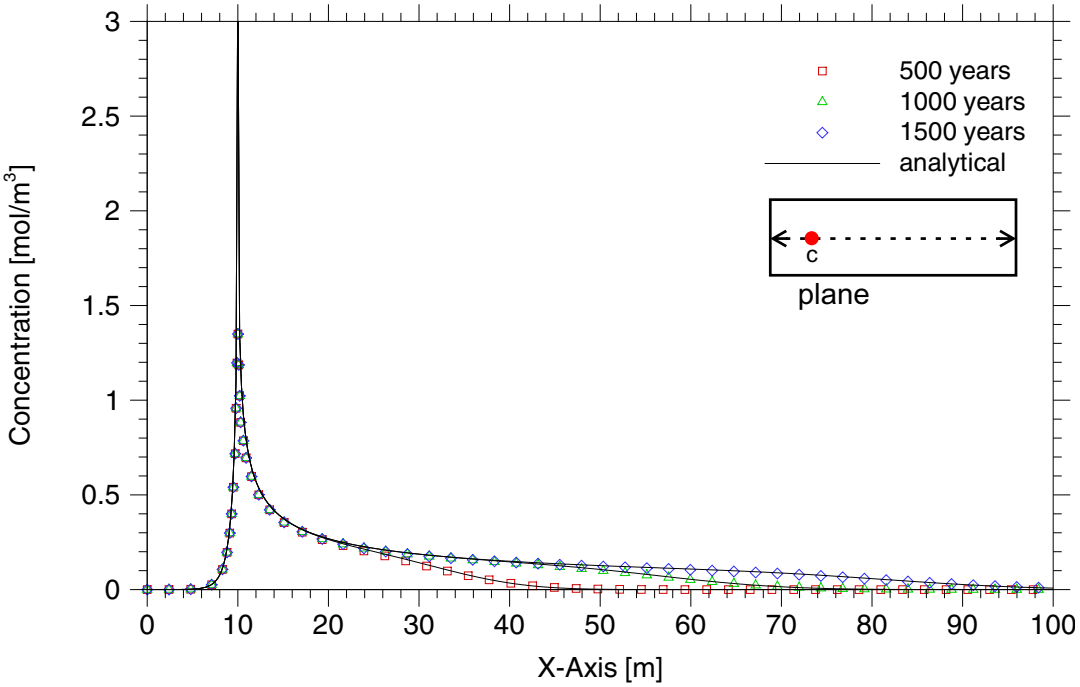

Fig. 7.44 Concentration along plane y=25 m
with K_d=0.01 m^3 kg^{-1} and $T_{1/2}$=5 730 a

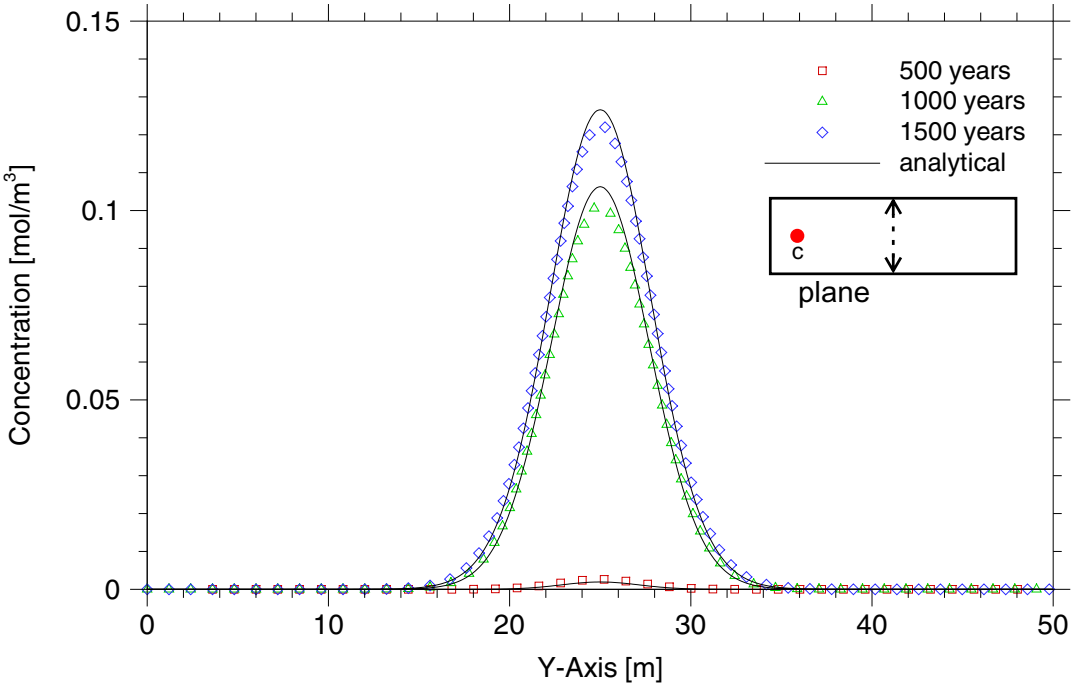

Fig. 7.45 Concentration along plane x=50 m
with K_d=0.01 m^3 kg^{-1} and $T_{1/2}$=5 730 a

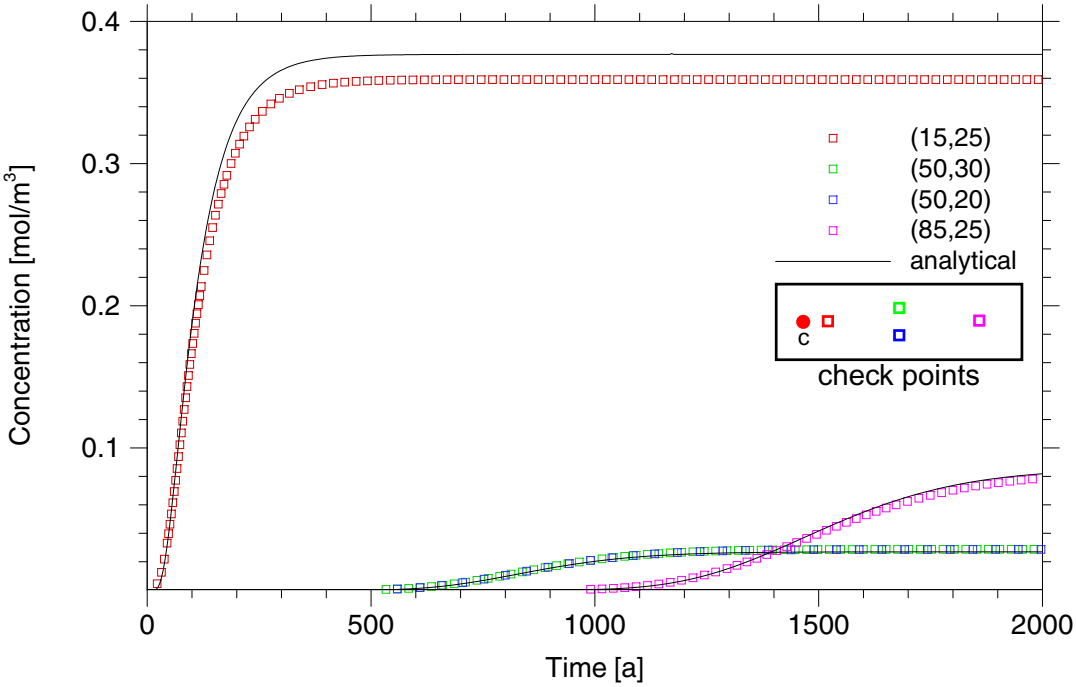

Fig. 7.46 Breakthrough curves at four points
with K_d = 0.01 m^3 kg^{-1} and $T_{1/2}$ = 5 730 a

Diagonal Model

In this case advection, dispersion, decay, and sorption are taken into account. Again the direction of Darcy flow is rotated by an angle of 26.6° and occurs diagonally to the model. In difference to the pulse injection a continuous inflow of 1 mol a^{-1} is injected at the point (20, 10). Right face and top side of the area serve as outflow boundaries, while the left side and the bottom side are kept impermeable.

In Fig. 7.47 the concentration distribution along flow direction is plotted. The concentration distribution transversal to flow direction is depicted in Fig. 7.48. In both of cases the concentrations are given for three different times, 500 a, 1 000 a, and 1 500 a. Fig. 7.49 shows breakthrough curves at four different points. In addition in Fig. 7.50 the adaptive grids for the diagonal flow are given at the times 10 a and 100 a.

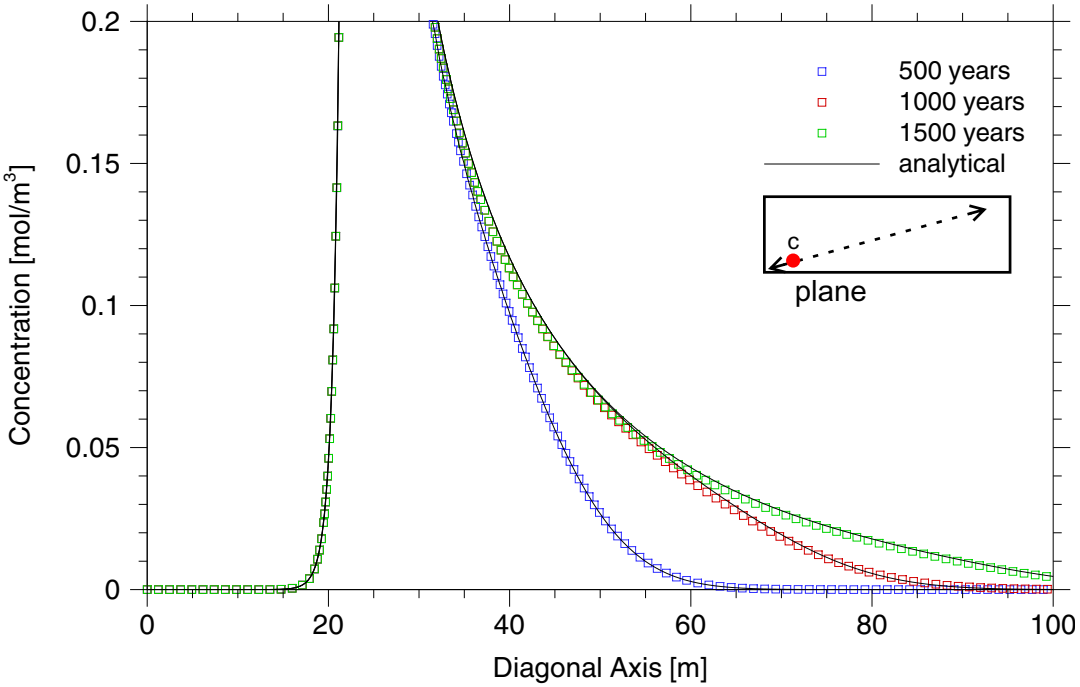

Fig. 7.47 Concentration along diagonal axis with K_d = 0.01 m^3 kg^{-1} and $T_{1/2}$ = 432 a

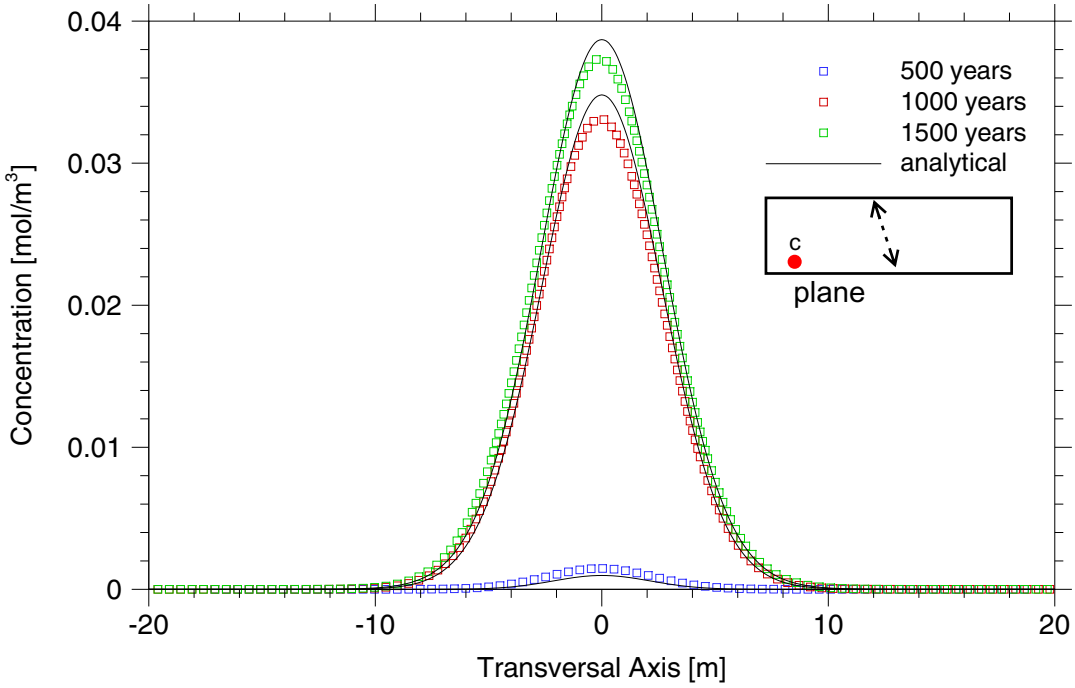

Fig. 7.48 Concentration along transversal axis with K_d = 0.01 m^3 kg^{-1} and $T_{1/2}$ = 432 a

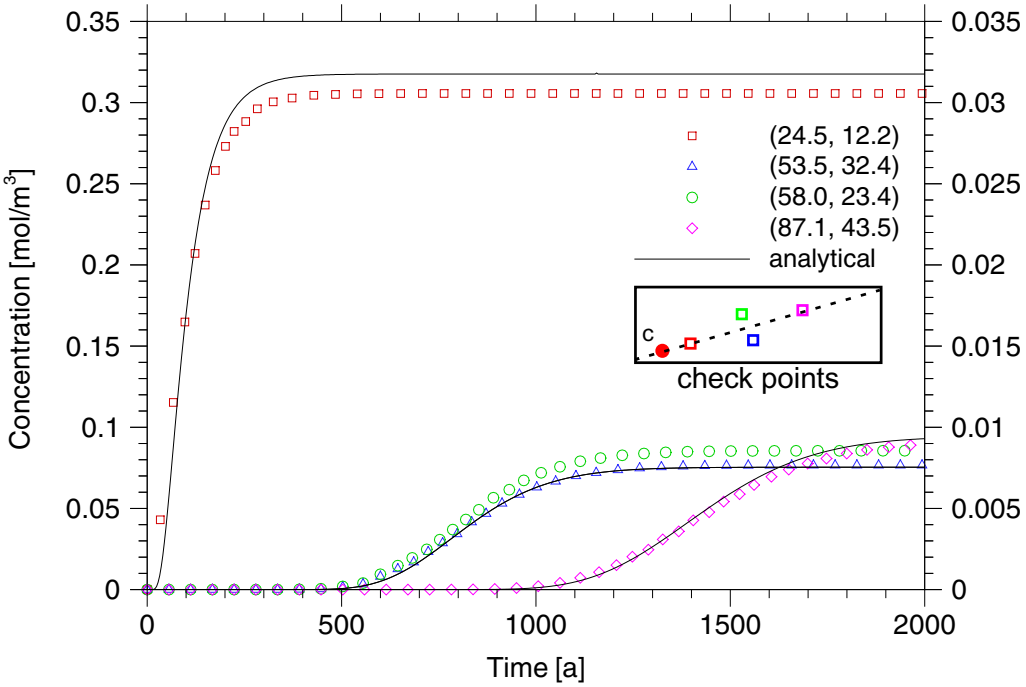

Fig. 7.49 Breakthrough curves at four points

K_d = 0.01 m^3 kg^{-1} and $T_{1/2}$ = 432 a.

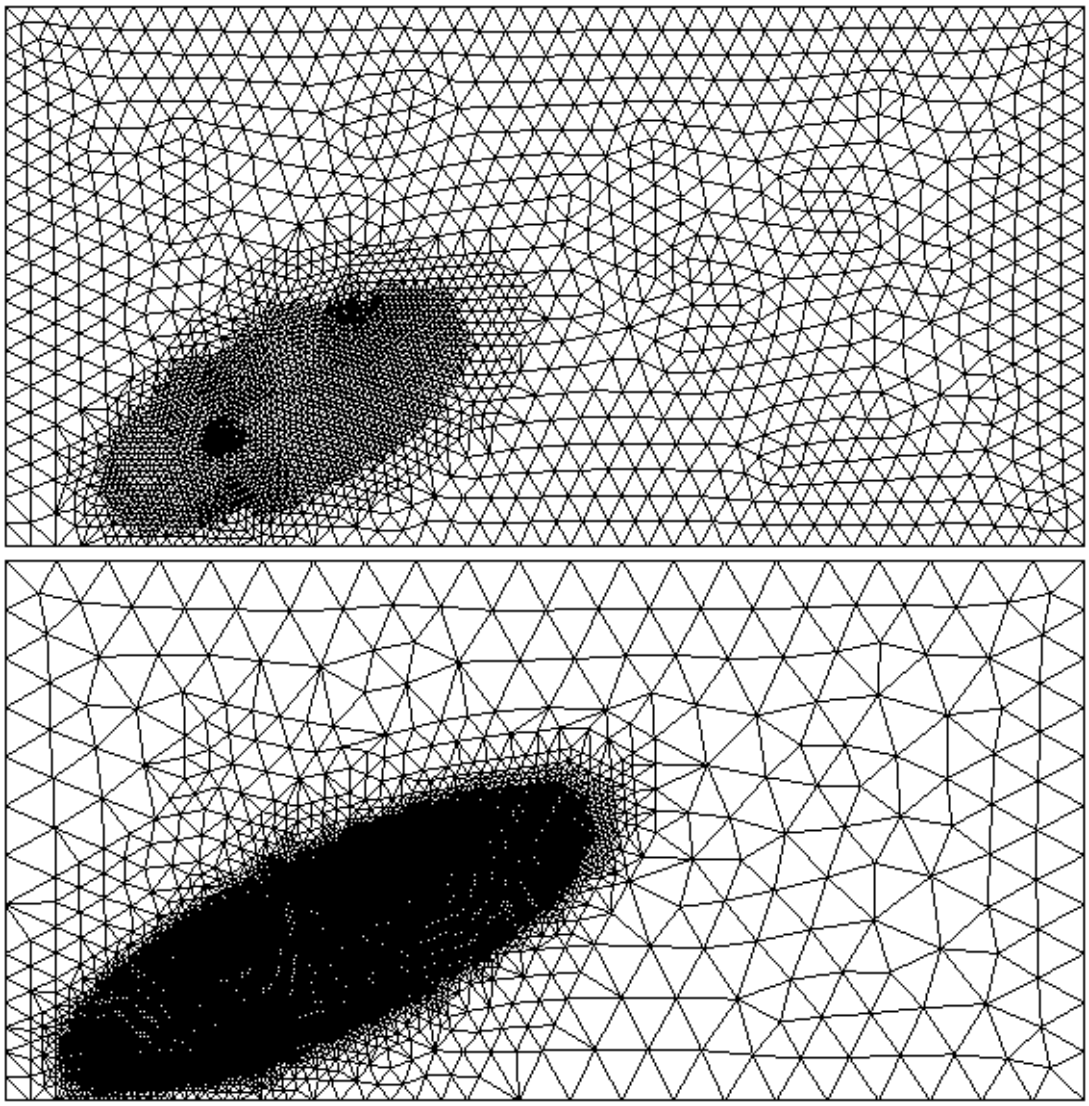

Fig. 7.50 Adaptive grids after 10 a and after 100 a

7.2.3 Three-Dimensional Test Case

In the three-dimensional case the analytical and numerical solution for a point-like pulse injection are compared. The model is shown in Fig. 7.51. The model extends to 420 m in length and has a cross section of 200 m x 200 m. The pollutant will be injected at the left side at point C(20, 0, 0). A parallel flow with constant Darcy velocity is presumed. The parameters of this case are compiled in Tab. 7.4. The analytical solution is used as initial condition for the numerical calculations. The three-dimensional analytical solution [10], [81] for pulse injection reads:

$$C_\delta(x,y,z,t) = \frac{C_0}{8nR\sqrt{\alpha_L\alpha_T\alpha_Z}\left(\pi\frac{ut}{R}\right)^{\frac{3}{2}}} e^{-\lambda t} \cdot F_t$$

with (7.55)

$$F_t = e^{\left(-\frac{\left(x-\frac{ut}{R}\right)^2}{4\alpha_L\frac{ut}{R}} - \frac{y^2}{4\alpha_T\frac{ut}{R}} - \frac{z^2}{4\alpha_Z\frac{ut}{R}}\right)}$$

In Fig. 7.52 the comparison between analytical and numerical solution of a three-dimensional point-like pulse injection is shown. Breakthrough curves at various points can be seen. These points have the following coordinates: p1(209,0,0), p2(240,0,0), and p3(265,0,0). The next three figures show the concentration distribution along the coordinate axes for various times, t_1=1100 s (red), t_2=1400 s (blue), and t_3=1700 s (green). In Fig. 7.53 the concentration distribution along the x-axis at y=0 m, z=0 m is depicted, whereas in Fig. 7.54 the concentration along the y-axis at x=265 m, z=0 m is given for the same time points. Finally Fig. 7.55 shows the concentration along the z-axis at x=265 m, y=0 m again at the same time points. Analytical and numerical solutions are in excellent agreement. At the time t_1=1 100 s the concentrations along y-, and z-axis are so small (c<40 mol m^{-3}) that they cannot be recognised in the figures. But nevertheless the agreement between analytical and numerical solutions is extremely well.

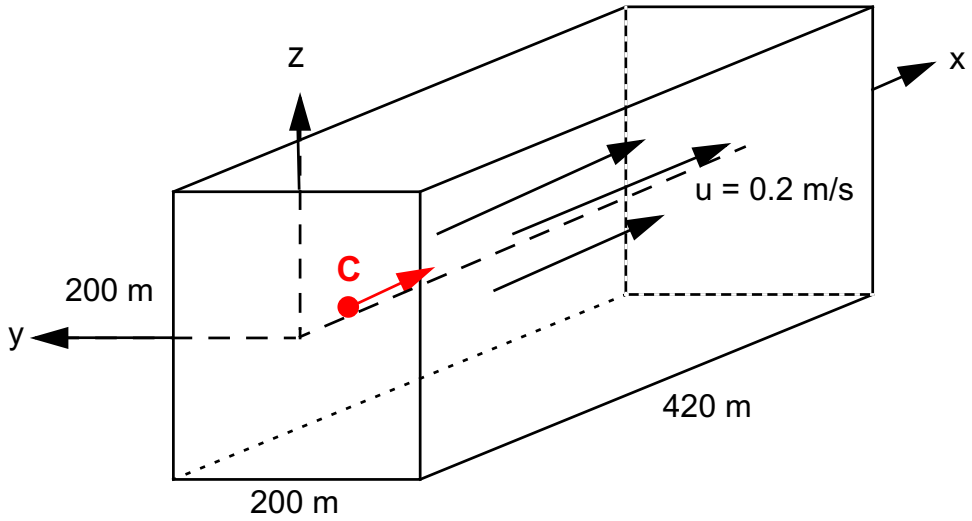

Fig. 7.51 Conceptual Model of the three-dimensional test case

Tab. 7.4 Parameters for pulse injection in three-dimensional case

Darcy velocity $\boldsymbol{q}$	0.2 m s^{-1}	diffusivity D_m	0.0 m^2 s^{-1}
porosity ϕ	0.15	dispersion α_L	1.5 m
decay constant λ	$5.0 \cdot 10^{-4}$ s^{-1}	dispersion α_T	0.3 m
distribution coefficient K_d	1.5 m^3 kg^{-1}		
location of pollutant source: x = 20 m, y = 0 m, z = 0 m			
initial condition:			
analytical solution after 1 000 s with			
m_m = 10^9 mol			

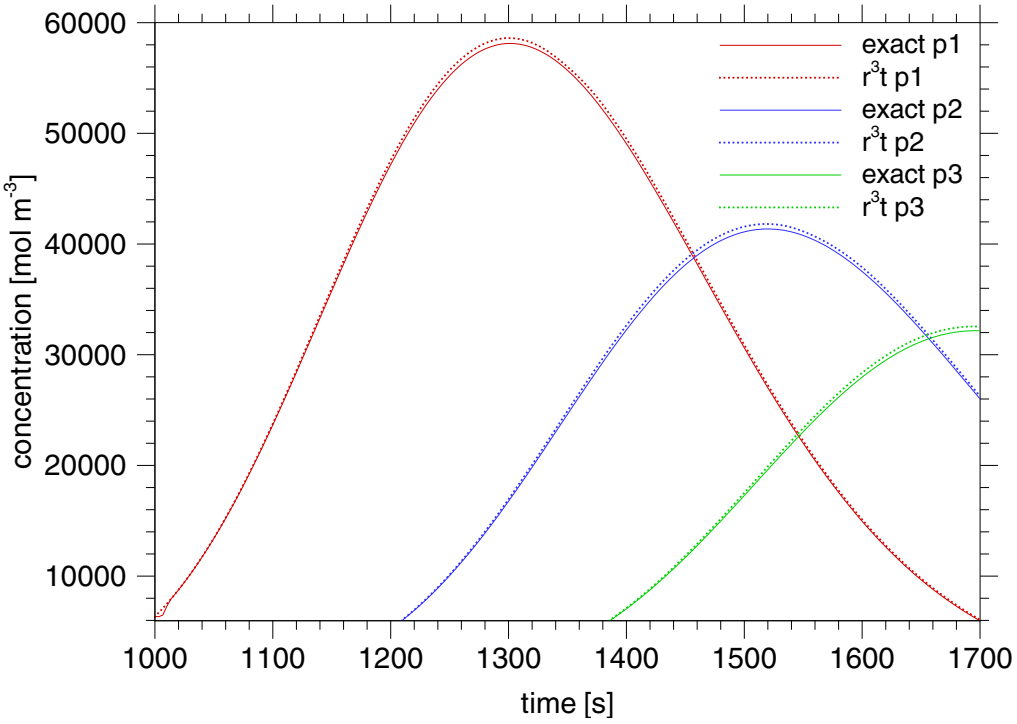

Fig. 7.52 Breakthrough curves in the three-dimensional test case at various points

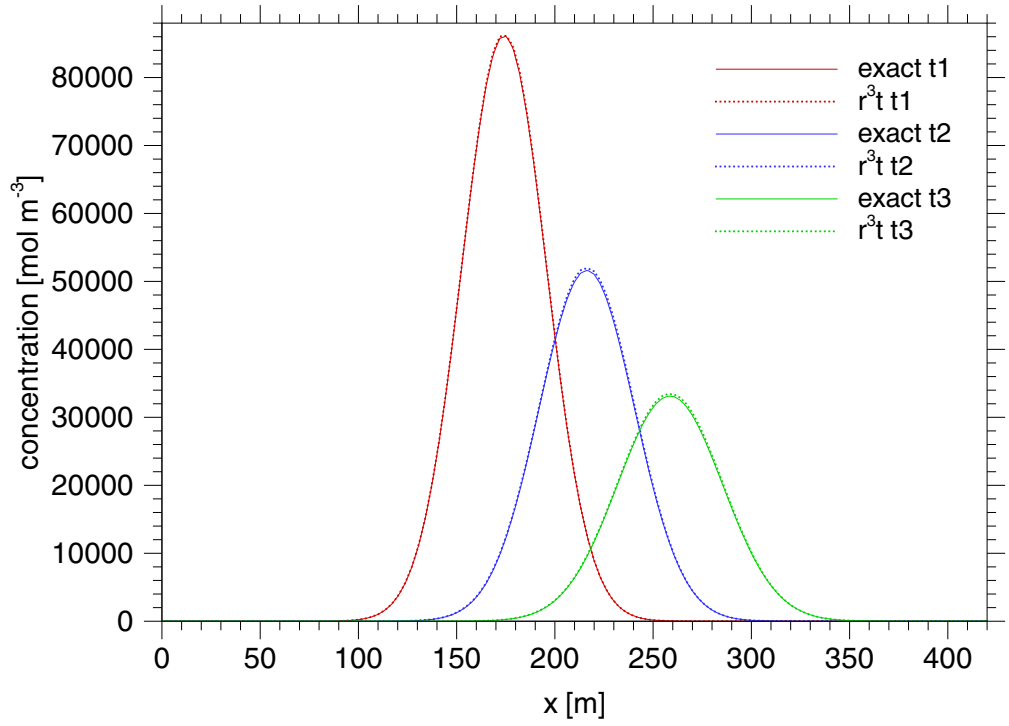

Fig. 7.53 Concentration distribution in x-direction at various time points

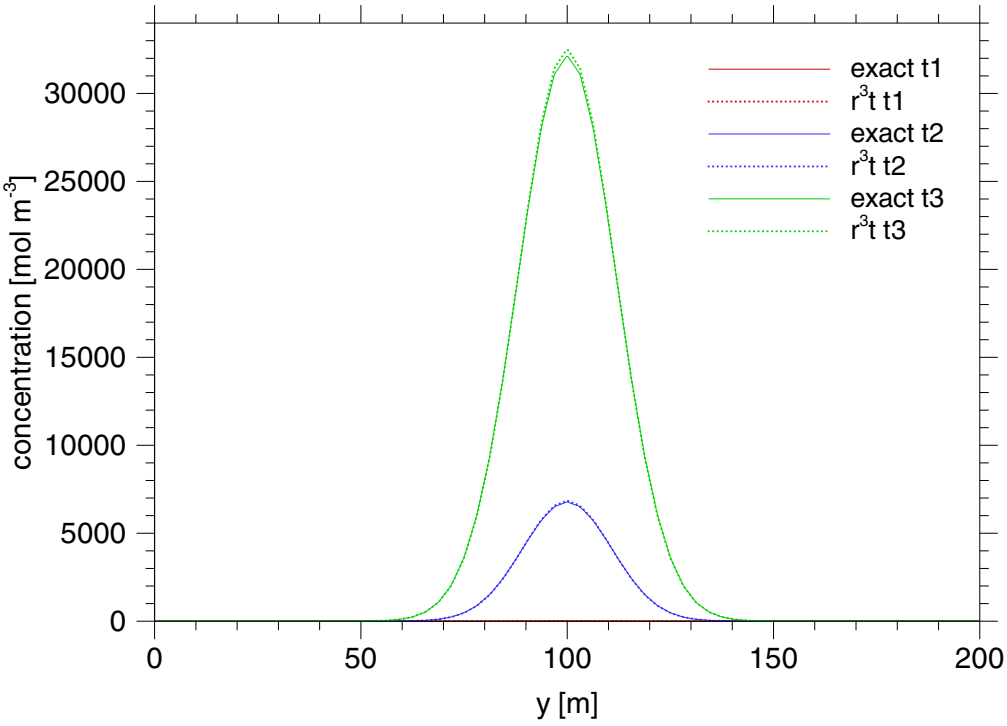

Fig. 7.54 Concentration distribution in y-direction at various time points

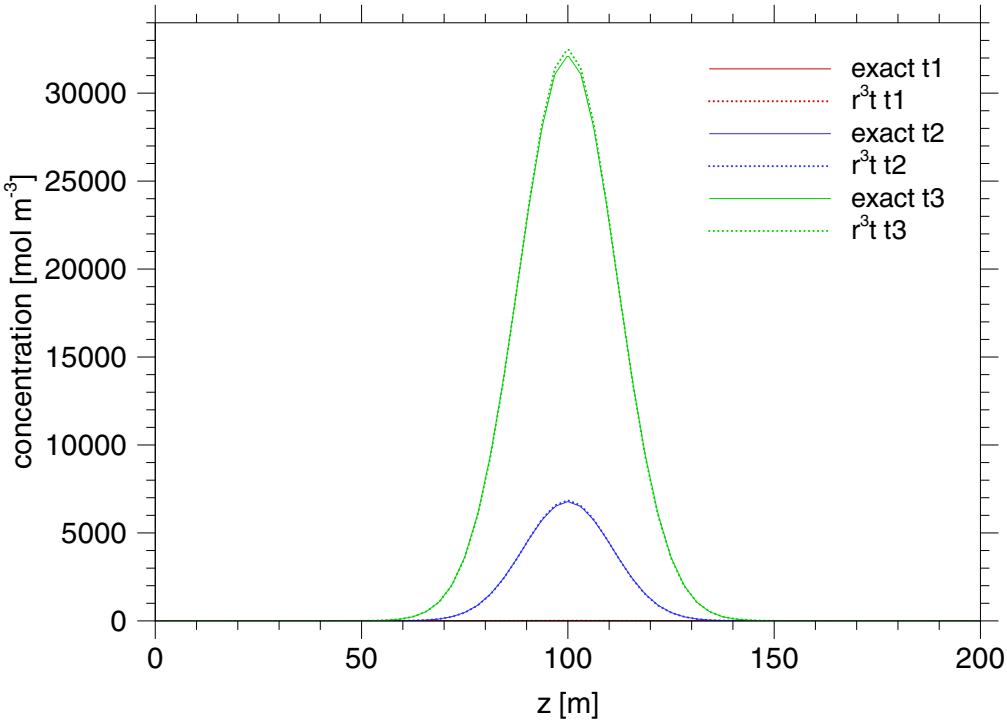

Fig. 7.55 Concentration distribution in z-direction at various time points

7.3 Comparison with Numerical Solutions

For verification of numerical transport models one has to rely on the comparison of results with other numerical codes in case of heterogeneous model area and/or non-linear sorption isothermes. In this case simulations with the codes CHETLIN and CHETNIS [90] to model one-dimensional pollutant transport with linear and non-linear sorption, respectively, are used.

7.3.1 Linear Sorption

In this subchapter test cases are described which deal with linear equilibrium sorption. This kind of sorption modelling is well-known as K_d-concept. First of all one-dimensional problems are investigated. They have the advantage that for certain conditions results can be compared to results of the CHETLIN model [90]. For test cases taking into account linear equilibrium sorption the coupling to the element-specific sorption does not exist.

Since r^3t is tested at great length for linear sorption in connection with analytical solutions this chapter focusses on applications for heterogeneous regions. Anyhow at least one test case concentrates on the comparison with the numerical model CHETLIN in the case of a homogeneous region.

7.3.1.1 Homogeneous Domain

This test case is essentially the same as described in subchapter 7.2.1 with the exception of the parameter values. The model is dealing with a homogeneous domain with constant Darcy velocity. It is about a one-dimensional problem with δ-shaped inflow of pollutant. The modelled area is depicted in Fig. 7.23 and the parameters are given in Tab. 7.5. In Fig. 7.56 the comparison of results of r^3t and CHETLIN simulations are shown.

Tab. 7.5 Parameters of homogeneous model

Darcy velocity $\boldsymbol{q}$	$2.0 \cdot 10^{-8}$ m s^{-1}	diffusivity D_m	0.0 m^2 s^{-1}
porosity ϕ	0.2 / 0.5 / 1.0	dispersion α_L	1.0 m
half-life $T_{1/2}$	$1.0 \cdot 10^{10}$ a	dispersion α_T	0.0 m
distribution coefficient K_d	$1.5 \cdot 10^{-4}$ m^3 kg^{-1}	inflow:	
rock density ρ_r	2500 kg m^{-3}	j_m=1.·10^{-10} mol s^{-1}	
fluid density ρ_f	1000 kg m^{-3}	for $0 \le t \le 1.\cdot 10^9$ s	

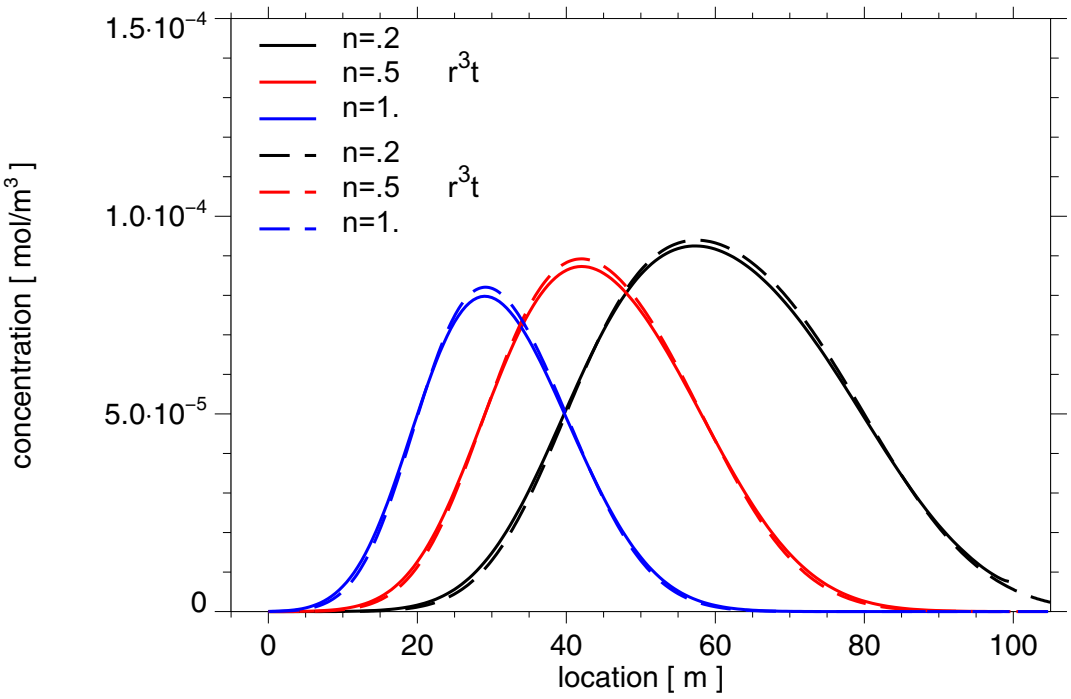

Fig. 7.56 r^{3}t and CHETLIN simulations using different porosities

7.3.1.2 Heterogeneous Domains

Up to now two two-dimensional modelling domains representing a one-dimensional transport problem were investigated with respect to sorption. Both models comprise of three subdomains with different sorption coefficients, as illustrated in Fig. 7.57.

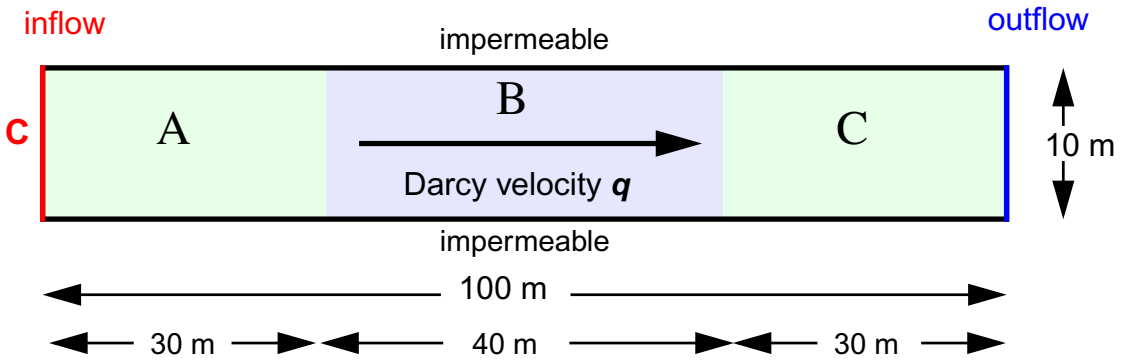

Fig. 7.57 Conceptual model for heterogeneous domains

The models have a length of 100 m and a width of 10 m. A parallel fluid flow is defined with a constant Darcy velocity of $2 \cdot 10^{-8}$ m s^{-1}. At the inflow boundary a source is located which releases 20 mol of solute over a period of $3.16 \cdot 10^{7}$ s and $1 \cdot 10^{12}$ s, respectively. The former case is considered to be a short pulse while the latter case represents a continuous source. The rock density is 2500 kg m^{-3}, fluid density 1000 kg m^{-3}, the porosity 0.2, the longitudinal dispersion length 1.0 m and the transversal dispersion length 0 m. Diffusion was not considered. The model parameters are described in Tab. 7.6. The different order of K_d-values in both models should be noted.

Methods of model checking

The results are given in terms of breakthrough curves at three control points as indicated in Fig. 7.58. The curves are taken then to check the transport time for the solute front as well as the peaks to the respective control point. Additionally, the maximum value of the solute concentration can be checked in the case of constant solute inflow.

Tab. 7.6 Parameters of models

Darcy velocity q	$2.0 \cdot 10^{-8}$ m s^{-1}	diffusivity D_m	0.0 m^2 s^{-1}
porosity ϕ	0.2	dispersion α_L	1.0 m
half-life $T_{1/2}$	$1.0 \cdot 10^{10}$ a	dispersion α_T	0.0 m
rock density ρ_r	2500 kg m^{-3}		
fluid density ρ_f	1000 kg m^{-3}		
short pulse:		constant inflow	
j_m=$6.33 \cdot 10^{-7}$ mol s^{-1}		j_m=$2.0 \cdot 10^{-11}$ mol s^{-1}	
for $0 \le t \le 3.16 \cdot 10^7$ s		for $0 \le t \le 1.0 \cdot 10^{12}$ s	
distribution coefficient K_d	model 1	model 2	
	A: $1.0 \cdot 10^{-2}$ m^3 kg^{-1}	A: $1.0 \cdot 10^{-1}$ m^3 kg^{-1}	
	B: $1.0 \cdot 10^{-1}$ m^3 kg^{-1}	B: $1.0 \cdot 10^{-2}$ m^3 kg^{-1}	
	C: $1.0 \cdot 10^{-2}$ m^3 kg^{-1}	C: $1.0 \cdot 10^{-1}$ m^3 kg^{-1}	

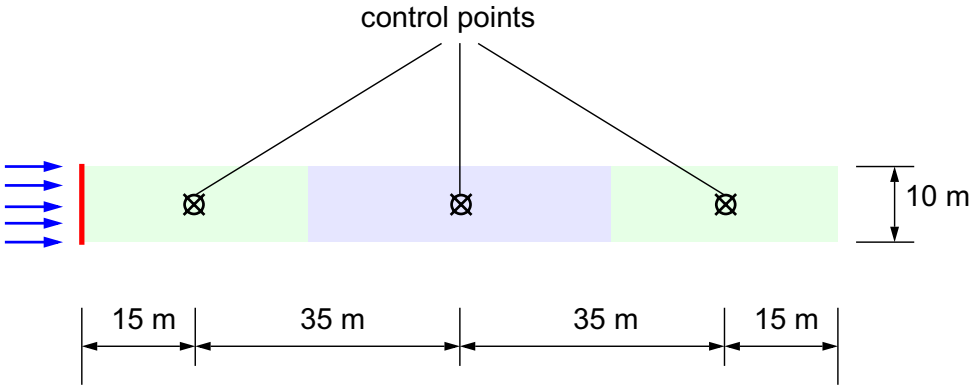

Fig. 7.58 Control points (cp) in the models for breakthrough curves

The travel time of the solute front and the solute peak, respectively are considered here. For this purpose the position of the front is defined as the position of the point where the concentration reaches 50%. The mean travel time Δt_a per metre of a solute particle without regarding retention can be calculated as

$$\Delta t_a = \frac{\phi}{q} = 10^7 \text{ s m}^{-1} = 0.3171 \text{ a m}^{-1} \qquad (7.56)$$

using the Darcy velocity q and the porosity ϕ. For a homogeneous model section with a constant linear sorption coefficient K_d and with rock density ρ_r the travel time increases by the retardation factor R which is determined by

$$R = 1 + \frac{1 - \phi}{\phi} \rho_r K_d \qquad (7.57)$$

R amounts to 101 for K_d=0.01 m^3 kg^{-1} and to 1001 for K_d=0.1 m^3 kg^{-1}. From these data the arrival times at the control points can be calculated. The necessary data and the results are compiled in Tab. 7.7 for model 1 and in Tab. 7.8 for model 2.

Tab. 7.7 Model 1: Arrival times of solute fronts/peaks at control points (cp)

	left section	middle section	right section
length [m]	30	40	30
retardation factor [-]	101	1001	101
velocity [m s^{-1}]	0.0312	0.00315	0.0312
travel time [a]	961	12 697	961
arrival time at cp [a]	480	7309	14 138

Tab. 7.8 Model 2: Arrival times of solute fronts/peaks at control points (cp)

	left section	middle section	right section
length [m]	30	40	30
retardation factor [-]	1001	101	1001
velocity [m s^{-1}]	0.00315	0.0312	0.00315
travel time [a]	9522	1281	9522
arrival time at cp [a]	4761	10163	15565

For constant fluid inflow and a constant solute source the maximum concentration value c_{max} can easily be calculated by the ratio of solute mass flux $\dot{m}_c$ and the volumetric fluid flux Q.

$$c_{max} = \frac{\dot{m}_c}{Q}. \qquad (7.58)$$

The mass flux amounts to $\dot{m}_c$ = 2·10^{-11} mol s^{-1} resulting in a maximum concentration of c_{max}= 0.0001 mol m^{-3}.

As an additional check the model simulations were rerun with CHETLIN [90] instead of r^{3}t. The results of CHETLIN were compared with the results of r^{3}t. It has to be noted that the results of CHETLIN are given at increasing time intervals which makes the polygonal shape of the breakthrough curves in the graphs increasingly observable with time.

CHETLIN yields a slightly faster breakthrough than r^{3}t. In general the corresponding peaks of the solute pulses do not differ more than 1 %. Only at the left side the difference at the control point in Model 2 amounts to 2 %. However, the differences between the results of r^{3}t and CHETLIN are hardly discernable in the graphical comparisons given in Fig. 7.59 to 7.62.

The breakthrough curves of model 1 with constant solute inflow are shown in Fig. 7.59 and the time when the concentration reaches 50 % at the control points is marked as well. The theoretically derived maximum concentration value is matched by the simulation. A comparison of the modelling results with the breakthrough times calculated is given in Tab. 7.9 which reveals a maximum error in the model of 1.5 %.

The breakthrough curves for model 1 with pulse source are shown in Fig. 7.60 and the time when the concentration peak reaches the control points is marked as well. A comparison of the modelling results with the breakthrough times calculated is given in Tab. 7.10. It reveals a maximum error of 10.5 % for the arrival times.

The corresponding results for model 2 with constant solute inflow are shown in Fig. 7.61. The theoretically derived maximum concentration is matched by the simulation. A comparison of the modelling results with the breakthrough times calculated is given in Tab. 7.11. It reveals a maximum error of 2.2 % for the arrival times.

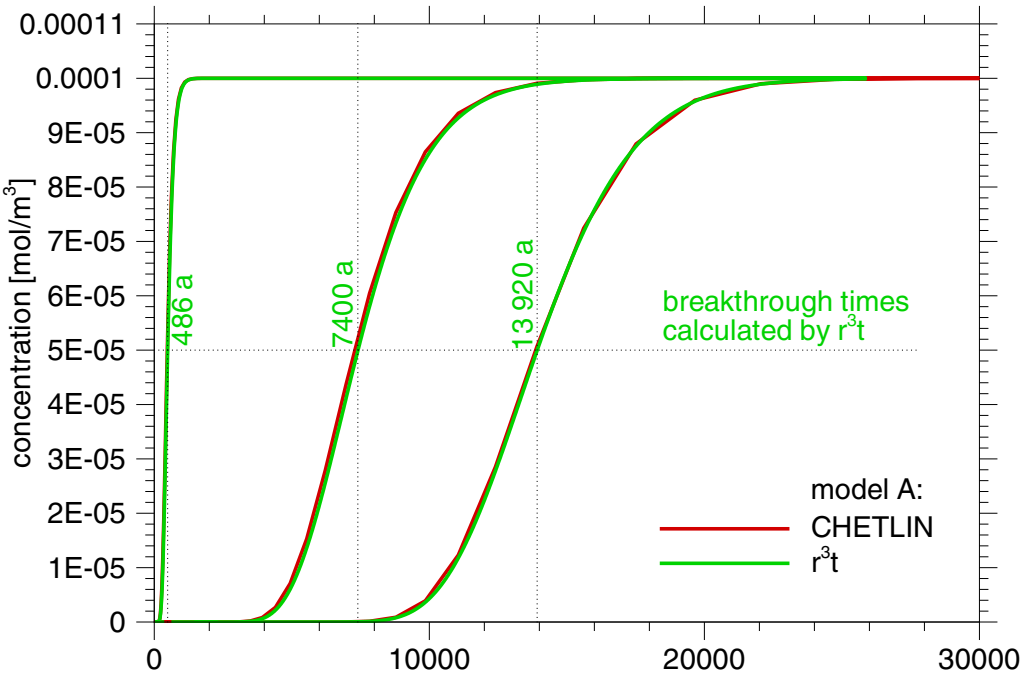

Fig. 7.59 Breakthrough curves at the control points for model 1 with a constant solute source

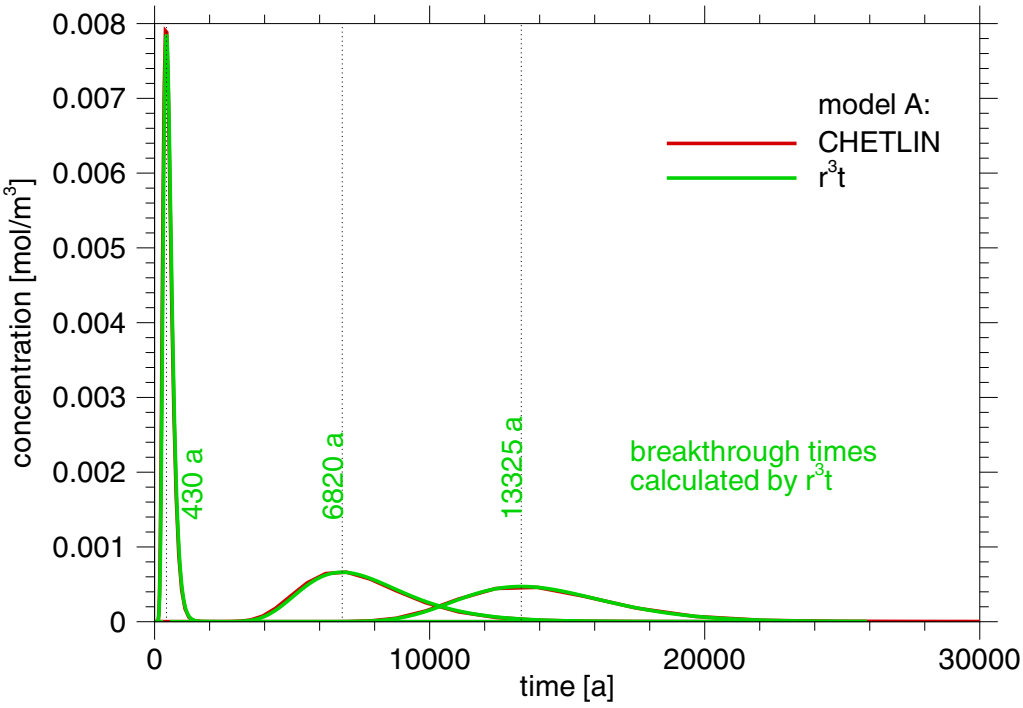

Fig. 7.60 Breakthrough curves at the control points for model 1 with a pulse source

Tab. 7.9 Comparison of arrival times for model 1 with a continuous source (theoretically and numerically calculated)

	left domain	middle domain	right domain
theoretical value [a]	480	7 309	14 138
numerically calculated [a]	486	7 400	13 920
difference [a]	6	91	218
error [%]	1.3	1.2	1.5

The breakthrough curves for model 2 with pulse source are shown in Fig. 7.62 and the time when the concentration peak reaches the control points is marked. A comparison of the modelling results with the breakthrough times calculated is given in Tab. 7.12. It reveals a maximum error of 10.8 % for the arrival times.

Tab. 7.10 Comparison of arrival times for model 1 with a pulse source (theoretically and numerically calculated)

	left domain	middle domain	right domain
theoretical value [a]	480	7 309	14 138
numerically calculated [a]	430	6 820	13 325
difference [a]	50	489	813
error [%]	10.5	6.7	5.7

7.3.1.3 Performance with different numerical options

Some considerations concerning the simulator performance will be exemplified using the last test case in subchapter 7.3.1.2, namely grid convergence and improvements for advection-dominated transport processes. Grid convergence is a prerequisite for confidence in the numerical results. Using r^3t grid refinement can easily be performed by changing the refinement-level parameter. An increase of the refinement level by 1 means that the element size of the finest mesh used in the multigrid solver is halved. In order to demonstrate grid convergence it is thus sufficient to show that a further increase of the refinement level only yields negligible differences in the results.

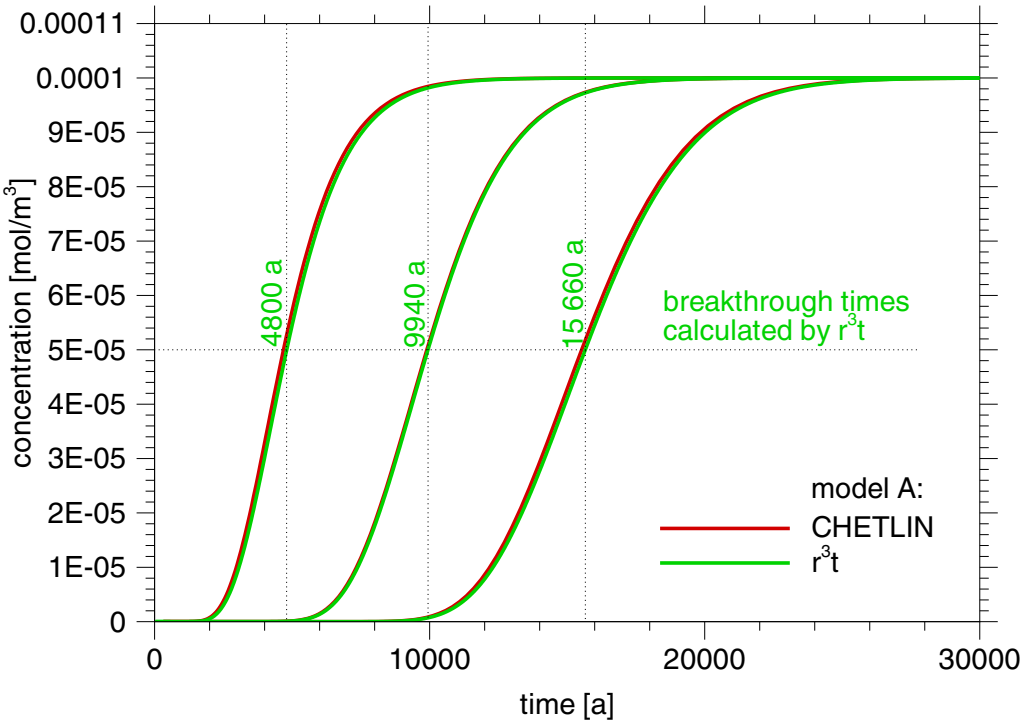

Fig. 7.61 Breakthrough curves at the control points for model 2 with a continuous solute source

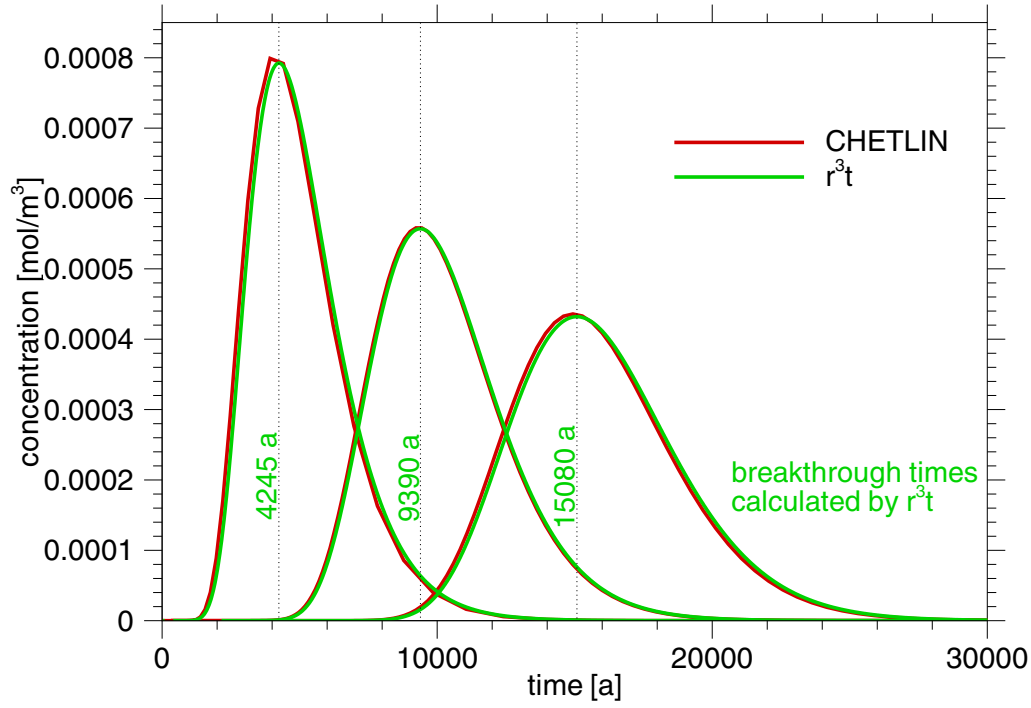

Fig. 7.62 Breakthrough curves at the control points for model 2 with a pulse source

Tab. 7.11 Comparison of arrival times for model 2 with a continuous source (theoretically and numerically calculated)

	left domain	middle domain	right domain
theoretical value [a]	4761	10 163	15 565
numerically calculated [a]	4800	9940	15 660
difference [a]	39	223	95
error [%]	0.8	2.2	0.6

Tab. 7.12 Comparison of arrival times for model 2 with a pulse source (theoretically and numerically calculated)

	left domain	middle domain	right domain
theoretical value [a]	4761	10 163	15 565
numerically calculated [a]	4245	9390	15 080
difference [a]	516	773	485
error [%]	10.8	7.6	3.1

Fig. 7.63 shows the breakthrough curves at the control points for the first three refinement levels. Breakthrough times for the model with refinement level 3 as used in chapter 7.3.1 are indicated. The differences are most prominent at the control point close to the inflow boundary. The coarse grid corresponding to refinement level 1 leads to a noticeable dampening of the peak, a deformation of the peak and a little phase shift. But between levels 2 and 3 the first breakthrough curve changes only very slightly and the curves at the two other control points can hardly be discerned at all. It is therefore not necessary to increase the refinement level beyond 3.

In case of dominant advective transport two alternative options to improve the numerical performance of the r^{3}t-code are offered by the preprocessor: upwinding or the method of characteristics (MOC). Fig. 7.64 shows the improvement of the results of Model 2 using these methods with a refinement level of 2. Here, the analytically calculated breakthrough times are indicated. Keeping in mind the results presented in chapter 7.3.1, the solution is clearly the one fitted best using the MOC. With the upwind method the peak value is significantly lower and without MOC or upwinding even lower than that. On the other hand, the peaks pass the control points later and thus they are slightly more close to the analytically calculated breakthrough times.

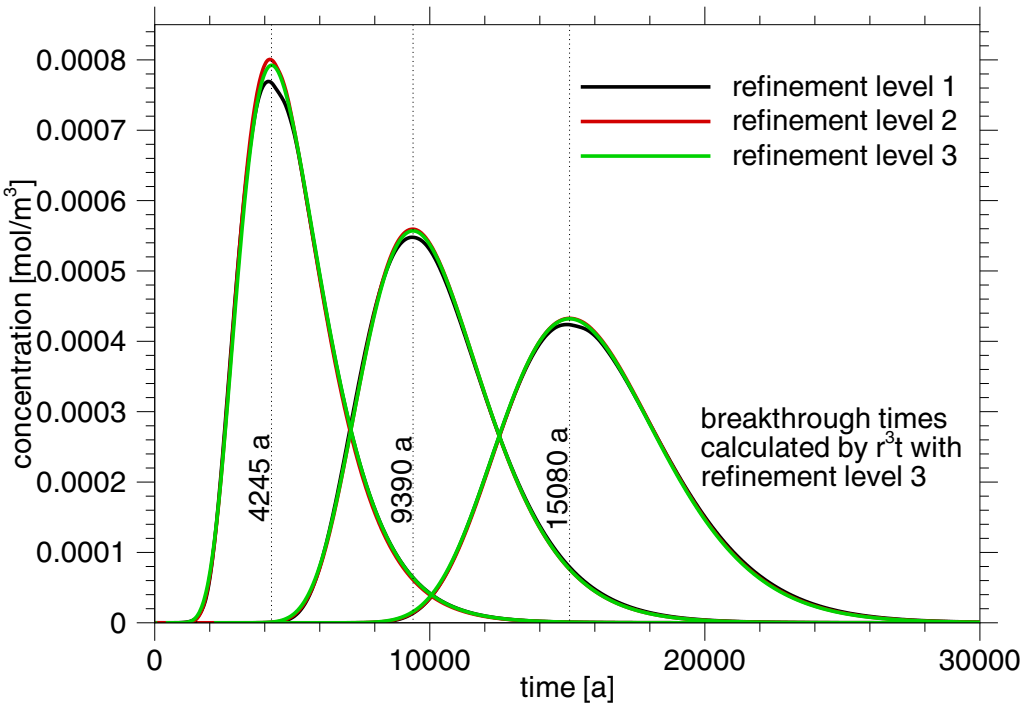

Fig. 7.63 Breakthrough curves for model 2 with different refinement levels

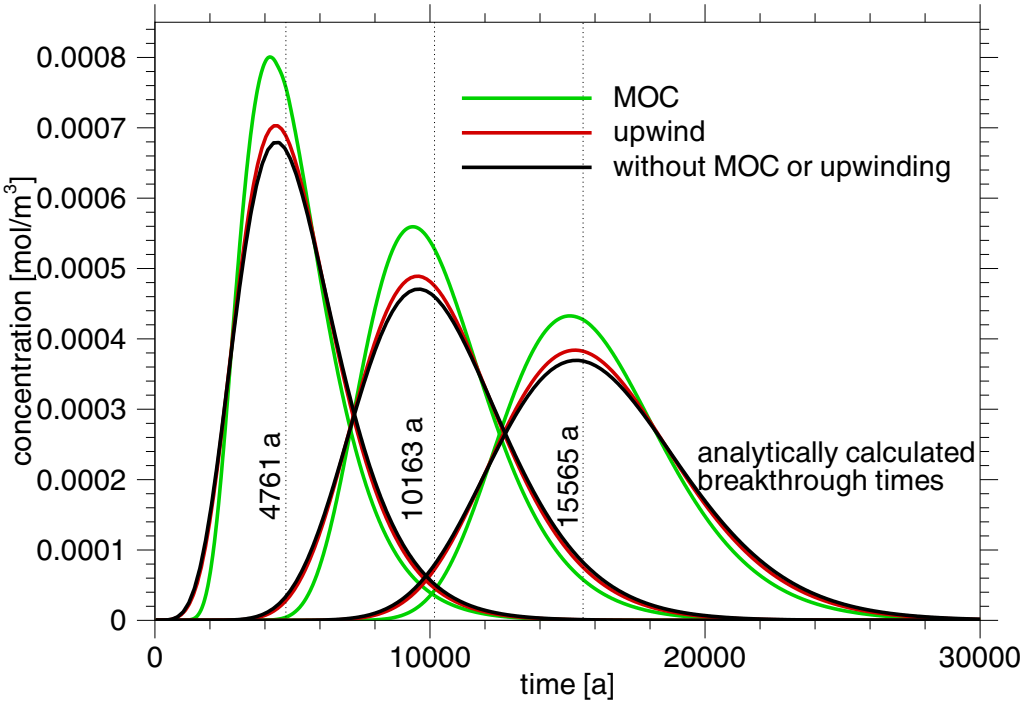

Fig. 7.64 Breakthrough curves for model 2 with different numerical schemes

This comparison does obviously not allow any general conclusions concerning the quality of the results. The effectiveness of the schemes depends on the specific transport problem. Here, the grid peclet number of the coarsest grid amounts approximately to 5 which is too high to be handled by a standard finite difference simulator, but perfectly within an acceptable range for a standard finite element simulator. So the comparison may give an impression without being taken as a general guideline.

7.3.2 Non-Linear Sorption

In the case of non-linear sorption only one-dimensional test cases are performed for a Freundlich isotherm. In Tab. 7.13 the parameters used are compiled. It is the same model

Tab. 7.13 Parameters for one-dimensional models with non-linear sorption

Darcy velocity $\boldsymbol{q}$	$2.0 \cdot 10^{-8}$ m s^{-1}	diffusivity D_m	0.0 m^2 s^{-1}
porosity ϕ	0.2	dispersion α_L	1.0 m
half-life $T_{1/2}$	10^{10} y	dispersion α_T	0.0 m
Freundlich isotherm	K_{nl} 0.01 m^3 kg^{-1}	p 0.736	
pulse			
boundary condition	10^9 s (cp. Fig. 7.65)		
concentration	$1.0 \cdot 10^{-4}$ mol m^{-3}		

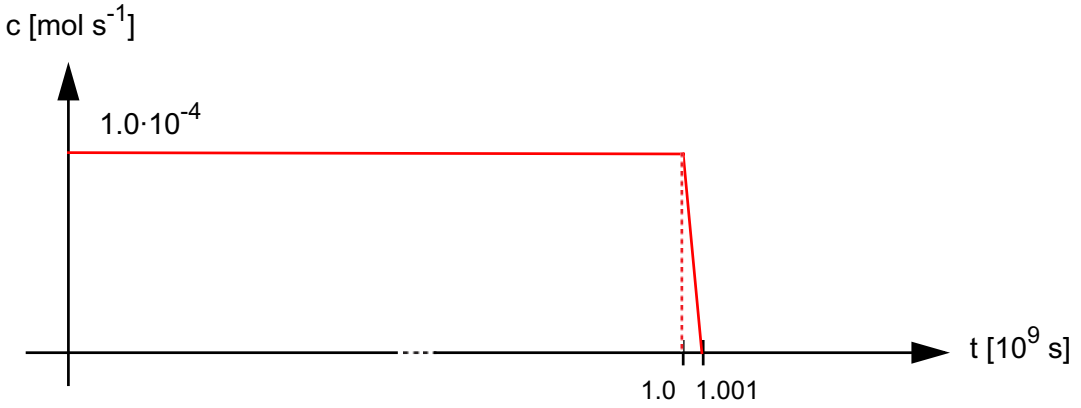

Fig. 7.65 Boundary condition at the inflow front

as the one depicted in Fig. 7.23, i.e. 100 m in length and 10 m in breadth. The pollutant

is injected at the entire left side. It lasts 10^9 s and afterwards it decreases within 10^7 s to zero. For non-linear sorption there exists no analytic solution. One has to rely on the com-

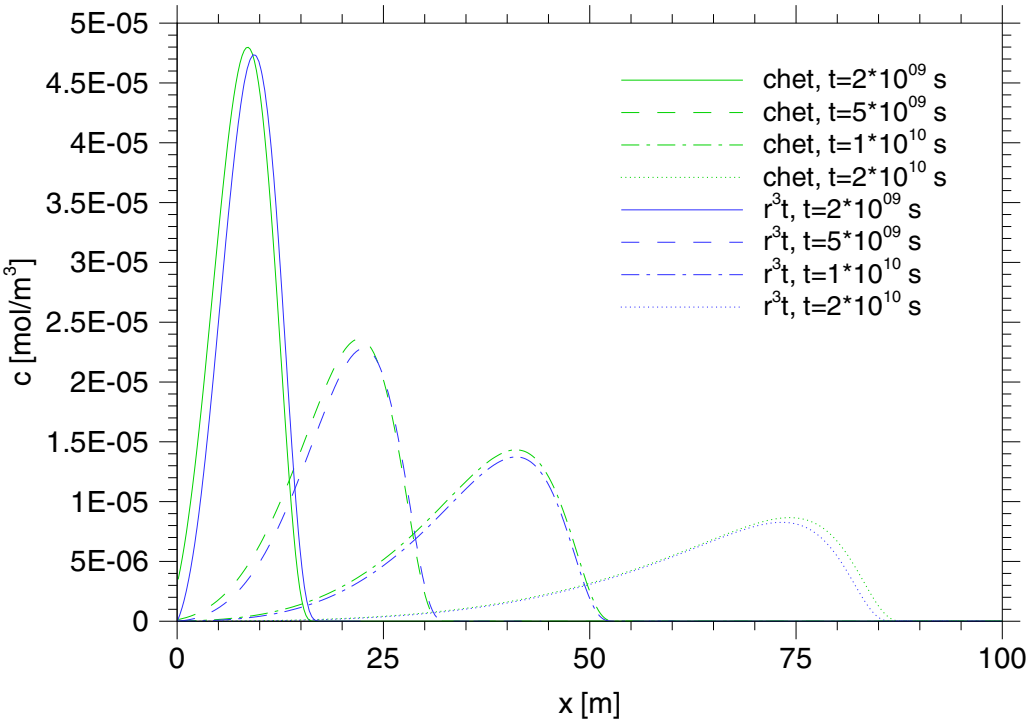

Fig. 7.66 Results for non-linear sorption: results from r^3t and CHETNIS

parison with other numerical codes. In Fig. 7.66 the comparison of model results from r^3t and CHETNIS [90] is shown for various times. One can easily notice that the agreement in this case is not as good as in the case of linear sorption, although both codes successfully passed test against asymptotic solutions which were performed (cp. subsection 7.1.5.2 and [90]). It is reckoned the small discrepancy is due to the somewhat different handling of the boundary conditions.

8 Applications of r^{3}t

In this chapter two applications are exemplified, first a two-dimensional test case and second a three-dimensional. Both cases are performed using the same radionuclide inventory with 24 radionuclides and 8 fission products.

8.1 Two-Dimensional Modelling

As a first example a two-dimensional area in the x-z plane is chosen. The vertical cross section of this area extends about 6 km in length and about 150 m in depth. In Fig. 8.1 the modelled area the associated boundary conditions concerning the density driven flow are depicted. Note that every illustration is exaggerated by a factor of 10. The modelled area consists of two highly permeable aquifers (k_a =10^{-12} m^2). The lower aquifer is in contact with a salt dome. This aquifer is connected to the upper aquifer by a window within a clay layer of low permeability (k_c =10^{-16} m^2). The impermeable boundaries are shown black and the boundary to the salt dome is red. The domain which is characterised by hydrostatic pressure of fresh water is depicted in blue, recharge area in green and the region with constant outflow in margenta. The boundaries of the hydrogeologic layers are shown in grey. The point where the radionuclides enter the overburden is marked.

A simulation of density driven groundwater flow with the code d^{3}f [45] results in a quasi stationary flow field. In Fig. 8.2 the density distribution together with the flow pattern is shown. The main flow direction is from the right and water mainly flows diffusively through the left part of the clay layer.

Tab. 8.1 presents the considered radionuclides which enter the overburden at the marked point (cp. Fig. 8.1). Radionuclides which are discussed in the following in more detail are in bold. It is about U-234 with half-live of 245 000 a, Th-230 with half-live of 75 400 a and Ra-226 with half-live of 1 600 a. The radionuclide inventory consists of parts of the four decay chains and additionally eight fission products. It is taken from [18]. In Fig. 8.3 the inflow rate of selected radionuclides are shown.

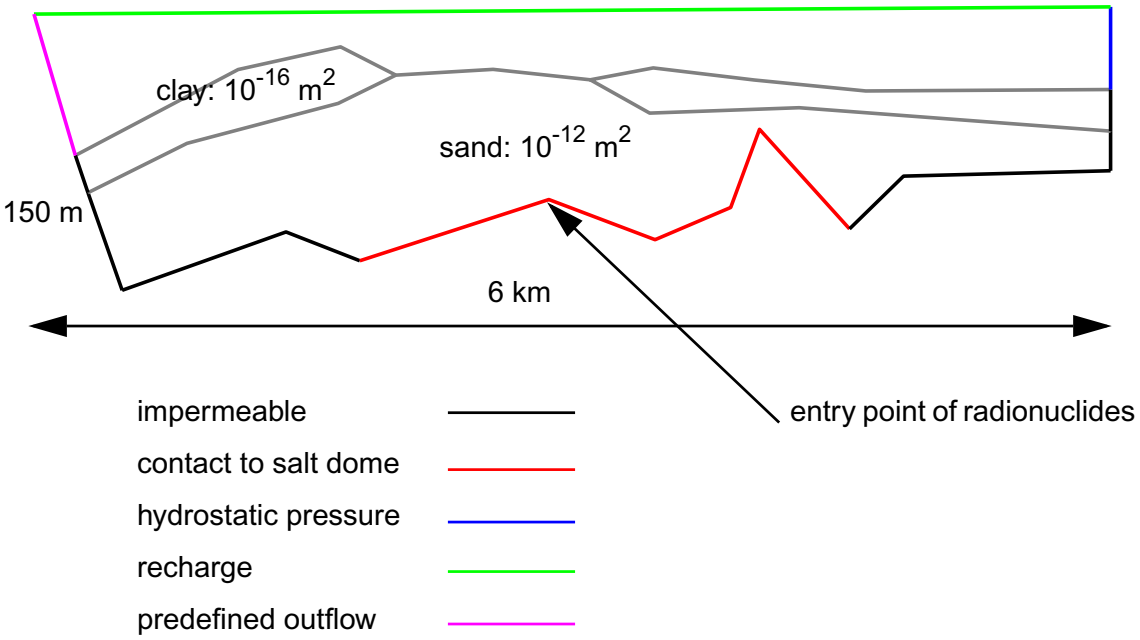

Fig. 8.1 Modelled area and boundary conditions

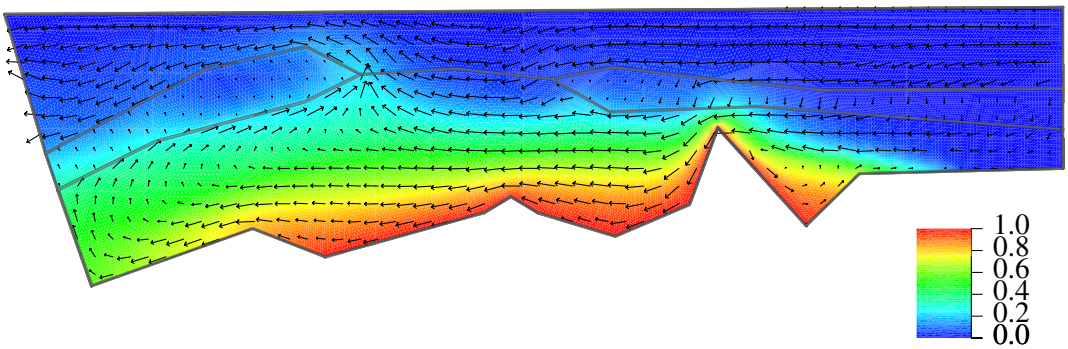

Fig. 8.2 Density-driven flow field and salt concentration distribution

The radionuclides which are compiled in Tab. 8.1 are expelled out from the mine working through the salt dome into the overburden. It is assumed that the expelled contaminated brine has no influence on the groundwater flow field. The inflow of radionuclides corresponds to [18] assuming the reference case with higher brine volume.

In Tab. 8.2 the various K_D values for the radionuclides are compiled for the media sand and clay. Fig. 8.4 to Fig. 8.6 show the temporal development of the radionuclides U-234, Th-230 and Ra-226 in each case at times 1 000 a, 2 000 a, and 10 000 a, respectively.

Tab. 8.1 Spectrum of radionuclides and decay scheme

Pu-244	Cm-244	Pu-241	Cm-246	Am-243
Pu-240		Am-241	Pu-242 Am-242	Pu-239
U-236		Np-237	U-238 Pu-238	U-235
Th-232	U-232	U-233	**U-234**	Pa-231
Ra-228		Th-229	**Th-230**	Ac-227
			Ra-226	
			Pb-210	
+ activation and fission products:				
C-14, Ni-59, Se-79, Zr-93, Nb-94, Tc-99, I-129, Cs-135				

In Fig. 8.4 the concentration of U-234 with time is depicted. Due to the small retention in sand (K_d=7·10^{-4} m^3 kg^{-1}) U-234 is relatively fast transported, while in clay transport is considerably slower because of the stronger retention (K_d=0.01 m^3 kg^{-1}) and porosity (ϕ=0.04). Hence this leads to an accumulation of Uranium in the clay horizon.

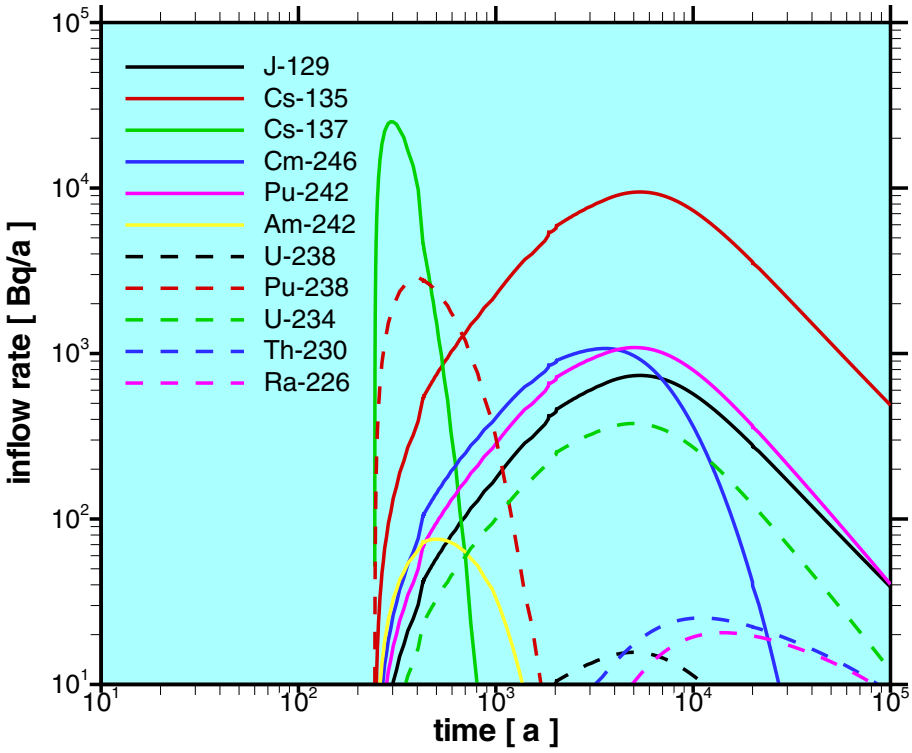

Fig. 8.3 Inflow rates for selected radionuclides

Consequently the total concentration of uranium is larger in clay than in sand. As can be seen in Fig. 8.5 Th-230 shows in comparison to uranium in sand a slow transportation due to the strong retention (K_d=1 m^3 kg^{-1}). This can be seen especially at t=1 000 a. At later times the concentration profile of Th-230 is more and more affected by the radioactive decay of its mother nuclide U-234 (cp. Fig. 8.5 middle and lower illustrations). This results in higher concentration of Th-230 in clay than in sand, since the total concentration of the mother nuclide U-234 is much higher in clay than in sand. One can clearly distinguish the inflowed Th-230 from thorium which was formed by radioactive decay. Ra-226 which is shown in Fig. 8.6 has a similar behaviour like U-234, since the retention of radium in sand (K_d=4·10^{-4} m^3 kg^{-1}) is comparable with that of uranium in sand. The more than three orders of magnitude smaller concentration corresponds to the smaller inflow (cp. Fig. 8.3). After 10 000 a a significant amount of the inflowed Ra-226 has decayed on its pathway. At the same time Ra-226 is reproduced by decay of Th-230.

Tab. 8.2 K_d values for the radionuclides in different media

radionuclide	sand K_d [m^3 kg^{-1}]	clay K_d [m^3 kg^{-1}]
Pu	0.08	1
Cm	0.1	1
U	7·10^{-4}	0.01
Th	1	1
Ra	4·10^{-4}	0.03
Am	0.1	1
Np	0.001	0.005
Pb	0.08	1
Pa	1	1
Ac	0.02	1

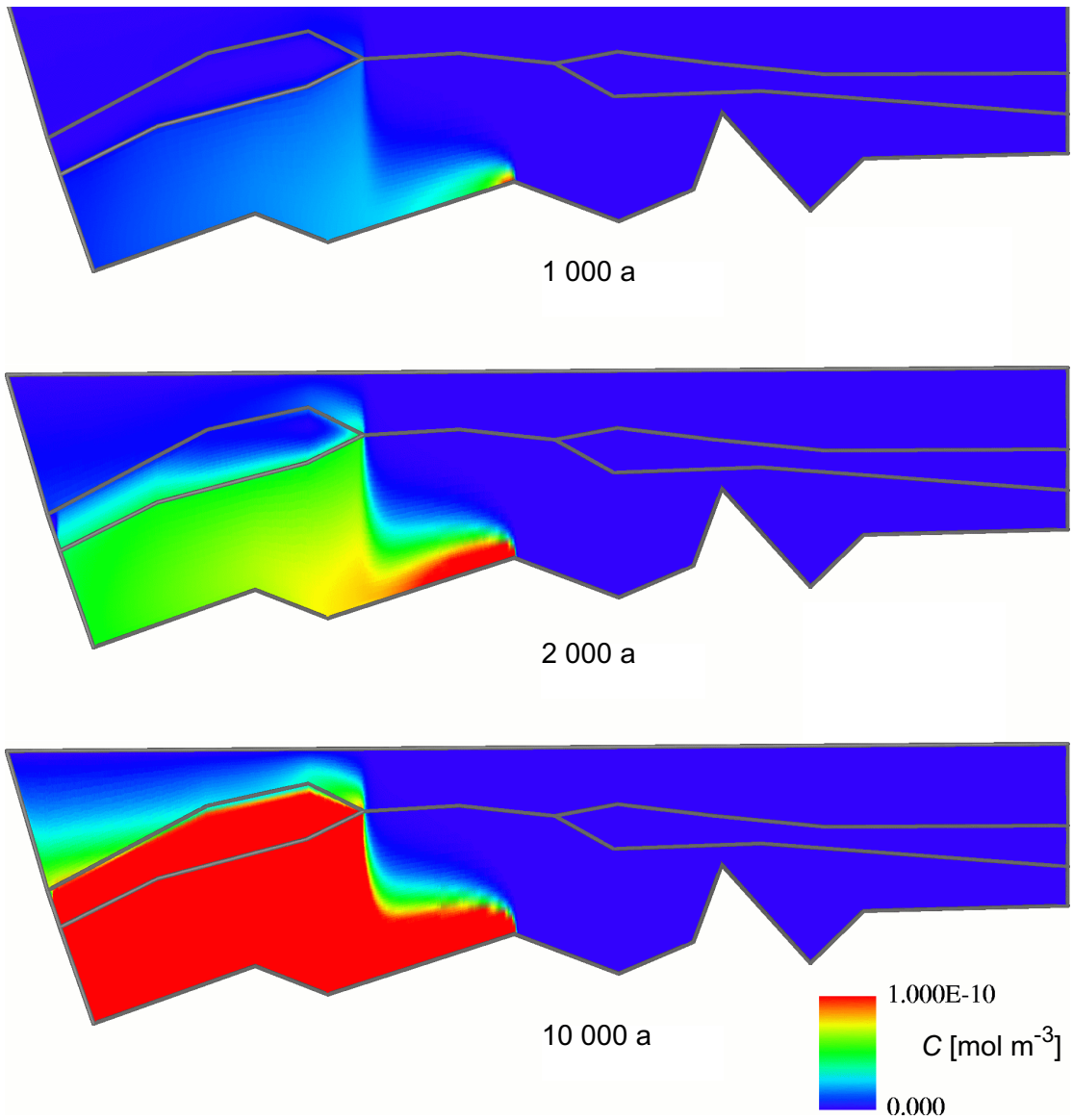

Fig. 8.4 Temporal development of the U-234 concentration [mol m^{-3}]

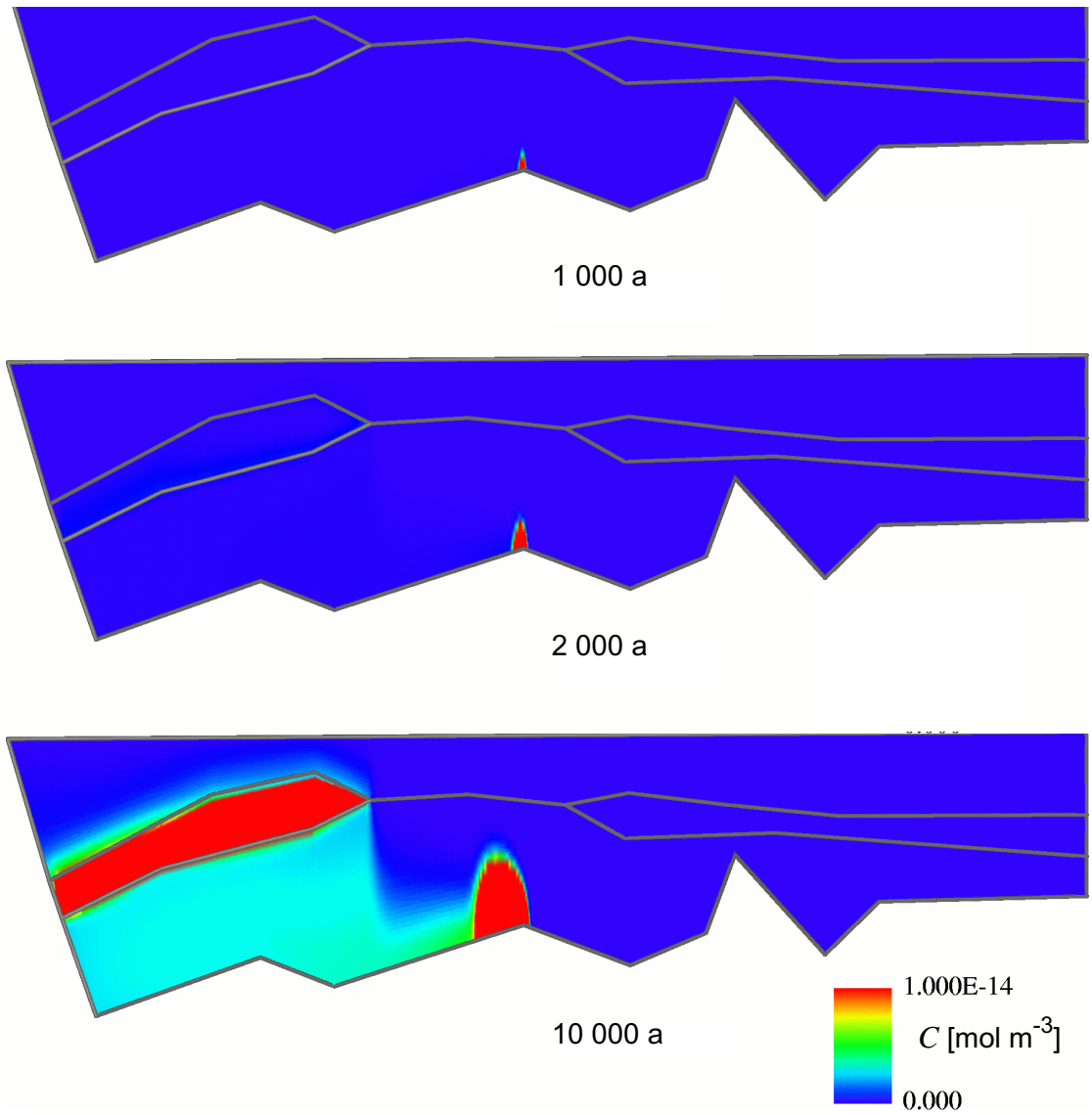

Fig. 8.5 Temporal development of the Th-230 concentration [mol m^{-3}]

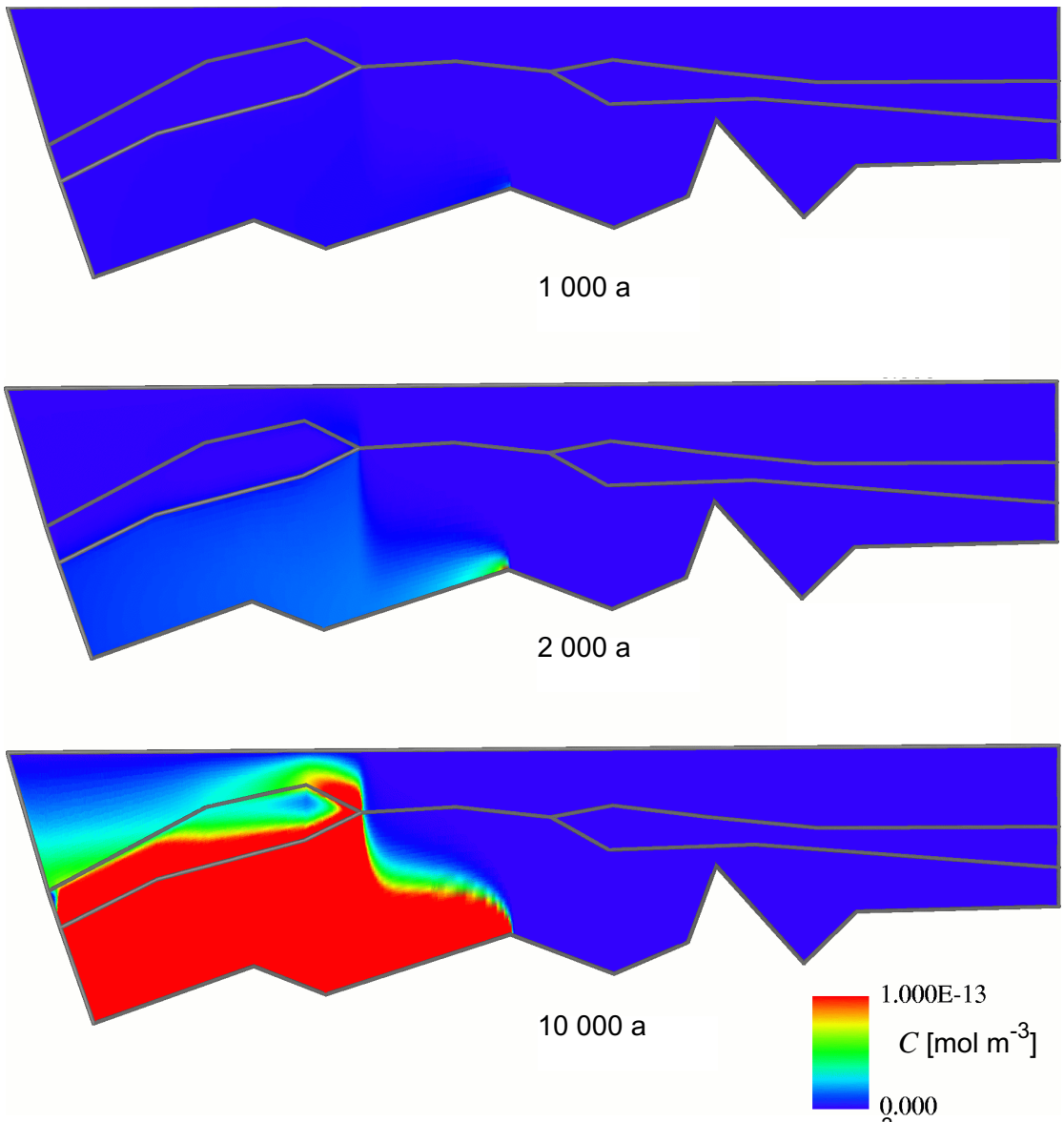

Fig. 8.6 Temporal development of the Ra-226 concentration [mol m^{-3}]

8.2 Three-Dimensional Modelling

The two-dimensional model described in section 8.1 which is extended in the third spatial dimension serves as basis for the three-dimensional test case. In this case the modelled area extends about 6 000 m in length, about 4 000 m in breadth, and about 1 500 m in depth, see Fig. 8.7. Again the modelled area consists of high permeable aquifers (k_a =10^{-12} m^2) which are depicted in Fig. 8.7 in green and blue. The lower aquifer is connected to the upper one by a window within a low permeable clay layer (k_a =10^{-16} m^2) which is shown in red. The lower aquifer is in contact to a salt dome where salt is dissolved. The contact region is modelled as circle with centre coordinates of 1 600 m and 2 200 m in x- and y- orientation, respectively. The radius extends to 1 080 m. Inflow of freshwater takes place at the right surface of the aquifer above the clay layer, while outflow is possible at the left surface of the aquifer above the clay layer. On the top surface two wells are modelled not too far from each other. The coordinates of the sinks are (600 m, 2 100 m) and (1 100 m, 2 000 m). The production rate of both of the wells are 7 000 m^3 d^{-1}.

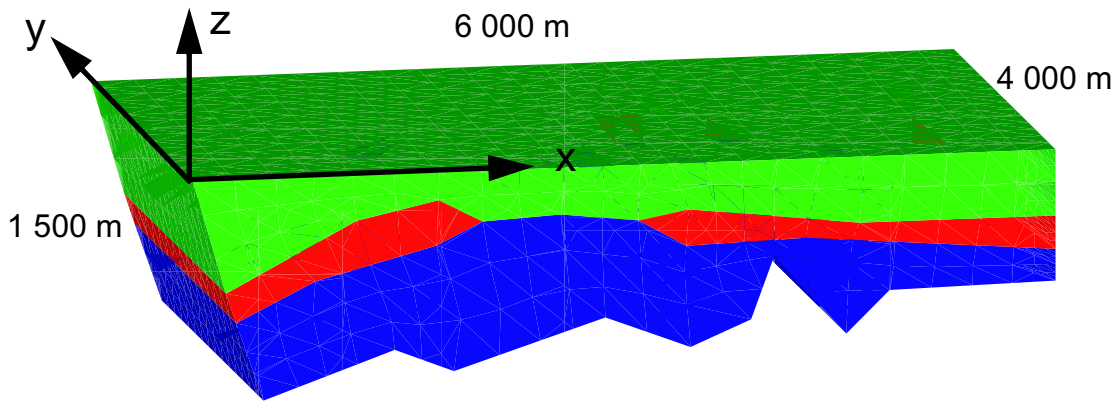

Fig. 8.7 Three-dimensional model and its layers

Again the density driven groundwater simulation is performed with the code d^{3}f [45]. It results in a quasi stationary flow field. In Fig. 8.8 the salt concentration together with the flow pattern on a vertical lengthwise clipping plane is shown. This clipping plane is located near the two points of withdrawal. One can clearly recognise the principal flow direction from right to left and that water mainly flows diffusively through the clay layer. In addition one sees the convergent flow towards the wells.

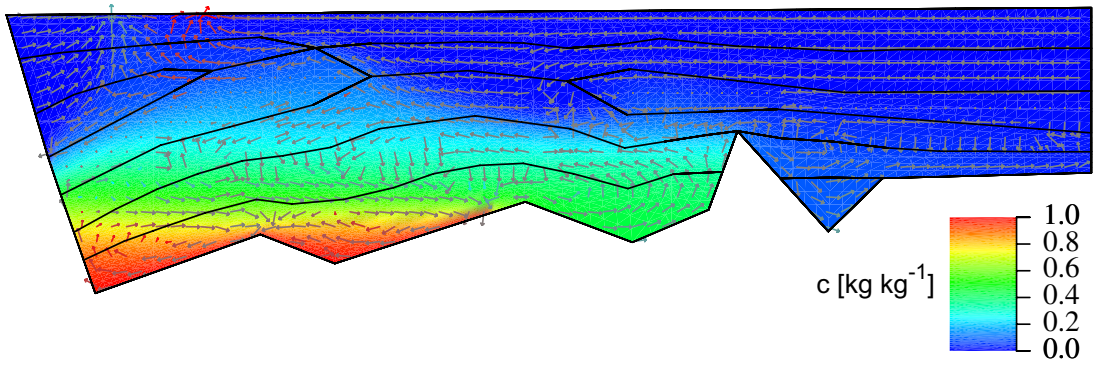

Fig. 8.8 Flow velocity on a lengthwise clipping plane in the centre

The inventory of the considered radionuclides and their inflow rates are the same as in the two-dimensional case (cp. Tab. 8.1 and Fig. 8.3). The radionuclides are squeezed out from the mine working through the salt dome into the overburden at the bottom surface. It is assumed that the squeezed out contaminated brine has no influence on the groundwater flow field. The inflow of radionuclides corresponds to [18] assuming the reference case with enlarged brine volume. In Tab. 8.2 the various K_d values for the radionuclides are compiled for the media sand and clay.

In order to show the efficiency of r^{3}t one could show pictures of the temporal development of any of the 34 radionuclides in a multitude of different plots like isolines, breakthrough curves and so forth. Instead of doing so only one radionuclide (U-236) is selected to illustrate the results of three-dimensional model simulations. In Figs. 8.9 to 8.12 the concentration distribution of U-236 is depicted at model times of 500 a and 10 000 a on both vertical lengthwise and transverse clipping planes. On Figs. 8.9 and 8.11 (500 a) one realises the point of entry where the radionuclides are released into the overburden. One recognises the transport backwards to the principle flow direction due to local flow effects. Figs. 8.10 and 8.12 show the concentration distribution after 10 000 a. On both figures the influence of the clay layers can be found. Almost no radionuclides are transported into the clay domain. They flow around the clay layer directly into the production wells.

8.3 CPU-Time Used

In Tab. 8.3 the computation time used for two- and three-dimensional model simulations is compiled. In all cases 26 radionuclides are considered. The simulations for the activation and fission products are performed separately, so they are not taken into considera-

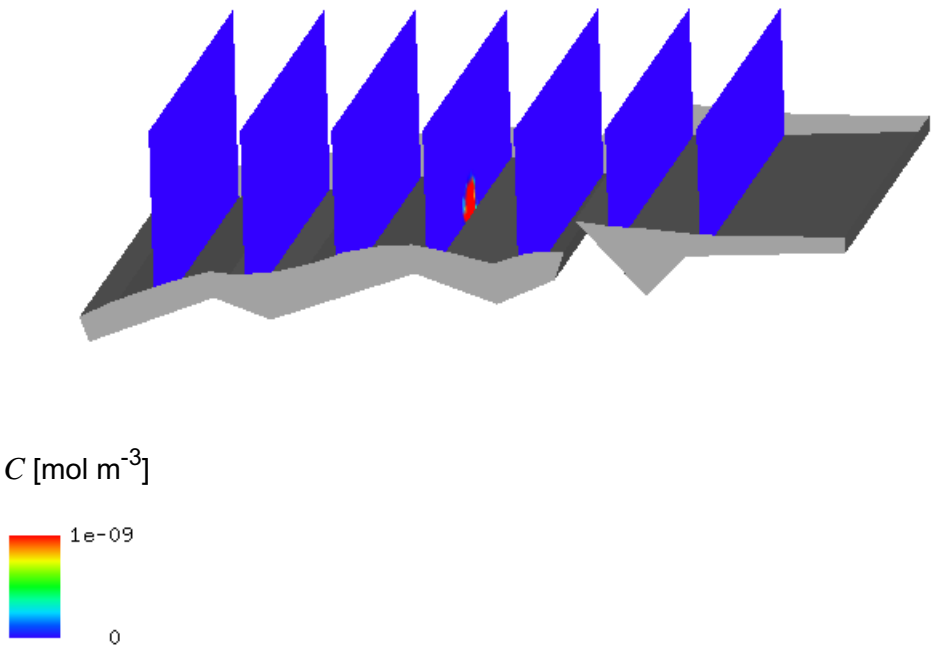

Fig. 8.9 Concentration of U-236 on transverse clipping planes at 500 a

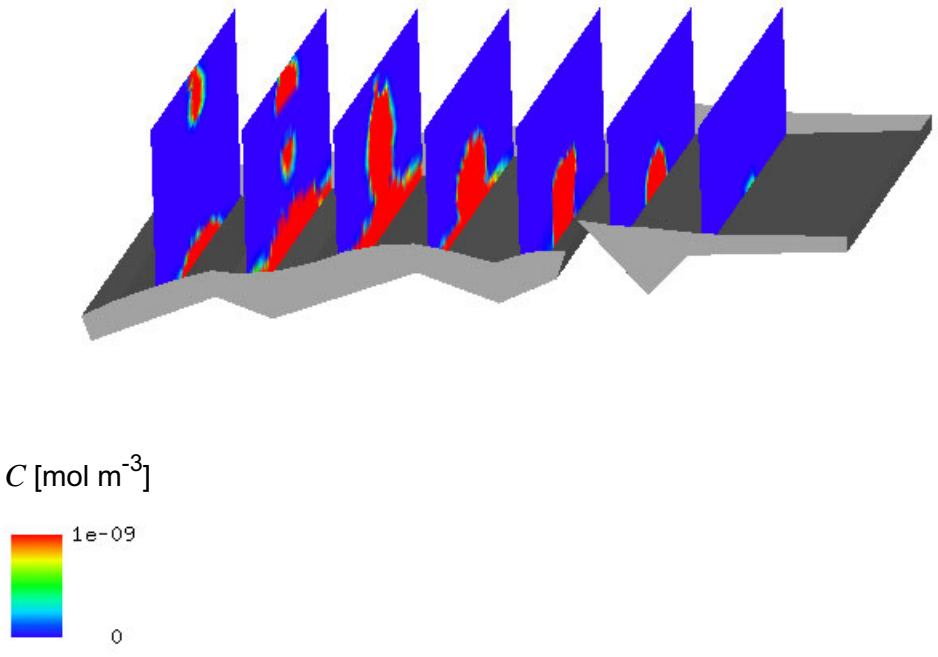

Fig. 8.10 Concentration of U-236 on transverse clipping planes at 10 000 a

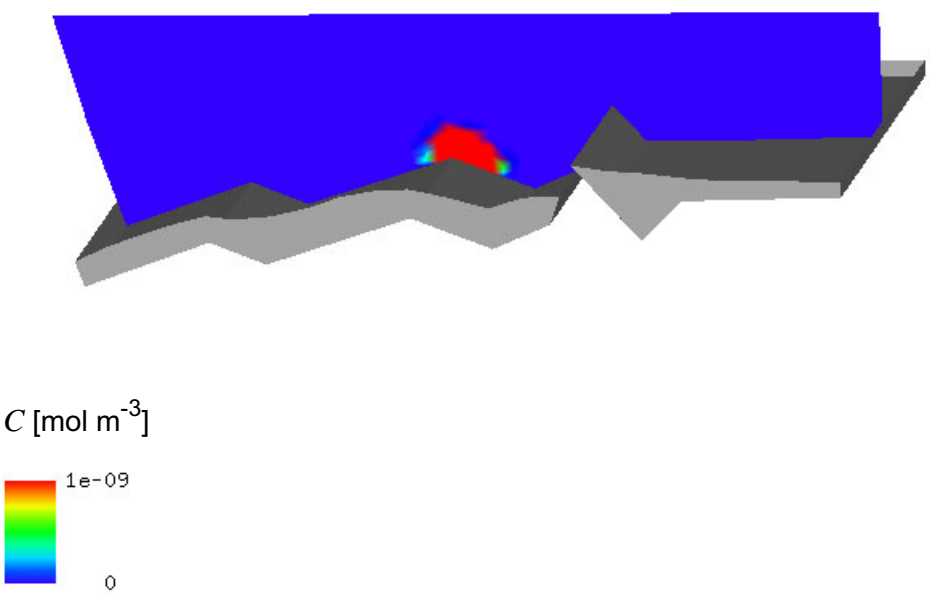

Fig. 8.11 Concentration of U-236 on a lengthwise clipping plane at 500 a

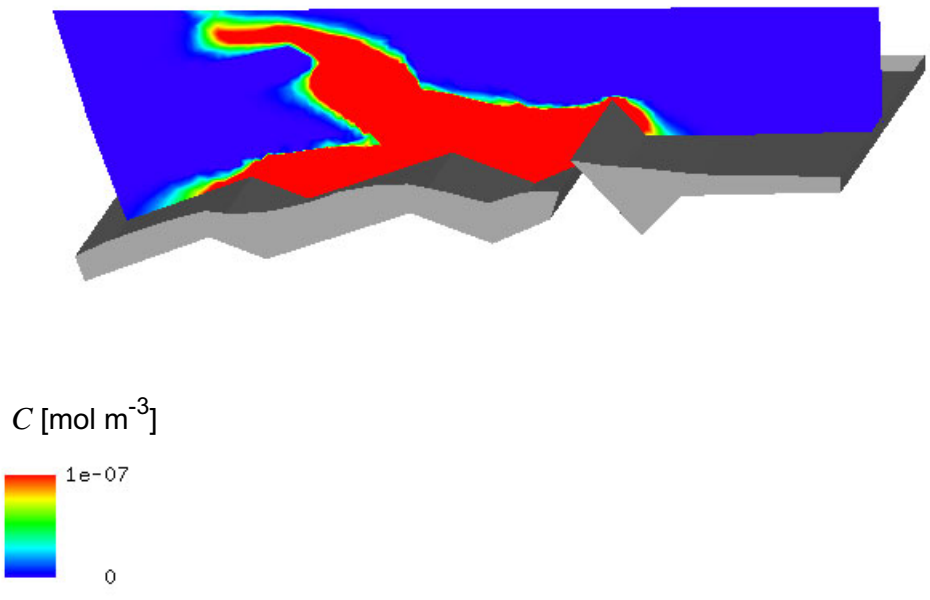

Fig. 8.12 Concentration of U-236 on a lengthwise clipping plane at 10 000 a

tion. For two-dimensional as well as for three-dimensional modelling uniform and adaptive grid refinement were used. The model time ranges all cases from 0 to 10 000 years. The simulations are performed with different numbers of processors and even different processors. The simulation time of about 19 h on an Athlon cluster with 72 processors for three-dimensional adaptive modelling provides confidence in the performing of radionuclide migration simulations within a convenient period of time for realistic inventories in large and complex regions.

Tab. 8.3 CPU-time used for two- and three-dimensional model simulations

number of elements	number of time steps	total elapsed time [h]	number of processors	kind of processor
2-dim. uniform 75 000	3 800	5.5	30	Pentium II 0.4 Ghz
2-dim. adaptive 350 000	3 800	14.5	64	Pentium II 0.4 GHz
3-dim. uniform 530 000	3 600	13.0	16	Athlon 1.6 GHz
3-dim. adaptive 580 000	3 600	18.5	72	Athlon 1.6 GHz
3-dim. adaptive 5 000 000	3 600	28.5	128	Athlon 1.6 GHz

9 Conclusion and Outlook

Up to now in nearly every case in safety assessments the migration of pollutants through the geosphere was modelled one-dimensionally. This was due to the fact that all available computer codes were able to consider simultaneously all relevant retention processes for nuclear decay chains and for large three-dimensional regions. One-dimensional transport models have the disadvantage that the migration pathway has to be determined with particle-tracking algorithms from the velocity field of a three-dimensional flow model. In previously performed safety assessments simulations with one-dimensional migration models considered besides advection, diffusion, radioactive decay, and longitudinal dispersion the retention by adsorption. Both linear and non-linear sorption isotherms were applied.

Recently the computer code r^3t was developed to overcome the restrictions in transport modelling described above. The new code is closely related to d^3f, a computer code to model density-driven flow. Both codes are based on the software toolbox UG which serves for solving partial differential equations.

9.1 The Present State of Development of r^3t

Several independent teams which also participated in the d^3f development worked on this project on their own responsibility. Thus for the successful realisation a close cooperation was required. The main results of the different teams are summarised below.

One part of this work was focused on the impact that small-scale variability might have on the transport behaviour on large scales. It is shown that the applied method of averaging is very important for modelling and understanding of experimental data. It is distinguished between two different averaging procedures - the ensemble and effective averaging. In linear theory, it is assumed that the averages become equal as soon as the solute has spread over some longitudinal correlation lengths. In non-linear transport theory, it was proven that already in the very simple case of fluctuating velocities, the ensemble average generates artificial spreading effects which do not vanish even in the asymptotic regime. The difference between ensemble and effective averaging becomes much more pronounced in the case of variable Freundlich exponents. In particular, the ensemble dispersion will never represent the real mixing behaviour. After all, non-linear

transport processes should be modelled with care. A kind of naive modelling can lead to considerable mistakes in general predictions of concentration peaks, first-arrival times, migration and location of contaminants.

The next part deals with the development of numerical algorithms and the coding of r^{3}t. The software tool r^{3}t is based on the numerical library UG (Unstructured Grids), analogously to d^{3}f. The main purpose of r^{3}t is to realise numerical simulations of radionuclide transport using up to now the results of d^{3}f for the modelling of groundwater flow with variable or constant fluid density. Moreover, the geometrical modelling of computational domains, the grid generation were realised with tools available in d^{3}f. The geometrical and physical data, like the description of computational domain, the model parameters, etc., are defined using a straightforward format of seven configurable files.

To control the numerical parameters, the script files with UG programming language are used. To make the runs of r^{3}t as simple as possible for typical users, the most important parameters are collected in the single file “defaults.scr”. This is the only file that should be modified by user to control specific requirements. Several other parameters can be defined in the file “advance.scr”. This file is meant only for advanced users. These parameters do not need to be changed in typical applications. A general single run script file “r3t.scr” was developed. Its commands realise the numerical simulation.

The numerical library UG is available for several parallel computer platforms. Computations with r^{3}t can be realised on parallel computers. Hence large-scale simulations with enormous requirements on computer memory and computation times are possible.

To obtain a discretisation-independent numerical solution one has to refine the computational grid locally and to use reasonable time steps. An effective error indicator of numerical errors for standard discretisation methods of “convection-diffusion-dispersion-reaction partial differential equations” was developed. To estimate the time discretisation error, some well-known indicators like the Courant number appear to be appropriate. As there are several numerical algorithms available in r^{3}t, including some non-standard ones, different error indicators are necessary for the control of time and space discretisation errors.

Natural and robust solvers for numerical simulations that are realised on hierarchical grid structures are the multigrid solvers. In fact, such solvers are the most important part of the UG library and they are used successfully also in r^{3}t. A very large number of partial differential equations coupled with ordinary differential equations have to be solved with r^{3}t. Such difficult tasks must be performed with an optimal format for discretisation matrices, otherwise the requirements on the size of computer memory can make the computations impracticable.

All numerical algorithms applied for solving radionuclide transport problems are based on finite volume methods. Together with an appropriate discretisation of boundary conditions, all numerical schemes meet the condition of mass preserving on a local and a global level. The decay reactions can be described by very high decay rates that result in impracticable restrictions on the size of time steps. To overcome this difficulty, the exact solution of ordinary differential equations describing the decay reactions was implemented.

Too long time steps may yield unphysical oscillations in numerical solutions. To overcome such situations, a new second-order explicit discretisation scheme for convection equation with flux limiter was developed and implemented. This method was extended, together with a special local flux limiter to avoid unphysical oscillations with unstructured grids as required by r^{3}t.

Even if the reaction equations are solved exactly and the convection equations with some higher precision, they can only be combined with the so-called “operator splitting approach”. This works very well if the two involved operators commute, otherwise a large time splitting error can occur. For the system of convection equations with different retardation factors that are coupled through decay reactions, such large time splitting errors can occur. A new second-order explicit discretisation method was developed and implemented for this type of equations.

A new flux-based method of characteristics for the convection-dominated transport, and later also for coupled system of convection equations was developed and implemented. Moreover, the flux-based method of characteristics for systems of transport equations includes in a natural way the treatment of decay reactions, avoiding the time splitting error of standard operator splitting methods.

Finally, for the case of transport with equilibrium non-linear sorption, appropriate extensions of the previous explicit methods were implemented in r^{3}t to correctly resolve shock formations in numerical solutions.

Together with the possibility to use parallel computations of complex applications, the simulator r^{3}t offers the highest level software tools for realistic computations of problems dealing with radionuclides transport in subsurface.

To ensure an efficient manageability of the simulator of the software package r^{3}t graphical user interfaces (GUI) are developed which are appropriate to the treated problems. By use of these GUIs pre- and postprocessing is carried out.

By means of the preprocessor all data which are required to perform a simulation are generated or changed. It consists of two parts. The first is responsible for the model data which describe the problem, and the second serves for the numerical control of the simulator. Both of them are coded in Java as a platform independent tool. The problem description is based on the geometry description of the groundwater flow code d^{3}f. The d^{3}f input file geometry is adopted without any change. In seven input files the required model data are made available. In an eighth file the parameters to control numerics are given. But these parameters may be modified only in a restricted range to avoid numerical errors or even program aborts.

The postprocessor is based on the postprocessor of d^{3}f which is constructed on GRAPE (**GRA**phical **P**rogramming **E**nvironment). In the extended version of r^{3}t the handling of the postprocessor itself is simplified. Additionally it is enabled to process huge amounts of multidimensional data. Further on it is advanced by some new presentation and data reduction techniques.

9.2 Verification and Application

Several tests for the verification of r^{3}t are presented. The proposed methods can be used for a-posteriori test of any numerical code for simulating solute transport. One is the re-identification of the transport parameters, e.g. transport velocity and dispersion coefficients, check of the total mass, check of the front velocity for transport with a permanent solute injection. The other method is the comparison with analytical solutions. These tests

were used for the verification of homogeneous solute transport. Analytical or semi-analytical solutions are developed for unidirectional, homogeneous flow in one, two, and three dimensions. A huge variety of test cases are performed comparing analytical with numerical results of r^3t. Further on numerical results of r^3t were compared to numerical results of other computer codes for linear and non-linear sorption.

The presented results are produced with the final version of r^3t. The numerical results are in very good agreement with the expected theoretical values. Especially, the sharpness of the concentration front in the case of non-linear adsorption of Freundlich type is excellently resolved.

To show the capability of r^3t, a two- and a three-dimensional test case are performed. In both cases realistic flow fields assessed with the flow simulator d^3f are used. Likewise in both simulations the same sources of radionuclides with 26 isotopes and identical inflow rates are taken into consideration. In both of the test cases plausibility arguments for the transport hold. The plumes of pollutants clearly show the heterogeneities of the underlying flow patterns and hence of the geometry of the problem. The simulations were performed on a cluster of PCs. For instance, an example for the transport of 26 radionuclides in a three-dimensional, complex domain with 5 millions of grid points was realised using 128 processors of an Athlon-based PC cluster. It took about 29 h to model the transport for 10 000 y.

9.3 Desirable Further Development

Similar to the development of d^3f the actual state of r^3t cannot be considered as complete. Since r^3t is a most recently developed computer code it seems quite normal that the available software infrastructure is actually not as advanced as for established transport codes. For the same reason one has to allow for small errors and deficiencies, but these will be detected in the course of future applications of r^3t.

Besides the testing and applying of r^3t it is very important to elaborate the r^3t code. The most severe bottleneck in the usage of r^3t is the limited linkage to groundwater codes. Up to now only results of d^3f modelling may be used as input for r^3t simulations. One should be careful, because not only the flow field has to be transferred but also the geometrical information of the hydrogeology.

Some other enhancements would considerably improve the range of application for r^3t considerably. But these are only conceivable in connection with further developments of d^3f. The most important are:

- the connection to a Geo Information System (GIS),
- the modelling of free water tables,
- the explicit modelling of fractures,
- the coupling to a speciation code.

9.4 Summary

Upon completion of the program suite r^3t it becomes feasible to model three-dimensional transport through porous and equivalent porous media for spacious and heterogeneous modelling areas. The following transport effects are considered; advection, diffusion, and dispersion. Furthermore, every relevant retention and interaction effects which are important for long-term safety analyses are included. These are equilibrium sorption, kinetically controlled sorption, diffusion into immobile pore waters, and precipitation. The processes of complexation, colloid-borne radionuclide transport and matrix diffusion may be considered at least approximately by skilful choice of parameters. Speciation is not a part of the computer code r^3t.

The development of efficient solvers for a system of linear or non-linear coupled “advection-diffusion-dispersion-reaction” equations enables to solve the appropriate large system of discrete equations within appropriate periods of time. It becomes feasible to solve systems of coupled differential equations on serial and parallel computers. Hence progress is achieved not only in the area of long-term safety analysis and stochastical transport modelling but also on the field of numerics and software engineering.

10 References

[1] Abulaban, A.; Nieber, J. L.: Modeling the effects of nonlinear equilibrium sorption of solute plumes in saturated heterogeneous porous media. Advances in Water Resources 23, 893-905, 2000.

[2] Aho, A. V.; Sethi, R.; Ullman, J. D.: Compilers: Principles, Techniques and Tools. Addison-Wesley, 1986.

[3] Arens, G.; Hossain, S.; Fein, E.: SWIFT: Intera Simulator for Waste Injection Flow and Transport, Version: GSF2. GSF-Bericht 28/90. GSF - Forschungszentrum für Umwelt und Gesundheit GmbH, Braunschweig, 1992.

[4] Attinger, S.; Dentz, M.; Kinzelbach, H.; Kinzelbach, W.: Temporal behaviour of a solute cloud in a chemically heterogeneous porous medium, J. Fluid Mech. 386, 77-104, 1999.

[5] Attinger, S.; Dimitrova Micha, J.; Kinzelbach, W.: Multiscale modeling of non-linearly adsorbing solute transport. SIAM Multiscale Model. Simul. 3 (1), 408-431, 2003.

[6] Barrett, J.W.; Knabner, P: An improved error bound for a Lagrange-Galerkin method for contaminant transport with non-Lipschitzian adsorption kinetics. SIAM J. Numer. Anal. 35(5): 1862-1882 (electronic), 1998.

[7] Bastian, P.; Birken, K.; Eckstein, K.; Johannsen, K.; Lang, S.; Neuss, N.; Rentz-Reichert, H.: UG - A Flexible Software Toolbox for Solving Partial Differential Equations. Computing and Visualization in Science 1, 1, 27-40, 1997.

[8] Bastian, P.; Lang, S.: Couplex Benchmark Computations with UG. Technical report 31, IWR, Universität Heidelberg, 2002.

[9] Bateman, H.: The solution of a system of differential equations occurring in the theory of radio-active transformations. Cambr. Phil Soc. Proc. 5, 423-427, 1910.

[10] Bauer, P.: Transport einer Zerfallskette im porösen Medium: Analytische Lösungen und deren Anwendung. Master's thesis, ETH Zürich, 1999.

[11] Bauer, P.; Attinger, S.; Kinzelbach, W.: Transport of a decay chain in homogeneous porous media: analytical solutions. J. Contam. Hydrol. 49, 217-239, 2001.

[12] Bellin, A.; Rinaldo, A.; Bosma, W. J. P.; van der Zee, S. E. T. M.; Rubin, Y.: Linear equilibrium adsorbing solute transport in physically and chemically heterogeneous porous formations, 1. Analytical solutions. Water Resour. Res. 29 (12), 4019-4030, 1993.

[13] Bellin, A.; Rinaldo, A.; Bosma, W. J. P.; van der Zee, S. E. T. M.; Rubin, Y.: Linear equilibrium adsorbing solute transport in physically and chemically heterogeneous porous formations, 2. Numerical solutions. Water Resour. Res. 29 (12), 4031-4043, 1993.

[14] Berglund, S.; Cvetkovic, V.: Contaminant displacement in aquifers: Coupled effects of flow heterogeneity and nonlinear sorption. Water Resour. Res. 32, 23-32,1996.

[15] Berglund, S.; Fiori, A.: Influence of transverse mixing on the breakthrough of sorbing solute in a heterogeneous aquifer. Water Resour. Res. 33 (3), 399-405, 1997.

[16] Bosma, J.P.; van der Zee, S.E.A.T.M.: Dispersion of a continuously injected, non-linear adsorbing solute ion chemically or physically heterogeneous porous formations. Journal of Contaminant Hydrology 18, 181-198, 1995.

[17] Bosma, J. P.; van der Zee, S. E. A. T. M.: Plume development of nonlinear adsorbing solute in heterogeneous media. Water Resour. Res. 32 (6), 1569-1584, 1996.

[18] Brenner, J.; Buhmann, D.; Kühle, T.: Einfluss netzwerkartiger Strukturen der Grubenhohlräume auf die Langzeitsicherheit eines Endlagers im Salinar.

Gesellschaft für Anlagen- und Reaktorsicherheit (GRS) mbH, GRS-163, Braunschweig 2000.

[19] Buhmann, D.; Nies, A.; Storck, R.: Analyse der Langzeitsicherheit von Endlagerkonzepten für wärmeerzeugende radioaktive Abfälle. GSF-Bericht 27/91. GSF - Forschungszentrum für Umwelt und Gesundheit GmbH, Braunschweig 1991.

[20] Buhmann, D.: Relevance of near field and far field effects to the release of radionuclides from repositories with low level waste. Intern. Symp. on Experience in the Planning and Operation of Low Level Waste Disposal Facilities. p. 405-416, IAEA, Vienna, 17.-21. June 1996.

[21] Bürkle, D.; Ohlberger, M: Adaptive finite volume methods for displacement problems in porous media. Comput. Visual. Sci. 5(2): 95--106, 2002.

[22] Burr, D. T.; Sudicky, E. A.; Naff, R. L.: Nonreactive and reactive solute transport in three-dimensional heterogeneous porous media: Mean displacement, plume spreading, and uncertainty. Water Resour. Res. 30 (3), 791-815, 1994.

[23] Cirpka, O.: Choice of dispersion coefficients in reactive transport calculations on smoothed fields. J. Contam. Hydrol. 56 (3-4), 261-282, 2002.

[24] Cirpka, O.; Kitanidis, P.: Characterization of mixing and dilution in heterogeneous aquifers by means of temporal moments. Water Resour. Res. 36 (5), 1221-1263, 2000.

[25] Coats, K.H.; Smith, B.D.: Dead-end pore volume and dispersion in porous media. Society of Petroleum Engineers Journal, 4 (3), 73-84, 1964.

[26] Cushman, J. H.; Hu, B. X.; Deng, F. W.: Nonlocal reactive transport with physical and chemical heterogeneity: Localization errors. Water Resour. Res. 31 (9), 2219-2237, 1995.

[27] Dagan, G.: Solute transport in heterogeneous formations. J. Fluid Mech. 145, 151-177, 1984.

[28] Dagan, G.: Stochastic modeling of groundwater flow by unconditional and conditional probabilities: The inverse problem. Water Resour. Res. 21 (1), 65-72, 1985.

[29] Dagan, G.: Time-dependent macrodispersion for solute transport in anisotropic heterogeneous aquifers. Water Resour. Res. 14 (9), 1491-1500, 1988.

[30] Dagan, G.: Flow and Transport in Porous Formations. Springer New York, 1989.

[31] Dagan, G.: Transport in heterogeneous porous formations: Spatial moments, ergodicity, and effective dispersion. Water Resour. Res. 26 (6), 1281-1290, 1990.

[32] Dagan, G.: Dispersion of a passive solute in non-ergodic transport by steady velocity fields in heterogeneous formations. J. Fluid Mech. 233, 197-210, 1991.

[33] Dawson, C. N.; van Duijn, C. J.; Grundy, R.E.: Large time asymptotics in contaminant transport in porous media. SIAM J. Appl. Math. 56 (8), 965-993, 1996.

[34] Dawson, C.N.: Analysis of an upwind-mixed finite element method for non-linear contaminant transport equations. SIAM J. Numer. Anal. 35(5): 1709-1724 (electronic), 1998.

[35] Dawson, C.N.; Van Duijn C.J.; Wheeler, M.F.: Characteristic-galerkin methods for contaminant transport with nonequilibrium adsorption kinetics. SIAM J. Num. Anal. 31: 982-999, 1994.

[36] Deng, F.-W.; Cushman, J. H.; Delleur, J.W.: A Fast Fourier Transform Stochastic Analysis of the Contaminant Transport Problem. Water Resour. Res. 29 (9), 1993.

[37] Dentz, M.; Kinzelbach, H.; Attinger, S.; Kinzelbach, W.: Temporal behavior of a solute cloud in a heterogeneous porous medium 1. Point-like injection. Water Resour. Res. 36 (12), 3591-3604, 2000.

[38] Dimitrova Micha, J.; Attinger, S.; Kinzelbach, W.: Note on the transport of non-linearly reactive solute in a single heterogeneous formation. (submitted to Nuclear Science and Engineering), 2003.

[39] Dimitrova Micha, J.; Attinger, S.; Kinzelbach, W.: Influence of chemical heterogeneity on the large-scale transport of nonlinearly adsorbing solutes. (in preparation), 2003.

[40] Dimitrova Micha, J.; Attinger, S.; Kinzelbach, W.: Modeling of Ensemble and Real Mixing Behavior for Nonlinearly Adsorbing Transport. (submitted to Advances in Water Resources), 2003.

[41] Dimitrova Micha, J.; Attinger, S.; Kinzelbach, W.: Note on the transport of non-linearly reactive solute in a single heterogeneous formation. (submitted to Nuclear Science and Engineering), 2003.

[42] DOE/CAO-1996-2184, Title 40 CFR Part 191 Compliance Certification Application for the Waste Isolation Pilot Plant, United States Department of Energy, Carlsbad, New Mexico, October 1996.

[43] Fein, E. (ed.): r^3t - A Program Suite to Model Transport and Retention of Radionuclides. User's Manual. Gesellschaft für Anlagen- und Reaktorsicherheit (GRS) mbH, Anlage zu GRS-192, Braunschweig, 2004.

[44] Fein, E. (ed.): r^3t - A Program Suite to Model Transport and Retention of Radionuclides. Test Case Library. Gesellschaft für Anlagen- und Reaktorsicherheit (GRS) mbH, Anlage zu GRS-192, Braunschweig, 2004.

[45] Fein, E.; Schneider, A.: Ein Programmpaket zur Modellierung Dichteströmungen. Gesellschaft für Anlagen- und Reaktorsicherheit (GRS) mbH, GRS-139, Braunschweig, 1999.

[46] Fiori, A.: Finite Peclet extension of Dagan's solution to transport in anisotropic heterogeneous formations. Water Resour. Res. 32 (1), 193-198, 1996.

[47] Fiori, A.: On the influence of pore-scale dispersion in nonergodic transport in heterogeneous formations. Transport in Porous Media 30, 57-73, 1998.

[48] Frolkovič, P.: Maximum principle and local mass balance for numerical solutions of transport equation coupled with variable density flow. Acta Mathematica Universitatis Comenianae 67, 1, 137-157, 1998.

[49] Frolkovič, P.: Discretization. In: d^3f - ein Programmpaket zur Modellierung von Dichteströmungen, Gesellschaft für Anlagen- und Reaktorsicherheit (GRS) mbH, GRS-139, ISBN 3-923875-97-5, Braunschweig, 1999.
see also http://www.iwr.uni-heidelelberg.de/$\sim$Peter.Frolkovic

[50] Frolkovič, P.: Flux-based method of characteristics for contaminant transport in flowing groundwater. Computing and Visualization in Science 5, 2, 73-83, 2002.

[51] Frolkovič, P.: Flux-based method of characteristics for coupled transport equations in porous media. Computing and Visualization in Science, to appear, 2004.

[52] Frolkovič, P.: The Simulator. Methods used. In: r^3t - A Program Suite to Model Transport and Retention of Radionuclides. User's Manual. Gesellschaft für Anlagen- und Reaktorsicherheit (GRS) mbH, Anlage zu GRS-192, Braunschweig, 2004.

[53] Frolkovič, P.; Geiser, J.: Numerical simulations of radionuclides transport in double porosity media with sorption. Proceedings of Algorithmy 2000, 28--36, 2000.

[54] Frolkovič, P.; Geiser, J.: Discretization methods with discrete minimum and maximum property for convection dominated transport in porous media. In: Numerical Methods and Applications, Lecture Notes in Computer Science 2542, eds: Dimov, I. et al., Springer-Verlag, Berlin Heidelberg, 445-453, 2003.

[55] Frolkovič, P.; Geiser, J.; Wittum, G.: New second order discretization scheme for system of transport equations coupled through first-order reactions. (in preparation), 2003.

[56] Frolkovič, P.; Mikula, K.: Flux-based level set method: A finite volume method for evolving interfaces. IWR Interdisziplinäres Zentrum für Wissenschaftliches Rechnen, Universität Heidelberg, Preprint 15, 2003.

[57] Frolkovič, P.: The software tool r^3t and the numerical methods: final report. Interdisziplinäres Zentrum für Wissenschaftliches Rechnen, Heidelberg, November 18, 2003.

[58] Garabedian, S. P.; Le Blanc, D. R.; Gelhar, L. W.; Celia, M. A.: Large-scale natural gradient test in sand gravel, Cape Cod, Massachusetts: Analysis of spatial moments for a nonreactive tracer. Water Resour. Res. 27 (5), 911-924, 1991.

[59] Geiser, J.: Numerical simulation of a model for transport and reaction of radionuclides. Proceedings of LSSC 01 (submitted), 2001.

[60] Geiser, J.: Lecture on Discretization methods for system of convection-diffusion-reaction equations and applications realized with paralel computers. In: Workshop on Parallel and adaptive computing. Hohenwart, 2003.

[61] Geiser, J.: Diskretisierungsverfahren für Systeme von Konvektions-Diffusions-Dispresions-Reaktions-Gleichungen und Anwendungen. PhD thesis, Universität Heidelberg, 2003.

[62] Gelhar, L. W.: Stochastic Subsurface Hydrology. Englewood Cliffs, NJ, 1993.

[63] Gelhar, L. W.; Axness, C. L.: Three-Dimensional Stochastic Analysis of Macrodispersion in Aquifers. Water Resour. Res. 19 (1), 161-180, 1983.

[64] Goodwin, B.W.; McConell, D.B.; Andres, T.H.; Hajas, W.C.; Le Neveu, D.M.; Melnyk, T.W.; Shermann, G.R.; Stephens, M.E.; Szekely, J.G.; Bera, P.C.; Cosgrove, C.M.; Dougan, K.D.; Keeling, S.B.; Kitson, C.J.; Kummen, B.C.; Oliver, S.E.; Witzke, K.; Wojciechowski, L.; Wikjord, A.G.: The Disposal of Canada's Nuclear Fuel Waste: Postclosure Assessment of a Reference System. AECL-10717. August 1994.

[65] Grundy, R. E.; van Duijn, C. J.; Dawson, C. N.: Asymptotic profiles with finite mass ion one-dimensional contaminant transport through porous media: The fast reaction case. Q. Journal of Mech. appl. Math. 47 (1), 69-106, 1994.

[66] T. Ikeda, T.: Maximum principle in finite element models for convection-diffusion phenomena. North-Holland, Amsterdam, New York, Oxford, 1983.

[67] Johannsen, K.: Aligned 3D-finite-volumes for convection-diffusion-problems. In: Finite Volumes for Complex Applications. eds: Benkhaldoun, F.; Vilsmeier,R.: Hermes, Paris, 291-300, 1996.

[68] Johnson, C.: The streamline diffusion finite element method for compressible and incompressible fluid flow. Finite Element Method in Fluids VII, Huntsville, 1989.

[69] Häfner, F.; Sames, D.; Voigt, H.-D.: Wärme- und Stofftransport. Mathematische Methoden. Springer-Verlag Berlin Heidelberg New York, 1992.

[70] Hinz, C.; Gaston, L. A.; Selim, H. M.: Effect of sorption isotherm type on predictions of solute mobility in soil. Water Resour. Res. 30 (11), 3013-3021, 1994.

[71] Hirsekorn, R.-P-; Nies, A.; Rausch, H.; Storck, R.: Performance Assessment of Confinements for Medium-Level and Alpha-Contaminated Waste (PACOMA): Rock Salt Option. EUR 13 634 EN, GSF-Bericht 12/91. Kommission der Europäischen Gemeinschaften, GSF - Forschungszentrum für Umwelt und Gesundheit GmbH, Brüssel-Luxemburg 1991.

[72] Hu, B. X.; Deng, F.-W.; Cushman, J. H.: Nonlocal reactive transport with physical and chemical heterogeneity: Linear nonequilibrium sorption with random K_d. Water Resour. Res. 32 (9), 2239-2252, 1995.

[73] Jaekel, U.,; Georgescu, A.; Vereecken, H.; Asymptotic analysis of nonlinear equilibrium solute transport in porous media. Water Resour. Res. 32 (10), 3093-3098, 1996.

[74] Jakob, A.; Hadermann, F.; Rösel, F.: Radionuclide chain transport with matrix diffusion and nonlinear sorption. Technical Report 90-13, NAGRA, Baden, February 1990.

[75] Kacur, J.: Solution of degenerate convection-diffusion problems by the method of characteristics. SIAM J. Numer. Anal. 39(3): 858-879, 2001.

[76] Kacur, J.; Frolkovič, P.: Semi-analytival solutions for contaminant transport with nonlinear sorption in 1 D. Preprint 2002 - 24, IWR Interdisziplinäres Zentrum für Wissenschaftliches Rechnen, Universität Heidelberg, 2002.

[77] Kacur, J.; Van Keer, R.: Solution of contaminant transport with adsorption in porous media by the method of characteristics. Math. Model. and Numer. Anal. 35 (5): 981-1006, 2001.

[78] Karlsen, K.H.; Ohlberger, M.: A note on the uniqueness of entropy solutions of nonlinear degenerate parabolic equations. J. Math. Anal. Appl. 275(1): 439-458, 2002.

[79] Kinniburgh, D. J.; Barker, J. A.; Whitfield, W.: A Comparison of Some Simple Adsorption Isotherms for Describing Divalent Cation Adsorption by Ferryhydrite. J. Coll. Interf. Sci. 35 (2), 370-384, 1983.

[80] Kinniburgh, D. G.: Multipurpose sorption isotherm. Environ. Sci. Technol. 20, 895-904, 1986.

[81] Kinzelbach, W.: Numerische Methoden zur Modellierung des Transports von Schadstoffen im Grundwasser. Schriftenreihe gwf Wasser, Abwasser; Band 21, Oldenbourg Verlag, 1987.

[82] Kinzelbach, W.; Dimitrova, J. M.; Attinger, S.; Bauer, P.: Development of a Tool for Simulating Radionuclide Transport and Reactions in Groundwater: Final report. Institute of Hydromechanics and Water Resources Management, ETH Hönggerberg, 8093 Zurich, Switzerland, November 3, 2003.

[83] Kitanidis, P. K.: Prediction by the method of moments of transport in a heterogeneous formation. J.of Hydrology 102, 453-473, 1988.

[84] Kitanidis, ,P. K.: Analysis of macrodispersion through volume averaging: Moment equations. Stochastic Hydrology and Hydraulics , 5-25, 1992.

[85] Klöfkorn, R.; Kröner, D.; Ohlberger, M.: Local adaptive methods for convection dominated problems. Internat. J. Numer. Methods Fluids 40(1-2): 79-91, 2002.

[86] Koch, D. L.;J Brandy, J.F.: A non-local description of advection-diffusion with application to dispersion in porous media. J. Fluid Mech. 180, 387-403, 1987.

[87] Kröner, D.; Küther, M.; Ohlberger, M.; Rohde, C.: A posteriori error estimates and adaptive methods for hyperbolic and convection dominated parabolic conservation laws. Submitted to the book project, Kirkilionis, M.; Krömker, S.; Rannacher, R.; Tomi, F. (Eds.): Trends in Nonlinear Analysis, Springer, 2001.

[88] Kröner, D.; Ohlberger, M.: A-posteriori error estimates for upwind finite volume schemes for nonlinear conservation laws in multi dimensions. Math. Comput. 69: 25-39, 2000.

[89] Kröner, D.; Ohlberger, M.; Bürkle, D.; Klöfkörn, R.: A posteriori error estimates and adaptivity for finite volume approximations. Institut für Mathematik, Freiburg, December 3, 2002.

[90] Kühle, T.; Zude, F.; Lührmann, L.: Das eindimensionale Transportprogramm CHET1 unter Berücksichtigung der Sorption nach dem K_d-Konzept. Gesellschaft für Anlagen- und Reaktorsicherheit (GRS) mbH, GRS-124, Braunschweig 1996.

Lührmann, L.; Noseck, U.: Das eindimensionale Transportprogramm CHET2 unter Berücksichtigung nichtlinearer, elementspezifischer Gleichgewichtssorption. Gesellschaft für Anlagen- und Reaktorsicherheit (GRS) mbH, GRS-125, Braunschweig 1996.

[91] Küther, M.; Ohlberger, M.: Adaptive second order central schemes on unstructured staggered grids. Submitted to: Proceedings of Hyp 2002, Pasadena, 2002.

[92] Lang, S.: Parallele Numerische Simulation instationärer Probleme mit adaptiven Methoden auf unstrukturierten Gittern. PhD thesis, Institut für Wasserbau, Universität Stuttgart, Mitteilungen Heft 110, 2001.

[93] Lampe, M.: Parallele Visualisierung - Ein Vergleich. PhD thesis, Universität Heidelberg, 2003.

[94] LeVeque, R. J.: Finite Volume Methods for Hyperbolic Problems. Cambridge Texts in Applied Mathematics, Cambridge University Press, 2002.

[95] Lührmann, L.; Noseck, U.; Tix, C.: Model of contaminant transport in porous media in the presence of colloids applied to actinide migration in column experiments. Water Resources Research 34, No. 3, 421-426, 1998.

[96] Lube, G.; Tobiska, L.: A nonconforming finite element method of streamline-diffusion type for the incompressible Navier-Stokes equation. J. Comp. Math. 8, 147-158, 1990.

[97] Mathcad 2000 Benutzerhandbuch. MathSoft, Inc. 101 Main Street, Cambridge, Massachusetts 02142, USA, http://www.mathsoft.com/, 2000.

[98] McDonald, M. G.; Harbaugh, A. W.: A modular three-dimensional finite-difference ground-water flow model A1. U.S. Geological Survey, Techniques of Water-Resources Investigations 6, Reston, VA, 1988.

[99] Metzger, D.; Kinzelbach, H.; Kinzelbach, W,: Effective dispersion of a solute cloud in a chemically heterogeneous porous medium: Comparison of two ensemble-averaging procedures. Water Resour. Res. 32 (11), 3311-3319, 1996.

[100] Miralles-Wilhelm, F.,; Gelhar, L. W.: Stochastic analysis of sorption macrokinetics in heterogeneous aquifers: Water Resour. Res. 32 (6), 1996.

[101] Naff, R.L.: Arrival times and temporal moments of breakthrough curves for an imperfectly stratified aquifer. Water Resour. Res. 28 (1), 53-68, 1992.

[102] Nagra: Kristallin I - Safety assessment report. NAGRA Technical report 93-22. Wettlingen, Juli 1994.

[103] Neuman, S. P.: Eulerian-Langrangian Theory of Transport in Space-Time Non-stationarity Velocity Fields: Nonlocal Formalism by Conditional Moments and Weak Approximation. Water Resour. Res. 29 (3), 633-645, 1993.

[104] Neuß, N.: A new sparse-matrix storage method for adaptively solving large systems of reaction-diffusion-transport equations. Computing, 68, 19-36, 2002.

[105] Noseck, U.: Gegenüberstellung einiger Langzeitsicherheitsanalysen für Endlager in Granit- und Salzformationen. Gesellschaft für Anlagen- und Reaktorsicherheit (GRS) mbH, GRS-135, Braunschweig 1996.

[106] Ohlberger, M.: A posteriori error estimates and adaptive methods for convection dominated transport processes. Dissertation: published online in FreiDok: http://www.freidok.uni-freiburg.de/volltexte/178 , Mathematische Fakultät, Universität Freiburg, 2001.

[107] Ohlberger, M.: A posteriori error estimates for finite volume approximations to singularly perturbed nonlinear convection-diffusion equations. Numer. Math. 87(4): 737-761, 2001.

[108] Ohlberger, M.: A posteriori error estimates for vertex centered finite volume approximations of convection-diffusion-reaction equations. M2AN Math. Model. Numer. Anal. 35(2): 355-387, 2001.

[109] Ohlberger, M.: A posteriori error estimate for finite volume approximations of convection diffusion problems. Proceedings of the 3nd International Symposium on: Finite Volumes For Complex Applications - Problems And Perspectives, Porquerolles (2002), 753-760, Hermes Science Publications, Paris, 2002.

[110] Ohlberger, M.: Higher order finite volume methods on selfadaptive grids for convection dominated reactive transport problems in porous media. Preprint 02-25, Mathematische Fakultät, Universität Freiburg, 2002.

[111] Ohlberger, M.; Rohde, C.: Adaptive finite volume approximations for weakly coupled convection dominated parabolic systems. IMA J. Numer. Anal. 22(2): 253-280, 2002.

[112] Parkhurst, D. L.; Thorstensen, D. C.; Plummer, L. N.: PHREEQE - A computer program for geochemical calculations. U.S. Geol. Suvey Water Resour. Invest. Rep., 80-96, 1980.

[113] Prabhakar Clement, T.: Generalized solution to multispecies transport equations coupled with a first-order reaction network. Water Resources Research 37, 1, 157-163, 2001.

[114] Projekt Sicherheitsstudien Entsorgung (PSE): Zusammenfassender Abschlußbericht, Kapitel 4, Entwicklung eines sicherheitsanalytischen Instrumentariums für das geologische Endlager für radioaktive Abfälle in einem Salzstock. Hahn-Meitner Institut, Berlin 1985.

[115] Rajaram, H.,; Gelhar, L. W.: Plume scale-dependent dispersion in heterogeneous aquifers 1. Lagrangian analysis in a stratified aquifer. Water Resour. Res. 29 (9), 3249-3260, 1993.

[116] Rajaram, H.; Gelhar, L. W.: Plume scale-dependent dispersion in heterogeneous aquifers 2. Eulerian analysis and three-dimensional aquifers. Water Resour. Res. 29 (9), 3261-3276, 1993.

[117] Robin, M. J. L.,; Gutjahr, A. L.; Wilson, J. L.: Cross-correlated random field generation with the direct Fourier transform method. Water Resour. Res. 29 (7), 2385-2397, 1993.

[118] Rumpf, M.; Preußer, T.; Lenz, M.: Vizualisation: Final Report. Institut für Mathematik, Universität Universität Duisburg-Essen, December 4, 2003.

[119] Rumynin, V. G.: Spatial variability of adsorption parameters of the Cambrian sandy aquifer: Summary of field and laboratory investigations. Internal Report 2002.

[120] Schweingruber, M.: Löslichkeits- und Speziationsberechnungen für U, Pu, Np und Th in natürlichen Grundwässern - Theorie, thermodynamische Dateien und erste Anwendungen. Eidg. Institut für reaktorforschung Würenlingen, Schweiz, EIR-Bericht 449, 1981.

[121] Severino, G.; Dagan, G.; van Duijn, C. J.: A note on transport of a pulse of non-linearly reactive solute in a heterogeneous formation. Comp. Geosciences 4, 275-286, 2000.

[122] SKI Project-90. Volume I and II. Statens Kärnkraftinspektion Swedish Nuclear Power Inspectorate Stockholm, SWEDEN, SKI Technical Report 91:23, August 1991.

Statens Karnkraftinspektion: SKI Site-94. Deep Repository Performance Assessment Project, Volume I, SKI TR 96:36, Stockholm, Dezember 1996.

Statens Karnkraftinspektion: SKI Site-94. Deep Repository Performance Assessment Project, Volume II, SKI TR 91:23, Stockholm, Dezember 1996.

[123] Smith, P. A.; Gautschi, A.; Vomvoris, S.; Zuidema, P.; Mazurek, M.: The development of a safety assessment model of the geosphere for a repository sited in the crystalline basement of northern Switzerland. J. Cont. Hydrol., 26, (309-324), 1997.

[124] Spasito, G.: The Thermodynamics of Soil Solution. Oxford University Press New York, 1981.

[125] Srivastava, R.; Brusseau, M. L.: Nonideal transport of reactive solutes in heterogeneous porous media: 1. Numerical model development and moments analysis. J. Contam. Hydrol. 24, 117-143, 1996.

[126] Srivastava, R.M.; Brusseau, L.: Nonideal transport of reactive solutes in heterogeneous porous media 2: Quantitativeanalysis of the Borden natural-gradient field experiment. J. Contam. Hydrol. 28, 115-155, 1997.

[127] Storck, R.: Die Option Salz in PAGIS: Randbedingungen, Sicherheitsberechnungen und Ergebnisse. In: PAGIS Performance Assessment of Geological Isolation Systems for Radioactive Waste, Sitzungsbericht des PAGIS-Informationstages, Madrid, 30.06.1989, EUR 12 676 DE, S. 91-101. Kommission der Europäischen Gemeinschaften, Brüssel-Luxemburg 1990.

[128] Storck, R.; Buhmann, D.; Hirsekorn, R.-P.; Kühle, T.; Lührmann, L.: Das Programmpaket EMOS zur Analyse der Langzeitsicherheit eines Endlagers für radioaktive Abfälle. Version 5. Gesellschaft für Anlagen- und Reaktorsicherheit (GRS) mbH, GRS-122, Braunschweig 1996.

[129] Strang, G.: On the construction and comparision of difference schemes. SIAM J. Numer. Anal. 5, 506-517,1968.

[130] Suckow, A.: Isotopenhydrologische und Edelgaspaläotemperatur-Untersuchungen im Deckgebirge über dem Salzstock Gorleben. Dissertation, Fakultät der Physik der Universität Heidelberg, 1993.

[131] Sudicky, E. A.: A natural gradient experiment on solute transport in a sand aquifer: Spatial variability of hydraulic conductivity and its role in the dispersion process. Water Resour. Res. 22 (13), 2069-2082, 1986.

[132] Svensk Kärnbränslehantering AB: SKB 91 - Final disposal of spent nuclear fuel. Importance of the bedrock for safety. SKB TR 92:20. May 1992.

[133] Tompson, A. F. B.: Numerical simulation of chemical migration in physically and chemically heterogeneous porous media. Water Resour. Res. 29 (11), 3709-3726, 1993.

[134] Tompson, A.F.P.; Gelhar, L.W.: Numerical simulation of solute transport in three dimensional, randomly heterogeneous porous media. Water Resour. Res. 26 (10), 2541-2562, 1990.

[135] Tompson, A.F.P.; Jackson, K.J.: Reactive transport in heterogeneous systems: An overview. Mineralogical Society of America, vol. 4 Reviews in Mineralogy 4, 269-310, Washington, D.C., 1996.

[136] Van der Zee, S.: Analytical traveling wave solutions for transport with non-linear and nonequilibrium adsorption. Water Resour. Res. 26 (10), 2563-2578, 1990.

[137] Van Duijn, C. J.; Grundy, R. E.; Dawson, C.N.: Large time profiles in reactive solute transport. Transport in Porous Media 27 (1), 57-84, 1997.Vieno T.; Hautojärvi, A.; Koskinen, L.; Nordman,H.: TVO-92 - Safety Analysis of spent Fuel Disposal. YJT-92-33 E, December 1992.

[138] Vieno, T.; Nordman, H.: TILA-96 - Interim Report on Safety Assessment of Spent Fuel Disposal. Posiva-96-17, Helsinki, December 1996.

[139] Wang, H.; Ewing, R.E.; Celia, M.A.: Eulerian-Lagrangian localized adjoint methods for reactive transport with biodegradation. Numer. Methods Partial Differ. Equations 11(3): 229-254, 1995.

[140] Weber, W. J.; McGinley, P. M.; Katz, P.M.: Sorption Phenomena in Subsurface Systems: Concepts, Models and Effects of Contaminant Fate and Transport. Water Resour. Res. 25 (5), 499-528), 1991.

[141] Weber, W. J.; McGinley, P. M.; Katz, L. E.: A Distributed Reactivity Model for Sorption by Soils and Sediments. 1. Conceptual Basis and Equilibrium Assessments. Environ. Sci. Technol. 26, 1955-1962, 1992.

[142] Wittum, G.:Multi-Grid Methods: An Introduction. Institut für Computeranwendungen, Universität Stuttgart, Preprint 95/5, 1995.

[143] Wolery, T. J.: EQ3NR, A Computer Program for Geochemical Aqueous Speciation Solubility Calculations: Theoretical Manual. User's Guide and related Documentation (Version 7.0). Lawrence Livermoore National Laboratories, Livermoore, CA, 1992.

[144] Wolery, T. J.; Daveler, S.: EQ6, A Computer Program for Reaction Path Modelling of Aqueous Geochemical Systems: Theoretical Manual. User's Guide and related Documentation (Version 7.0). Lawrence Livermoore National Laboratories, Livermoore, CA, 1992.

[145] Zheng, C.; Wang, P. P.: MT3DMS: A modular three-dimensional multi-species transport model for simulation of advection, dispersion and chemical reactions of contaminants in groundwater systems; documentation and user's guide. U.S. Army Engineer Research and Development Center ,Vicksburg , 1999.

[146] Zhang, Y.; Zhang, D.: Nonergodic solute transport in three-dimensional heterogeneous isotropic aquifers. Water Resour. Res. 32, 2955-2963, 1996.

[147] Zhang, Y.; Zhang, D.: Time-dependent dispersion of nonergodic plumes in two-dimensional heterogeneous aquifers. J. of Hydrologic Engineering 2, 91-94, 1997.

11 Nomenclature

In this chapter the notation which is used throughout this report and some definitions concerning concentrations are given.

11.1 Notation

l	superscript for dissolved radionuclides (liquid)
p	superscript for precipitated radionuclides (precipitated)
ad	superscript for sorbed radionuclides (adsorbed)
i	number of the radionuclide i,
$k(i)$	numbers of the mothers of the radionuclide i,
$e(i)$	element to which the radionuclide i belongs,
s	subscript for salt
r	subscript for rock
C_i	concentration of the ith radionuclide referring to the pore volume [mol m^{-3}]
σ_i	concentration of the ith radionuclide referring to the pore volume [kg m^{-3}]
χ_i	mass fraction of the i^{th} radionuclide [kg kg^{-1}],
χ_s	salt mass fraction [kg kg^{-1}],
ξ_i	mass fraction of the i^{th} radionuclide within immobile pore water [kg kg^{-1}],
m_i	mass of the i^{th} radionuclide [kg],
m_r	rock mass [kg],
n_i	mol number of the i^{th} radionuclide [mol],
M_i	molecular weight of the i^{th} radionuclide [kg mol^{-1}],
ρ_f	fluid density [kg m^{-3}],
ρ_r	bulk density [kg m^{-3}],

V_{por} pore volume = volume of the solution [m^3],

V_{fest} rock volume [m^3],

C_i^l concentration of the i^{th} dissolved radionuclide referring to the pore volume [mol m^{-3}]

$C_{e(i)}^l$ concentration of the dissolved element to which the i^{th} radionuclide belongs referring to the pore volume [mol m^{-3}]

C_i^{ad} concentration of the i^{th} sorbed radionuclide referring to the rock mass [mol kg^{-1}]

C_i^p concentration of the i^{th} precipitated radionuclide referring to the pore volume [mol m^{-3}],

G_i^l concentration of the i^{th} radionuclide dissolved within immobile pore water referring to the pore volume [mol m^{-3}]

G_i^{ad} concentration of the i^{th} radionuclide sorbed within immobile pore water referring to the rock mass [mol kg^{-1}]

$\boldsymbol{q}$ Darcy's velocity [m s^{-1}],

$\boldsymbol{D}^{e(i)}$ element-specific tensor of diffusion or dispersion [m^2 s^{-1}],

$\boldsymbol{D}^s$ specific tensor of diffusion or dispersion for salt [m^2 s^{-1}],

D_m molecular diffusion constant [m^2 s^{-1}],

α_L longitudinal dispersion length [m],

α_T transverse dispersion length [m],

$\boldsymbol{I}$ symmetric unity tensor,

$\boldsymbol{q}\boldsymbol{q}$ dyadic product

λ_i decay constant of the i^{th} radionuclide [s^{-1}],

$T_{1/2}^{i}$ half-life of the i^{th} radionuclide [s]

$K_d^{e(i)}$ element-specific K_d-value [$m^3\ kg^{-1}$],

$b = b^{e(i)}$ element-specific sorption constant of isotherme after Langmuir [$m^3\ mol^{-1}$],

$\kappa = \kappa^{e(i)}$ element-specific sorption capacity after Langmuir [$mol\ kg^{-1}$],

$K_{nl} = K_{nl}^{e(i)}$ element-specific sorption constant of isotherme after Freundlich [$m^3\ kg^{-1}$],

$p = p^{e(i)}$ element-specific exponent of isotherme after Freundlich [-],

$k_\alpha^{e(i)}$ element-specific reaction constant for kinetically controlled sorption [s^{-1}],

ϕ effective porosity (mobile part of aquifer) [-],

ϕ_{im} porosity of immobile part of aquifer [-] (total porosity = $\phi + \phi_{im}$),

g factor, which describes the distribution of the available rock surface between mobile and immobile pore space [-], $g \in [0,1]$

$\alpha^{e(i)}$ element-specific exchange rate after Coats-Smith [s^{-1}],

Q_i sinks or sources of the i^{th} radionuclide [$kg\ m^{-3}\ s^{-1}$],

$\tilde{Q}_i$ sinks or sources of the i^{th} radionuclide [$mol\ m^{-3}\ s^{-1}$],

$\vec{n}$ unit vector normal to a surface, oriented outward,

Γ surface of a volume.

11.2 Definition of Concentrations

There exist different ways to define concentrations. The most important in connection with the modelling of radionuclide (pollutant) transport by density driven flow are compiled in this section.

The mass m_i of i^{th} pollutant is given by:

$$m_i = n_i \cdot M_i \text{ [kg]},$$

with the mole number n_i and the molecular weight M_i.

The fluid density ρ_f in which salt and pollutants i are dissolved is stated as

$$\rho_f = \frac{m_{NaCl} + m_{H_2O} + \sum_j m_j}{V_{por}} \text{ [kg m}^{-3}\text{]}$$

If the impact of dissolved pollutants on the fluid density ρ_f is negligible the fluid density is:

$$\rho_f \approx \frac{m_{NaCl} + m_{H_2O}}{V_{por}} \text{ [kg m}^{-3}\text{].}$$

The mass fraction of the i^{th} component is given by:

$$\chi_i = \frac{m_i}{m_{NaCl} + m_{H_2O} + \sum_j m_j} \text{ [kg kg}^{-1}\text{]}$$

$$\approx \frac{m^i}{m_{NaCl} + m_{H_2O}}$$

The concentration of the i^{th} radionuclide referred to the pore volume reads

$$\sigma_i = \frac{m_i}{V_{por}} = \rho_f \chi_i \text{ [kg m}^{-3}\text{]}$$

or:

$$C_i = \frac{n_i}{V_{por}} \text{ [mol m}^{-3}\text{]}$$

From that the following connecting between χ_i, C_i, and σ_i arise:

$$C_i = \frac{\sigma_i}{M_i} = \rho_f \frac{\chi_i}{M_i} \text{ [mol m}^{-3}\text{]}$$

Analogue to that one gets the concentration C_i^{ad} for sorbed pollutant from bulk density ρ_r and the mass fraction χ_i^{ad} of the i^{th} pollutant referring to the rock mass:

$$\rho_r = \frac{m_r}{V_{fest}} \text{ [kg m}^{-3}\text{] and } \chi_i^{ad} = \frac{m_i^{ad}}{m_r + \sum_j m_j^{ad}} \approx \frac{m_i^{ad}}{m_r} \text{ [kg kg}^{-1}\text{]}$$

$$\sigma_i^{ad} = \frac{1 - \phi}{\phi} \rho_r \chi_i^{ad} = \frac{m_i^{ad}}{V_{por}} \text{ [kg m}^{-3}\text{]}$$

App. A Formulae for the Solution of Transport of a Decay Chain

Tab. A.1 Coefficients A_i^i for transport in 1D unidirectional flow

M_i^0 is the amount of substance introduced during the Delta pulse, Q_i is the flux of substance per unit time, A is the cross-section of the aquifer and $\alpha_i = \frac{1}{2\alpha_{11}}\left(1 - \sqrt{1 + \frac{4\alpha_{11}R_i(s+\lambda_j)}{u}}\right)$

Constant Dirichlet boundary condition; transient case	$A_i^i = \frac{c_i^0}{s} - \sum_{j=1}^{i-1} A_j^i$
Constant Dirichlet boundary condition; steady-state case	$A_i^i = c_i^0 - \sum_{j=1}^{i-1} A_j^i$
Delta-type Dirichlet boundary condition; transient case	$A_i^i = \frac{M_i^0}{\mu R_i A} - \sum_{j=1}^{i-1} A_j^i$
Constant Cauchy boundary condition; transient case	$A_i^i = -\frac{\alpha_i}{R_i(s+\lambda_i)}\frac{Q_i}{sA} - \frac{\alpha_i}{R_i(s+\lambda_i)}\sum_{j=1}^{i-1}\frac{R_j(s+\lambda_j)}{\alpha_j}A_j^i$
Constant Cauchy boundary condition; steady-state case	$A_i^i = -\frac{\alpha_i}{R_i\lambda_i}\frac{Q_i}{A} - \frac{\alpha_i}{R_i\lambda_i}\sum_{j=1}^{i-1}\frac{R_j\lambda_j}{\alpha_j}A_j^i$
Delta-type Cauchy boundary condition; transient case	$A_i^i = -\frac{\alpha_i}{R_i(s+\lambda_i)}\frac{M_i^0}{R_i A} - \frac{\alpha_i}{R_i(s+\lambda_i)}\sum_{j=1}^{i-1}\frac{R_j(s+\lambda_j)}{\alpha_j}A_j^i$

Tab. A.2 Formulae for analytical inversion of Laplace transformed solutions for 1D homogenous unidirectional flow

Formula in Laplace domain	Formula in time domain
$\exp\left(\frac{x}{2\alpha_{11}}\sqrt{1+\frac{4\alpha_{11}R_i(s+\lambda_j)}{u}}\right)$	$\frac{x}{t\sqrt{\frac{4\pi\alpha_{11}ut}{R_i}}}\exp\left(-\frac{x^2}{\frac{4\alpha_{11}ut}{R_i}}-\frac{ut}{4R_i\alpha_{11}}-\lambda t\right)$
$\frac{1}{s}\exp\left(\frac{x}{2\alpha_{11}}\sqrt{1+\frac{4\alpha_{11}R_i(s+\lambda_j)}{u}}\right)$	$\frac{1}{2}\left(e^{\frac{-xv}{2\alpha_{11}}}\operatorname{erfc}\left(\frac{x-uvt}{\sqrt{4\pi\alpha_{11}ut}}\right)\right.$ $\left.+e^{\frac{xv}{2\alpha_{11}}}\operatorname{erfc}\left(\frac{x+uvt}{\sqrt{4\pi\alpha_{11}ut}}\right)\right)$ with $v=\sqrt{1+\frac{4\alpha_{11}R_i\lambda_j}{u}}$
$\frac{1}{s+a}\exp\left(\frac{x}{2\alpha_{11}}\sqrt{1+\frac{4\alpha_{11}R_i(s+\lambda_j)}{u}}\right)$	$\frac{e^{-\alpha t}}{2}\left(e^{\frac{-xv}{2\alpha_{11}}}\operatorname{erfc}\left(\frac{x-uvt}{\sqrt{4\pi\alpha_{11}ut}}\right)\right.$ $\left.+e^{\frac{xv}{2\alpha_{11}}}\operatorname{erfc}\left(\frac{x+uvt}{\sqrt{4\pi\alpha_{11}ut}}\right)\right)$ with $v=\sqrt{1+\frac{4\alpha_{11}R_i(\lambda_j-a)}{u}}$

The calculation of the results for the decay chain is performed by means of the calculation tool MATLAB. The explicit MATLAB-codes can be downloaded from *http://www.ihw.ethz.ch/soft/decay.html*.

Tab. A.3 Coefficients A_i^i for transport in 2D unidirectional flow
M_j^0 denotes the mass input during Delta pulse and $\dot{M}_j^0$ is the source strength.

Constant point source; transient case	$A_i^i = \frac{1}{s2\pi\phi du\sqrt{\alpha_{11}\alpha_{22}}} \sum_{j=1}^{i-1} \left(\prod_{p=j}^{i-1} \frac{R_p\lambda_p}{R_p(s+\lambda_p)} \right) \dot{M}_j^0 - R_i(s+\lambda_i) \sum_{j=1}^{i-1} \frac{A_j^i}{R_j(s+\lambda_j)}$
Constant point source; steady-state case	$A_i^i = \frac{1}{2\pi\phi du\sqrt{\alpha_{11}\alpha_{22}}} \sum_{j=1}^{i-1} \dot{M}_j^0 - k_i \sum_{j=1}^{i-1} \frac{A_j^i}{k_j}$
Delta-type point source; transient case	$A_i^i = \frac{1}{2\pi\phi du\sqrt{\alpha_{11}\alpha_{22}}} \sum_{j=1}^{i} \left(\prod_{p=j}^{i-1} \frac{R_p\lambda_p}{R_p(s+\lambda_p)} \right) M_j^0 - R_i(s+\lambda_i) \sum_{j=1}^{i-1} \frac{A_j^i}{R_j(s+\lambda_j)}$

Tab. A.4 Formulae for analytical inversion of Laplace transformed solutions for 2D homogenous unidirectional flow

Formula in Laplace domain	Formula in time domain
$K_0\left(\frac{\sqrt{\left(1+\frac{4\alpha_{11}R_i(s+\lambda_i)}{u}\right)\left(x^2+\frac{\alpha_{11}}{\alpha_{22}}y^2\right)}}{2\alpha_{11}}\right)$	$\frac{1}{2t}\exp\left(-\frac{x^2+\frac{\alpha_{11}}{\alpha_{22}}y^2}{4\alpha_{11}\frac{ut}{R_i}}-\frac{u^2t}{4D_{11}R_i}-\lambda t\right)$
$\frac{1}{s}K_0\left(\frac{\sqrt{\left(1+\frac{4\alpha_{11}R_i(s+\lambda_i)}{u}\right)\left(x^2+\frac{\alpha_{11}}{\alpha_{22}}y^2\right)}}{2\alpha_{11}}\right)$	$\frac{1}{2}H\left(\frac{x^2+\frac{\alpha_{11}}{\alpha_{22}}y^2}{4\alpha_{11}\frac{ut}{R_i}},\frac{\sqrt{\left(1+\frac{4\alpha_{11}R_i\lambda_i}{u}\right)\left(x^2+\frac{\alpha_{11}}{\alpha_{22}}y^2\right)}}{2\alpha_{11}}\right)$
$\frac{1}{s+a}K_0\left(\frac{\sqrt{\left(1+\frac{4\alpha_{11}R_i(s+\lambda_i)}{u}\right)\left(x^2+\frac{\alpha_{11}}{\alpha_{22}}y^2\right)}}{2\alpha_{11}}\right)$	$\frac{e^{-at}}{2}H\left(\frac{x^2+\frac{\alpha_{11}}{\alpha_{22}}y^2}{4\alpha_{11}\frac{ut}{R_i}},\sqrt{\frac{\left(1+\frac{4\alpha_{11}R_i\lambda_i}{u}\right)\left(x^2+\frac{\alpha_{11}}{\alpha_{22}}y^2\right)}{2\alpha_{11}}}\right)$
	$H(x,y)=\int_x^\infty\frac{1}{t}\exp\left(-\left(t-\frac{y^2}{4t}\right)\right)dt$ Hantush-function

Tab. A.5 Coefficients A_i^i for transport in 3D unidirectional flow

Constant point source; transient case	$A_i^i = \frac{1}{s4\pi\phi\sqrt{u^3\alpha_{11}\alpha_{22}\alpha_{33}}} \sum_{j=1}^{i} \left(\prod_{p=j}^{i-1} \frac{R_p\lambda_p}{R_p(s+\lambda_p)} \right) \dot{M}_j^0 - R_i(s+\lambda_i) \sum_{j=1}^{i-1} \frac{A_j^i}{R_j(s+\lambda_j)}$
Constant point source; steady-state case	$A_i^i = \frac{1}{4\pi\phi\sqrt{u^3\alpha_{11}\alpha_{22}\alpha_{33}}} \sum_{j=1}^{i} \dot{M}_j^0 - R_i\lambda_i \sum_{j=1}^{i-1} \frac{A_j^i}{R_j\lambda_j}$
Delta type point source; transient case	$A_i^i = \frac{1}{4\pi\phi\sqrt{u^3\alpha_{11}\alpha_{22}\alpha_{33}}} \sum_{j=1}^{i} \left(\prod_{p=j}^{i-1} \frac{R_p\lambda_p}{R_p(s+\lambda_p)} \right) M_j^0 - R_i(s+\lambda_i) \sum_{j=1}^{i-1} \frac{A_j^i}{R_j(s+\lambda_j)}$

Tab. A.6 Formulae for analytical inversion of Laplace transformed solutions for 3D homogenous unidirectional flow

Formula in Laplace domain	Formula in time domain
$\exp\left(\frac{\sqrt{\left(1+\frac{4\alpha_{11}(R_i(s+\lambda_i))}{u}\right)\left(x^2+\frac{\alpha_{11}}{\alpha_{22}}y^2+\frac{\alpha_{11}}{\alpha_{33}}z^2\right)}}{2\alpha_{11}}\right)$	$\frac{\sqrt{x^2+\frac{\alpha_{11}}{\alpha_{22}}y^2+\frac{\alpha_{11}}{\alpha_{33}}z^2}}{t\sqrt{4\pi\alpha_{11}\frac{ut}{R_i}}}\times$ $\exp\left(\frac{x^2+\frac{\alpha_{11}}{\alpha_{22}}y^2+\frac{\alpha_{11}}{\alpha_{33}}z^2}{4\alpha_{11}\frac{ut}{R_i}}\right)\times$ $\exp\left(-\frac{ut}{4\alpha_{11}R_i}-\lambda t\right)$
$\frac{1}{s}\exp\left(\frac{\sqrt{\left(1+\frac{4\alpha_{11}(R_i(s+\lambda_i))}{u}\right)\left(x^2+\frac{\alpha_{11}}{\alpha_{22}}y^2+\frac{\alpha_{11}}{\alpha_{33}}z^2\right)}}{2\alpha_{11}}\right)$	$\frac{1}{2}\left(e^{\frac{-rv}{2\alpha_{11}}}erfc\left(\frac{r-vt}{\sqrt{4\alpha_{11}ut}}\right)+ e^{\frac{rv}{2\alpha_{11}}}erfc\left(\frac{r+vt}{\sqrt{4\alpha_{11}ut}}\right)\right)$ $r=\sqrt{x^2+\frac{\alpha_{11}}{\alpha_{22}}y^2+\frac{\alpha_{11}}{\alpha_{33}}z^2}$ $v=\sqrt{1+\frac{4\alpha_{11}R_i\lambda_i}{u}}$
$\frac{1}{s+a}\exp\left(\frac{\sqrt{\left(1+\frac{4\alpha_{11}(R_i(s+\lambda_i))}{u}\right)\left(x^2+\frac{\alpha_{11}}{\alpha_{22}}y^2+\frac{\alpha_{11}}{\alpha_{33}}z^2\right)}}{2\alpha_{11}}\right)$	$\frac{e^{-at}}{2}\left(e^{\frac{-rv}{2\alpha_{11}}}erfc\left(\frac{r-vt}{\sqrt{4\alpha_{11}ut}}\right)+ e^{\frac{rv}{2\alpha_{11}}}erfc\left(\frac{r+vt}{\sqrt{4\alpha_{11}ut}}\right)\right)$ $r=\sqrt{x^2+\frac{\alpha_{11}}{\alpha_{22}}y^2+\frac{\alpha_{11}}{\alpha_{33}}z^2}$ $v=\sqrt{1+\frac{4\alpha_{11}R_i(\lambda_i-a)}{u}}$

Tab. A.7 Coefficients A_i^i for transport in 2D and 3D radial flow
M_i^0 are the mass inputs during delta pulse and Q is the water inflow rate at the origin. Γ denotes the gamma function

Constant boundary condition; transient case	$A_i^i = \frac{c_i^0}{s\bar{\Omega}_i(s,0)} - \frac{1}{\bar{\Omega}_i(s,0)} \sum_{j=1}^{i-1} \bar{\Omega}_i(s,0) A_j^i$
Constant boundary condition; steady-state case	$A_i^i = \frac{c_i^0}{s\bar{\Omega}_i(0,0)} - \frac{1}{\bar{\Omega}_i(0,0)} \sum_{j=1}^{i-1} \bar{\Omega}_i(0,0) A_j^i$
Delta type boundary condition; transient case	$A_i^i = \frac{M_i^0}{QR_i\bar{\Omega}_i(s,0)} - \frac{1}{\bar{\Omega}_i(s,0)} \sum_{j=1}^{i-1} \bar{\Omega}_i(s,0) A_j^i$
2D radial flow	$\bar{\Omega}_i(s,0) = \mathrm{Ai}\left(\frac{1}{4}\left(\frac{G}{\alpha_r^2 R_i(s+\lambda_i)}\right)^{\frac{2}{3}}\right)$
3D radial flow	$\bar{\Omega}_i(s,0) = \sqrt{\pi}\frac{\left(\frac{R_i(s+\lambda_i)}{\alpha_r G}\right)^{\frac{1}{8}}}{\Gamma\left(\frac{3}{4} + \frac{1}{16}\sqrt{\frac{G}{\alpha_r^3 R_i(s+\lambda_i)}}\right)}$

App. B Correlation Function in 1D and 2D

A Gaussian shaped correlation function with anisotropic correlation lengths l_x in horizontal and l_y in vertical direction of the medium is given as

$$w_{ij}(\boldsymbol{x} - \boldsymbol{x}') = \sigma_f^2 \bar{u}^2 P_{ij}(\boldsymbol{x} - \boldsymbol{x}')$$
$$\exp\left(-\frac{(x_1 - x'_1)^2}{l_x^2}\right)\exp\left(-\frac{(x_2 - x'_2)^2}{l_y^2}\right)\exp\left(-\frac{(x_3 - x'_3)^2}{l_y^2}\right) \qquad \text{(B.1)}$$

Here, σ_f^2 is the variance of the log-conductivity fields. The operator P_{ij} ensures divergence free velocity fields.

In order to explicitly calculate the two-dimensional correlation function (B.1) we apply the projector P_{ij} to the Gauss-shaped kernel. Thus, the correlation functions can be written as the following integral expressions

$$w_{ij}(\boldsymbol{x}) = \sigma_f^2 \bar{u}^2 \left\{ \exp\left(-\frac{\boldsymbol{x}^2}{2l_0}\right)\delta_{1i}\delta_{1j} - \partial_{x_1}\partial_{x_2}\left(\exp\left(-\frac{\boldsymbol{x}^2}{2l_0}\right) * G(\boldsymbol{x})\right)\delta_{1j} \right.$$
$$\left. - \partial_{x_1}\partial_{x_2}\left(\exp\left(-\frac{\boldsymbol{x}^2}{2l_0}\right)G(\boldsymbol{x})\right)\delta_{1i} - \partial_{x_1}\partial_{x_2}\partial_{x_i}\partial_{x_j}\left(\exp\left(-\frac{\boldsymbol{x}^2}{2l_0}\right) * (G(\boldsymbol{x}) * G(\boldsymbol{x}))\right)\right\} \qquad \text{(B.2)}$$

where $G(\boldsymbol{x})$ is the Green's function of the Laplace problem:

$$\nabla^2 G(\boldsymbol{x},\boldsymbol{x}') = \delta^d(\boldsymbol{x} - \boldsymbol{x}'). \qquad \text{(B.3)}$$

The convolution integrals in expression (B.2) can be solved using the technique presented in [28]. Explicit results can be evaluated only for an isotropic medium as a function of $r = \sqrt{x_1^2 + x_2^2}$, x_1 and x_2. The longitudinal correlation function in this case becomes

$$
\begin{aligned}
w_{11}(x_1,x_2) \;=\; \sigma_f^2\bar{u}^2\Bigg\{ & \exp\left(-\frac{r^2}{l_0^2}\right)+\frac{l_0^2}{4}\Bigg[\left(-\frac{1}{r^2}-\frac{4x_1^2}{r^4}+\frac{8x_1^4}{r^6}\right.\\
& \left.-\frac{l_0^2}{r^4}+\frac{24l_0^2x_1^2}{r^6}-\frac{24l_0^2x_1^4}{r^8}\right)\\
& +\exp\left(-\frac{r^2}{l_0^2}\right)\Bigg(-\frac{8x_1^2}{l_0^2r^2}+\frac{4x_1^4}{l_0^2r^4}-\frac{20x_1^2}{r^4}+\frac{4}{r^2}\\
& \left.+\frac{16x_1^4}{r^6}+\frac{3l_0^2}{r^4}-\frac{24l_0^2x_1^2}{r^6}+\frac{24l_0^2x_1^4}{r^8}\right)\Bigg]\Bigg\}
\end{aligned}
\qquad \text{(B.4)}
$$

The expression for the correlation function in transverse direction is evaluated as

$$
\begin{aligned}
w_{22}(x_1,x_2) \;=\; \sigma_f^2\bar{u}^2\frac{l_0^2}{2}\Bigg\{ & \left(\frac{1}{r^2}-\frac{24(x_1^2+x_2^2)}{r^4}+\frac{8x_1^2x_2^2}{r^6}\right.\\
& \left.-\frac{l_0^2}{r^4}+\frac{4l_0^2(x_1^2+x_2^2)}{r^6}-\frac{24l_0^2x_1^2x_2^2}{r^8}\right)\\
& +\exp\left(-\frac{r^2}{l_0^2}\right)\Bigg(\frac{x_1^2x_2^2}{l_0^2r^4}-\frac{2(x_1^2+x_2^2)}{r^4}-\frac{16x_1^2x_2^2}{r^6}\\
& \left.+\frac{l_0^2}{r^4}-\frac{4l_0^2(x_1^2+x_2^2)}{r^6}+\frac{24l_0^2x_1^2x_2^2}{r^8}\right)\Bigg\}
\end{aligned}
\qquad \text{(B.5)}
$$

These results are used in sections 5.2.2 and 5.2.4 and for evaluation of the semi-analytical results in lowest order perturbation theory.

The longitudinal correlation function (B.4) can easily be simplified to transport in one spatial dimension:

$$
w_{11}(x_1) \;=\; \sigma_f^2\bar{u}^2\left\{\exp\left(-\frac{x_1^2}{l_0^2}\right)+\frac{l_0^2}{4}\left(\frac{3}{x_1^2}-\frac{l_0^2}{x_1^4}\exp\left(-\frac{x_1^2}{l_0^2}\right)\left(\frac{4}{l_0^2}+\frac{3l_0^2}{l_0^2r^4}\right)\right)\right\}. \qquad \text{(B.6)}
$$

App. C Derivation of the Ensemble Averaged Dispersion in the Purely Advective Case

Expression (5.13) can be evaluated using a standard mathematical program such as MAPLE or MATHEMATICA. The result is written by means of the general hypergeometric function $F(a,b,z)$:

$$D_{11}^{\mathrm{ens}}(t) = \frac{\sqrt{\pi}}{2}\sigma_f^2 \bar{u} l_0 \left\{ -p^{p-1}\left(\frac{\tau_{adv}}{t}\right)^p \left(\frac{3}{2} - F\left(\left[-1+\frac{p}{2(1-p)}\right],\left[\frac{p}{2(1-p)}\right],-z(t)\right)\right)\right.$$

$$+ p^{-p}\frac{(1-p)^{p-1}}{2-p}\left(\frac{t}{\tau_{adv}}\right)^p F\left(\left[\frac{1}{2},1+\frac{p}{2(1-p)}\right],\left[\frac{3}{2},2+\frac{p}{2(1-p)}\right],-z(t)\right) \qquad \text{(C.1)}$$

$$\left. -p^{\frac{p(3-p)}{1-p}}(1-p)^{3(1-p)}\left(\frac{\tau_{adv}}{t}\right)^{3p}\left(1-F\left(\left[\frac{p}{2(1-p)}\right],\left[1+\frac{p}{2(1-p)}\right],-zt\right)\right)\right\}$$

where

$$z(t) = \frac{1}{2}p^{-2p}(1-p)^{-2(1-p)}\left(\frac{t}{\tau_{adv}}\right)^p \qquad \text{(C.2)}$$

and τ_{adv} given in (5.16).

For $t \to \infty$ this expression approaches the asymptotic value, given in formula (5.15).

The pre-asymptotic behaviour of D_{11}^{eff} can be calculated in the same manner.

App. D Concentration Dependence of the Effective Dispersion

The inverse function of $\tilde{F}^*(c,\exp(\mu_x),\sigma_x^2)$ is found to be

$$\begin{aligned}&\tilde{F}^*(C,\exp(\mu_x),\sigma_x^2)\\ &= \exp\left(\frac{1}{2\sigma_x^2\exp(\mu_x)}(-2-\sigma_x^2\exp(\mu_x)+\right.\\ &\quad\left.+\sqrt{4+2\sigma_x^2\exp(\mu_x)\left(1+2\ln\left(\frac{C}{k_d}\right)+\sigma_x^4\exp(2\mu_x)\right)}\right)\end{aligned} \qquad (D.1)$$

and depends on the statistical properties of the random field. This result can be used for further calculation of the effective transport behaviour and the effective dispersion coefficient.

Expression (5.68) is evaluated using the mathematical software MAPLE. Inserting the expressions for the inverse functions F^* and F and performing integration with respect to C, the result can be written as:

$$\begin{aligned}\xi(\boldsymbol{y}) &= 1-\frac{2\exp\left(\frac{1}{2\sigma_x^2}\left(2\mu_x\sigma_x^2+2\exp(2\mu_x)+\sigma_x^2\exp(-\mu_x)\right)\right)}{\sqrt{4+4\sigma_x^2\exp(\mu_x)\left(1+2\ln\left(\frac{C}{k_d}\right)\right)}}\times\\ &\times\frac{\exp\left(-\frac{1}{2\sigma_x^2}\left(-\exp(2\mu_x)\sqrt{4+4\sigma_x^2\exp(\mu_x)\left(1+2\ln\left(\frac{C}{k_d}\right)\right)}\right)\right)}{\sqrt{4+4\sigma_x^2\exp(\mu_x)\left(1+2\ln\left(\frac{C}{k_d}\right)\right)}}\times\\ &\times p(\boldsymbol{y})C^{-\frac{1}{p(\boldsymbol{y})}}\\ &= 1-\delta D\left(\ln\left(\frac{C}{k_d}\right),\exp(\mu_x),\sigma_x^2\right)p(\boldsymbol{y})C^{-\frac{1}{p(\boldsymbol{y})}}\end{aligned} \qquad (D.2)$$

Expanding $C^{-\frac{1}{p(\boldsymbol{y})}}$ in Taylor series and averaging over a stochastic ensemble, in lowest order one obtains

$$\overline{\chi(\boldsymbol{y})\xi(\boldsymbol{y})} \quad = \quad \delta D\left(\ln\left(\frac{C}{k_d}\right), \exp(\mu_x), \sigma_x^2\right) \overline{\chi(\boldsymbol{y}) p(\boldsymbol{y})}. \qquad \text{(D.3)}$$

Thus, the effective dispersion coefficient can be written as

$$\boldsymbol{D}^{\text{eff}}(c_0) \quad = \quad \boldsymbol{D} \; + \; \delta D\left(\ln\left(\frac{C}{k_d}\right), \exp(\mu_x), \sigma_x^2\right) \overline{\chi(\boldsymbol{y}, c_0) p(\boldsymbol{y})} \qquad \text{(D.4)}$$

by replacing C by

$$C \quad = \quad k_d C_0^{\exp(\mu_x)\left(1 \; + \; \frac{\sigma_x^2}{2}\exp(\mu_x)\left(1 \; + \; \ln\left(\frac{c_0}{c^{in}}\right)\exp(\mu_x)\right)\right)} \qquad \text{(D.5)}$$

in the expression for $\delta D\left(\ln\left(\frac{C}{k_d}\right), \exp(\mu_x), \sigma_x^2\right)$.

App. E Publications

Papers

Attinger, S.; Dimitrova Micha, J.; Kinzelbach, W.: Transport of a Nonlinear Adsorbing Solute in Heterogeneous Porous Media I: Analytical Results. Water Resources Research (submitted).

Attinger, S.; Dimitrova Micha, J.; Kinzelbach, W.: Multiscale modeling of nonlinearly adsorbing solute transport. SIAM Multiscale Model. Simul. 3 (1), 408-431, 2003.

Bauer, P.; Attinger, S., Kinzelbach, W.: Transport of a Decay Chain in Homogeneous Porous Media: Analytical Solutions. Journal of Contaminant Hydology 49, 217-239, 2001.

Bürkle, D.; Ohlberger, M.: Adaptive finite volume methods for displacement problems in porous media. Computing and Visualization in Science 5(2): 95-106, 2002. cp Proceedings of Algorithmy 2000, 28-36, 2000.

Bürkle, D.; Preußer, T.; Rumpf, M.: Transport and Anisotropic Diffusion in Time-Dependent Flow Visualization. Proceedings IEEE Visualization, 2001.

Dimitrova Micha, J.; Attinger, S.; Kinzelbach, W.: Transport of a Nonlinear Adsorbing Solute in Heterogeneous Porous Media II: Numerical Results. Water Resources Research (submitted).

Dimitrova Micha, J.; Attinger, S.; Kinzelbach, W.: Influence of chemical heterogeneity on the large-scale transport of nonlinearly adsorbing solutes. (in preparation), 2003.

Dimitrova Micha, J.; Attinger, S.; Kinzelbach, W.: Modeling of Ensemble and Real Mixing Behavior for Nonlinearly Adsorbing Transport. (submitted to Advances in Water Resources), 2003.

Dimitrova Micha, J.; Attinger, S.; Kinzelbach, W.: Note on the transport of non-linearly reactive solute in a single heterogeneous formation. (submitted to Nuclear Science and Engineering), 2003.

Feuchter, D.; Stemmermann, U.; Wittum, G.: Description and generation of geometies and grids for layered domains. Proceedings of the 17th GAMM-Seminar, Leipzig, 2001.

Frolkovič, P.: Computational simulations of radionuclides transport in double porosity medium with adsorption. Computer methods for engineering in porous media flow and transport. Besancon, France, July 2000. CEMRACS, Marseille, France, August 2000.

Frolkovič, P.: Flux-based method of characteristics for complex transport problems. Mathematical and Computational Issues in the Geosciences. Boulder, Colorado, USA, June 2001.

Frolkovič, P.: Flux-based method of characteristics for contaminant transport in flowing groundwater. Computing and Visualization in Sience 5, 2, 73-83, 2002.

Frolkovič, P.: Flux-based methods of charactistics for transport problems in groundwater flows induced by sources and sinks. In Hassanizadeh, S. M.; Schotting, R. J.; Gray, W. G.; Pinder, G. F. (eds.): Computational Methods in Water Resources 2, 979-986, Elsvier, 2002.

Frolkovič, P.: Flux-based methods of characteristics for complex transport problems in porous medium. Algoritmy, Podbanske, Slovakia, September 2002.

Frolkovič, P.: Solving large systems of coupled parabolic transport and reaction problems. Mathematical and Computational Issues in the Geosciences, Austin, USA, March 2003.

Frolkovič, P.: Flux-based methods of characteristics for coupled transport equations in porous media. Computing and Visualization in Sience, (to appear), 2004.

Frolkovič, P.; Geiser, J.: Numerical Simulations of Radionuclides Transport in Double Porosity Media with Sorption. In Handlovicova, A. et al. (eds.): Algoritmy 2000, 28-36, Slovak University of Technology, Bratislava, 2000.

Frolkovič, P.; Geiser, J.: Transport of Radionuclides in Flowing Groundwater. Algoritmy, Podbanske, Slovakia, September 2001.

Frolkovič, P.; Geiser, J.: Discretization Methods with Discrete Minimum and Maximum Property for convection Dominated Transport in Porous Media. In Dimov, I. et al. (eds.), Numerical Methods and Applications, Lecture Notes in Computer Science 2542, 445-453,Springer-Verlag, Berlin Heidelberg, 2004.

Frolkovič, P.; Geiser, J.; Lampe, M.: Transport von Radionucliden im fliessenden Wasser, WIR-Baden-Württemberg, Stuttgart, Oktober 2001.

Frolkovič, P.; Mikula, K.: Flux-based level set method: A finite volume method for evolving interfaces. IWR Interdisziplinäres Zentrum für Wissenschaftliches Rechnen, Universität Heidelberg, Preprint 15, 2003.

Fuchs, A.: Almost Regular Triangulations of Trimmed NURBS-Solids. Engineering with Computers 17: 55-65, 2001.

Fuchs, A.; Wittum, G.: Arte - a grid generator for the domains with thin layers. Preprint , IWR, Universität Heidelberg, (to appear), 2003.

Geiser, J.: Numerical simulation of radionuclide transport. Algoritmy, Podbanske, Slovakia, September 2000.

Geiser, J.: Numerical simulation of a model for transport and reaction of radionuclides. In Margenov, S.; Wasniewski, J.; Yalamov, P. (eds.), Large Scale Scientific Computations of Engineering and Environmental Problems, 487-496, Springer, 2001.

Geiser, J.: Modified discretization methods for system of transport equation in porous media and applications. NMA, Borovets, Bulgaria, August 2002.

Geiser, J.: Numerical Simulation of a Model for Transport and Reaktion of Radionuclides with an Explicit Coupling Method between Transport and Reaction. Proceedings of Algoritmy 2002 Conference on Scientific Computing, Vysoke Tatry, Podbanske, September 8-13, 2002.

Geiser, J.: Numerical simulations of a model for transport and reaction of radionuclides. Hilbert-Conference, Kaliningrad, Russia, September 2002.

Geiser, J.: Numerical simulations of radioactive contaminants transport in flowing groundwater with locally adapted multi-level grids. European Multigrid Conference, Hohenwart, Germany, October 2002.

Geiser, J.: Discretisation methods for convection-diffusion-reaction equations and applications done with the parallel program-tool r^3t. Parallel Adaptive Computing, Hohenwart, Germany, November 2003.

Haasdonk, B.; Ohlberger, M.; Rumpf, M.; Schmidt, A.; Siebert, K.G.: Multiresolution visualization of adaptive finite element simulations. Computing 70, 3, 181-204, 2003.

Herbin, R.; Ohlberger, M.: A posteriori error estimate for finite volume approximations of convection diffusion Problems. Proc. of 3rd International Symposium on: Finite Volumes for Complex Applications - Problems and Perspectives. Porquerolles, 753-760, Hermes Penton Ltd, 2002.

Kacur, J.; Frolkovič, P.: Semi-analytival solutions for contaminant transport with non-linear sorption in 1 D. Preprint 2002 - 24, Interdisziplinäres Zentrum für Wissenschaftliches Rechnen der Universität Heidelberg, 2002.

Karlsen, K.H.; Ohlberger, M.: A note on the uniqueness of entropy solutions of non-linear degenerate parabolic equations. J. Math. Anal. Appl., 275(1): 439-458, 2002.

Klöfkorn, R.; Kröner, D.; Ohlberger, M.: Local adaptive methods for convection dominated problems. Internat. J. Numer. Methods Fluids, 40(1-2): 79-91, 2002.

Kröner, D.; Küther, M.; Ohlberger, M.; Rohde, C.: A posteriori error estimates and adaptive methods for hyperbolic and convection dominated parabolic conservation laws.
In: Kirkilionis, M.; Krömker, S.; Rannacher, R.; Tomi, F. (Eds.): Trends in Non-linear Analysis, 289-306, Springer Berlin/Heidelberg , 2003.

Küther, M,; Ohlberger, M.: Adaptive second order central schemes on unstructured staggered grids. In: Hou, T. Y.; Tadmor, E. (Eds.): Hyperbolic Problems: Theory, Numerics, Applications. 675-684, Pasadena, 2002.

Lampe, M.: Using MPPs for on-line visualization of Large-Scale Scientific Simulations. USNCCM, Albuquerque, USA, July 2003.

Mikula, K.; Preußer, T.; Rumpf, M.: Morphological image sequenceprocessing. Computing and Visualization in Science, to appear, 2003.

Ohlberger, M.: A posteriori error estimates for finite volume approximations to singularly perturbed nonlinear convection-diffusion equations. Numer. Math. 87(4): 737-761, 2001.

Ohlberger, M.: A posteriori error estimates for vertex centered finite volume approximations of convection-diffusion-reaction equations. M2AN Mathematical Modelling and Numerical Analysis 35(2): 355-387, 2001.

Ohlberger, M.: A posteriori error estimate for finite volume approximations of convection diffusion problems. Proceedings of the 3nd International Symposium on: Finite Volumes For Complex Applications - Problems And Perspectives, Porquerolles, 753-760, Hermes Science Publications, Paris, 2002.

Ohlberger, M.: Higher order finite volume methods on selfadaptive grids for convection dominated reactive transport problems in porous media. Preprint 02-25, Mathematische Fakultät, Universität Freiburg, Computing and Visualization in Science (accepted for publication) 2002.

Ohlberger, M.; Rohde, C.: Adaptive finite volume approximations for weakly coupled convection dominated parabolic systems. IMA Journal of Numerical Analysis 22(2): 253-280, 2002.

Preußer, T.; Rumpf, M.: A Level Set Method for Anisotropic Geometric Diffusion in 3D Image Processing. SIAM Journal Applied Mathematics, (submitted).

Preußer, T.; Rumpf, M.: Extracting motion velocities from 3D image sequences and coupled spatio-temporal smoothing. In Proc. SPIE Visual Data Analysis, 2003.

Wittum, G.: Multigrid methods for density driven flow and transport. IMA, USA, 2002.

Theses

Bauer, P.: Transport einer Zerfallskette im porösen Medium: Analytische Lösungen und deren Anwendung. Master's thesis, ETH Zürich, 1999.

Ohlberger, M.: A posteriori error estimates and adaptive methods for convection dominated transport processes. Dissertation: published online in FreiDok: http://www.freidok.uni-freiburg.de/volltexte/178, Mathematische Fakultät, Universität Freiburg, 2001.

Dimitrova Micha, J.: Transport of Nonlinearly Adsorbing Solutes in Heterogeneous Porous Media. Eidgenössische Technische Hochschule Zürich, Ph.D. Thesis No. 15171, 2003.

Geiser, J.: Diskretisierungsverfahren für Systeme von Konvektions-Diffusions-Dispersions-Reaktionsgleichungen und Anwendungen. PhD Thesis, 2004.

Lampe. M.: Parallele Visualisierung - Ein Vergleich. PhD Thesis, 2004.

App. F Meetings

During the life-span of the project the following events were organised:

event	date	place	organizer
1. Statusgespräch	March 10.1999	Heidelberg	Prof. Wittum
2. Statusgespräch	September 30- October 1, 1999	Braunschweig	GRS
3. Statusgespräch	March 28-29, 2000	Freiburg	Prof. Kröner
4. Statusgespräch	November 8-9, 2000	Zürich	Prof. Kinzelbach
5. Statusgespräch	June 26-27, 2001	Bonn	Prof. Rumpf
6. Statusgespräch	November 28-30,2001	Braunschweig	GRS
7. Statusgespräch	June 4-6, 2002	Zürich	Prof. Kinzelbach
8. Statusgespräch	September 18, 2002	Heidelberg	Prof. Wittum

Table of Figures

List of Tables